Government of Western Australia

Department of
Mines and Petroleum

REPORT
113

AN INTEGRATED GEOLOGICAL AND GEOPHYSICAL STUDY OF THE WEST ARUNTA OROGEN AND ITS MINERAL PROSPECTIVITY

by A Joly, MC Dentith, A Porwal, CV Spaggiari, IM Tyler, and TC McCuaig

ROYALTIES FOR REGIONS
EXPLORATION INCENTIVE SCHEME

Centre for EXPLORATION TARGETING

Geological Survey of Western Australia

Government of **Western Australia**
Department of **Mines and Petroleum**

REPORT 113

AN INTEGRATED GEOLOGICAL AND GEOPHYSICAL STUDY OF THE WEST ARUNTA OROGEN AND ITS MINERAL PROSPECTIVITY

by
A Joly[1], MC Dentith[1], A Porwal[1,2], CV Spaggiari, IM Tyler, and TC McCuaig[1]

[1] **Centre for Exploration Targeting, The University of Western Australia, Crawley WA 6009, Australia**

[2] **Indian Institute of Technology Bombay, Powai, Mumbai 400076, India**

Perth 2013

Geological Survey of Western Australia

MINISTER FOR MINES AND PETROLEUM
Hon. Bill Marmion MLA

DIRECTOR GENERAL, DEPARTMENT OF MINES AND PETROLEUM
Richard Sellers

EXECUTIVE DIRECTOR, GEOLOGICAL SURVEY OF WESTERN AUSTRALIA
Rick Rogerson

REFERENCE
The recommended reference for this publication is:
Joly, A, Dentith, MC, Porwal, A, Spaggiari, CV, Tyler, IM and McCuaig, TC 2013, An integrated geological and geophysical study of the west Arunta Orogen and its mineral prospectivity: Geological Survey of Western Australia, Report 113, 89p.

National Library of Australia Cataloguing-in-Publication entry

Author:	A. Joly ... (et al.)
Title:	An integrated geological and geophysical study of the west Arunta Orogen and its mineral prospectivity
ISBN:	9781741684384
Subjects:	Geology–Western Australia. Geology, Stratigraphic–Proterozoic. Metamorphic rocks–Western Australia. Orogeny–Western Australia
Other Authors/Contributors:	Joly, A. Geological Survey of Western Australia
Series:	Report (Geological Survey of Western Australia); 113
Dewey Number:	551.820941

ISSN 0508–4741

Grid references in this publication refer to the Geocentric Datum of Australia 1994 (GDA94). Locations mentioned in the text are referenced using Map Grid Australia (MGA) coordinates, Zone 52. All locations are quoted to at least the nearest 100 m.

Copy editor: SR White
Cartography: CS Schroder
Desktop publishing: RL Hitchings
Printed by Images on Paper, Perth, Western Australia

Published 2013 by Geological Survey of Western Australia
This Report is published in digital format (PDF), as part of a digital dataset, and is available online at <www.dmp.wa.gov.au/GSWApublications>.

Further details of geological publications and maps produced by the Geological Survey of Western Australia are available from:
Information Centre
Department of Mines and Petroleum
100 Plain Street
EAST PERTH WESTERN AUSTRALIA 6004
Telephone: +61 8 9222 3459 Facsimile: +61 8 9222 3444
www.dmp.wa.gov.au/GSWApublications

Cover photograph: Aerial view of outcrops of the Mount Webb Granite, east of Kiwirrkurra.

Contents

Figures

Tables

Appendix

An integrated geological and geophysical study of the west Arunta Orogen and its mineral prospectivity

by

A Joly[1], MC Dentith[1], A Porwal[1,2], CV Spaggiari, IM Tyler, TC McCuaig[1]

Abstract

There has been minimal mineral exploration in the Paleoproterozoic west Arunta Orogen and in its cover rocks, located in remote east-central Western Australia. In this study, an integrated geological–geophysical approach, incorporating all available geoscientific data, was used to interpret the gross structure and deformation history of the region. The resulting geological and geophysical maps were then used for a GIS-based prospectivity analysis based on the mineral systems approach.

The west Arunta Orogen is interpreted as a basement-involved, thick-skinned, fold–thrust terrain with fault blocks comprising both the Paleoproterozoic basement and rocks from overlying sedimentary basins. Two major deformation events control the current architecture of the west Arunta Orogen. The earliest (D_1) trend west-northwest, and are controlled by the Central Australian Suture (CAS), which has a long and complex history. Reactivation of D_1 structures during the Alice Springs Orogeny was mostly responsible for the present structural configuration, modified by northeast-trending D_2 structures at or near the margins of the Neoproterozoic Murraba Basin and Phanerozoic Canning Basin.

Reconnaissance-scale mineral prospectivity mapping for gold, uranium, and sediment-exhalative (SedEx) style base-metal mineralization incorporates spatial analysis techniques for data integration and analysis. The targeting criteria selected were based on a mineral systems model for deposit formation and the approach used involves production of a series of predictor maps based on the occurrence of geological features associated with the relevant model. Each predictor map was then related to metal source, fluid pathways, and chemical and physical trap zones.

For the gold prospectivity analysis, both a knowledge-driven fuzzy model and a data-driven weights-of-evidence (WofE) model were implemented. The output from both analyses was compared in order to identify the most prospective areas for gold exploration in the west Arunta Orogen along the Central Australian Suture and the D_1 structures. One of these areas contains known gold mineralization.

A knowledge-driven prospectivity analysis was carried out for unconformity-related uranium, surficial uranium, and SedEx lead–zinc deposits. Data-driven analyses were not implemented for these deposit types because there are very few known occurrences in the area. Potential targets for unconformity-related uranium deposits in the west Arunta Orogen highlight very similar areas to the prospectivity analysis for gold. Lake Mackay appears to be the best area in which to conduct further investigation for surficial uranium deposits. A few areas prospective for SedEx deposits were identified, although the west Arunta Orogen does not appear very prospective for this type of deposit due of the low lead and zinc values in the available geochemical dataset, as well as the absence of evaporite in the area analysed.

KEYWORDS: GIS, structural terranes, gold, uranium, base metals, mineralization, mineral prospectivity, geochemical data, Central Australian Suture, west Arunta Orogen, Western Australia

[1] Centre for Exploration Targeting, The University of Western Australia, Crawley WA 6009, Australia

[2] Indian Institute of Technology Bombay, Powai, Mumbai 400076, India

Introduction

The Exploration Incentive Scheme (EIS) is a Western Australian State Government initiative that aims to encourage exploration in Western Australia for the long-term sustainability of the State's resources sector. Through the EIS, the Geological Survey of Western Australia (GSWA) is delivering new, high-quality, exploration-relevant geoscientific datasets to industry for selected greenfields areas in the State. It has been recognized that a series of targeting products can help junior-to-mid-sized exploration companies translate the geoscientific datasets into actual ground acquisition, and aid critical decision-making for drill targets.

GSWA contracted the Centre for Exploration Targeting (CET) at The University of Western Australia to provide exploration targeting products, on a terrane-by-terrane basis. The exploration targeting products include a study of the 4D architecture of each terrane based on an integration of geological and geophysical data, a mineral system analysis of selected commodities and mineral deposit types, and the creation of a series of exploration targeting products.

The first area in Western Australia to be analysed in this fashion is the west Arunta Orogen. The three principal objectives of this collaborative project are: 1) to define the present day geometry in 3D and then understand the 4D evolution of the terrane, based on an interpretation of all available geoscientific datasets; 2) to determine which deposit types are most likely to be present in the west Arunta Orogen; 3) to identify the most prospective areas for each deposit type in the study area using prospectivity analysis based on the understanding of relevant mineralizing systems and the geological synthesis. Prospectivity analysis has been undertaken in the west Arunta Orogen for orogenic and intrusive gold, surficial and unconformity-style uranium, and sediment-exhalative (SedEx) type base metals.

The aim of this project is an improved understanding of the geology and mineralization potential of the west Arunta Orogen, and the generation of a series of targeting products that can be used by explorers in the area.

Geological and tectonic history of the Arunta Orogen

The west Arunta Orogen is the western-most part of the Arunta Orogen (equivalent to the Arunta Region in the Northern Territory), and lies across the Western Australian – Northern Territory border, centred on approximately 22.4° S and 128° E (Fig. 1). The area is extremely remote and outcrop is poor. As a consequence, the geology is poorly understood. Equivalent rocks in the Northern Territory extend over a much larger area and have been the subject of significant study. Consequently, much that is known or inferred about the west Arunta Orogen is based on studies undertaken within the Northern Territory.

The geology of the west Arunta Orogen was mapped by Wells (1968) and Blake (1977) for the MacDonald and Webb 1:250 000-scale geological map sheets, respectively, and is very briefly described by Myers (1990). Wyborn et al. (1998) undertook U–Pb zircon geochronology and geochemistry on granites and felsic volcanic rocks, and mafic dykes in the area. Abeysinghe (2003) briefly described the few known occurrences of mineralization. More recently, Spaggiari et al. (2008) described new exploration datasets from the area, which are the foundation of much of the work comprising this report.

The North Australian Craton

The northern parts of Western Australia, the Northern Territory, and Queensland are underlain by the North Australian Craton (NAC; Plumb, 1979; Plumb et al.,

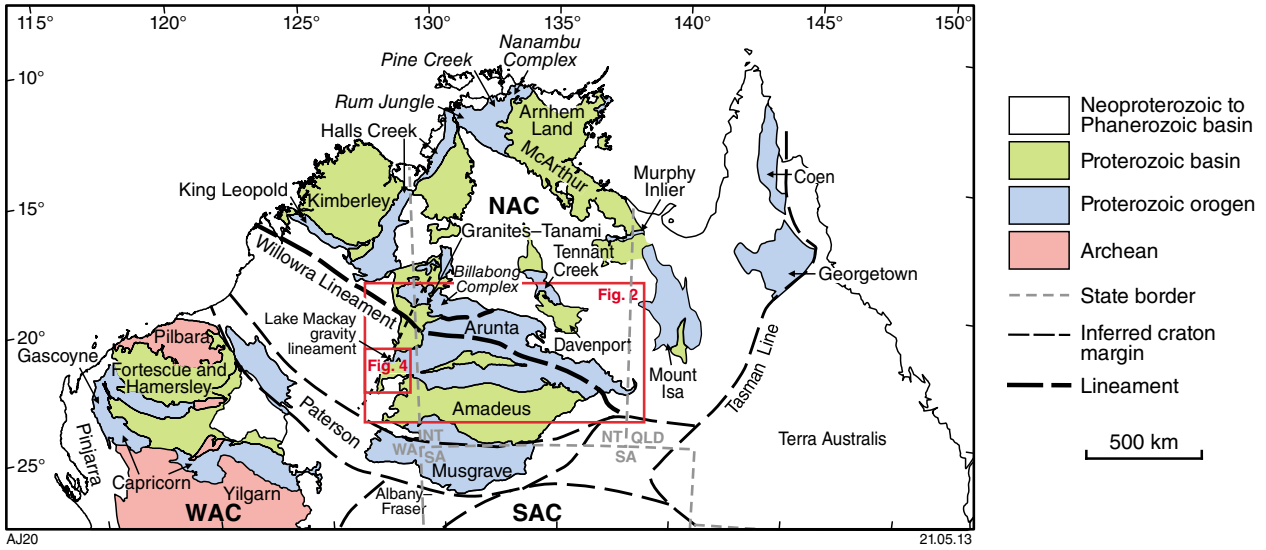

Figure 1. Location of Archean terrains and cratonic boundaries in the North Australian Craton (modified from Bagas et al., 2010). The West, South, and North Australian Cratons are labeled, respectively, WAC, SAC, and NAC. The location of Figures 2 and 4 are shown by red frames

1981; Myers et al., 1996). The Arunta Orogen occupies the southernmost part of the craton (Fig. 1). The NAC extends north to the Australian coast and underlies at least part of the adjoining continental shelf (Cawood and Korsch, 2008). The NAC is bounded to the south and southwest by the Musgrave and Paterson Orogens, and to the east by the Terra Australis Orogen (Fig. 1).

The NAC includes Neorchean to Paleoproterozoic cratonic elements (e.g. Rum Jungle, Nanumbu, and Billabong complexes) between Paleoproterozoic orogens (e.g. Halls Creek, King Leopold, Pine Creek, Mount Isa, Tennant Creek, Granites–Tanami, Georgetown, Coen, and Arunta). Late Paleoproterozoic basins (e.g. Kimberley, Victoria River, and McArthur), as well as Proterozoic and Phanerozoic cover successions, conceal relationships between the orogens and the cratonic elements.

Limited exposures of the Archean basement of the NAC occur in the Pine Creek, Tanami, and west Arnhem Land regions, with ages ranging from 2.67 Ga to 2.50 Ga (Page et al., 1995; Cross et al., 2005; Worden et al., 2008; Hollis et al., 2008, 2009). The nature of the basement remains unclear across much of the NAC, although geophysical (Shaw et al., 1995) and isotopic (Shaw and Black, 1991; Zhao and McCulloch, 1995) evidence suggests that Neoarchean to Paleoproterozoic continental crust is widespread.

The Arunta Orogen

The Arunta Orogen (Fig. 2) includes both basement and overlying basin sequences. Studies in the Northern Territory have shown that the Arunta Orogen has a complex stratigraphic, structural, and metamorphic history extending from the Paleoproterozoic to the Paleozoic (Collins and Shaw, 1995; Mawby et al., 1999; Hand and Buick, 2001; Scrimgeour and Raith, 2001a; Buick et al., 2001; Claoué-Long and Hoatson, 2005). The orogen comprises three distinct, largely fault-bounded, east–west-oriented provinces with distinct protolith ages and histories (Scrimgeour, 2004): the 1840–1710 Ma Aileron Province (the largest), the exotic 1690–1600 Ma Warumpi Province, and the Neoproterozoic to Cambrian Irindina Province (Fig. 2). The Aileron Province is separated from the Granites–Tanami Orogen to the north by the extension of the Willowra Lineament (Fig. 1). A negative aeromagnetic response partly coincides with the Willowra Gravity Ridge, which may represent a paleosuture zone formed at c. 1864 Ma (Bagas et al., 2008).

The oldest outcropping rocks recognized in the Aileron Province (Fig. 2) are polydeformed psammitic and pelitic rocks, the 1840–1835 Ma Lander Rock Formation (Scrimgeour, 2006a). These were intruded by igneous rocks during two major events (Fig. 3): the Stafford Event (1810–1790 Ma), which produced voluminous granitic and lesser mafic intrusions and marked the onset of a long-lived, north-dipping subduction at the southern NAC margin, and the Yambah Event (1780–1770 Ma), which produced similar magmatism during dominantly compressional deformation related to back-arc closure (Scrimgeour, 2006b). The Stafford Event is characterized by high temperature, low pressure metamorphism due to high heat flow from felsic and mafic magmatism, and both extensional and compressional structures (Scrimgeour, 2006b).

During the Yambah Event and subsequent Inkamulla Event (Fig. 3) that span the period 1780–1745 Ma, back-arc basin closure was followed by renewed back-arc to arc magmatism mainly to the south and then southeast, accompanied by back-arc basin sedimentation, localized high temperature and low pressure metamorphism, and deformation (Maidment et al., 2005; Scrimgeour, 2006a,b). Granitic rocks produced during this time include calc-alkaline to trondhjemitic plutons, which have subduction-related magmatic affinities (Zhao and McCulloch, 1995). Between 1730–1700 Ma, the eastern

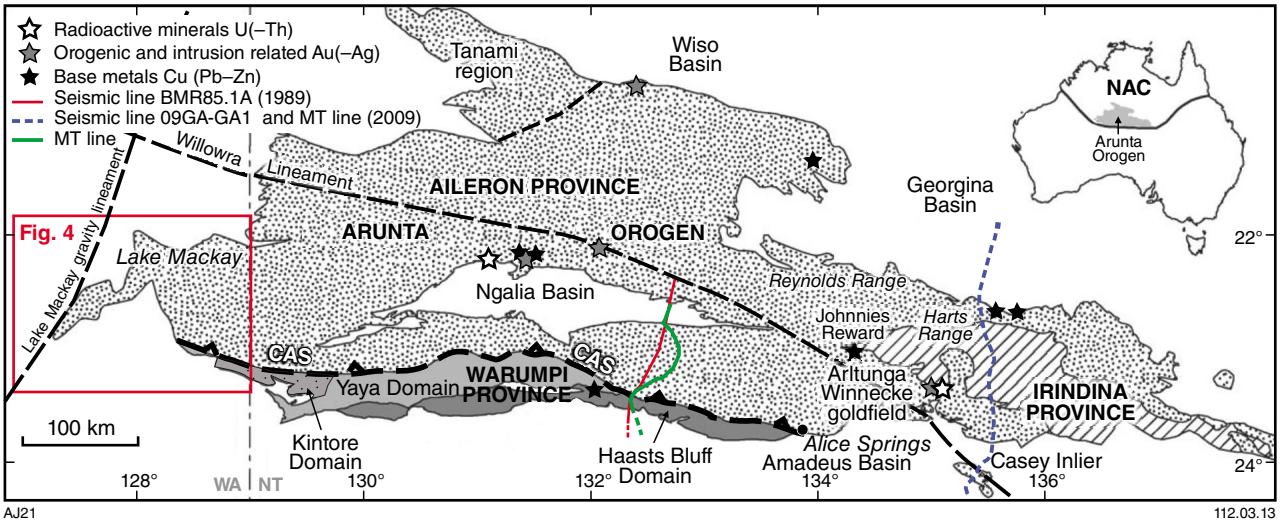

Figure 2. Map of the Arunta Orogen, showing the Warumpi Province and the location of the area in Figure 4 (modified from Scrimgeour et al., 2005a). Inset shows the location of the Arunta Orogen within the North Australian Craton (NAC). CAS: Central Australian Suture. Red, green, and blue-dashed line traces correspond to the magnetotelluric and seismic survey locations (Goleby et al., 1988; Selway et al., 2009; Korsch et al., 2011)

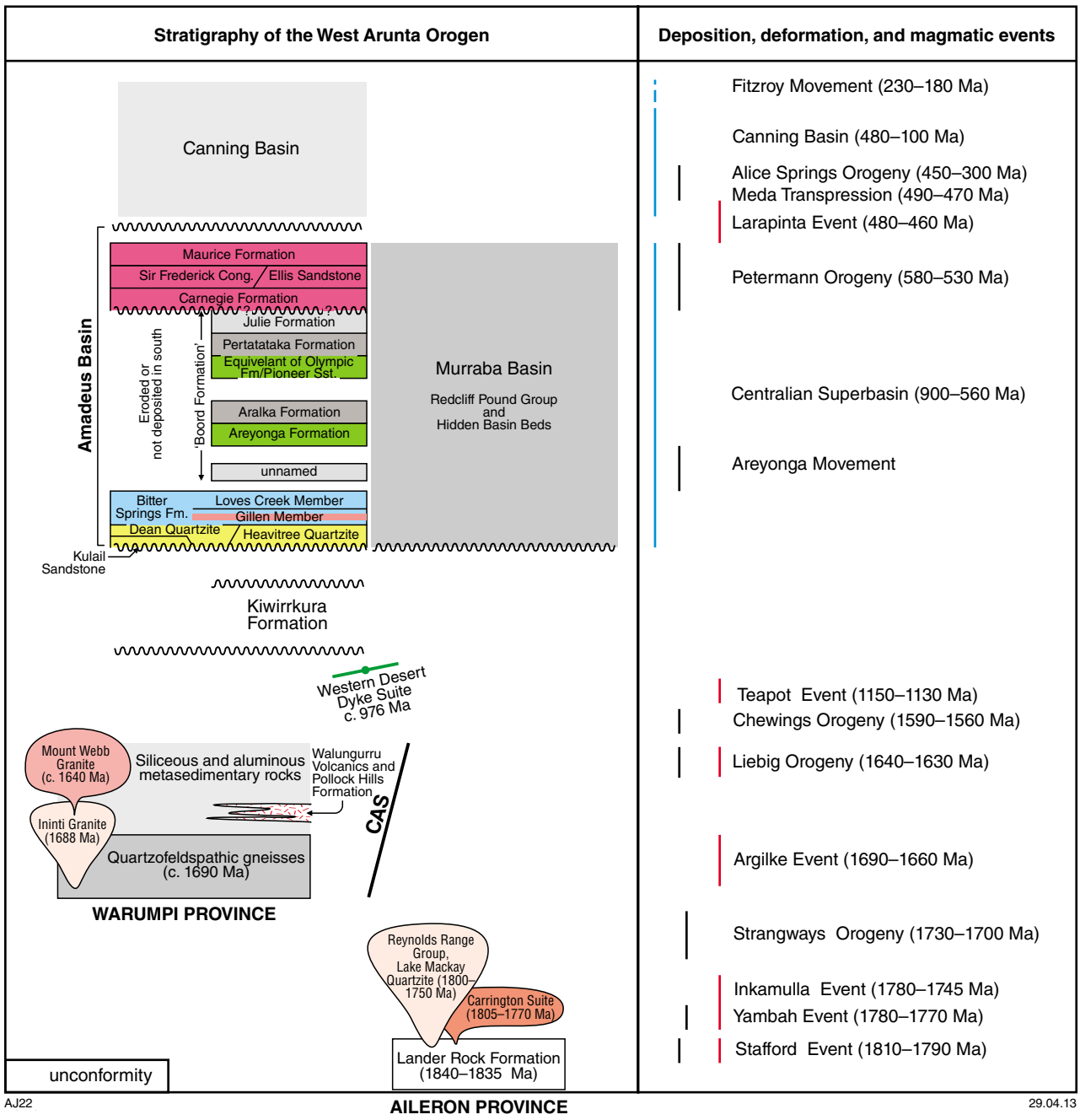

Figure 3. **Schematic sketch of the stratigraphy of the west Arunta Orogen, and deposition, deformation, and magmatic episodes in the Arunta Region, some of which have been identified in the west Arunta Orogen. CAS: Central Australian Suture. Deposition events correspond to blue lines, deformation events to black lines, and magmatism to red lines**

part of the Arunta Orogen was affected by another major, high-grade metamorphic event, the Strangways Orogeny, that may have marked collision and the termination of north-dipping subduction (Fig. 3; Norman and Clarke, 1990; Scrimgeour, 2006b).

The Irindina Province (Fig. 2) comprises highly deformed granites that are structurally interleaved with the upper amphibolite to granulite facies metasedimentary and metavolcanic rocks of the Harts Range Metamorphic Complex (Maidment et al., 2002). Dominating the Irindina Province, this complex comprises granulite-facies pelite, psammite, metamafic rocks, and calc-silicate rocks of Neoproterozoic to Cambrian age; these are time equivalents of the adjacent Amadeus and Georgina Basins (Maidment, 2005; IR Scrimgeour, written comm.). A zone of orthogneiss near the northern margin of outcrop, previously mapped as Harts Range Group, has been found to be Paleoproterozoic in age, and is therefore part of the Aileron Province (Buick et al., 2001; Maidment et al., 2002). Megacrystic gneiss within an area mapped as Irindina Gneiss in the northern Harts Range (Fig.2), and similar granitic gneiss in the southeastern Harts Range, have SHRIMP U–Pb zircon ages of 1745 ± 6 Ma and 1746 ± 6 Ma, respectively (Maidment, 2005). These are the oldest gneisses dated in the area.

The southernmost part of the Arunta Orogen is the Warumpi Province (Fig. 2), which consists of three fault-bounded domains of variable metamorphic grade and distinct protolith ages: the largely amphibolite facies Haasts Bluff Domain in the south, the dominantly granulite facies Yaya Domain in the north, and the smaller greenschist facies Kintore Domain to the west (Scrimgeour et al., 2005a; Close et al., 2006). The Warumpi Province has been interpreted as a continental magmatic arc that formed outboard of the NAC during the period 1690–1660 Ma, and was subsequently accreted to its southern margin (Scrimgeour et al., 2005a; Close et al., 2006; IR Scrimgeour, written comm.).

The Warumpi and Aileron provinces are separated by a series of major faults and shear zones that have been collectively termed the Central Australian Suture (CAS; Figs 2 and 4; Close et al., 2004; Scrimgeour et al., 2005a). This suture is interpreted to have initially formed during the 1640–1630 Ma Liebig Orogeny, a major tectonothermal event interpreted to be the result of oblique accretion of the Warumpi Province onto the NAC (Scrimgeour et al., 2005a; IR Scrimgeour, written comm.). The dominance of 1690–1635 Ma magmatism south of the suture has been interpreted to reflect south-dipping subduction at this time, which is also supported by magnetotelluric imaging (Scrimgeour et al., 2005a; Selway et al., 2009; IR Scrimgeour, written comm.). Deformation and metamorphism was strongly partitioned in the Warumpi Province during the Liebig Orogeny — indicative of oblique accretion — with some parts undergoing compression and deep burial followed by rapid exhumation, while other parts remained at shallower crustal levels or underwent extension (Close et al., 2005; Scrimgeour et al., 2005a).

The Redbank Thrust Zone (RTZ; Shaw and Black., 1991), or Redbank Thrust system (Biermeier et al., 2003), is a major, north-dipping, crustal-scale structure that is part of the CAS (Figs 2 and 4) that has had at least two major episodes of movement: the first at amphibolite-facies, most likely during the 1590–1560 Ma Chewings Orogeny (Fig. 3), and the second at greenschist-facies during the intracratonic, 450–300 Ma Alice Springs Orogeny (Shaw and Black, 1991; Biermeier et al., 2003; IR Scrimgeour, written comm.). A north-northeasterly trending feature visible in potential field data for the region was termed the Lake Mackay gravity lineament by Shaw et al. (1984). The lineament appears to be associated with a major structure that marks the western limit of the Arunta Orogen, and also the southeastern extent of the Canning Basin. The Lake Mackay gravity lineament could extend northwards to the Granites–Tanami Orogen (Shaw et al., 1991).

The Chewings Orogeny (Fig. 3) is largely characterized by south-directed thrusting and tectonic transport, mylonitic deformation (Teyssier et al., 1988; Vry et al., 1996), and granulite-facies metamorphism throughout much of the central and southern Arunta Region (Rubatto et al., 2001; Hand and Buick, 2001). In the Warumpi Province, metamorphism associated with this event varies from greenschist to upper amphibolite facies (Scrimgeour, 2006b). No known magmatism is associated with this event. The southern half of the Arunta Region was also affected by the Teapot Event during the period 1150–1130 Ma, a mainly thermal and magmatic event represented by local intrusions and resetting of isotopic systems (Claoué-Long and Hoatson, 2005; Scrimgeour, 2006b).

The c. 560 Ma Petermann Orogeny in central Australia occurred at about the same time as the King Leopold Orogeny in the Kimberley to the north, and the Paterson Orogeny at the northeastern edge of the Pilbara Craton to the west (Tyler, 2005). These linked events gave rise to a widespread unconformity prior to extrusion of c. 508 Ma Cambrian basaltic rocks of the extensive Kalkarindji Continental Flood Basalt Province that originally extended across 300 000 km^2 of northern Australia (Hanley and Wingate, 2000; Glass and Phillips, 2006). The 560–460 Ma mafic magmatic Larapinta Event (Fig. 3) is recognized in the fault-bounded Irindina Province to the east (Buick et al., 2001; Maidment et al., 2005).

The last major event to have affected much of the Arunta Region was the intracratonic Alice Springs Orogeny (Fig. 3), a long-lived compressional event that spanned the period 450–300 Ma (Korsch and Lindsay, 1989; Shaw et al., 1992a; Dunlap and Tessyier, 1995; Haines et al., 2001; Scrimgeour, 2006b). The orogeny produced south-vergent thrusting, folding, and substantial reworking of the CAS (Scrimgeour, 2006b). During thrusting of parts of the Warumpi Province, the basement was interleaved with overlying Heavitree Quartzite and Bitter Springs Formation of the Amadeus Basin, particularly in the eastern parts of the Arunta Region (Flöttmann and Hand, 1999), although this may also be the case in the west Arunta Orogen. A major decollement has been interpreted within the Bitter Springs Formation, with thin-skinned deformation interpreted at higher structural levels (Flöttmann and Hand, 1999). In the Belt Range and the Amunurunga Range on the Mt Liebig 1: 250 000-scale

map sheet in the Northern Territory, basement-cored asymmetric folds and steeply dipping thrusts are interpreted to represent thicker skinned deformation (Scrimgeour et al., 2005b).

The west Arunta Orogen

The west Arunta Orogen is that part of the Arunta Region west of longitude 129° E, i.e. within Western Australia (Figs 2 and 4). The dominant structural feature is the west-northwest trending CAS, which is expressed as a broad, sinuous fault zone that defines the boundary between the Aileron Province to the north and the much smaller Warumpi Province to the south. The west Arunta Orogen is unconformably overlain by sedimentary rocks of the Amadeus, Murraba, and Canning basins. Its western extent coincides with the Lake Mackay gravity lineament (Figs. 1, 2, and 4).

The oldest exposed rocks of the Aileron Province are part of the Lander Rock Formation (Fig. 3), comprising polydeformed psammitic and pelitic rocks, and minor, interbedded banded iron-formation. Limited exposures of metabasalt, metarhyolite, and metavolcaniclastic rocks just north of the CAS have been tentatively included in the Lander Rock Formation (GSWA, 2009b), but they have not been mapped in detail or dated, and may be fault slivers of the younger Walungurru Volcanics of the Warumpi Province (Fig. 3). The Lander Rock Formation contains detrital zircons with dominantly 1880–1840 Ma age components, along with a minor component extending back to the Neoarchean (Fig. 5; Claoué-Long and Hoatson, 2005; Claoué-Long et al., 2008; Kirkland et al., 2009a). In the Northern Territory, the formation is intruded by 1810–1790 Ma igneous rocks associated with the Stafford Event (Claoué-Long and Hoatson, 2005; Claoué-Long and Edgoose, 2008), but there are no known exposures of these rocks in the west Arunta Orogen.

The Lander Rock Formation is intruded in the west Arunta Orogen by granitic rocks of the Carrington Suite (Fig. 3; 1805–1770 Ma; Edgoose et al., 2008), such as the Dwarf Well Granite (Figs. 4 and 5), dated at 1773 ± 6 Ma (Kirkland et al., 2009b). This age also coincides with the Yambah Event. The Dwarf Well Granite is overlain

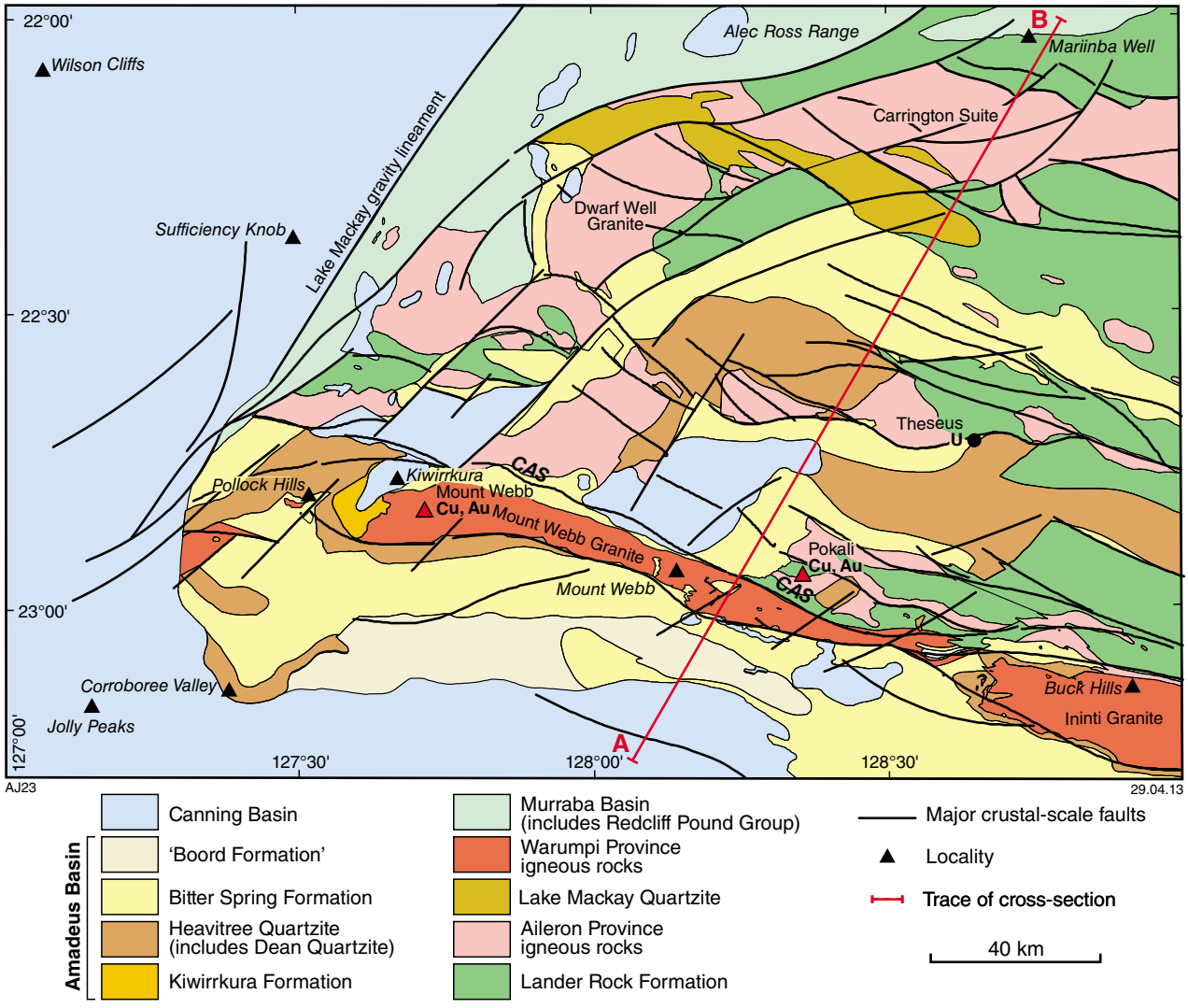

Figure 4. Geological map of the west Arunta Orogen. CAS: Central Australian Suture; A–B: trace of the modelled gravity profile (Fig. 22). The geology is a simplified version of the interpreted bedrock geology in GSWA (2009b)

by deformed and strongly recrystallized quartzite (Lake Mackay Quartzite; Figs. 4 and 5), which has a maximum depositional age of 1750 ± 19 Ma, significant age components at c. 1849, 1964, and 2307 Ma, and several minor age components spanning the range 2695–1750 Ma (Kirkland et al., 2009c; Fig. 5). This quartzite may correlate with the Reynolds Range Group (Fig. 3), which has a maximum depositional age of 1798 ± 10 Ma (Claoué-Long et al., 2008), or may be younger.

The Warumpi Province in the west Arunta Orogen is dominated by greenschist-facies rocks of the Kintore Domain (Fig. 2). These rocks are variably deformed; some have no pervasive fabric, whereas others have strong fabrics or are mylonitic, particularly near the CAS. The oldest rocks are high-K, calc-alkaline granites emplaced during the Argilke Igneous Event, interpreted as part of a continental arc that formed outboard of the NAC between 1690 and 1660 Ma (Close et al., 2005; IR Scrimgeour, written comm.). These rocks include the Ininti Granite (Fig. 3), which, in the west Arunta Orogen, is a strongly foliated metasyenogranite containing metasedimentary xenoliths and pegmatite veins parallel to the foliation. Zircons from this metasyenogranite yielded an igneous crystallisation age of 1691 ± 5 Ma (Kirkland et al., 2009d), which is identical within error to the Ininti Granite dated in the Northern Territory at 1688 ± 8 Ma (Worden et al., 2008).

The granitic rocks intrude and are overlain by supracrustal rocks that include felsic and intermediate volcanic and volcaniclastic rocks (Walungurru Volcanics and Pollock Hills Formation), and the Mount Webb Granite. The Walungurru Volcanics are a succession of volcanic and volcaniclastic rocks with a wide range of felsic, intermediate, and mafic compositions that have an overall calc-alkaline affinity (IR Scrimgeour, written comm.). In the west Arunta Orogen, zircons from a massive metarhyodacite with well-preserved igneous textures form a single population that has an age of 1650 ± 4 Ma, interpreted as the age of magmatic crystallization of the rhyodacite (Kirkland et al., 2009e).

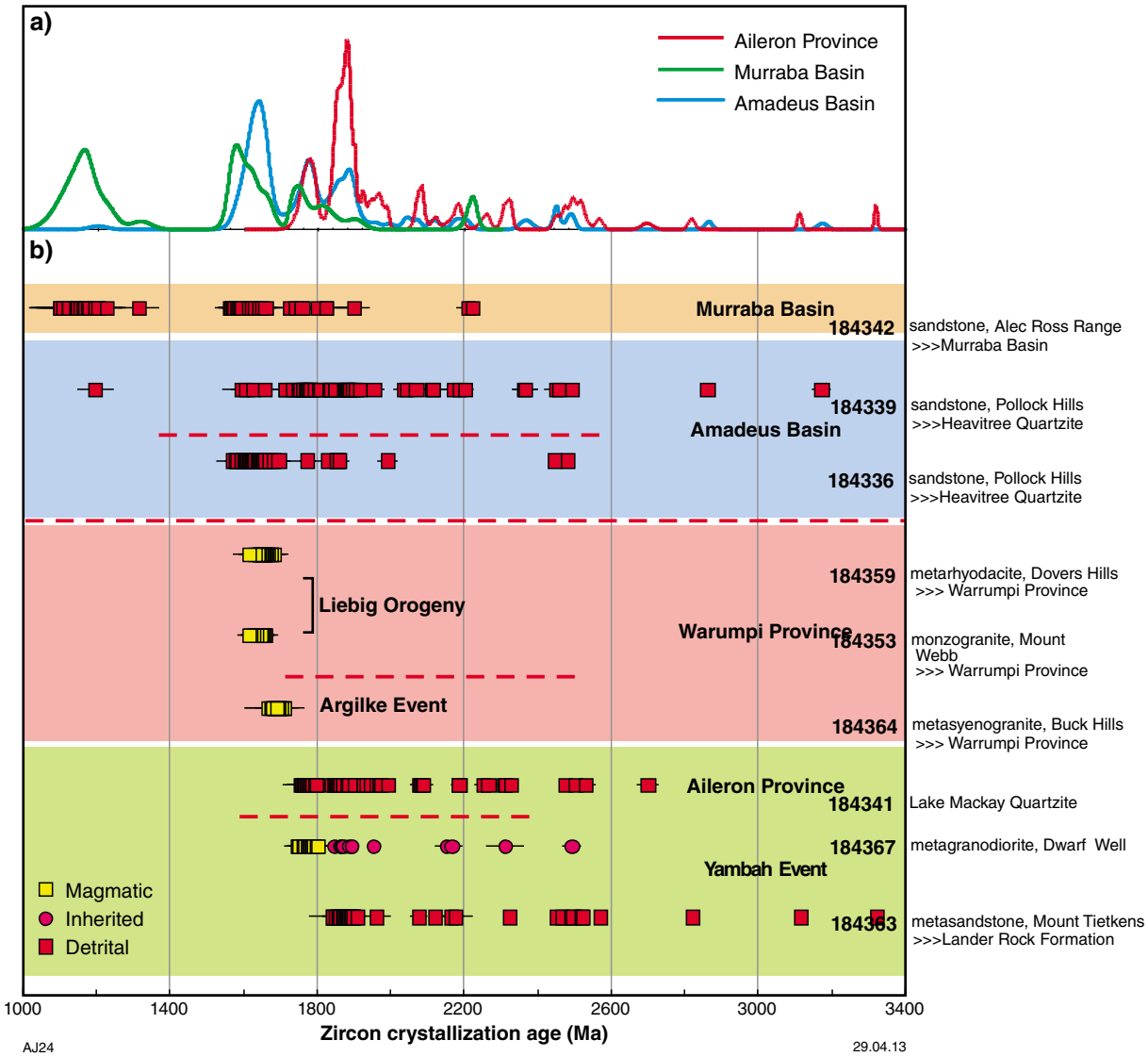

Figure 5. Detrical zircon age data for the west Arunta Orogen: a) detrital zircon age component spectra for rocks from the Aileron Province, Murraba and Amadeus Basins; b) time–space diagram showing SHRIMP U–Pb ages from the Murraba and Amadeus Basins, and Warumpi and Aileron Provinces (data from Kirkland et al., 2009a–i).

The Pollock Hills Formation was inferred to have formed coevally with intrusion of the Mount Webb Granite at c. 1640 Ma (Wyborn et al., 1998), but has recently given a U–Pb zircon age of c. 1670 Ma (Wingate, 2012). The formation consists of metadacitic and metarhyodacitic volcanic rocks, mostly with well-preserved igneous textures, and associated volcaniclastic rocks. Zircons from three samples of the Mount Webb Granite have yielded SHRIMP U–Pb ages of 1643 ± 4, 1639 ± 5, and 1639 ± 5 Ma (Wyborn et al., 1998). More recently, zircons from a biotite–hornblende monzogranite, yielded an age of 1640 ± 7 Ma, interpreted as the age of magmatic crystallization (Fig. 5; Kirkland et al., 2009f). The Mount Webb Granite has been interpreted to have locally been subjected to extensive magmatic sodic–calcic and sericitic alteration (Wyborn et al., 1998).

Fault rocks affected by substantial volumes of fluid crop out just south of the CAS, and also adjacent to Mount Webb (Figs 3 and 4). The protoliths of these rocks are unrecognizable in the field due to hydrothermal alteration, but there is some indication that they may have been granitic and dacitic rocks. They exhibit quartz stockwork veining, hydrothermal brecciation with jigsaw fit, biotite veins, and cataclastic textures (Spaggiari et al., 2008).

Granitic and volcanic rocks of the Warumpi Province in the west Arunta Orogen have been intruded by the newly named, northwesterly trending Western Desert Dyke Suite that crop out mostly east of Kiwirrkura. Baddleyite from these dolerite dykes has been dated at 972 ± 8 Ma, while zircons have yielded an age of 976 ± 3 Ma (Wyborn et al., 1998). These dykes are about 100 million years younger than the Stuart Pass Dolerite dykes farther east, dated at 1076 ± 33 Ma with a well-defined Sm–Nd mineral isochron (Zhao and McCulloch, 1993).

Unconformable cover sequences

Murraba Basin

The Aileron Province is unconformably overlain in the north by part of the approximately 2000 m thick, gently folded, sedimentary succession of the Neoproterozoic Murraba Basin. This is dominated by siliciclastic rocks, mainly quartzite with conglomerate, shale, siltstone, limestone, chert, mudstone, and dolostone. In the west Arunta Orogen, coarse-grained to pebbly sandstones that are part of this basin are exposed in the Alec Ross Range (Fig. 4) where they are locally folded and faulted, and unconformably overlie the Lander Rock Formation. These rocks are assigned to the Munyu Sandstone, part of the Redcliff Pound Group (Fig. 3). Detrital zircons have yielded a maximum depositional age of 1155 ± 14 Ma (conservative estimate based on 15 analyses), with significant age components at c. 1161, 1575, 1743, and 1808 Ma (Fig. 5a), and minor components in the range 2222–1099 Ma (Fig. 5; Kirkland et al., 2009g). The Murraba Basin probably correlates with the lower Amadeus Basin succession although evaporites and carbonates equivalent to the Bitter Springs Formation have not been found (Grey, 1990; Tyler, 2005).

Amadeus Basin

The Amadeus Basin is an east–west trending structural remnant of the extensive intracratonic Centralian Superbasin (e.g. Walter et al., 1995; Haines et al., 2001; Korsch and Kennard, 1991; Fig. 3). In the Northern Territory, the Neoproterozoic succession is overlain by a thick Paleozoic succession, but in Western Australia only small outliers of Paleozoic rocks are known, and most of the succession is Neoproterozoic to Cambrian in age (Haines et al., 2010). Recent work in Western Australia has shown strong lithostratigraphic similarities with well-defined units in the Neoproterozoic to early Cambrian part of the basin in the Northern Territory (Haines et al., 2010).

The Kiwirrkura Formation, a succession of red-weathering lithic sandstone, quartz sandstone, and conglomerate that outcrops in the Pollock Hills, west of Kiwirrkura (Fig. 4), was formerly thought to be part of the Paleoproterozoic Pollock Hills Formation (Blake, 1977). However, most of the detritus making up the Kiwirrkura Formation appears to be sourced locally from the Pollock Hills Formation. Detrital zircons, which have yielded a maximum depositional age of 1570 ± 22 Ma, have significant age components at c. 1855 and 1640 Ma, and several minor components spanning the range 2482–1570 Ma (Fig. 5; Kirkland et al., 2009h). These data suggest the Kiwirrkura Formation is not part of the Amadeus Basin succession, but lies somewhere between the Pollock Hills Formation and the Amadeus Basin.

The basal unit of the Amadeus Basin is the Heavitree Quartzite in the north, and its equivalent on the southern margin, the Dean Quartzite (Weste, 1989; Korsch and Kennard, 1991; Lindsay and Korsch, 1991; Lindsay, 1999). The Dean Quartzite is locally underlain by a lithic and feldspathic unit, the Kulail Sandstone (Close et al., 2003a,b). Coarse-grained to pebbly sandstone intercalated with sandstone and minor siltstone from the basal Heavitree Quartzite was collected from an exposure in a series of low, rugged hills, in the western Pollock Hills (Fig. 4). Detrital zircons from the sample yielded a maximum depositional age of 1198 ± 24 Ma, with significant age components at c. 1625, 1774, 1837, and 1884 Ma, and several minor components in the range 3173–1198 Ma (Fig. 5; Kirkland et al., 2009i).

The Heavitree and Dean Quartzites are overlain by the Bitter Springs Formation, a mixed succession of carbonate, siliciclastic, evaporitic, and minor, dominantly mafic, volcanic rocks (Shaw et al., 1991; Haines et al., 2010). In the Northern Territory, the Bitter Springs Formation is subdivided into, in ascending order, the Gillen, Loves Creek, and Johnnys Creek Members (Fig. 3), with a regional disconformity at the base of the Loves Creek Member (Ambrose, 2006). Recent work in Western Australia has recognised the Gillen and Loves Creek Members (Haines et al., 2010). The Gillen Member contains a halite unit that has caused considerable halotectonic deformation, producing complex fold patterns (Dyson and Marshall, 2007, Marshal and Dyson, 2007; Dentith and Cowan, 2011).

Disconformably overlying the Bitter Springs Formation in the northern half of the basin is a succession of

units correlated with the Areyonga, Aralka, Olympic, Pertatataka, and Julie Formations of the northeastern Amadeus Basin. These rocks include two glacial units, several disconformities, and significant pre- and post-glacial intervals (Haines et al., 2010). The thick, immature, siliciclastic Carnegie Formation was formerly thought to interfinger with the top part of the then-named 'Boord Formation' (Haines et al., 2010; Fig. 3), rocks of which are now assigned to the five separate formations listed above. Recent stratigraphic reinterpretation (PW Haines, written comm.) places the Carnegie Formation over the Julie Formation (Fig. 3). In the southern half of the WA Amadeus Basin, the Carnegie Formation lies directly over Bitter Springs Formation and has a clear basal unconformity due to uplift at the initiation of the Petermann Orogeny. All of the Carnegie Formation and the overlying siliciclastic Sir Frederick Conglomerate, Ellis Sandstone, and Maurice Formations are interpreted to have been deposited during the c. 580–530 Ma Petermann Orogeny (Haines et al., 2010), and may thus extend into the Cambrian.

Several outliers of Amadeus Basin rocks occur overlying the west Arunta Orogen north of the main basin (Fig. 4). A succession of immature, red-brown sandstone and conglomerate (the 'Angus Hills beds') was correlated with the Devonian Pertnjara Group of the eastern Amadeus Basin, but more recent work suggests they may be part of the older Petermann Orogeny clastic succession described above (Haines et al., 2010).

The period of extension that led to the formation of the Centralian Superbasin (of which the Amadeus Basin is a part) took place between 900 and 560 Ma (Fig. 3; Korsch and Kennard, 1991). The tectonic history of the Amadeus Basin is complex and controversial, with up to nine separate extensional and compressional tectonic events defined in some publications. Moreover, the tectonic history is almost entirely based on studies of the basin in the Northern Territory. A particular problem is the degree to which regional convergent tectonics versus halotectonics created 'compressional' structures. There is general agreement that there is a decollement horizon at the level of the evaporites in the Bitter Springs Formation. The Areyonga Movement, a basin-wide structural event in the mid Neoproterozoic, may have initiated movement of salt. Halotectonics continued during later tectonic events. Regional deformation events affecting the Western Australian basin succession include the Paterson, King Leopold, and Petermann Orogenies (late Neoproterozoic to Cambrian), and the Alice Springs Orogeny (mid-Paleozoic). The Alice Springs Orogeny may have had more effect on the west Arunta Orogen than the Petermann Orogeny, as the entire Amadeus Basin sedimentary succession appears to have been variably deformed at this later time. The event is interpreted to have produced an approximately east–west trending fold and thrust belt, and probably reactivated the CAS (cf. Hand and Sandiford, 1999; Haines et al., 2001).

Canning Basin

The southeastern edge of the Canning Basin covers the western part of the west Arunta Orogen and overlying Amadeus Basin. This large, pericratonic Early Ordovician to Early Cretaceous basin contains a succession of marine and non-marine siliciclastic and marine carbonate rocks more than 15 km thick (Kennard et al., 1994). The partly faulted southeastern edge of the basin, part of the Ryan Shelf, is poorly known due to its remoteness, difficult access, and extensive Cenozoic cover (Hocking et al., 2008). The Ryan Shelf is one of a series of shelves, platforms, and embayments that flank the Kidson Sub-basin, and which typically contain thin sedimentary sections (<1 km) of Devonian to Early Cretaceous age (Hocking et al., 2008).

The following structural history of the Canning Basin is based on Kennard et al. (1994). The earliest phase of subsidence occurred in the Early Ordovician and was associated with approximately northeast–southwest oriented extension (c. 490–470 Ma). Extension, rifting, and subsidence continued intermittently until the mid-Carboniferous inversion of Devonian normal faults. This is referred to as the Meda Transpression and was probably the basin's response to the Alice Springs Orogeny. Following further extension and rifting, the last major phase of deformation occurred in the Late Triassic to earliest Jurassic. Referred to as the Fitzroy Movement, this comprised regional, dextral strike-slip faulting on dominantly northwest–southeast trending structures. This is a significant tectonic episode with estimates of up to 3 km for the amount of material eroded in the basin.

Deep crustal structure from geophysical datasets

Deep-penetrating geophysical data are available across the Arunta Orogen and adjacent areas as seismic data and magnetotelluric data. These data were not acquired within the west Arunta Orogen, but are useful in that they provide large-scale tectonic and architectural context.

In order to understand very large amplitude gravity variations near the CAS, variations in teleseismic travel times were modelled in terms of a major offset in the Moho; specifically a 20 km change in Moho depth over a horizontal distance of about 50 km, apparently associated with the Redbank Thrust Zone (Lambeck et al., 1988). Deep seismic reflection profiling (Fig. 6a; BMR85.1A) was conducted as a follow-up to that study (Goleby et al., 1988; Wright et al., 1990). Data were collected to 20 s two-way travel time (TWT; approximately 60 km depth) along four traverses. Following this, reprocessing of the reflection data focussing on the migration of the upper 10 s TWT (approximately 30 km) enabled previously published interpretations to be refined (Korsch et al., 1998). The reflection profiling confirmed that the dominant feature of the crust of the Arunta Orogen is a series of planar structures that dip about 40° to the north, and that these structures penetrate to depths of greater than 20 km (Fig. 6a; Goleby et al., 1989; Shaw et al., 1992b). The presence of large, hanging-wall anticlines reveals that the faults are top-to-the-south, crustal-scale thrusts. These structures, together with the Moho offset, indicate that massive shortening involving the entire crust has occurred in this part of central Australia.

a) Seismic line BMR85.1A (Goleby et al., 1989)

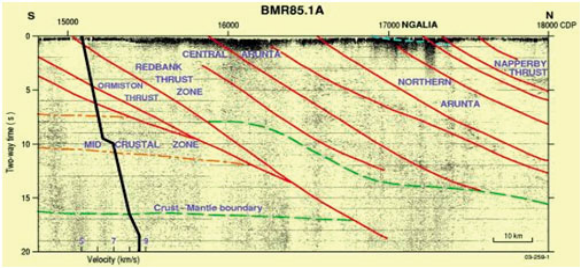

b) Seismic line 09GA-GA1 (Korsch et al., 2011)

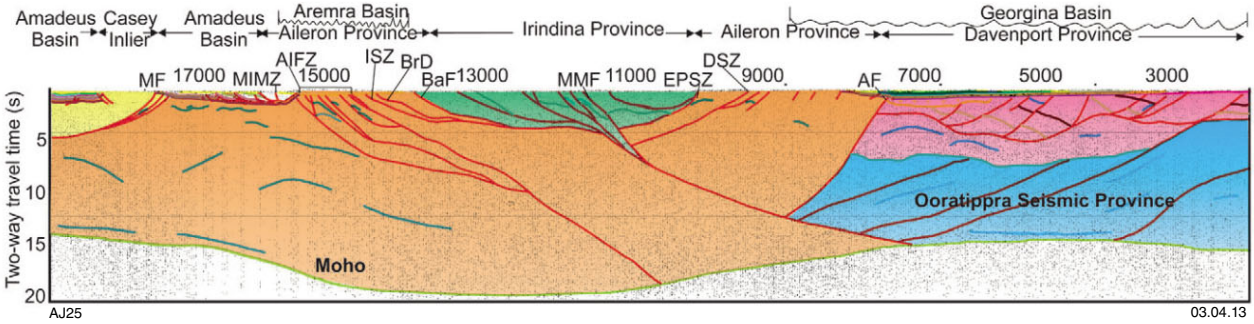

Figure 6. (a) Seismic data along the profile BMR85.1A (location shown in Fig. 2), from Goleby et al., 1989; b) migrated seismic section for the Georgina–Arunta seismic line 09GA-GA1 showing interpretation and key provinces. Fault abbreviations: MF – Milly Fault; MIMZ – Mount Isobel Mylonite Zone; AIFZ – Atnarta Imbricate Fault Zone; ISZ – Illogwa Shear Zone; BrD – Bruna Detachment; BaF – Basil Fault; MMF – Mount Mary Fault; EPSZ – Entire Point Shear Zone; DSZ – Delny Shear Zone; AF – Atuckera Fault. Display shows vertical scale equal to horizontal scale (assuming crustal velocity of 6000 m/s)

More recently, a 373 km seismic line 09GA-GA1 (Fig. 6b; Korsch et al., 2011), funded by Geoscience Australia and the Northern Territory Geological Survey, was acquired. The Georgina–Arunta seismic traverse extends from the southern Davenport Ranges (Fig. 1) across the southern Georgina Basin, then across the entire eastern Arunta region east of the Harts Range, and into the Amadeus Basin (Fig. 2). Seventy-five fold seismic reflection data were acquired to 20 s TWT, providing an image of the crust and upper mantle to a depth of c. 60 km (Nakamura et al., 2011). The 09GA-GA1 seismic traverse was proposed for two main reasons: firstly, to investigate the possibility of structural and stratigraphic hydrocarbon traps formed during the Late Ordovician to Carboniferous (450–300 Ma) Alice Springs Orogeny in the Amadeus and Georgina basins (Fig. 2); secondly, to image the crustal architecture in Central Australia, as well as to provide new insights into the tectonic setting and geodynamics of the Aileron and Irindina provinces (Korsch et al., 2011). To a first approximation, beneath the Neoproterozoic to Early Paleozoic sedimentary basins, the crust can be divided into five distinct regions: the Casey Inlier, the Aileron, Irindina, and Davenport Provinces, and the Ooratippra Seismic Province (Fig. 6b). These regions are separated from each other by major, crustal-scale faults. These large-scale structures are likely to have controlled copper, gold, base metal, and uranium mineralization (Huston et al., 2011).

The seismic section shows that the Irindina Province now has the geometry of a doubly-vergent orogen, controlled by a master thrust that connects to the Moho. The thickest crust in the seismic section occurs almost entirely under the Irindina Province, where the Aileron Province is nearly 60 km thick (20 s TWT), compared to 40–45 km (14 s TWT) at the northern and southern ends of the section. This thickening cannot be attributed solely to thrusting of the Irindina Province southwards over the Aileron Province, as this would imply that the Aileron crust was originally anomalously very thick in this region alone. Therefore, additional thrusting within the Aileron Province, such as the crustal-scale Atnarta Imbricate Fault Zone, is likely to have also played a significant role in crustal thickening (Korsch et al., 2011). An intense change in the nature of the seismic reflectivity occurs across the Atuckera Fault Zone in the northern part of the Georgina–Arunta seismic line. The crustal scale of this change and the reflectivity contrast across the fault zone are consistent with an interpretation that this fault zone represents an ancient suture between two different crustal blocks, the Aileron and the Davenport Provinces. Therefore, the Atuckera Fault Zone could represent the collision zone between the Granites–Tanami and the Arunta Regions (Fig.1; Goleby et al., 2009; Korsch et al., 2011).

Magnetotelluric (MT) data were acquired along a 360 km traverse, from the Amadeus Basin in the south to the Arunta Orogen in the north, crossing the CAS towards the southern part of the line (Fig. 2a). The MT technique

is a natural-source electromagnetic method used to map electrical conductivity variations at crustal to lithospheric scales (Jones, 1999; Simpson and Bahr, 2005; Vozoff, 1986). MT involves recording temporal variations in natural electric and magnetic fields and deriving an Earth response function, which contains information about the vertical and lateral variations in electrical resistivity. Three dominant features are evident in the final crustal resistivity model reaching 150 km in depth (Fig.7a; Selway et al., 2009):

1. A region with a resistivity of 10–500 Ω·m and a surface location that corresponds with the Amadeus Basin, labelled A in Figure 7a. Basinal sedimentary rocks have a higher conductivity than the surrounding crystalline rock.
2. A region with a resistivity of 1000–4000 Ω·m that underlies region A and has an outcrop location that corresponds with the Warumpi Province, labelled B in Figure 7a. This region is very resistive and displays no evidence of being intersected by crustal- or lithospheric-scale structures.
3. A region with a resistivity of 100–1000 Ω·m and a surface location that corresponds with the NAC, labelled C in Figure 7a.

The lithospheric-scale resistivity contrasts are interpreted as representing a south-dipping paleosubduction zone (Selway et al., 2009), consistent with the interpretations of Scrimgeour et al. (2005a), reaching 150 km depth (40 s TWT). On the lithospheric scale, the MT data suggest that the NAC was transported southward beneath the Warumpi Province, most likely during the 1.64 Ga Liebig Orogeny, which corresponds to the amalgamation of the Warumpi Province and NAC (Scrimgeour et al., 2005a; Selway et al., 2009).

An MT survey was also conducted at the same time and location as the seismic line 09GA-GA1 in 2009 (Fig. 2). The MT data (Fig. 7b) were acquired at 39 locations (18 locations acquired both broadband and long-period data, 21 locations acquired broadband data only) with site spacings of 5–20 km (Nakamura et al., 2009).

In terms of electrical conductivity, both the Amadeus and Georgina basins are more conductive than the surrounding, resistive basement (Fig. 7b). The region of the Atnarta Imbricate Fault Zone (AIFZ) appears to be more resistive in the magnetotelluric image, compared to the Aileron Province to the north, and also to the region immediately to the south, beneath the Amadeus Basin. There is a significant change in resistivity across the Atuckera

a) MT line (Selway et al., 2009)

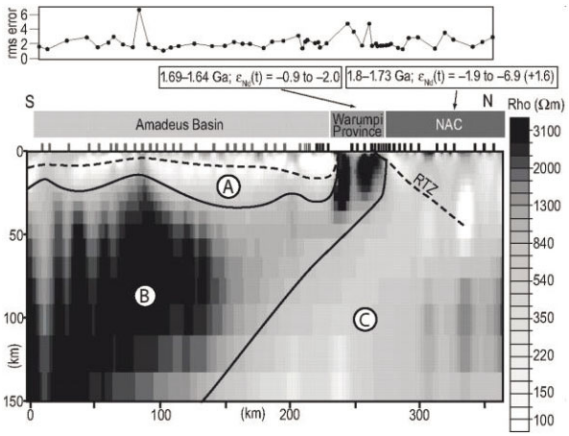

b) MT line (Korsch et al., 2011)

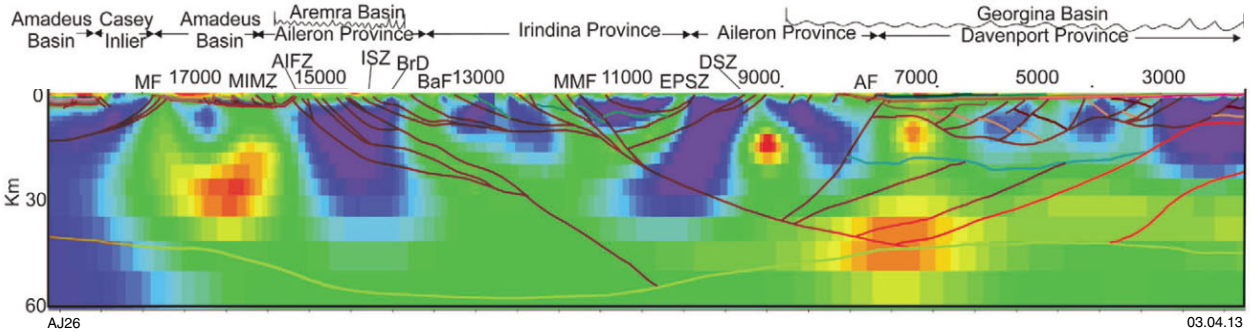

Figure 7. a) MT model, showing outcrop extent of Amadeus Basin, Warumpi Province, and NAC. Representative Nd values of magmatic rocks are calculated at t = 1.64 Ga (after Selway et al., 2009). Solid lines mark boundaries of regions A, B, and C discussed in text. Dashed lines show interpretations from the 1985 deep seismic reflection line, marking the base of the Amadeus Basin and the Redbank Thrust Zone (RTZ, part of the Central Australian Suture); b) preliminary MT model, to depth of 60 km (see details in Nakamura et al., 2011) with overlain simplified linework from interpretation of seismic section (Fig. 6b). Colours range from dark blue for most resistive at c. 100 000 Rho (Ω·m) to red for least resistive, <10 Rho. Fault abbreviations as for Figure 6

Fault Zone (AF), where the crust is much less resistive to the north. Within the northern Aileron Province, the Paleoproterozoic Kanandra Granulite (Scrimgeour and Raith, 2001b) occurs between the Entire Point Shear Zone (EPSZ) and the Delny Shear Zone (DSZ, Fig. 7b), and is marked by a zone of high electrical resistivity, separating two less resistive zones. The Irindina Province appears more resistive in the magnetotelluric image, compared to the Aileron Province below it (Fig. 7b). The lower crust of the Davenport Province appears to be much more conductive than the more resistive middle to upper crust (Korsch et al., 2011).

The seismic data (Fig. 6) depict only the top 60 km of the crust (20 s TWT). The north-dipping orientation of the crustal-scale structures in Figure 6 is consistent with the upper crust MT data of Selway et al. (2009) and Nakamura et al. (2011). These structures correspond to the Paleoproterozoic crustal architecture (Goleby et al., 1988; Wright et al., 1990; Korsch et al., 2011). The asthenospheric-scale south-dipping structure (Selway et al., 2009), on the other hand, is interpreted as a 1.64 Ga paleosuture.

Mineral deposits

The prolonged tectonic activity in the Arunta Region has resulted in terranes that host abundant and diverse metallogenic systems (Close and Scrimgeour, 2009). Mineral systems that developed during the Paleoproterozoic include VHMS and carbonate replacement Zn–Cu–Pb, pegmatite-hosted Sn–Ta–W, IOCG, mafic magmatic-hosted Ni–Cu sulfide and V–Ti magnetite, and felsic magmatic-related Mo–W, REE and U systems (Fig. 2, Scrimgeour, 2006a). The Mesoproterozoic–Neoproterozoic was characterized by mesothermal W, REE, P, U, Th, Cu and Ag mineralization. Mineralization styles that developed during widespread Paleozoic intraplate deformation include intrusion-related REE, U, Th, and Ni–Cu (Hoatson et al., 2005), shear zone-hosted Cu, and mesothermal Au (Scrimgeour, 2006b).

Despite this, the Arunta Region has a very limited history of mining and exploration, and although several mines have operated, total production is low. The deposits mined include gold, copper, lead and zinc, tin–tungsten–tantalum, fluorite, and mica. Exploration has been limited, partly due to poor outcrop, isolation, and a perception that the region is too highly metamorphosed to host significant deposits.

The west Arunta Orogen has the potential to host significant mineral resources including gold, based on the occurrence of sub-economic mineralization elsewhere in the orogen, such as in the Arltunga and Winnecke goldfields, east of Alice Springs (Fig. 2). These have produced 2758 kg and 41 kg of gold, respectively (e.g. Mackie, 1984; Ahmad et al., 1999). The gold mineralization occurs in a zone of greenschist-facies deformation, associated with structural interleaving of the Arunta Region and basal Amadeus Basin in nappe–thrust complexes formed during the Alice Springs Orogeny (Warren et al., 1974, 1975). Given the strong geological affinities between the gold-rich Tanami Region and the Aileron Province of the Arunta Orogen, gold exploration programs have been conducted over areas of the northern and western Arunta Region. This has led to discoveries of new gold prospects, for example in the Lake Mackay and Reynolds Range regions, although extensive areas remain unexplored (Ahmad et al., 2009).

Gold also occurs within some base metal deposits in the Arunta Region. Meteoric Resources (2009) confirmed priority right of application over a large 10 km x 8 km gold anomaly identified in regolith geochemistry by the Geological Survey of Western Australia in the west Arunta Orogen (over the Mount Webb Granite area; Figs 4 and 8). Importantly, the Mount Webb anomaly (Fig. 8) is supported by a large number of other anomalous elements including As, Cu, Zn, U, Co, Sn, Sc, Ce, Nd, Sm, Tl, Y, La, and Ni, some of which are shown in Figure 8. Some of these associated anomalies (such as arsenic) are 20 km long. The large extent and multi-element nature of the anomalism shows characteristics similar to those shown by large hydrothermal alteration and mineralization systems.

Consequently, there is current exploration interest in the Arunta Orogen. The Johnnies Reward Cu–Pb–Au–Zn–Ag prospect (Fig. 2) was originally interpreted to be a VHMS deposit (Warren and Shaw, 1985), but is now considered to have more affinities with IOCG deposits (Huston et al., 2006). Base metal deposits include the Clark and Mount Hardy copper prospects in Mount Doreen (Fruzetti, 1971), which are hosted in quartz veins and pegmatite within the Lander Rock Formation.

Implications for prospectivity analysis of the west Arunta Orogen

The review of geological and geophysical research on the Arunta Orogen and its mineral deposits suggests the following may be relevant to a prospectivity analysis for the west Arunta Orogen:

1. The orogen has a long and complex tectonic history with planar discontinuities (of various types) present suitable for reactivation in multiple orientations. However, east–west oriented, northerly dipping tectonic fabrics seems to be dominant, with geophysical data showing that the major structures extend to the base of the crust. These crustal scale structures offset the Moho (Figs 6 and 7) and are likely to be conduits for any mineralizing fluids as they tap the mantle. Likewise, the south-dipping paleosuture (Fig. 7a) is probably the zone of highest permeability.

2. The present-day outcrop patterns (Fig. 4) show regions of sedimentary rocks bounded by faults. This suggests the present-day map is largely the result of post-basin tectonics and the tectonic events affecting the adjacent sedimentary basins must be considered. The main tectonic event affecting the northern margin of the Amadeus Basin is the Alice Springs Orogeny and this gave rise to dominantly east–west trending

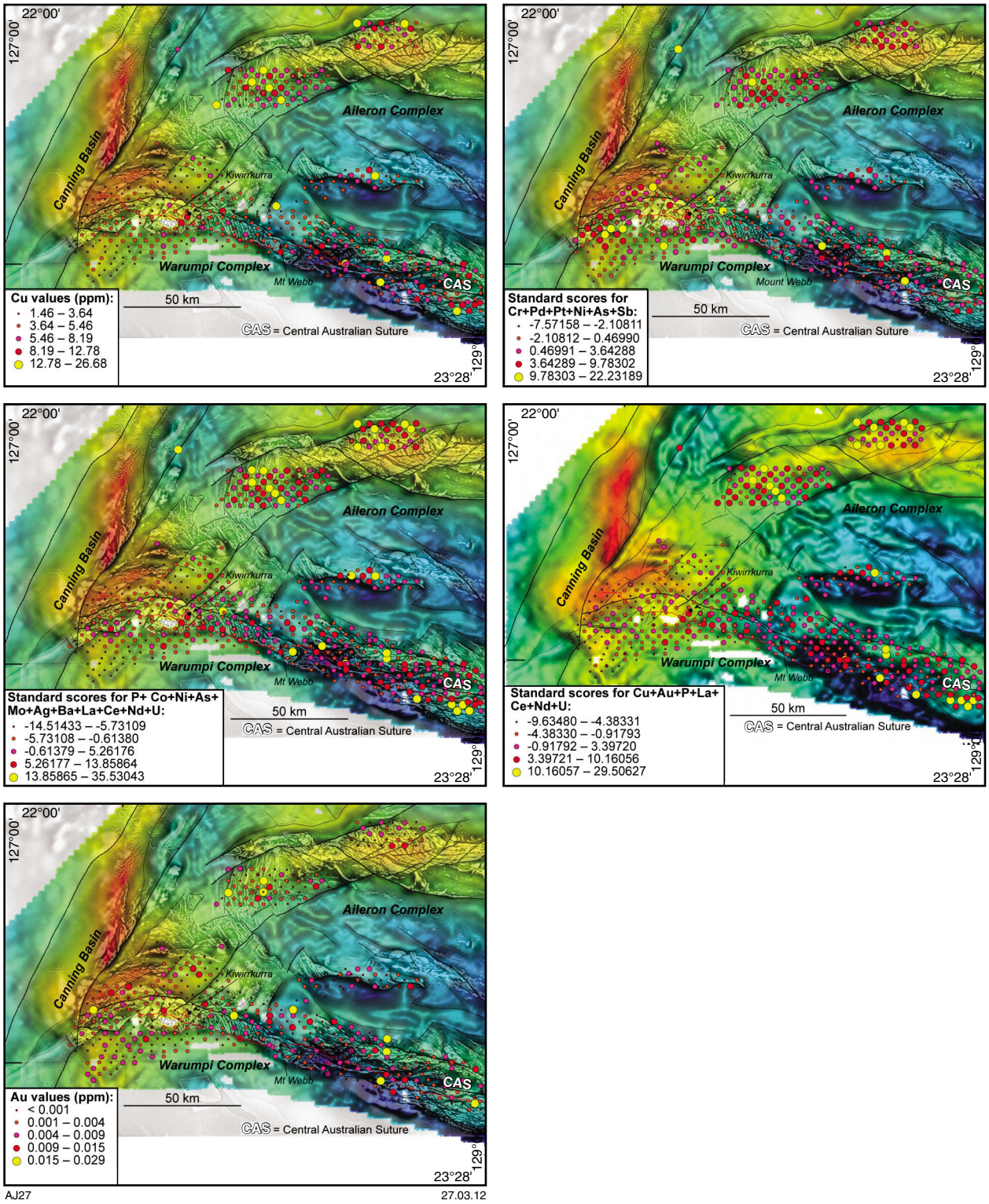

Figure 8. Regolith sample metal values over draped image of gravity with first vertical derivative magnetics (from Spaggiari et al., 2008)

folds and faults. It is almost certain that this event reactivated pre-existing structures with similar trends.

3. Tectonic events in the Canning Basin mostly involved extensional movements on northwest–southeast trending structures, and thus did not favour reactivation of the main east–west tectonic fabric in the Arunta Orogen. However, the Fitzroy Movement involved dextral transpressional faulting along the NW-oriented Fitzroy Trough (Smith et al., 1999). Structures oriented northeast–southwest that occur near the western margin of the west Arunta Orogen (Fig. 4), were reactivated as normal faults during what is one of the youngest tectonic events to affect the region.

Radiometric data

Airborne radiometric measurements were made in the study area in conjunction with an aeromagnetic survey (see the section 'Gravity and magnetic data' below). Survey line spacing was 400 m and mean terrain clearance was 80 m. Figure 9 is a ternary image produced from the radiometric data.

There is no outcrop over at least 80 % of the west Arunta Orogen, which is dominated by flat to weakly undulating sand plain with elongate, roughly east–west trending, sand dunes (e.g. areas β and ζ in Fig. 9) The distribution and type of dunes varies. Dunes may be widely spaced (kilometre-scale) and several kilometres long, or closely spaced net-dune systems (Spaggiari et al., 2008).

The ternary image has strong spatial correlations with some of the known bedrock geological units. In the Amadeus Basin, e.g. near Corroboree Valley (δ in Fig. 9), the image appears darker than the surrounding units, indicating low concentrations of K, U, and Th. Farther to the east, the response indicates a greater contribution from K, possibly due to detritus from the Ininti Granite. A few areas, such as in the (salt) Lake Mackay (α in Fig. 9), and between Mount Webb and Pollock Hills (θ in Fig. 9), appear white indicating the presence of all three radio-elements. These are areas of shallow or exposed bedrock. Overall, the radiometric data broadly correlate with some larger structures (e.g. the major NE-trending fault in the Aileron Province), and also indicate soil composition, which is related to underlying bedrock.

Regolith geochemistry

A mostly 1.5 to 2.5 m thick sand plain (Fitzgerald, 1998; Spaggiari et al., 2008) covers approximately 80% of the west Arunta Orogen area. More than 500 regolith samples

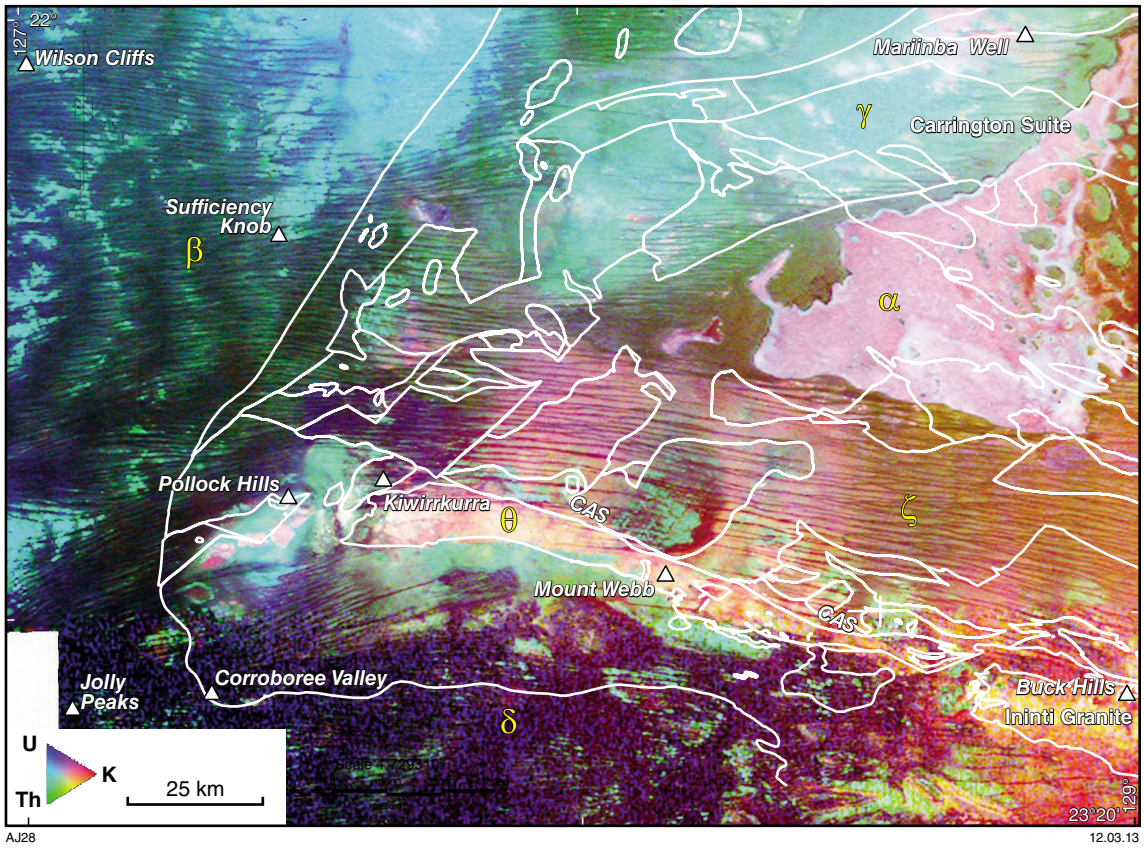

Figure 9. Ternary image (RGB = K, Th, U channels) of radiometric data from the west Arunta Orogen. Major geological boundaries are shown as thin white lines, and prospects as triangular symbols (modified from GSWA, 2009). Note the elongate features, which correspond to sand dunes. Greek letters refer to particular areas that are described in the section 'Radiometric data'

were collected for geochemical analysis, predominantly within an east–west corridor extending from the Pollock Hills to Mount Webb, and covering the CAS (see details in Spaggiari et al., 2008). Figure 8 shows the sample locations and assay results for selected elements and combinations of elements. There is strong relationship between Au, granite, and known mineralization regardless of sample medium (Spaggiari et al., 2008). This suggests that at the scale of sampling, regolith transport does not cause any major dislocation between regolith and parent rock. To avoid any transported regolith, filtered data were used.

Gravity and magnetic data

Two regional, government-acquired geophysical datasets were used as the principal basis for the geological interpretation of the west Arunta Orogen:

1. Aeromagnetic data, 400 m line spacing, 80 m mean terrain clearance, flown N–S.
2. Gravity data, 4042 stations at nominal 2.5 km spacing, height determined by differential GPS.

To help interpret these data, physical property data were sought, although few data were found.

Petrophysical data

Magnetic susceptibility

Little magnetic susceptibility data is available (Table 1). The data are very limited in geographical extent, all coming from the vicinity of Mount Webb (Fig. 4). These data show the Heavitree Quartzite to be, as expected, non-magnetic. None of the basement units is particularly susceptible, but the range is sufficient to produce easily recognizable anomalies in the magnetic data. Wyborn et al. (1998) noted that alternation significantly reduces magnetic susceptibility.

There are no magnetic susceptibility data from the successions comprising the sedimentary basins proper. However, the nature of the lithologies in the Canning Basin sequence suggest they will be effectively non-magnetic, a conclusion supported by inspection of magnetic data to the west of the study area. Interestingly, and in contrast to the Canning Basin, magnetic data from the Amadeus Basin show patterns consistent with stratigraphically controlled variations in rock magnetism (see Section on 'Magnetic data interpretation products'). Publications describing magnetic data from the Amadeus Basin refer to volcanic rocks in the Bitter Springs Formation as a source of magnetic anomalies (Burgess et al., 2002; Schroder and Gorter, 1984). However, the magnetic datasets contain 'stratigraphic' anomalies in areas where no volcanics are expected. These may be sourced from 'recessive shale units' (Foss and Marshall, 2005). Also to be considered is that evaporite units may be responsible for observed magnetic variations.

Density

No density data are available from the west Arunta Orogen, but there are limited data associated with geophysical modelling of the major variations in gravity that occur to the east in the Northern Territory. Lambeck et al. (1988) listed 'average' densities from basement units. Values for gneisses ranged from 2.68 to 2.95 g/cm^3 (depending mostly on the amount of mafic material), whereas granitic rocks and metasedimentary rocks were assigned a density of 2.72 g/cm^3.

There are numerous bulk density logs from wells in the Amadeus and Canning Basins, although in the former case these are all in the Northern Territory and in the latter case a lack of stratigraphic control for the sedimentary rocks in the west Arunta Orogen prevents anything more than broad inferences being drawn. A review of density data from numerous wells from the Canning Basin shows the Permian succession to vary in density between approximately 2.25 and 2.50 g/cm^3. The variations in density within the Amadeus Basin are potentially much more complex.

Table 1. Magnetic susceptibility data from the Mount Webb area. (L. Wyborn written comm. and Wyborn et al., 1998)

Geological formation	*Geological unit*	*SI x10^{-5} (Min)*	*SI x10^{-5} (Max)*
Dolerite dykes	Dolerite dyke swarms	1000	3000
Heavitree Quartzite	Amadeus basin	10	20
Mt Webb Granite – albitite	Warumpi Province	10	20
Mt Webb Granite – aplite	Warumpi Province	0	5
Mt Webb Granite – diorite	Warumpi Province	4000	5000
Mt Webb Granite – granite	Warumpi Province	0	600
Mt Webb Granite – granodiorite	Warumpi Province	200	400
Mt Webb Granite – porphyry	Warumpi Province	10	2000
Mt Webb Granite – tonalite	Warumpi Province	1500	2000
Pollock Hills Formation – chert	Warumpi Province	60	80
Pollock Hills Formation – lavas	Warumpi Province	10	4000
Pollock Hills Formation – rhyodacite	Warumpi Province	20	5000
Pollock Hills Formation – tuff	Warumpi Province	100	2000

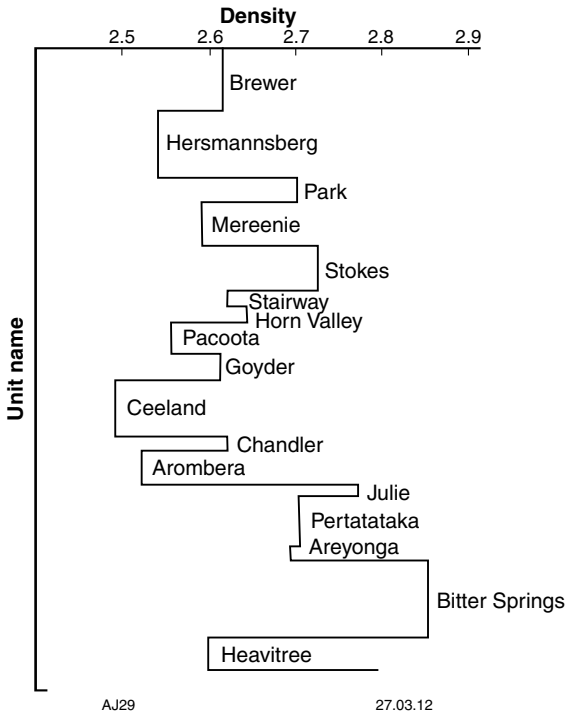

Figure 10. Summary of stratigraphically controlled variations in density within the Amadeus Basin (from Schroder and Gorter, 1984)

The Heavitree Quartzite has an average density of 2.55 g/cm^3 (Fig. 10). The overlying Bitter Springs Formation is shown as having a density of 2.85 g/cm^3. The situation within the Bitter Springs Formation is actually more complicated than shown in Figure 10 as there are low density evaporites and higher density mafic rocks within the unit. Moreover, the 'average' value is comparable to those quoted for the basement rocks. The density log from the Magee-1 well (located in the Northern Territory), which penetrated basement, confirms that the Bitter Springs Formation has a comparatively high density, about 0.3 g/cm^3 greater than the overlying units, although the absolute densities are ~0.3 g/cm^3 lower than shown in Figure 10. Evaporite units have densities of about 0.3 g/cm^3 lower than adjacent sediments. The well did not intersect volcanics. Importantly, in Magee-1, there is no density contrast between basement and the Bitter Springs Formation.

Implications of petrophysical data for interpretation of gravity and magnetic imagery

The density data from the Amadeus Basin sedimentary rocks and the basement rocks of the west Arunta Orogen show that reliably assigning geological significance to observed variations in gravity is extremely difficult, particularly in the third dimension. The reason for this is that there are numerous contrasts in density within both the cover succession and within the basement, and it is possible that no overall density contrast exists between cover and basement rocks.

The magnetic data are more easily interpreted. The basement units comprise various lithotypes that have sufficient contrasts in magnetic susceptibility to produce easily detected changes in total magnetic intensity (TMI) with the available survey specifications. Basement areas are likely to show significant magnetic 'texture' because of the amount and complexity of lithological variations, and the effects of alteration. The mafic volcanics within the Bitter Springs Formation should give rise to readily identifiable linear anomalies within the areas where the unit outcrops or is near the surface. Evaporite units and other sedimentary stratigraphic variations probably produce subtle magnetic anomalies, which will only be observable where the basement is at sufficient depth to produce a smooth magnetic response. These stratigraphically sourced anomalies may only be apparent in enhanced data products.

For the reasons outlined above, the interpretation of the gravity and magnetic data focussed on identification of linear features, rather than 'mapping' of lithological entities.

Gravity data interpretation products

Three forms of the gridded Bouguer anomaly data from the west Arunta Orogen were selected as most useful and used as the basis for the interpretation. The Bouguer anomaly data are shown as a simple pseudo-colour image in Figure 11. Total variation in Bouguer gravity is about 600 gu. As is usually the case, there is a significant long wavelength component of variation caused by deep-seated features, so to highlight features associated with density contrasts in the near surface, a first vertical derivative (Fig.12) and residual gravity image (Fig.13) were produced. The residual image was produced by subtracting the upward continued (by 5000 m) Bouguer anomaly data from the Bouguer anomaly data. The upward continuation acts as a low-pass filter, so subtracting this from the Bouguer gravity removes long wavelength variations.

Magnetic data interpretation products

The gridded total magnetic intensity (TMI) data are shown in Figure 14. Total variation in TMI is about 7000 nT. The TMI data are notable for their significant long wavelength component of variation, indicative of deep magnetic sources. These mostly occur where the basin fill is mapped at surface and are due to magnetic sources in the underlying basement. To assist with interpretation, a series of enhanced products were produced from the TMI by Cowan Geodata Services Ltd. Figure 15 shows the data reduced to pole; this transform ideally removes the dipole nature of magnetic responses, placing responses directly over their source. Figure 16 shows the first vertical derivative of the TMI. This transform emphasizes shallow

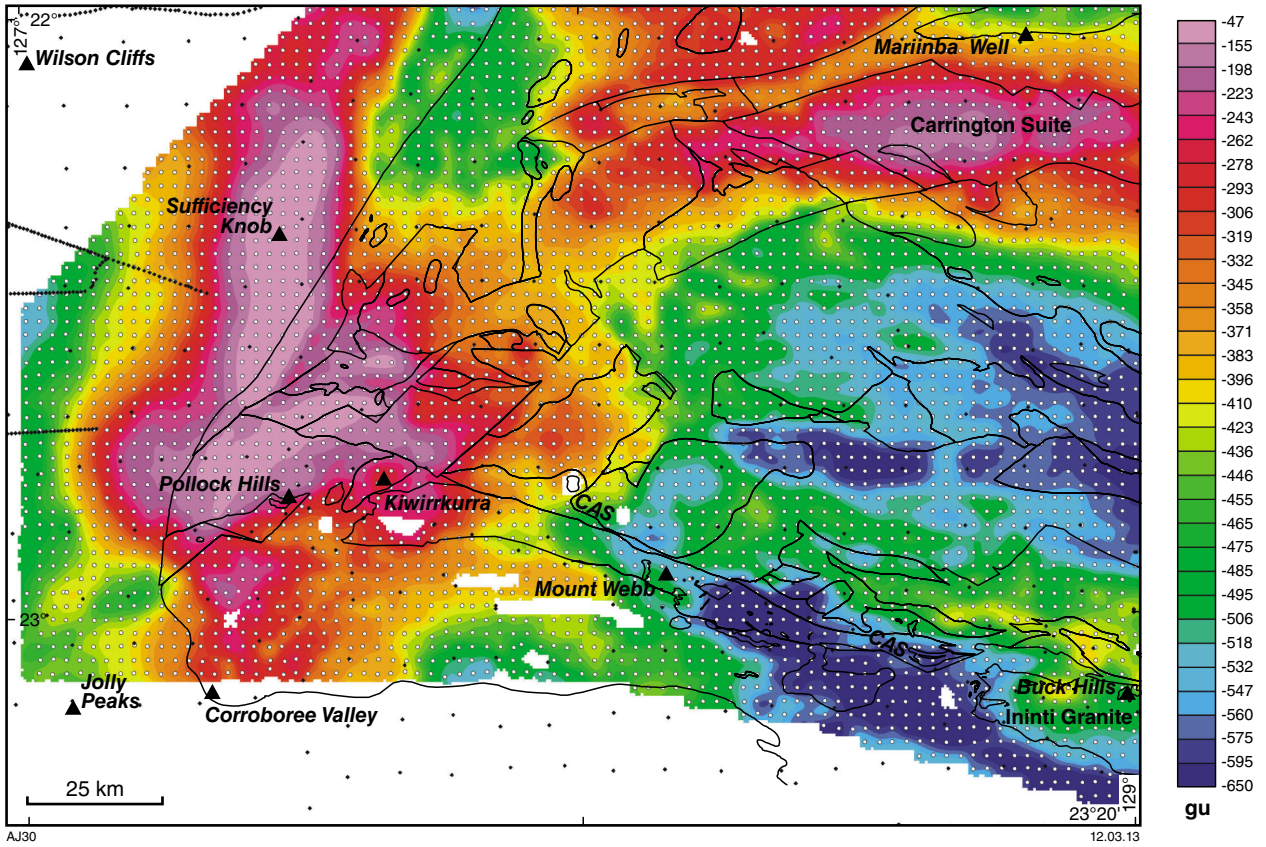

Figure 11. Bouguer anomaly gravity map of the west Arunta Orogen. Major geological boundaries are shown as thin black lines, localities as triangular symbols, locations of the old gravity stations as black dots, and recent gravity stations as white dots

responses. The results were passed through an automatic gain control filter, which enhances subtle responses within the data. Figures 17 and 18 are wavelength-based filtered products. The residual data were derived using a Hamming filter, and the separation filtered image is based on differential upward continuation to isolate the wavelengths of interest. In both cases, parameters were selected on a trial and error basis, and were designed to emphasize features originating from the bedrock geology in the top few hundred meters; that is, to suppress responses from the surficial cover and from deep basement.

Interpretation of gravity and magnetic data

The various interpretation products described above were used, in association with available outcrop data, to create a 'pseudo' geological map. As noted previously, emphasis was placed on identification of linear features because complicated variations in physical properties made interpretation of texture and amplitude variations for lithological mapping extremely difficult. For this reason, lithological and stratigraphic distribution data from the interpreted bedrock geology map in GSWA (2009) were used.

All interpretation products contributed to the overall interpretation, but for the purpose of discussion it is useful to refer to an overlay of the residual gravity and magnetic data (Fig.19). An immediately obvious characteristic of Figure 19 is that there is a poor correlation between the gravity and magnetic data in several places. As would normally be the case, the exposed basement coincides with short wavelength variations in TMI and the basin fill has a much more subdued magnetic character.

What is unusual is the lack of consistency in the gravity responses. In many places, the areas of shallow basement inferred from the magnetic data do coincide with higher gravity values, but in other places the opposite is true; for example, immediately southeast of Mount Webb. In areas where the magnetic data suggest the basement is deep and sedimentary basin fill crops out, normally the gravity signature would tend to be comparatively low, but this is not the case. There are significant variations in gravity in the areas where moderate TMI wavelengths suggest the source of the variations is within the sedimentary succession.

Amadeus Basin

The magnetic response in the Amadeus Basin comprises long-wavelength variations originating from the basement

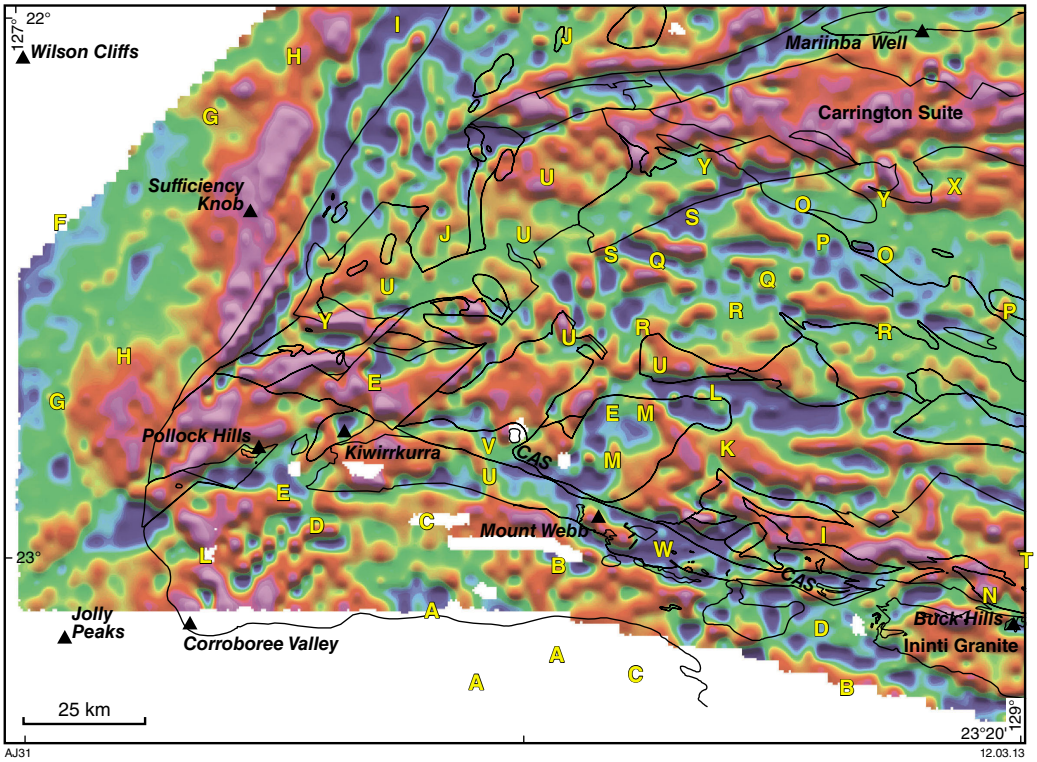

Figure 12. First vertical derivative of the Bouguer gravity map of the west Arunta Orogen. Major geological boundaries are shown as thin black lines, localities as triangular symbols. Letters refer to particular areas that are described in section 'Interpretation of gravity and magnetic data'

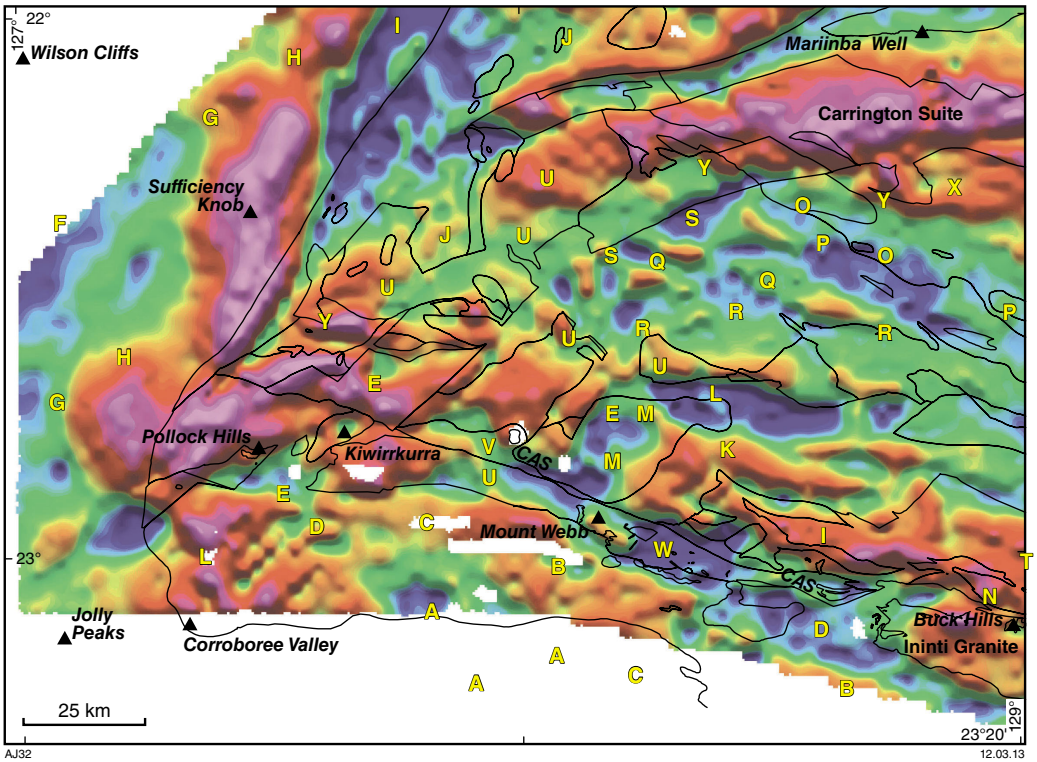

Figure 13. Residual gravity anomaly map of the west Arunta Orogen. Major geological boundaries are shown as thin black lines, localities as triangular symbols. Letters refer to particular areas that are described in section 'Interpretation of gravity and magnetic data'

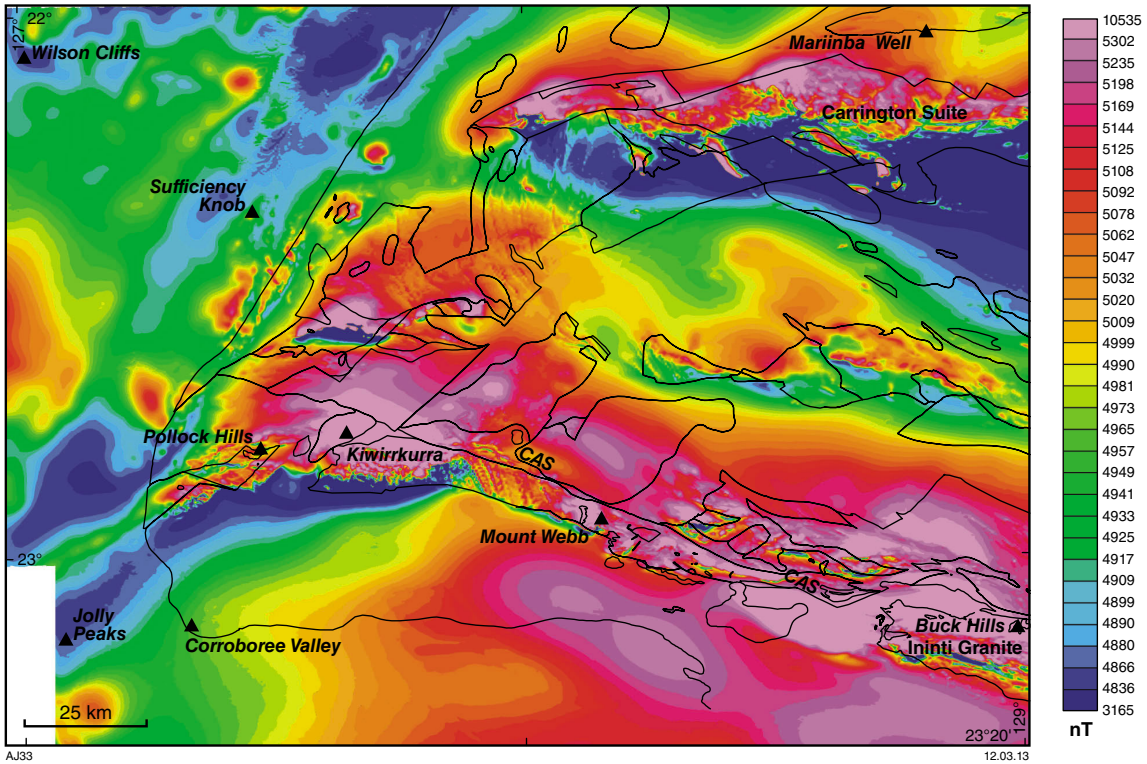

Figure 14. Total Magnetic Intensity (TMI) map of the west Arunta Orogen. Major geological boundaries are shown as thin black lines, localities as triangular symbols

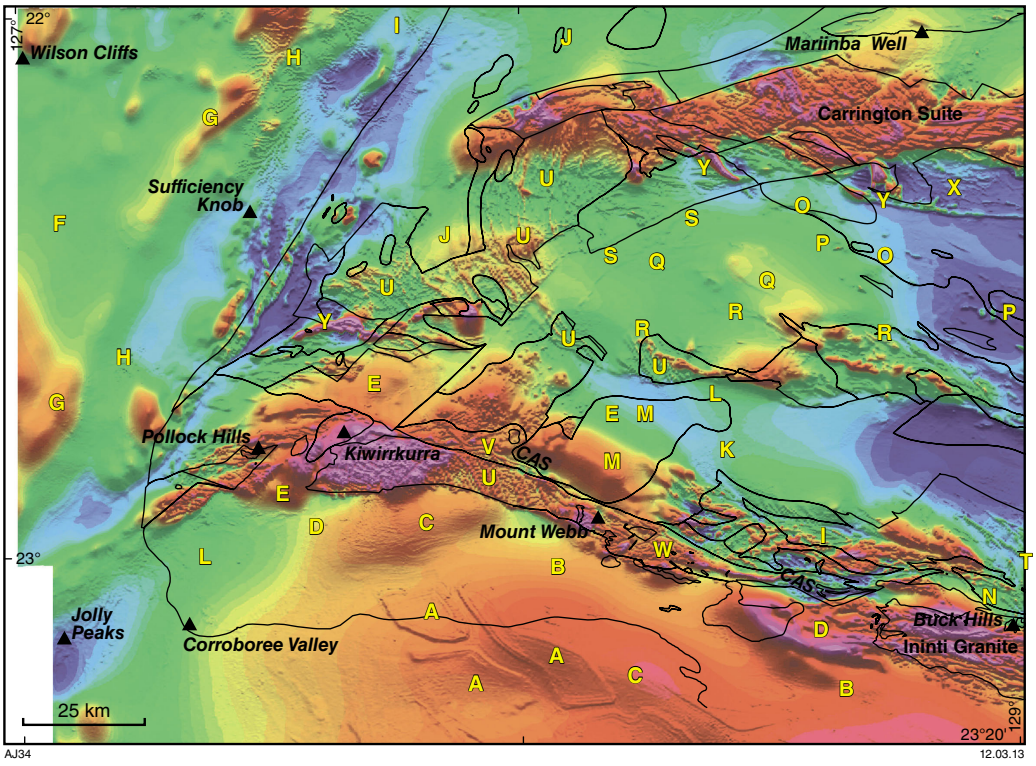

Figure 15. Reduced-to-pole magnetic map of the west Arunta Orogen. Major geological boundaries are shown as thin black lines, localities as triangular symbols. Letters refer to particular areas that are described in section 'Interpretation of gravity and magnetic data'

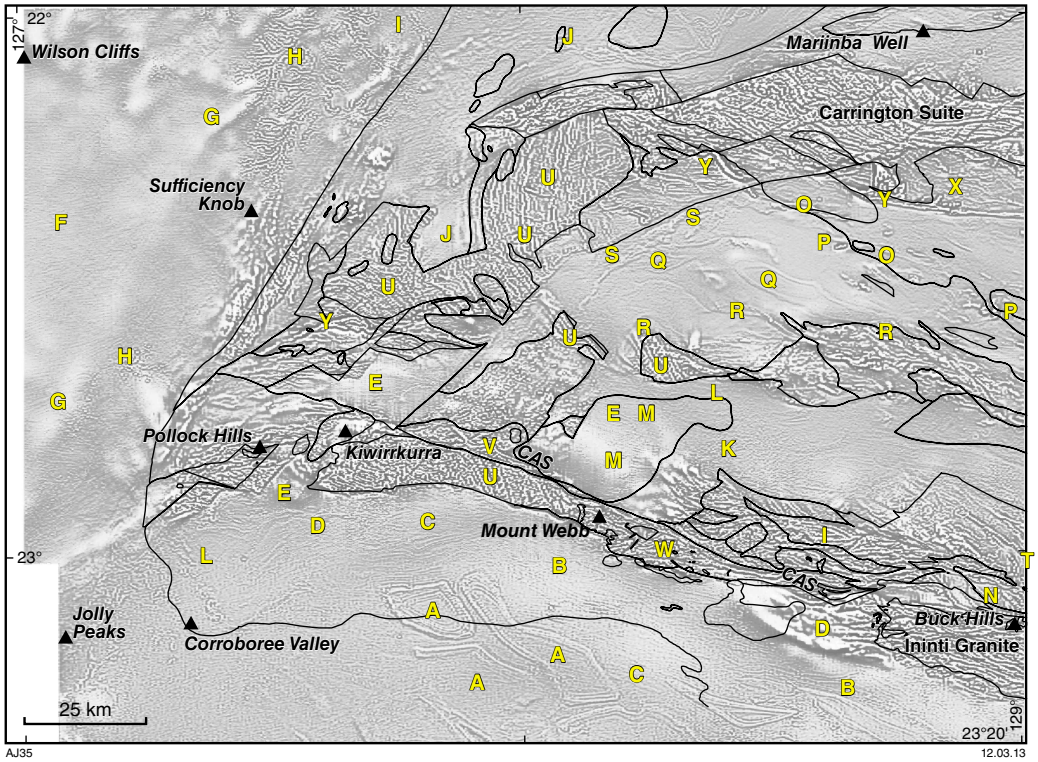

Figure 16. First vertical derivative, with automatic gain control enhancement, of the total magnetic intensity map of the west Arunta Orogen. Major geological boundaries are shown as thin black lines, localities as triangular symbols. Letters refer to particular areas that are described in section 'Interpretation of gravity and magnetic data'

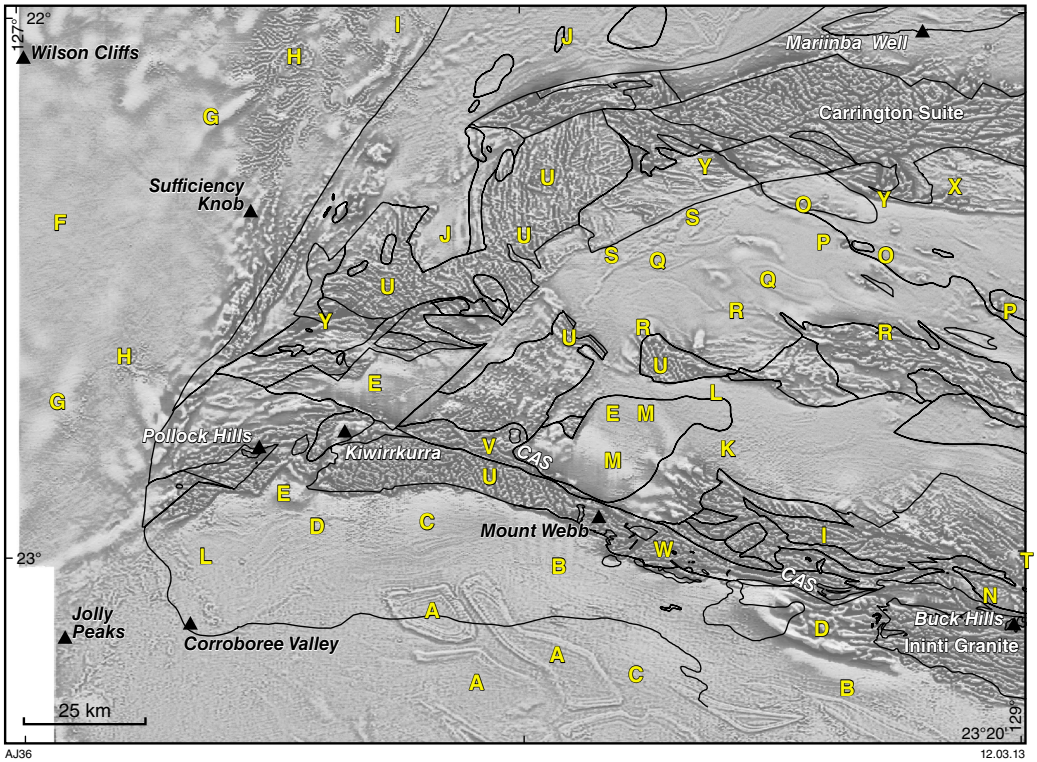

Figure 17. Separation (differential upward continuation) filtered image of the west Arunta Orogen TMI map. Major geological boundaries are shown as thin black lines, localities as triangular symbols. Letters refer to particular areas that are described in section 'Interpretation of gravity and magnetic data'

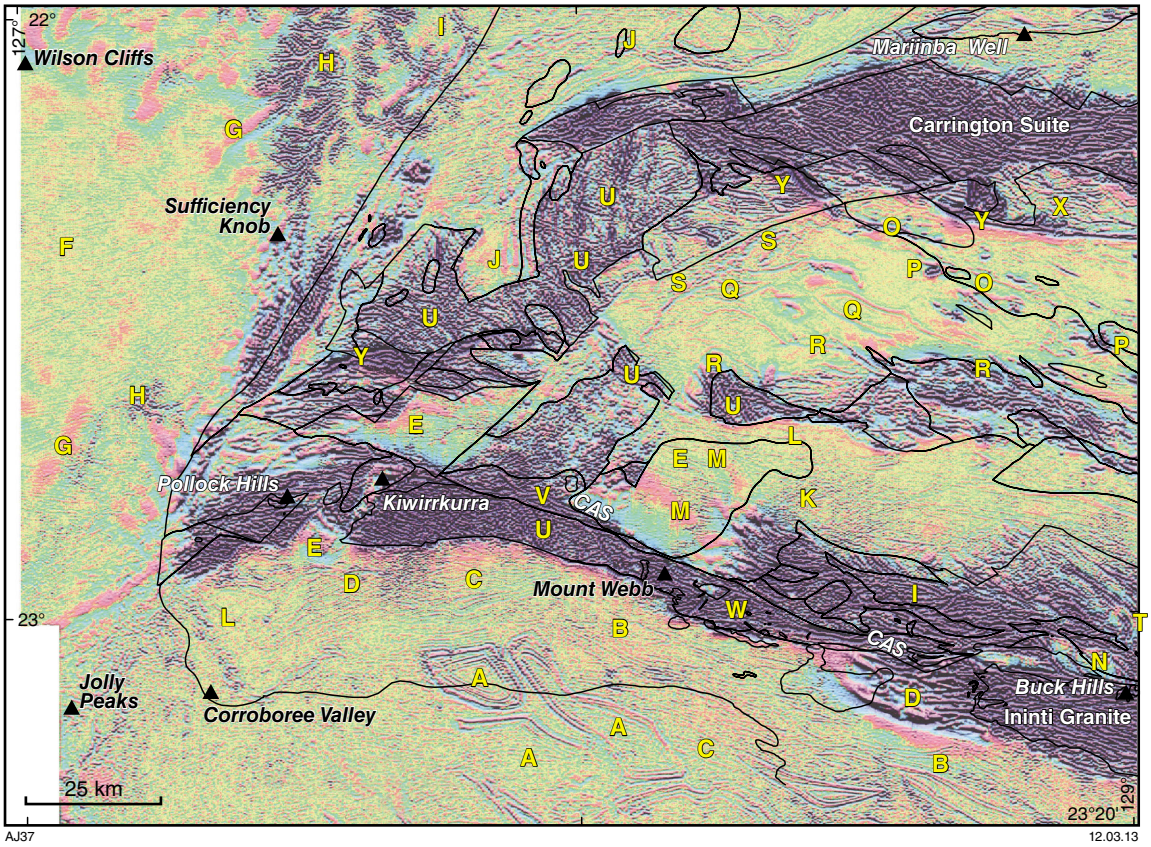

Figure 18. High-pass filtered image of the west Arunta Orogen TMI map. Major geological boundaries are shown as thin black lines, localities as triangular symbols. Letters refer to particular areas that are described in section 'Interpretation of gravity and magnetic data'

(C) on which are superimposed shorter wavelength linear anomalies of interpreted stratigraphic origin that form closures that are elongate in a west-northwest – east-southeast direction (A). These are best seen in Figure 17. Comparison with the 1:250 000 geological maps (Blake, 1977; Wells, 1968) shows the linear anomalies are probably from strata that overly the Bitter Springs Formation. In areas where the Bitter Springs Formation is mapped, magnetic responses of likely stratigraphic origin are still visible but these are weak. Nevertheless, some folding is evident and there is a general, weak 'linear' texture (B) to the magnetic data, best seen in Figures 17 and 18.

The gravity data do not extend far into the Amadeus Basin, but airborne data described by Dentith and Cowan (2011) show that closures in the magnetic anomalies coincide with negative gravity anomalies, as is also partly seen in Figure 13. Comparison with the available geological maps shows that the closures are structural basins and are interpreted as salt withdrawal basins. They form by lateral migration of salt due to overburden pressure and form characteristic polygonal outlines and box-fold geometries, separated by much shorter wavelength antiforms. The geological interpretation of these structures is based on their similarity to structures observed in the Gulf of Mexico (Jackson et al., 1995), plus the known presence of evaporites in the Gillen Member of the Bitter Springs Formation and numerous studies emphasizing the importance of halotectonic processes in the Amadeus Basin (e.g. Marshall and Dyson, 2007). The observed elongation of the basins is probably the result of deformation during the Alice Springs Orogeny.

Long wavelength variations in the magnetic data (C) tend to trend parallel to the basin margin, and higher than average gravity associated with these suggests they are the result of ridges in the basement in the subsurface. Their orientation parallel to the basin margin, and to the trend of structures formed in the Alice Springs Orogeny, suggests they could be of tectonic origin, i.e. associated with blind thrusts affecting the basement.

There is an excellent example near the Ininti Granite (D, Fig. 19) of how magnetic responses increase in wavelength as the depth to source increases. Rocks of the west Arunta Orogen are present beneath a veneer of Amadeus Basin sedimentary rocks. Further east (N), the subdued magnetic response suggests sedimentary rocks within the area predominantly comprise basement. In both cases, linear features suggest structural juxtaposition. The various linear features are distinctly curved, suggesting a shallow dip, and hence probable thrust faulting. The low gravity response in the eastern areas (W and D) is indicative of a sliver of basement underlain by low density sedimentary

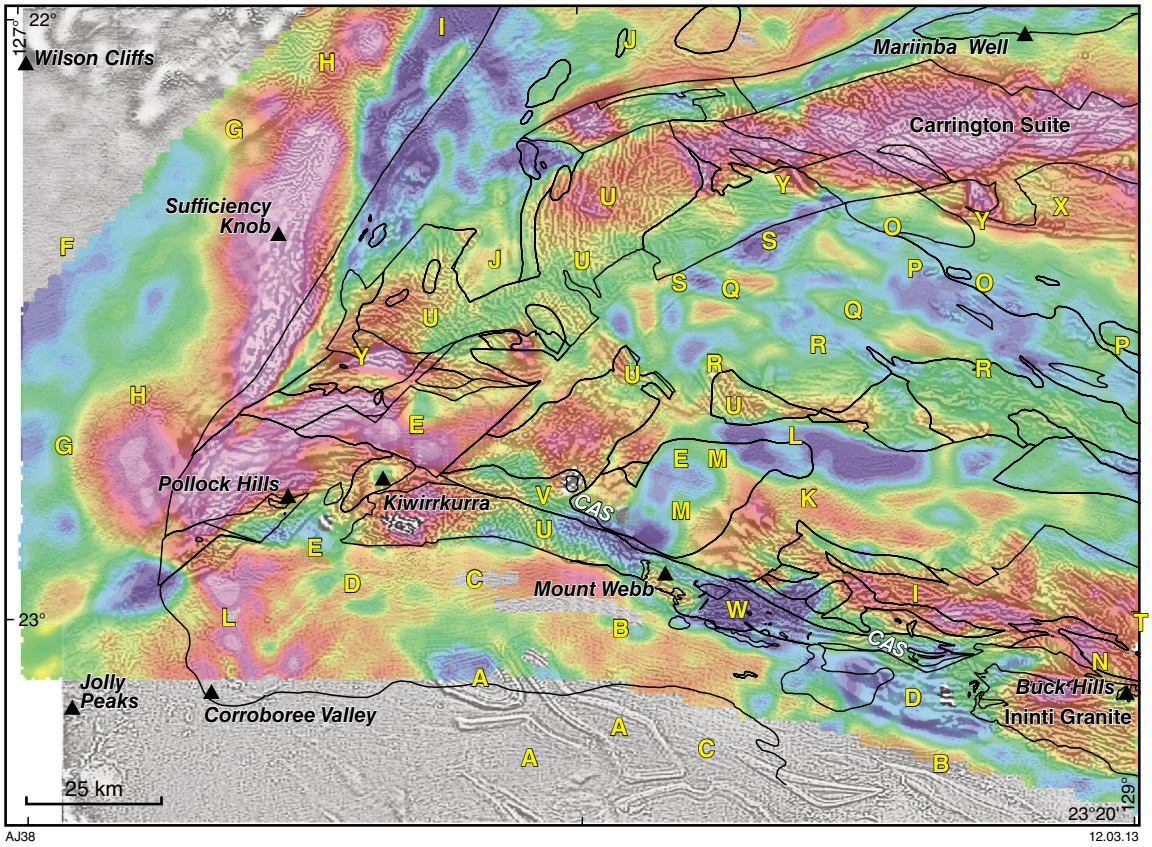

Figure 19. Residual gravity data (pseudocolour) overlay on residual TMI data (grey scale). Major geological boundaries are shown as thin black lines, localities as triangular symbols,. Letters refer to particular areas that are described in section 'Interpretation of gravity and magnetic data'.

rocks (Fig. 19). These correlations are significant features because they comprise evidence for a thick-skinned structural style with both basin fill and basement involved.

Murraba Basin

Based on gravity data, the Murraba Basin is thickest in the north of the study area (I, Fig. 13). In adjacent areas where this basin is mapped, short wavelength magnetic responses from the basement are evident. In some cases, the anomaly patterns are caused by the longer wavelength continuations of features seen in areas where the basement outcrops, which suggests a thinner basin fill.

Canning Basin

Sedimentary rocks assigned to the Canning Basin overlie those of the Amadeus Basin and are probably only of significant thickness in the area to the west of the west Arunta Orogen. Canning Basin sedimentary rocks are non-magnetic within the west Arunta Orogen (E, Fig. 17), and because of this there is usually a subdued to featureless magnetic response. In places, long wavelength variations are suggestive of deep basement. Gravity generally has a lower than normal response in these areas, but this may reflect the underlying Amadeus Basin succession. A region of such strata occurs south of Pollock Hills. The occurrences of Canning Basin sedimentary rocks are mostly bounded by northeast–southwest trending linear features, which offset the areas of basement outcrop. These are interpreted as late-stage faults (at least in terms of their youngest phase of movement). Given the parallel structural grain in the western part of the west Arunta Orogen, reactivation of pre-existing structures is very likely.

In the extreme west of the areas covered by the magnetic and gravity data there is a featureless magnetic response with low gravity values (F, Fig. 19), well within the Canning Basin. At the edge of the basin are a series of northeast–southwest trending linear features visible in short wavelength-enhancing magnetic images, and also as truncations of gravity anomalies. These basin-margin structures may be associated with intrusions in the basement, which are most clearly visible in the reduced to pole magnetic image (Fig. 15), labelled G.

Dendritic, short-wavelength magnetic variations are suggestive of a drainage system (H, Fig. 17). However, there is no evidence of these patterns in the radiometric image (Fig. 9), therefore they appear to predate the recent cover and dune system. They are interpreted as a north-

flowing paleodrainage filled with magnetic material from the west Arunta Orogen. There is evidence for northeast-trending structures controlling the paleodrainage. A smaller example of this kind of response occurs west of Pollock Hills.

Interpretation of basin structure

Sedimentary rocks, mostly of the Canning Basin, occur within two broad regions within the west Arunta Orogen (Fig. 4). The gravity response is generally low in these regions (F, A, Fig. 13), only achieving higher values where the western and northern outcrops of the basement occur, along the CAS (I, E, Fig. 13). The east-southeast to west-northwesterly trending area along the CAS (Fig. 11), which separates the northern and southern areas of basin fill, is associated with comparatively low gravity, although less so in the residual gravity image (Fig.13). Importantly, areas of low gravity occur under the area of basement outcrop that includes the Mount Webb area (or southeastern part of the CAS). This suggests that the outcropping basement is not indicative of the subsurface geology.

Shallow basement is likely to occur in areas where there is some magnetic texture and gravity is relatively high (K, Fig. 19). In some places, magnetic responses associated with outcropping basement can be traced as longer wavelength continuations into the basin; i.e. these responses are from equivalent features in the subsurface (M, Fig. 17). The lack of magnetic response coupled with low gravity suggests some areas where the sedimentary section is much thicker (L, Fig. 13). To the east there are some faint anomalies which could be stratigraphic in origin and the gravity is 'spotty'. For reasons outlined below, this may be an area where the Bitter Springs Formation is near the surface. It is possible the subdued responses further west are due to the Heavitree Quartzite. An alternative possibility is that sedimentary rocks of the Canning Basin occur here, i.e. they are more widespread than shown in Figure 4, and might be masking the responses from the Amadeus Basin sedimentary rocks.

The northern region of Amadeus Basin sedimentary rocks exhibits magnetic linear anomalies (O, Fig. 16) that trend northwest–southeast (parallel to the regional strike of the Amadeus Basin). The anomalies suggest a narrow elongate source and are tentatively interpreted as mafic lavas in the Bitter Springs Formation. Intense subcircular anomalies (P, Fig. 17) in this area are possibly intrusions associated with the lavas. Across most of the area, there are weak but easily recognizable anomalies defining fold closures (Q, Fig. 17). The geometries of these, and the patchy gravity response, suggest these are salt-related structures. As seen elsewhere, structures (linear features and possibly fold axes) are traceable from areas of basement outcrop out into the basin (R, Fig. 17). Adjacent to the basement outcrops in the west, the magnetic anomalies trend northeast–southwest, whereas the gravity responses are patchy, but are generally elongate northwest–southeast (S, Fig. 13). It is difficult to explain this lack of correspondence, which may suggest a thin-skinned (detached) structural style, or salt-related tectonics.

Warumpi Province

The area mapped as the Warumpi Province (Fig. 4) does not have a consistent geophysical response, as may be expected due to the presence of a variety of lithologies and structures. The responses are complex, but mostly linear and roughly west-northwesterly trending, consistent with the outcrop pattern. The reduced-to-pole magnetic data (Fig.15) show significant changes in TMI, with shapes and patterns indicative of both intrusive bodies and interleaved sheet-like units of differing magnetic properties. This main anomaly trend is crosscut markedly between Kiwirrkura and Mount Webb by northwest trending linear anomalies (U, Fig. 15), which very likely correspond to the mafic dykes of the Western Desert Dyke Suite that are exposed there. Equivalent anomalies are common in the western Aileron Province, but it is not clear why they only occur in this area of the Warumpi Province in the west Arunta Orogen. The CAS is clearly visible in the enhanced magnetic products, (e.g. V, Fig. 17).

As discussed earlier, an important geophysical response occurs where unequivocal basement magnetic anomalies coincide with unusually low gravity (W, Fig. 17). One possible explanation is a subsurface granitic intrusion. An alternative explanation is that these areas correspond to low-density sedimentary rocks, or even a salt diaper, below the basement. If true, this would be crucial evidence in favour of thick-skinned deformation and relatively thin slivers of the Aileron Province basement. There is evidence that the source of the low gravity is bounded by northeast trending faults; presumably reactivated structures, if the source is within the basin fill.

Aileron Province

The Lander Rock Formation has a distinct magnetic response comprising a modest TMI response, but with linear anomalies evident. This is consistent with the presence of pelitic rocks (low magnetic susceptibility) along with iron-rich shales and possibly volcanic metasedimentary rocks, which are likely to be more magnetic. Locally, fold closures are apparent (e.g. T, Fig. 17). Some areas shown as Lander Rock Formation in Figure 4 are now interpreted as Amadeus Basin sedimentary rocks, based on their signature in the reduced-to-pole magnetic image (e.g. X, Fig. 15). In some areas, linear anomalies interpreted as BIF are interpreted to occur in the Lander Rock Formation (Y, Fig. 15), but most occur in other units. These newly defined areas of BIF may be structural remnants of the Lander Rock Formation. Interbedded psammitic schist and BIF were mapped in outcrop near location Y (Fig. 15) and shown in GSWA (2009).

The remainder of the Aileron Province varies in TMI but has consistently linear texture. Northwest-trending dykes, possibly part of the same suite intruding the Warumpi Province to the south (the Western Desert Dyke Suite), are clearly seen in places (U, Fig. 15). Why the dykes are common in some areas and absent in others is not clear.

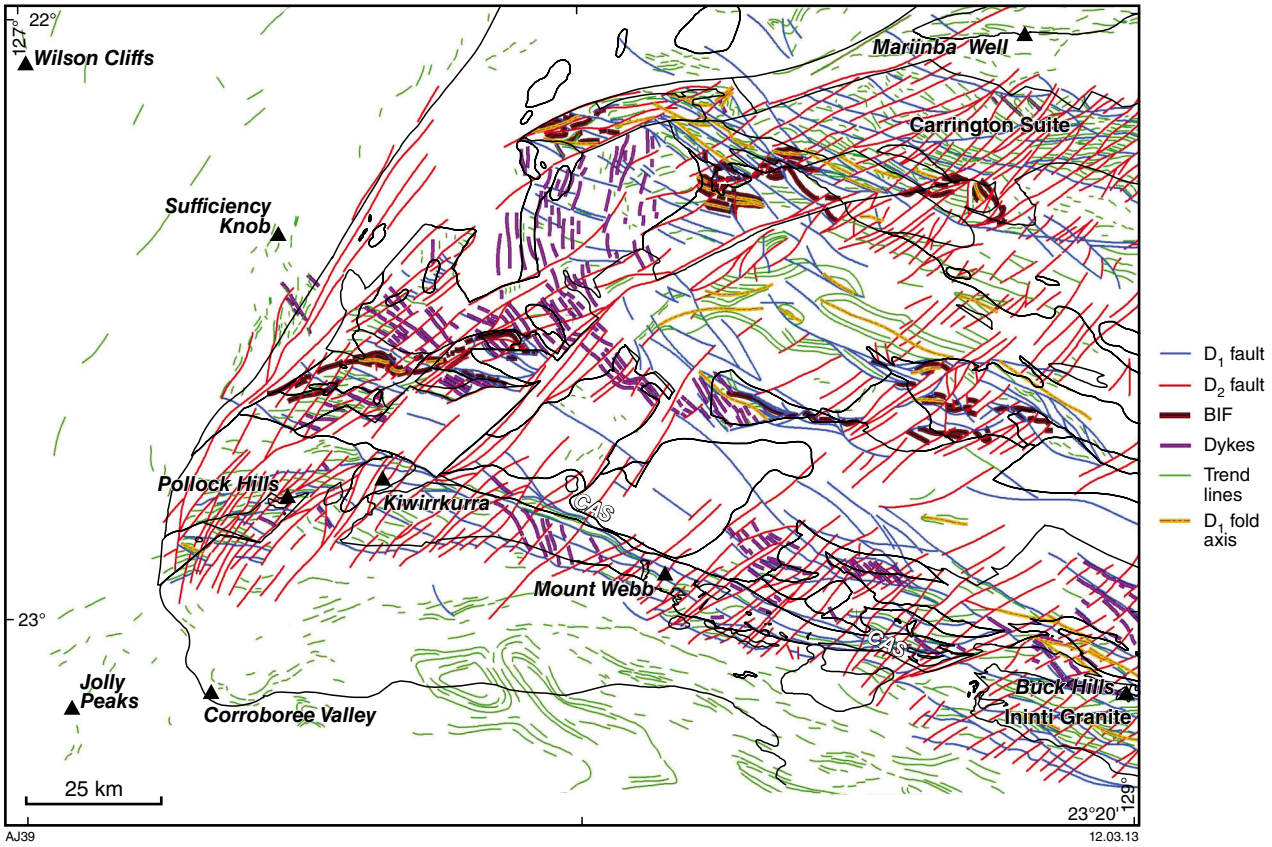

Figure 20. Interpretative structural map of the west Arunta Orogen, derived primarily from gravity and magnetic data (modified from the interpreted bedrock geology map in GSWA, 2009).

Potentially important features of the Aileron Province are the high amplitude magnetic anomalies which are mostly sinuous, or linear (Y, Fig. 15) and are interpreted as BIF. Where tightly folded, these appear as equidimensional positive anomalies (and are, in places, coincident with gravity highs), but in the higher spatial resolution versions (Figs 17 and 18) of the data, folding of the layered source is visible. It is difficult to be sure exactly how much BIF is present under cover. There is a continuum to lower amplitude anomalies, especially in the north, and these may be thin BIF layers.

Interpreted linear features

Given the complexly deformed multi-lithological nature of the units defined in the west Arunta Orogen, and the poor outcrop, the most useful features for prospectivity analysis are linear features. Linear features of the following types have been interpreted (Fig. 20):

1. faults — two generations, based primarily on orientation, identified from associated offsets and truncations of adjacent anomalies
2. trend lines — probably representing stratigraphic and metamorphic layering
3. BIF — a special case of the trend lines identified from their high amplitude TMI response
4. fold axes — based on closures of the trend lines
5. dykes — identified from crosscutting relationships with trend lines.

A summary of the inferred fault trends is shown in Figure 4: a west-northwesterly trending set includes the CAS, but a northeast–southwest trend is dominant. Structures of the latter trend dissect the outcrop pattern over much of the west Arunta Orogen. The crosscutting relationships between the two fault sets are variable, probably indicative of repeated reactivation. In most cases, the northeast-trending fault set appears to be younger and the control on outcrop pattern supports the conclusion that this is due to late-stage movements. The most likely tectonic event responsible for their formation is the Fitzroy Movement, recognized in the Canning Basin (Fig. 3).

Interpreted geological history of the west Arunta Orogen

Integrated interpretation of surface geology, and the gravity and aeromagnetic data, indicate there are two major deformation events that control the current architecture of the west Arunta Orogen. An early (D_1) set of structures trends west-northwest. The major examples of these faults probably dip north, as shown

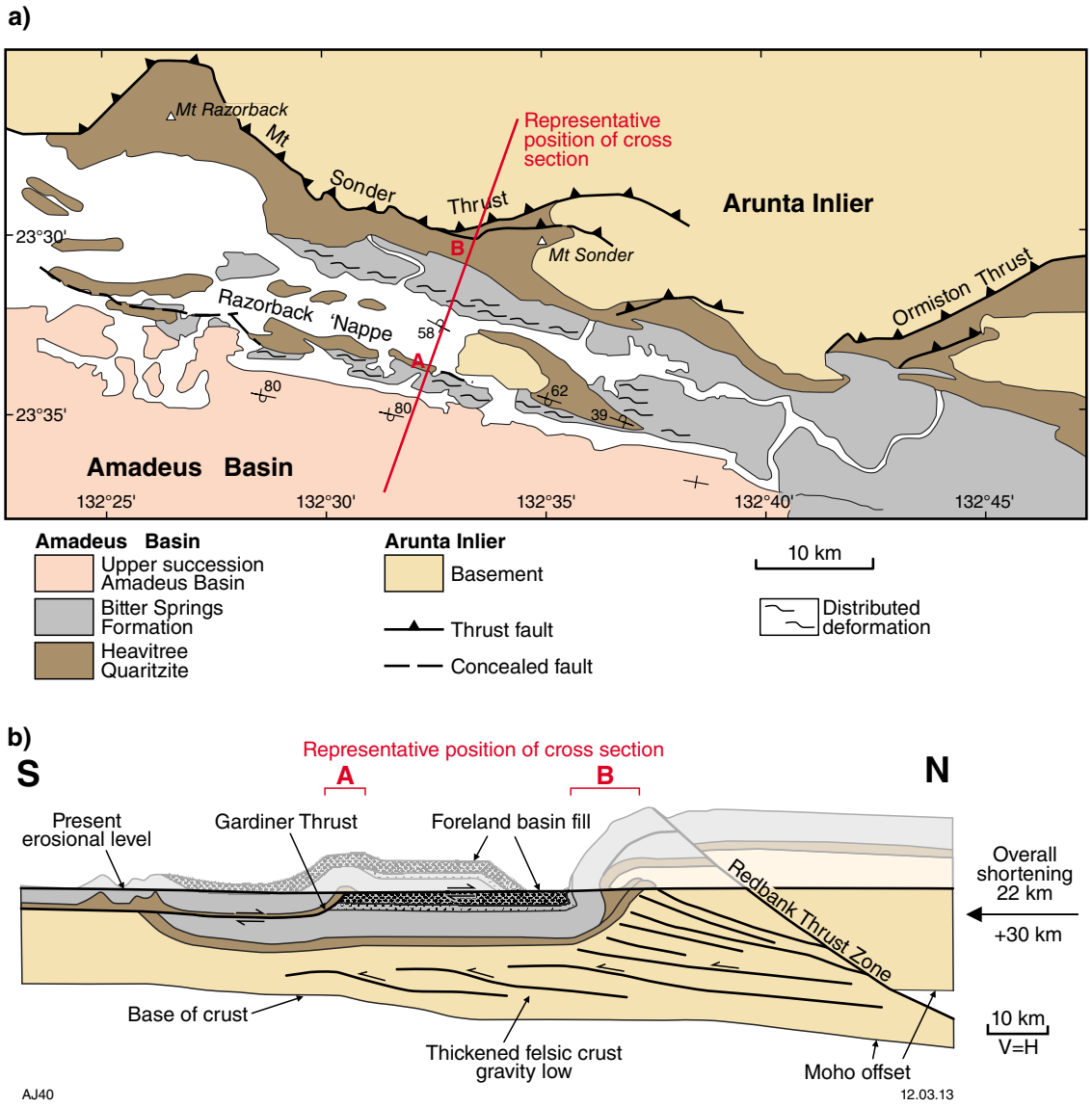

Figure 21. a) Basement-cored nappe structure of the northern margin of the Amadeus Basin, close to the Razorback structure (which is located at the footwall of the Redbank Thrust Zone). The lower succession of the Amadeus Basin comprises the Heavitree Quartzite and the Bitter Springs Formation; b) displacement along the Gardiner Thrust accommodates up to 30 km of shortening accumulated mostly after deposition of foreland sediment successions (from Flöttmann et al., 2004)

by the seismic datasets in the Northern Territory. Most of the fold axes have similar trends. As described above, fold axes and individual faults can be traced from basement into the unconformably overlying sedimentary succession. Faults of this orientation are likely to have had a long and complex history, such as the CAS, but it is probably reactivation of these structures during the Alice Springs Orogeny that is mostly responsible for the present structural configuration. Inconsistent responses in gravity and magnetic data, in particular negative Bouguer anomalies in areas where the magnetic data show that basement occurs at the surface, are interpreted as indicating that basement outcrops may be 'slivers' structurally emplaced within a succession comprising predominantly sedimentary rocks of the Amadeus Basin. This is the primary basis for interpreting a felsic, basement-involved, fold–thrust style of deformation within the west Arunta Orogen, during the Alice Springs Orogeny. A review of the literature on the style of deformation affecting the northern margin of the Amadeus Basin during the Alice Springs Orogeny strongly supports this interpretation (Fig. 21; Flottmann et al., 2004; Flottman and Hand, 1999). Flottmann and Hand (1999) specifically note that 'thin slivers of basement are incorporated into the hanging wall of individual thrusts.'

To test the idea that the west Arunta Orogen consists of a thick-skinned thrust belt, two-dimensional (2D) gravity forward modelling was completed on a cross section drawn perpendicular to the CAS (Figs 4 and 22).

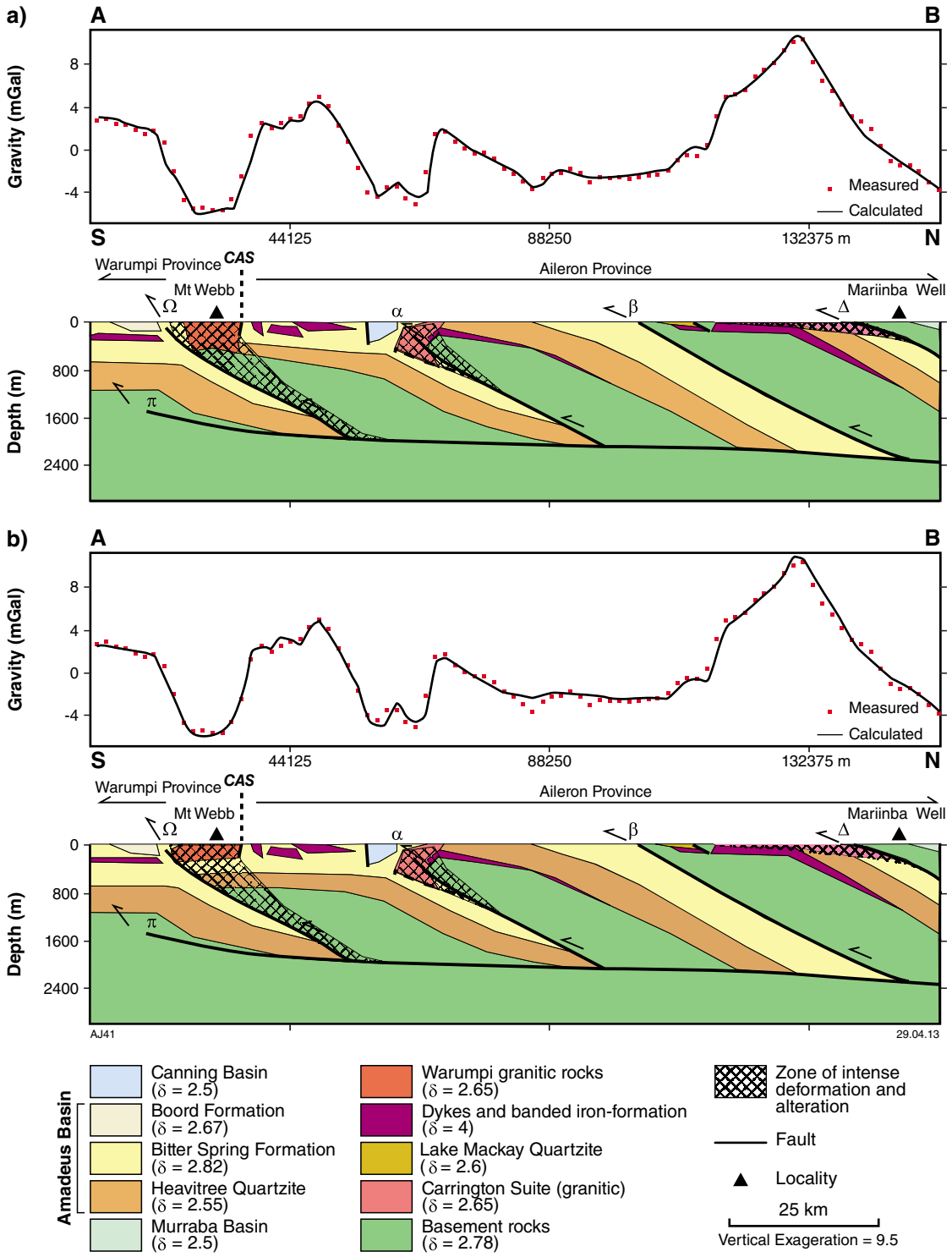

Figure 22. Model of residual Bouguer anomalies along the section A–B (see location on Fig. 4). α, β, Δ, Ω refer to particular areas that are described in the text

The cross section was interpreted with reference to the magnetic and gravity fields, the surface geology and the stratigraphy to determine the possible geometry of rock units in the subsurface, and structures at depth. Granitic rocks and the sedimentary basins (Murraba and Amadeus), are usually associated with low density, and so are represented by negative gravity anomalies on the cross section. In contrast, mafic dykes, BIF, Bitter Springs Formation, and the basement are mostly associated with higher gravity values. The Bitter Springs Formation may locally contain evaporite diapirs, which have very low density, although much of the original salt is probably now evacuated and dissolved.

The 2D gravity forward modelling was performed using Geosoft's GM-SYS software. In order to avoid edge effects, the model was extended by one third of the total profile length at each extremity. Residual gravity data were used because the intention was to model the density variations in the near surface. Average densities of the modelled geological units were derived from published sources (see section 'Petrophysical data') or estimated from the known lithologies in the study area. During modelling, the densities and the interpreted surface geology were fixed.

Two alternative models have been drawn to explain the gravity low running along the CAS. Although, as in any potential field modelling, the model is not unique, it demonstrates that the thick-skinned structural style is consistent with the gravity data for both modelled sections.

In Figure 22a, to the south of the CAS, the base of the Mount Webb Granite extends down to 600 m adjacent to the fault. This model suggests that the negative gravity anomaly underlying the eastern part of the Mount Webb Granite along the CAS reflects the geometry of the Mount Webb Granite. An alternative interpretation (Fig. 22b) shows the gravity low as a thin basement layer that overlies sedimentary rocks (or a salt diapir).

In both sections, a zone of intense deformation and alteration has been drawn in accordance with the geological map (Fig. 4), and the descriptions given in Wyborn et al. (1998). On the northern side of each modelled section, away from the CAS, antiformal thrust stacks and hanging-wall folds predominate, and control the shape of the upper 2 km of the crust. One of the key aspects of the interpretation of these sections is that a series of listric, north-dipping faults have brought Aileron Province basement to the surface, and that the basement structurally overlies basinal sedimentary rocks (α, β, Δ in Fig. 22). This observation is consistent with the observed northwest-trending structural grain and the south-directed vergence of thrusts and associated folds. Using the geological map as control, the Bitter Springs Formation is shown as truncated by the listric faults (π) and (Ω). Another important new modelled aspect in the section is that positive gravity and magnetic anomalies correspond with the dykes and BIF that are observed in the field (Spaggiari et al., 2008; GSWA, 2009).

As shown in Figure 20, D_2 structures trend northeast, and the most important of these coincide with, or are close to, the margins of the Canning and Murraba Basins. These structures probably acted as normal faults during the Fitzroy Movement in the Canning Basin. However, the structures are probably originally much older; in particular, the major structures that delineate the western extent of the Arunta Orogen.

Prospectivity modelling of Western Arunta Orogen

The mineral systems approach

Definition and main components

The mineral systems approach (MSA) to understanding mineral deposits (Fig. 23; cf. Wyborn et al., 1994) is based on the premise that mineral deposits are the focal points of geological systems that operate across a range of scales. The approach provides a holistic view of the entire process of mineralization in terms six key physico-chemical processes that must occur to form mineral deposits (Wyborn et al., 1994):

1. establishment of energy gradients to initiate and drive the mineral system
2. generation (or availability) of fluids for transporting metal
3. extraction of metal and chemical ligands for metal complexation in the fluids from suitable sources
4. migration of the metalliferous fluids to the trap regions (narrow focused fluid pathways)
5. modification of the metalliferous fluid composition in the trap region by physical and chemical processes, leading to deposition of the metal
6. preservation of the deposit through time.

From the point of view of prospectivity analysis, as the scale of study reduces from broad, regional scale to prospect scale, items lower in the list become more important. Consequently, the targeting elements and criteria vary with the scale of study (Table 2; McCuaig et al., 2010). As MSA is a generalized process-based framework, it can easily be adapted to different geological environments and deposit types. Indeed, multiple mineral deposit types can be realized and tested within a single mineral system (Knox-Robinson and Wyborn, 1997; Mishra and Panigrahi, 1999; Hagemann and Cassidy, 2000; Porwal, 2006; Markwitz et al., 2008; Kreuzer et al., 2008).

Mineral systems processes, active in the geological past, cannot be observed directly; therefore, they are inferred from geological features called targeting elements. Targeting elements are rarely directly mappable. Their presence is generally inferred from their responses in various geoscientific datasets, which are appropriately processed, generally in a GIS environment, to extract

Table 2. Scale dependence of targeting model parameters (modified from Wyborn et al., 1994)

Scale vs MSA constituent	*Source*	*Active pathways*	*Throttles (physical)*	*Depositional trap (scrubber, chemical)*	*Preservation*
Broad regional	*Critical*	*Critical*	*Less relevant*	*Less relevant*	*Less relevant*
	Mantle lithosphere	Upper crustal architecture			
	Magma series	Long-lived features			
	Geodynamic setting	Paleocraton margins?			
Camp	*Important*	*Critical*	*Critical*	*Critical*	*Important*
	Pressure–temperature windows	4D structural model	Small-scale damage zones	Alteration	Regolith character
	Magma series	Large-scale damage zones	Complexity	Chemical gradients	Degree of cover
			Competency contrasts		
			Permeability barriers		
Prospect	*Less relevant*	*Important*	*Critical*	*Critical*	*Critical*
		Large-scale damage zones	Damage zones	Alteration	Regolith character
			Dilational sites	Chemical gradients	
			Competency contrasts		
			Kinematics		

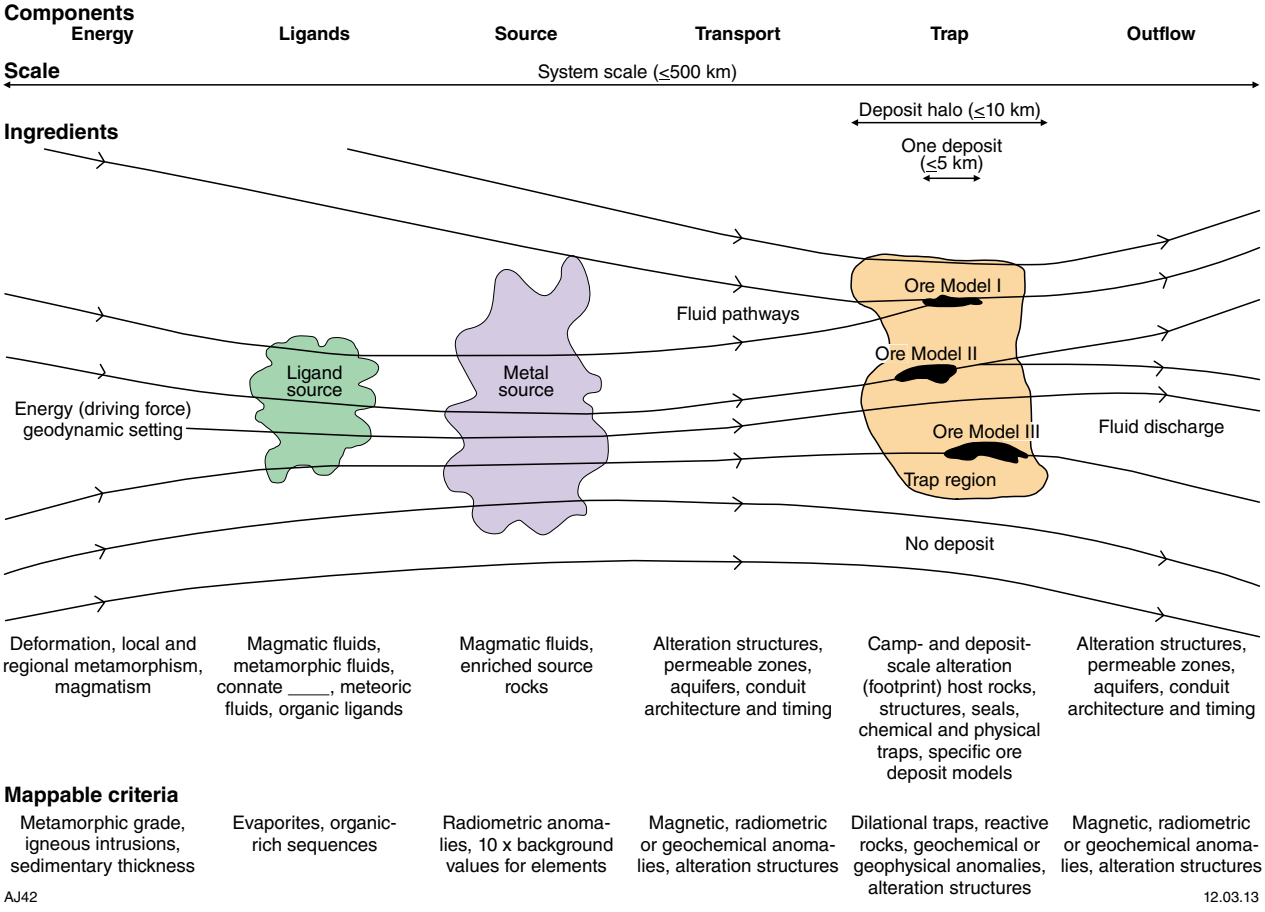

Figure 23. Schematic representation of the mineral systems approach (MSA; modified from Wyborn et al., 1994)

spatial proxies (Porwal and Kreuzer, 2010). In the context of mineral prospectivity mapping, spatial proxies are variously termed predictor maps, predictor patterns, evidential maps, or simply predictors. Although the critical components remain the same for all mineral systems, the constituent subprocesses and targeting elements for each component may vary considerably with deposit types and 4D geological settings of terranes. Therefore, it is important to identify the most appropriate targeting elements and spatial proxies for the deposit-type of interest, and its geological setting. As demonstrated by this study, the joint understanding of both geophysical and geological datasets can play a critical role in understanding mineral systems and identifying relevant exploration criteria.

A major advantage of the MSA is that it allows identification and prioritization of critical components for prospectivity analysis at a variety of scales ranging from the craton scale to deposit scale (Fig. 23, Table 2). Moreover, because MSA comprises a series of components that can be theoretically considered conditionally independent, the approach can be readily integrated into a spatial statistical framework for estimating the probability of mineral deposits in any area. For example, the overall probability of occurrence of a deposit of the targeted-type at a specific scale can be estimated from the individual probabilities of occurrence of the components that are considered critical at that scale. The probabilities for the occurrence of the mineral systems components can be assigned subjectively based on expert knowledge, or estimated empirically from the distribution of known mineral deposits. This kind of probabilistic approach can be used to demarcate exploration targets at a variety of scales.

Formulation of west Arunta Orogen mineral system models and model templates

The existence of known gold occurrences in the Mount Webb area (Fig. 24) indicates that both the Aileron and Warumpi Provinces have potential for the occurrence of orogenic gold and intrusive gold. Although sediment-exhalative (SedEx) deposits are not described in the west Arunta Orogen, they are likely to occur because of the presence of basinal brines that could interact with reduced sedimentary rock (e.g. Bitter Springs Formation). Likewise, the potential for unconformity-related uranium exists in areas where the basement occurs beneath younger sedimentary basins. The west Arunta Orogen also has potential for surficial uranium, associated with calcretes or playa sediments.

Although there is still much debate about genetic models of iron oxide–copper–gold (IOCG) deposits, they are considered unlikely to occur in the west Arunta Orogen. The current evidence for IOCG deposit formation implies large hydrothermal systems are associated with some form of underlying magmatism, with fluids derived from possible combinations of magmatic, evaporitic, and meteoric sources. In the west Arunta Orogen, although poorly exposed and explored, there appears to be a lack of widespread metasomatism and, in particular, a lack of voluminous regional sodic alteration, as well as a lack of outcropping mafic–ultramafic rocks.

Several rare earth element (REE), vanadium, molybdenum–tungsten, and copper mineral systems are known in the Arunta Orogen (Scrimgeour, 2006a). However, they are not analysed in this study because orogenic and intrusive gold, unconformity-related and surficial uranium, and SedEx deposits are thought by several companies to be the most prospective (Meteoric Resources, 2009; Toro Energy Ltd, 2009; Leach et al., 2010).

The new interpretation of the architecture of the west Arunta Orogen, described in previous sections above, was used to design mineral system model templates for the deposit types thought mostly likely to occur in the west Arunta Orogen (Table 3). This template summarizes the critical processes (source, pathway, physical throttle, and chemical scrubber) and constituent subprocesses involved in the formation of the different mineral deposit types, as well as their respective exploration criteria (targeting element in Table 3) and spatial proxies (or predictor maps; Table 3). The template is further used to guide the prospectivity analysis described in the following sections.

GIS-based automated prospectivity analysis

A mineral prospectivity model can be defined as a simplified mathematical function representing the relationship between targeting criteria (represented by predictor maps) and the targeted mineral deposits (Porwal, 2006). A variety of linear and non-linear functions are used to approximate the relationship between exploration criteria and mineral deposits. Based on the type of function used, mineral prospectivity models are classified as linear (e.g. weights-of-evidence) or non-linear (e.g. fuzzy, logistic regression, neural networks, neuro-fuzzy, Bayesian network classifiers). They have also been alternatively classified into knowledge-driven and data-driven, based on whether the model parameters are estimated using conceptual knowledge or empirical data.

Since the west Arunta Orogen is a greenfields area with just a few known prospects of any type, knowledge-driven fuzzy models are the most appropriate prospectivity analysis models for the orogen. However, here we also experiment with a data-driven weight of evidence model using high mineral oxide content points as training data. The mineral oxide contents were extracted from the GSWA state geochemistry dataset (GSWA, 2009a), Geoscience Australia's (GA) OZCHEM dataset (see GSWA, 2009b), and regolith geochemistry data (GSWA, 2009b). These data are analysed in their logarithm form. Subsequently, threshold values (which correspond to: $x(\log[X]) + 2\sigma(\log[X])$, where [X] is the element content; Singer and Kouda, 1999) were used to generate related predictor maps. Details are given in Cheng (2007). Element ratios and contents were interpolated using the inverse distance weight (IDW) algorithm. The IDW method is based on spatial autocorrelation theory; objects

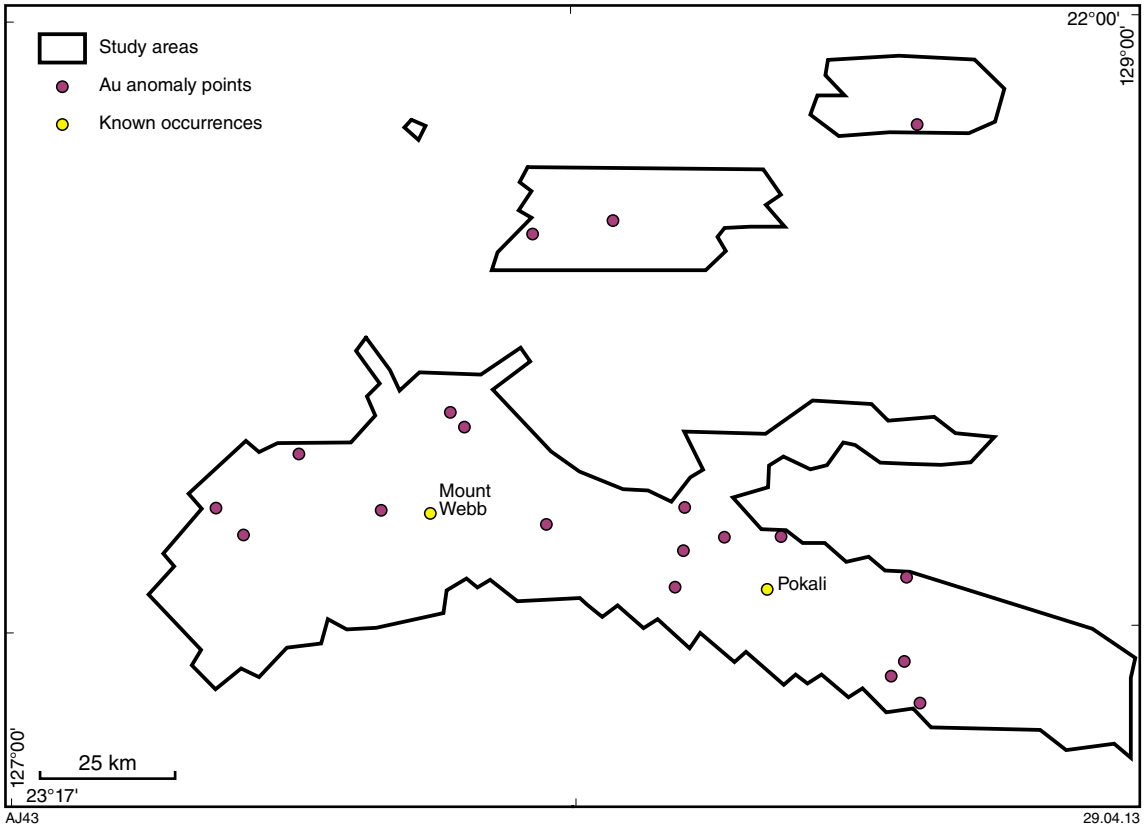

Figure 24. Location of gold training points with a gold content higher than 4 ppm (GSWA, 2009b; DMP, 2012)

that are close to one another are more alike than those that are farther apart. It is especially suitable if sample points are evenly distributed throughout the study area. Therefore, the IDW method is suitable for a regional geochemical dataset such as used here. ArcGIS software was used to carry out the analysis using a 100 m unit cell size, according to the overall accuracy of available data. Similarities in the factors affecting different mineral systems mean that most of the predictor maps that are created for one commodity can also be used for another in the same area.

Fuzzy model (knowledge-based GIS-driven prospectivity analysis)

Knowledge-driven analyses establish the relationship between the spatial exploration datasets and the targeted mineral deposits, based on conceptual exploration models. They are often employed in regions with few or no known mineral occurrences with which to 'train' the exploration datasets. Knowledge-driven techniques, such as fuzzy modelling, are subjective in that the 'explorer' determines the relative significance of the exploration datasets and assigns a significance weighting based on the exploration model. Knowledge-based prospectivity mapping is achieved by extracting the spatial relationships from exploration datasets on the basis of the exploration model, quantifying these spatial relationships, and integrating them using mathematical operators chosen by the user.

A generalized fuzzy model for mineral prospectivity mapping can be defined as follows. If X is a set of n predictor maps X_i (i = 1 to n) with r patterns (or classes) denoted generically by xij (j = 1 to r), then n fuzzy sets $\tilde{A}_i$ in X, containing 'favourable indicators for the targeted mineral deposit-type', can be defined as follows (Porwal et al., 2003):

$$\tilde{A}_i = (x_{ij}, \mu_{\tilde{A}_i}) \mid x_{ij} \in X_i \quad \text{(equation 1)}$$

where $\mu\tilde{A}_i$ is the membership function for estimating the fuzzy membership value of xij in the fuzzy set $\tilde{A}i$. The fuzzy membership function can be linear, Gaussian, or any other appropriate function. In the present study, we used the following linear function:

$$\mu_{\tilde{A}_i} = \frac{m_i \times w_j \times cf_i}{1000} \quad \text{(equation 2)}$$

where m_i is the map weight, w_j is the class weight and cf_i is the confidence factor. Map weights and confidence factors were subjectively assigned a value between 1 and 10 based on expert knowledge. Class weights were also assigned values between 1 and 10; however, classes that do not have any relation to mineralization are assigned very low class weights, close to zero, but never actually zero. Zero values are not assigned because these values, when transmitted through the fuzzy inference network, could render some areas entirely unprospective, even if they contained several highly favourable indicators.

Table 3. Camp-scale dependence of targeting model parameters of the west Arunta Orogen region

	Source		*Active pathway*		*Physical Throttle*		*Chemical Scrubber*	
Commodity	*Targeting element*	*Proxy/Predictor Map*	*Targeting element*	*Proxy/Predictor Map*	*Targeting element*	*Proxy/Predictor Map*	*Targeting element*	*Proxy/Predictor Map*
Orogenic gold	Stalled subduction + mantle metasomation	Arc signature magma Alkaline magmas? Adakites?	Trans-lithospheric fault	Major gravity breaks	Near Amadeus unconformities	Amadeus unconformities depth (magnetic low, gravity high)	Reducing stratigraphy	Spectral data (carbon-rich)
	Cannot be differentiated on scale of the West Arunta Orogen		Long-lived fault	Control on primary structure Control on intrusion distribution Control on volcanics distribution	Anticline	Structure interpretation	Iron-rich rocks (banded iron-formation/volcanic sediments)	Spectral data
			Accomodation zone – major fault interpretation	Geochemistry	Competency contrast	Groves's chart of rock type and relative strength	Chemical gradient	Map of rock reactivity
			Alteration (potassic, metals) on structures	Spectral data	Damage zone	Structure density	Gold anomalies	
Intrusive gold	Interpreted buried intrusion		As above		As above		As above	
					Carapace of intrusions	Circular magnetic + gravity anomalies	Limestones CO32-	Skarn
						Porphyry algorithm		
							Au anomalies	
Sediment exhalative (SedEx)	Evidence of evaporite (salt diapir)		As above (except potassic alteration)				Reduced stratigraphy	Carbon-rich rock
	Oxidised clastics, dominant basin fill (geology map)		Emphasis on basin margin faults?				Lead + zinc anomalies	
Sediment-hosted and unconformity-related uranium	As for sediment exhalative		As above		Near Amadeus unconformities	Structural interpretation	Reduced stratigraphy	Radiogenic anomalies
	Radiogenic basement	Intrusion geochemistry; radiometrics	Radiometric anomalies on structures		Thrust breaching unconformities at depth (magnetic + gravity)			

Map weight and class weight, respectively, indicate the importance of a predictor map and a class on the predictor map. The confidence factor is assigned to a predictor map based on the degree of representativeness (cf. McCuaig et al., 2010); that is, how closely it represents an exploration criterion. The predictor map gets a higher confidence factor if it directly maps the exploration criteria and a lower confidence factor if it is based on mapping the indirect response of the exploration criterion. Confidence factor is also used to account for the uncertainties in the primary dataset that is used to create a particular predictor map.

Fuzzy modelling is implemented in the following two steps: 1) assigning map weights, class weights and confidence factors, and estimating fuzzy membership values to create fuzzy predictor maps; 2) combining the fuzzy predictor maps using an appropriate fuzzy inference network to derive the fuzzy prospectivity map.

Assigning map weights, class weights, and confidence factors

Insights gained from the combined geological and geophysical studies, and knowledge of the MSA in the context of the west Arunta Orogen (Tables 3, 4, 6, 7, and 8), were used to assign the map weights and class weights. Fuzzy membership values for the predictor maps were estimated from the map weights, class weights, and confidence factor using the linear membership function given in equation 2. The map weight and the class weight were derived as outlined below, following Porwal et al. (2003). Based on subjective judgement, all potential patterns in a predictor map are ranked on a scale of 1 to 10. The most favourable pattern is ranked 10, whereas the least favourable pattern is ranked 1. In this scheme, the rank of a pattern is its class weight. As much as possible, the patterns are ranked at equal intervals. This method of allotting weights by ranking is simple, as most experts are likely to agree upon the favourability rank of a predictor pattern, but are likely to disagree upon its favourability weight. Similarly, based on their importance with respect to pertinent recognition criteria, all predictor maps were assigned map weights according to the same procedure for assigning class weights. The fuzzy membership values were mapped to create fuzzy predictor maps.

Combining fuzzy membership values

In a fuzzy system, the extraction and combination of different evidence is carried out by operators. Bonham-Carter (1994) described five operators that are commonly used for combining mineral exploration-related datasets. These are *fuzzy AND, fuzzy OR, fuzzy algebraic PRODUCT, fuzzy algebraic SUM,* and *fuzzy GAMMA* operators.

The *fuzzy AND* overlay type will return the minimum value of the sets the cell location belongs to. This technique is useful for identifying the least common denominator for the membership of all the input criteria. *Fuzzy AND* uses the following function in the evaluation:

$$FuzzyAndValue = min(arg_1, ..., arg_n)$$

Fuzzy OR is like the Boolean OR operator (logical union). The output membership values are controlled by the maximum value of the input map. This technique is useful for identifying the highest membership values for any of the input criteria. The function is defined as:

$$m_{Combination} = Max(m_A, m_B, m_C, \ldots\ldots)$$

Fuzzy algebraic PRODUCT is defined as:

$$mCombination = {}_{i=1}p^{n}(m_i)$$

where m_i is the fuzzy membership value of the ith map and $i= 1,2,3,...n$.

The combined fuzzy membership values tend to be very small due to the multiplying effect of several numbers less than 1; i.e. the effect is decreasing. This is equivalent to the product rule of probability theory.

Fuzzy algebric SUM is complementary to the algebric product, and is defined as:

$$m_{Combination} = 1 - {}_{i=1}p^{n}(1 - m_i)$$

where m_i is the fuzzy membership value of the ith map and $i = 1,2,3,...n$.

The result of this operation is always larger than or equal to the largest contributing fuzzy membership value; i.e. the effect is increasing.

Fuzzy GAMMA operator is defined as:

$$m_{Combination} = (fuzzy\ algebraic\ SUM)^{g} * (fuzzy\ algebraic\ PRODUCT)^{(1-g)}$$

The g value is arbitrary and ranges from 0 to 1. When g is equal to 0 then the combination is *fuzzy algebraic PRODUCT*. If g is equal to 1 then the combination is *fuzzy algebraic SUM*.

These operators provide greater flexibility than a weighted-sum or weighted-overlay model and let the expert incorporate greater sensitivity based on their knowledge of how the predictor maps interact. In practice, operators for combining predictor maps are relatively easy to select, but the fuzzy membership function may require some tuning of the parameters to properly represent expert knowledge.

Weights-of-evidence model (data-based GIS-driven prospectivity analysis)

The weights-of-evidence (WofE) technique is a data-driven quantitative method for combining evidence in support of a hypothesis. The WofE model has been widely used for mineral potential mapping. See Brown et al. (2004) and references cited therein.

Mineralization occurrence database

The set of mineral deposits point locations (showings, occurrences, etc.) is used to calculate the weight for each evidential theme, one weight per class, using the overlap relationships between the points and the various classes on the theme. The characteristics of the training points are

held in an attribute table. Point subsets may be selected using the values of attributes, such as deposit size, or deposit type. However, points are treated as being either present or absent in the model, and are not weighted by characteristics such as deposit size. The west Arunta Orogen contains only two gold showings (Mount Webb and Pokali; DMP, 2012) that could be used in the analysis. Instead, high gold content samples (with gold >1 ppm) were used as training points (deposits) for the WofE analysis (Fig. 24).

Methodology

In the WofE method, a series of binary predictor maps are combined to produce an output map of mineral potential, using a Bayesian model (Agterberg 1989; Agterberg and Bonham-Carter 1990; Bonham-Carter and Agterberg 1990). The spatial association is expressed in terms of WofE for each of the predictor maps. The WofE are combined with the prior probability of occurrence of the deposits using Bayes's rule in a log–linear form, under an assumption of conditional independence, to derive the posterior probability of occurrence of the deposits. Prior probability is a kind of probability based on prior experiences and analyses, whereas posterior probability is a probability assessment on the basis of new information as well as the revised, original prior probability. The method was originally developed for non-spatial applications for quantitative medical diagnosis (e.g. Lusted, 1968; Aspinall and Hill, 1983; Heckerman et al., 1992). Bonham-Carter (1994) provided an in-depth exposition of the WofE approach to mineral potential mapping. The model was implemented in the following three steps: 1) data pre-processing; 2) calculation of WofE; 3) calculation of posterior probabilities.

Data pre-processing

The nature of the data typically determines which statistical test will be employed by the investigators. There are two main types of data: categorical and continuous. A set of data is said to be categorical if the values or observations belonging to it can be sorted according to category. Each value is chosen from a set of non-overlapping categories; e.g. geology, stratigraphic groups, buffer corridors around linear structures. Continuous data are related to any value within a finite or infinite interval such as geophysical data, topographic data, or remote sensing data.

The data processing involves generalization and reclassification of the input predictor maps to reduce the number of classes. Although multiclass maps can be incorporated in the WofE modelling (e.g. Porwal et al., 2003), it is generally preferable to use binary (presence/absence) maps in the analysis because a large number of classes sometimes results in high variance of probabilities, and hence, less robust estimations. Moreover, the likelihood of violation of conditional independence increases with the number of predictor maps and number of patterns on each map (Pan and Harris, 2000).

All numerically continuous scale maps showing distances to various linear structures were converted into dichotomous maps using the method described by Bonham-Carter (1994). In brief, the technique involves estimating contrast values for cumulative distances from the structure, and estimating the distance at which the contrast value peaks. This distance is used as a threshold to determine the optimal buffer corridor around the structure, within which its spatial association with known deposits is maximized. A similar technique is used to reclassify the occurrence density maps.

Calculation of weights of evidence for predictor maps

The WofE of predictor maps were calculated using Bayes's Rule, which allows estimation of conditional probability of a deposit given the presence of a predictor map, from the probability of the predictor map given the presence of a deposit. Each dichotomous predictor pattern can be considered a binary, with present or absent status. The latter is calculated based on the spatial distribution of known deposits. Two weights are calculated for each predictor map; namely, W^+ (positive WofE) and W^- (negative WofE), using the following relations:

$$W^+ = \text{Log}\,(P(B|D) / P(B|DD)) \qquad \text{(equation 3)}$$

$$W^- = \text{Log}\,(P(BB|D) / P(BB|DD)) \qquad \text{(equation 4)}$$

where B and BB, respectively, represent the presence and absence of the predictor feature, and D and DD denote the presence and absence of deposits, respectively.

W^+ defines the conditional probability of finding a deposit given the presence of the predictor map, and hence quantifies the positive spatial association. W^- defines the conditional probability of finding a deposit given the absence of the predictor map, and thus quantifies the negative spatial association.

The net spatial association is defined by contrast ($= W^+ - W^-$). A positive contrast indicates a positive spatial association, while a negative contrast indicates a negative spatial association. Contrast values close to 0 indicate poor or no spatial association. Normalized values of contrast provide a measure of confidence in contrast values.

Combining predictor maps and calculation of posterior probabilities

Posterior probabilities are estimated by combining the conditional probabilities (or WofE) of various predictor maps using Bayes's equation in a log–linear form, under an assumption of conditional independence. The assumption of conditional independence simplifies the calculations; however, it is unrealistic in most modelling situations. Therefore, the posterior probabilities estimated using the WofE model generally tend to be artificially elevated and are best interpreted as measures of relative favourability rather than posterior probabilities sensu stricto.

Combining predictor maps in the WofE modelling involves generation of a unique conditions grid map (Bonham-Carter and Agterberg, 1990; Kemp et al., 1999). The attribute table associated with a unique conditions grid (unique conditions table) has one record per unique

condition class, and additional fields containing calculated variables can be added for each record.

Gold mineral systems

The joint geological and geophysical interpretation of the Paleoproterozoic–Mesoproterozoic Arunta Orogen led to the recognition of crustal-scale faults for the pathways and physical traps that are critical elements for gold mineralization. Other critical elements include the mechanical separation of gold from hydrothermal solutions, i.e. the actual deposition of the gold (mixing of fluids, reaction of the fluid with the surrounding wallrock, and placing the fluid under physical stress that induces a chemical change in the fluid).

Orogenic and intrusive-related gold deposits are interpreted as genetically distinct gold systems by a number of authors (e.g. Thomson et al., 1999; Lang and Baker, 2001; Hart, 2007). However, recent work (Hagemann and Cassidy, 2000) suggests intrusive-related gold deposits are a subclass of orogenic gold deposits. Their consideration of the temporal, spatial, and genetic similarities, as outlined previously, challenges the validity of a dual classification system. In the following section, granite as source (for the intrusive-related gold mineralization) is either taken into account, or not taken into account (for the orogenic gold system), during gold prospectivity analysis.

Predictor maps

In the following sections, the derivative predictor maps used to represent the critical components of both orogenic and intrusive-related gold mineral systems in the west Arunta Orogen (Table 3) are described. The prospectivity analysis was undertaken only on specific parts of the west Arunta Orogen because of uneven data coverage (Fig. 8). In the first instance, the prospectivity analysis has been undertaken over areas with high outcrop density and high geochemical sample density. This was necessary because many of the orogenic gold targeting elements, such as the chemical traps and pathways, are best represented by geochemical proxies. Other than source, all other predictor maps for all other critical processes (active pathways, physical throttle, and chemical scrubber) remain the same for both the intrusive-related and non-intrusive-related models.

Predictor maps for source

Mineralizing fluids could be derived from either or both of the c. 1770 Ma and c. 1685–1640 Ma granitic intrusions. Therefore, spatially, the mineralization is most likely to occur in the vicinity of granitic bodies, with the probability of a deposit being present decreasing with the increasing distance from the granites. A map showing distance to granitic bodies, based on the interpreted bedrock geology map in GSWA (2009b), was used as the predictor map for gold sources (Appendix, Map 1). This source predictor map was used to conduct the prospectivity analysis for intrusive-related gold, but not orogenic gold.

Predictor maps for pathways

Based on the new structural interpretation, the most likely critical pathways for transporting mineralizing fluids are D_1 and D_2 faults (Fig. 20). Most mineralization is therefore expected to occur in spatial proximity to these structures, and the closer an area is to the structure, the higher the probability of a deposit being present in that area. Therefore, the following predictor maps were created by mapping distances to the structures (Appendix, Maps 2 and 3; 5 km either side of D_1 and D_2 faults, respectively).

Crustal fluids need pathways to ascend, which are provided by extension of the crust and lithosphere. The largest and main D_1 and D_2 faults (Fig. 4) were identified from the magnetic and gravity data. Their intense, distinct, and laterally continuous signatures are readily identifiable on the potential field maps (Figs 11 and 14). They are likely to be crustal-scale structures as indicated by the seismic and MT data (Figs 6 and 7, respectively). Maps representing the distance to the main D_1 and D_2 faults were generated (Appendix, Maps 4 and 5) as these faults are the main discontinuities that could have transported the deep crustal fluid. This is why they have a high map weight of 9 ascribed to them (Table 4).

In principle, the structures that are associated with gold geochemical anomalies could be the best indicators of mineralization fluid passageways. To derive the predictor maps, high (positive) gold content over main D_1 and D_2 faults (Appendix, Maps 6 and 7) in a 1-km wide buffer zone around the main D_1 and D_2 structures were produced. High gold content values, derived by interpolating filtered surface geochemical data, were linked to the buffer zone. The same process was used for the predictor maps showing low to medium (positive) gold content over main D_1 and D_2 faults (Appendix, Maps 8 and 9).

Predictor maps for physical traps

Physical throttles are localities into which mineralization fluids are focused and, in the presence of a favourable geochemical environment, precipitate the metal (Wyborn et al., 1994). Fluids migrate into dilatational zones of high fracture-related permeability, which tend to occur where competency contrasts are high (Cox et al., 2001). The juxtaposition of rock units with high competency contrast tends to enhance the damage and dilatational zones into which fluids may be focused. Similarly, areas with a high density of geological contacts and structures could potentially focus the flow of mineralizing fluids; more so, if they also contain contacts with high competency contrasts. The predictor maps for physical traps described below were produced based on this rationale.

The ‘competency contrast across geological contacts’ map (Appendix, Map 10) was the first predictor map produced. Generalized lithological units in the area are attributed with a (relative) rheology value that was estimated using the chart shown in Figure 25. Each geological contact was then attributed with the difference in the rheology of the lithological units on each side. The competency contrast map was derived by allocating each unit cell with the value of the rheology difference of the nearest contact, up to a maximum distance of 1 km.

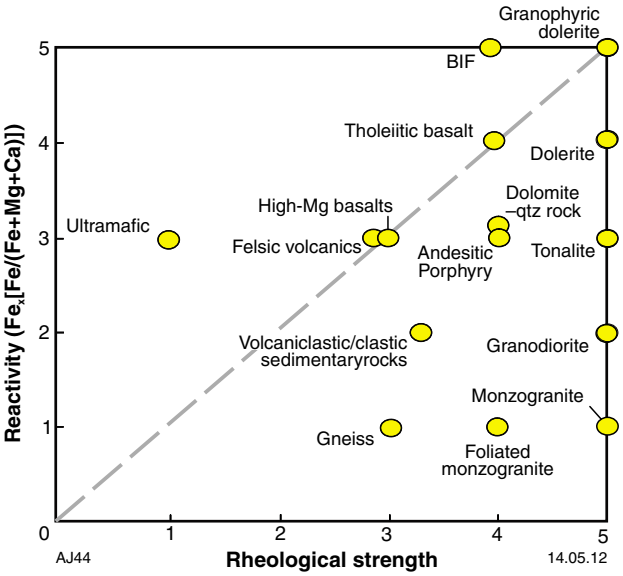

Figure 25. Relative chemical reactivity and rheological strengths for selected rocks (from Groves, 1993)

The 'geological contact density' map (Appendix 1, Map 11) was derived by mapping the density of geological contacts in every one square kilometre unit area of the selected area of the west Arunta Orogen.

The 'geological contact density weighted by competency contrast' map (Appendix, Map 12) was derived by mapping the competency-contrast-weighted geological contact densities per square kilometre.

Fold axes are conceptually good traps for hydrothermal fluids. We therefore produced a predictor map 'distance to fold axes' (Appendix, Map 13) based on the proximity to fold axes.

The 'fault density map' (Appendix, Map 14) was derived by estimating and mapping the density of all types of faults per square kilometre.

The intersections of D_1 and D_2 faults could provide the permeable channels for focused fluid movement. We therefore used mapped distances to the intersection points of these faults to derive the predictor map in Appendix 1, Map 15.

All fault intersections density map was constructured bycontouring the number of fault intersection per square kilometre (Appendix, Map 16). This indicates greater structural complexity, and hence, likely sites of fluid focusing.

Predictor maps for chemical traps

The main mechanism for gold deposition in the west Arunta Orogen is probably linked to fluid pressure drops (i.e. structurally-induced chemical change; c.f. McCuaig and Kerrich, 1998). These probably play an important role (aside from structural controls) in Fe-rich host rocks of the Arunta Orogen. Indeed, a key mechanism for gold deposition is through fluid – wall rock reactions in which iron-rich minerals in the wall rocks react with gold-sulphide complexes in the fluids, resulting in desulfidation of the fluids and breakdown of gold-sulphide complexes (Phillips and Groves, 1983; Mikucki, 1998). Consequently, upward migrating hydrothermal fluids may precipitate gold where there is a change in the reactivity of rocks.

The favoured traps for deposition of orogenic gold are Fe-rich (reduced) rocks (Groves et al., 1998; Hagemann and Cassidy, 2000). Gold deposition is inferred to result from catastrophic changes in physical conditions, abrupt changes in chemical gradient, phase separation, or fluid mixing. BIFs can provide very abrupt changes in chemical gradient, and the distribution of these rocks in the west Arunta Orogen was interpreted from the aeromagnetic data. Their density per square kilometre was then estimated and mapped to derive the predictor map showing BIF density (Appendix, Map 17).

All generalized lithological units were attributed with a (relative) chemical reactivity value that was estimated based on the sulfidation index given by the $Fe^{2+}/(Fe_{total}+Ca^{2+}+Mg^{2+})$ ratio (Fig. 25). Each contact was then attributed with the difference in chemical reactivity between the lithological units on each side of the contact. The reactivity contrast map (Appendix, Map 18) was derived by allocating to each unit cell the value of the chemical reactivity difference from the nearest contact, up to a maximum distance of 1 km.

The 'geological contact density weighted by reactivity contrast' map (Appendix, Map 19) was derived using the values in the chart shown in Figure 25, and by mapping the reactivity contrast-weighted geological contact densities per square kilometre.

Dolerite is conceptually a prospective host for gold because of its high chemical reactivity (Groves, 1993). The 'dolerite dyke density' map (Appendix, Map 20) was derived by estimating and mapping the density of dolerite dykes per square kilometre.

The arsenic and antimony contents, derived from the regolith database (Spaggiari et al., 2008) and geochemistry database (GSWA, 2009), can be indicators of gold presence (Phillips and Groves, 1983) and these contents were used to create the As and Sb predictor maps (Appendix, Maps 21 and 22).

The Fe content predictor map (Appendix, Map 23) is a good proxy for areas of desulfidation and the break-down of gold complexes due to fluid – wall rock reactions.

Gold content, derived from the regolith database (Spaggiari et al., 2008) and geochemistry database (GSWA, 2009a), is a direct indicator of the presence of gold. The gold content map (Appendix, Map 24) was used for validating the final output of the gold prospectivity analysis, i.e. to determine how well the prospectivity map predicts the anomalies in gold. For this reason, this map was not used as a predictor map.

Fuzzy model

Assigning map weights, class weights, and confidence factors

The map weights, class weights, confidence factors, and the fuzzy membership values for each of the 24 predictor maps used in this study, including the rationale for assigning these values, are shown in Table 4.

Combining fuzzy membership values

A three-stage inference network was designed to combine the fuzzy predictor maps (Fig. 26). In the first stage, the fuzzy predictor maps for source, pathway, chemical trap, and physical trap were combined using the *fuzzy OR* operator to create a single fuzzy predictor map for each critical component of the gold mineral system. This operator was selected because the presence of any one of the predictor maps is sufficient to infer the presence of the respective component. In the second stage, the fuzzy predictor maps for physical throttle and chemical trap was combined using the *fuzzy AND* operator to derive a single predictor map for traps. The *fuzzy AND* operator was selected because both the physical trap sites and the conducive geochemical environment are necessary for precipitation of gold from the mineralization fluids. Finally, the three fuzzy predictor maps for source, pathway, and trap were combined using the *fuzzy AND* operator to create the output fuzzy prospectivity map shown in Figure 27.

In a second inference network, we disregarded the source component and derived a prospectivity map based only on pathway and trap (Fig. 26).The second model was generated by removing the source; that is, by omitting the proximity to granite map from the analysis (Fig. 28). This model is based on the assumption that proximity to granite (source) is not a critical input for a camp-scale prospectivity analysis in the west Arunta Orogen. In fact, both outputs are quite similar in the zone excluding granite as a source. Moreover, the presence of potential sources in a gold system does not have major implications for the present case study. Indeed, the studied area corresponds to a camp-scale case, and source plays a more important role at craton scales (Table 2). The results are discussed in the section 'Gold prospectivity results'.

Weights-of-evidence gold model (data-based GIS-driven prospectivity analysis)

Data pre-processing, calculation of weights of evidence for predictor maps

The details of pre-processing used in this study are summarized in Table 5. The WofE and associated statistics were calculated using the 19 high gold content locations as training points. A unit cell size of 1 km^2 was used for estimating various probabilities. The results indicate that the following predictor maps show poor spatial association with the known deposits, and these predictor maps are excluded from further analysis: main D_1 and D_2 structures with low to medium Au content (Appendix, Maps 8 and 9), distance to fold closures (Appendix, Map 13), fault intersection density map (Appendix, Map 16), Fe-rich rock (BIF) map (Appendix, Map 17), and dolerite dyke density (Appendix, Map 20). The results for the remaining predictor maps are summarized in Table 5.

Combining predictor maps and calculation of posterior probabilities

The predictor maps were combined using digital overlay, which resulted in a unique condition grid map containing 6822 unique conditions. The WofE and the prior probability of gold deposits in the study area were used to calculate the posterior probabilities for the unique conditions, which were subsequently mapped in GIS to generate the prospectivity model shown in Figure 29. This prospectivity model does not take into account the source component. This map is a continuous-variable map that shows posterior probability values ranging from 0 to 1.

Gold prospectivity results

With the exception of areas π, α and γ (Fig. 28), the majority of the prospective targets delineated using the fuzzy analysis fall on the very high and high prospectivity zones delineated by the WofE analysis (€, β, ϕ, φ and Ω in Figs 28 and 29). A few of these areas are already being explored, for example at Pollock Hills (Ω) and Mount Webb (ϕ). All eight areas (Fig. 28) have a high *fuzzy AND* relative value varying from 0.32 – 0.44. Interestingly, most of the eight clusters do not correspond to the two known gold occurrences, which are located in areas of high to middle *fuzzy AND* relative value (0.26 – 0.31).

The probabilities associated with the targets defined through the WofE method are lower than those defined through the fuzzy method. The fuzzy method delineated larger targets than the WofE method. Therefore, the WofE method is considered to be more conservative. This may explain the absence of the targets π, γ, and α in the WofE analysis.

The WofE analysis is based on the spatial distribution of known high gold content in the study area. The spatial distribution of the known high gold anomalies does not show any particular orientation trend (Fig. 24). However, a west-northwest trend in the same orientation as the D_1 structures is clearly reflected in the WofE analysis (Fig. 29). Therefore, the empirical evidence suggests a strong control of D_1 structures over mineralization. This might explain the higher prospectivity zone (β) highlighted by the WofE analysis (Fig. 29).

Figures 28 and 29 highlight the CAS's influence on gold prospectivity. From studies of Archean terranes, it has long been recognized that major faults are important indicators of prospectivity, although it is adjacent smaller faults that preferentially host the gold (e.g. Groves et al., 1998; Joly et al., 2010, 2012). Deep-penetrating structures (crustal-scale according to seismic and MT data, Figs 6 and 7) provide pathways for metal transport or create suitable

Table 4. Fuzzy analysis for gold prospectivity analysis

Critical processes	*Input predictors map*	*Appendix map number*	*Fuzzy membership value map weight*	*Confidence factor*	*Rationale for expert knowledge based weight (fuzzy membership values)*	*Rationale for confidence factor*
Predictor maps for source						
	Granite source	1	7	7	Possible source	Interpreted bedrock geology used
Predictor maps for active pathways						
	Structures NW–SE D_1	2	8	9	Permeable structures for fluid movement	Well delimited from geology and geophysics
	Structures NE–SW D_2	3	7	9	Connection to Au uncertain, but conceptually permeable structures for fluid movement	Well delimited from geology and geophysics
	Main structures NW–SE D_1	4	9	7.5	Permeable structures for fluid movement (crustal features)	Delimited from geology and geophysics (but drawn approximatively)
	Main structures NE–SW D_2	5	7.5	7.5	Permeable structures for fluid movement (transfer features)	Delimited from geology and geophysics (but drawn approximatively)
	High (positive) gold anomalies over D_1 faults	6	9	7	Pathways associated with anomolously high Au values indicate fluid movement	Au values interpolation from relatively high density — main issues are data coverage, correct correlation of anomaly with a structure, and that values may be negative or unknown; given that the confidence in main D_1 and D_2 is 7.5
	High (positive) gold anomalies over D_2 faults	7	9	7	Pathways associated with anomolously high Au values indicate fluid movement	Au values interpolation from relatively high density — main issues are data coverage, correct correlation of anomaly with a structure, and that values may be negative or unknown; given that the confidence in main D_1 and D_2 is 7.5
	Moderate to low (positive) gold anomalies over D_1 faults	8	6.5	7	Pathways associated with anomolously high Au values indicate fluid movement	Au values interpolation from relatively high density — main issues are data coverage, correct correlation of anomaly with a structure, and that values may be negative or unknown
	Moderate to low (positive) gold anomalies over D_2 faults	9	6.5	7	Pathways associated with anomolously high Au values indicate fluid movement	Au values interpolation from relatively high density — main issues are data coverage, correct correlation of anomaly with a structure, and that values may be negative or unknown
Predictor maps for physical traps						
	Competency contrast across geological contact	10	9	7	Related to fracturing and opening up of spaces for fluid in-flow and ponding	Interpreted relative values from Grove's chart, not directly measured + interpreted bed rock geology

Table 4. continued

Critical processes	*Input predictors map*	*Appendix map number*	*Fuzzy membership value map weight*	*Confidence factor*	*Rationale for expert knowledge based weight (fuzzy membership values)*	*Rationale for confidence factor*
	Geological contact density	11	7	8	More geological contacts means more lithological contrasts — multilayer competency differences strongly influence fracture sizes and density distributions. Higher geological contact densities means there is an increased probability of competency differences, and hence increased fault/ fracture densities and dilation features	Interpreted geology used (should be higher than both of the comp contrast maps)
	Geological contact density weighted by competency contrast	12	9	7	See above — higher certainty as regards to the existence of competency contrasts	Interpreted relative values from Grove's chart, not directly measured + interpreted mapped geology; should be lower than contact density, and equal to compentency contrast across geological contacts = 7
	Fault density	14	7.5	9	Conceptually should have a good correlation with mineralisation — increased fault density implies greater structural complexity and more space, leading to fluid ponding	D_1 and D_2 structures mapped well, but high uncertainty regarding D_2 (same coefficient as faults predictor maps)
	Distance to fold axis	13	8	5	Good sites for fluid ponding	(Do not know if anticline or syncline)
	Distance to fault intersection	15	7.5	9	Good sites for fluid ponding	Given that confidence in D_1 and D_2 faults is high – 9 each
	Fault intersection density	16	8	9	Indicates greater structural complexity; fluid focussing	D_1 and D_2 structures mapped with high level of certainty
Predictor maps for chemical traps						
	Fe-rich rocks (banded iron-formation)	17	9	8	Higher reactivity across BIF contacts. Desulfidation of hydrothermal fluids as a result of reactions with iron oxides in the wall rocks; breakdown of gold sulfide complexes, precipitation of gold and Fe sulfides.	Interpreted geology from geophysics and geolgy well delimited
	Chemical contrast	18	9	7	Conceptually a good predictor in terms of Fe for sulphidation reactions — see above	Interpreted relative values from Grove's chart, not directly measured
	Chemical contrast density	19	9	7	Conceptually a good predictor in terms of Fe for sulphidation reactions — see above for contact density weighted by competency contrast	Interpreted relative values from Grove's chart, not directly measured
	Dolerite dyke density	20	6	8	Higher reactivity across dolerite contacts — higher iron contents and reactivity	Fuzzy membership value is 6 for the fact that they are crosscutting D_1–D_2 and interpreted from magnetic and gravity datasets

Table 4. continued

Critical processes	*Input predictors map*	*Appendix map number*	*Fuzzy membership value map weight*	*Confidence factor*	*Rationale for expert knowledge based weight (fuzzy membership values)*	*Rationale for confidence factor*
	Au anomaly (metal anomalies)	24	9	7.5	Direct indicator of gold presence — we used gold anomaly map for validating the output; i.e. how well the prospectivity map predicts the anomalies.	(Interpolation of values, and values may be negative or unknown)
	As anomaly (metal anomalies)	21	7	7.5	Indicator of gold presence	(Interpolation of values, and values may be negative or unknown)
	Sb anomaly (radiometry)	22	7	7.5	Indicator of gold presence	(Interpolation of values, and values may be negative or unknown)
	Fe map	23	8	7.5	For desulfidation and breaking down gold complexes due to fluid – wall rock reactions	(Interpolation of values, and values may be negative or unknown)

geometries for stress-driven fluid flow, and these fluids migrate through or diffuse away from the larger faults to depositional sites along the smaller faults.

Uranium mineral systems

Uranium deposits occur in a variety of igneous, hydrothermal, and sedimentary geological environments. The established uranium deposit classification schemes (Dahlkamp, 1978; Mashkovtsev et al., 1995; International Atomic Energy Agency, 2000; McKay and Miezitis, 2001; Organisation for Economic Co-operation and Development Nuclear Energy Agency, International Atomic Energy Agency, 2005) define 14 categories, based on host rocks, structural setting, and mineralogy of the deposit. This scheme is not optimal for prospectivity analysis and Kreuzer et al. (2010) grouped the different types of deposits into six uranium system models: surficial, sedimentary, igneous-related, metamorphic/metasomatic, unconformity-related, and vein-related uranium systems. The groupings are based on similarities in genetic processes, environments of ore formation, and MSA elements mappable at the regional to continent scale. Based on our current understanding of the geology, the west Arunta Orogen is considered prospective for unconformity-related and surficial uranium deposits. The WA airborne radiometric map depicts an aerially-extensive uranium channel radiometric anomaly located over the southern part of Lake Mackay, and was the main exploration driver behind Nova Energy applying for exploration tenements in the area. Toro Energy Limited has completed two detailed airborne surveys and an inaugural program of aircore drilling that led to the Theseus prospect discovery. There, highly anomalous uranium is associated with oxidised and reduced, interbedded sands and clays (Toro Energy Ltd, 2009, 2010).

Unconformity-related uranium mineral systems

Unconformity-related uranium deposits (Fig. 30) are a type of high-grade uranium deposit, the best known examples of which are the deposits in the Athabasca Basin in Canada. Examples in Australia include those in the Pine Creek Orogen and the Kintyre deposit in Western Australia (Ramaekers et al., 2007; Jefferson et al., 2007). In such deposits, mineralization is associated with the unconformity between a thick, Paleo- to Mesoproterozoic sandstone cover and an Archean to Paleoproterozoic crystalline basement (Table 3). The ore bodies usually occur along fractures in sandstone or in basement rocks. Mineralization occurs near the unconformity, usually, but not necessarily, in the basin sequence, and is spatially associated with basement faults that typically contain graphitic material (although this is not always the case with the Australian deposits, e.g. Pine Creek where most of the unconformity is in the basement). Uranium occurs mostly within uraninite with associated chlorite–hematite–sericite alteration and, in some cases, silica dissolution or deposition (silicified caps).

The west Arunta Orogen contains all the ingredients

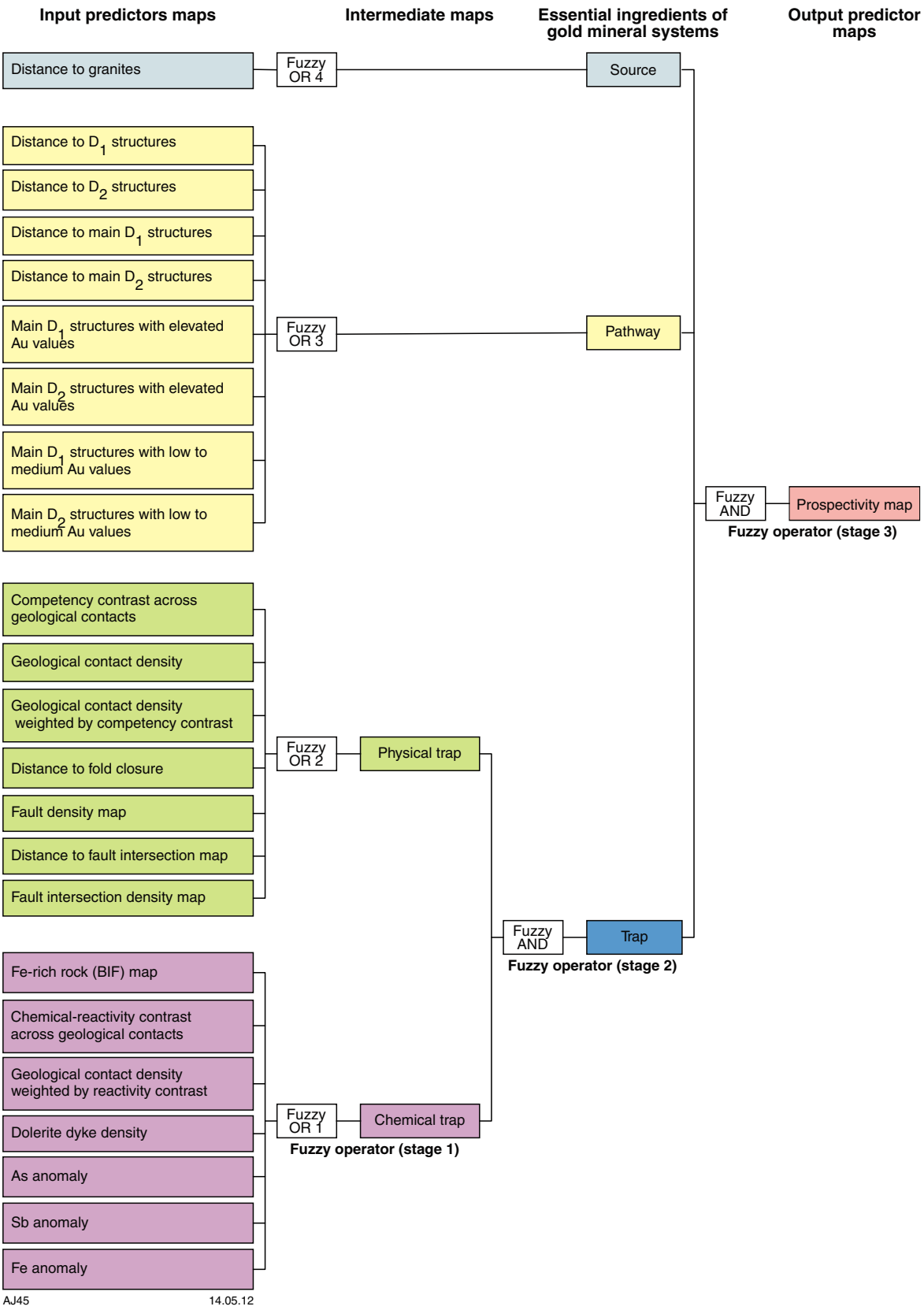

Figure 26. Multi-stage fuzzy inference network used for combining fuzzy gold predictor maps

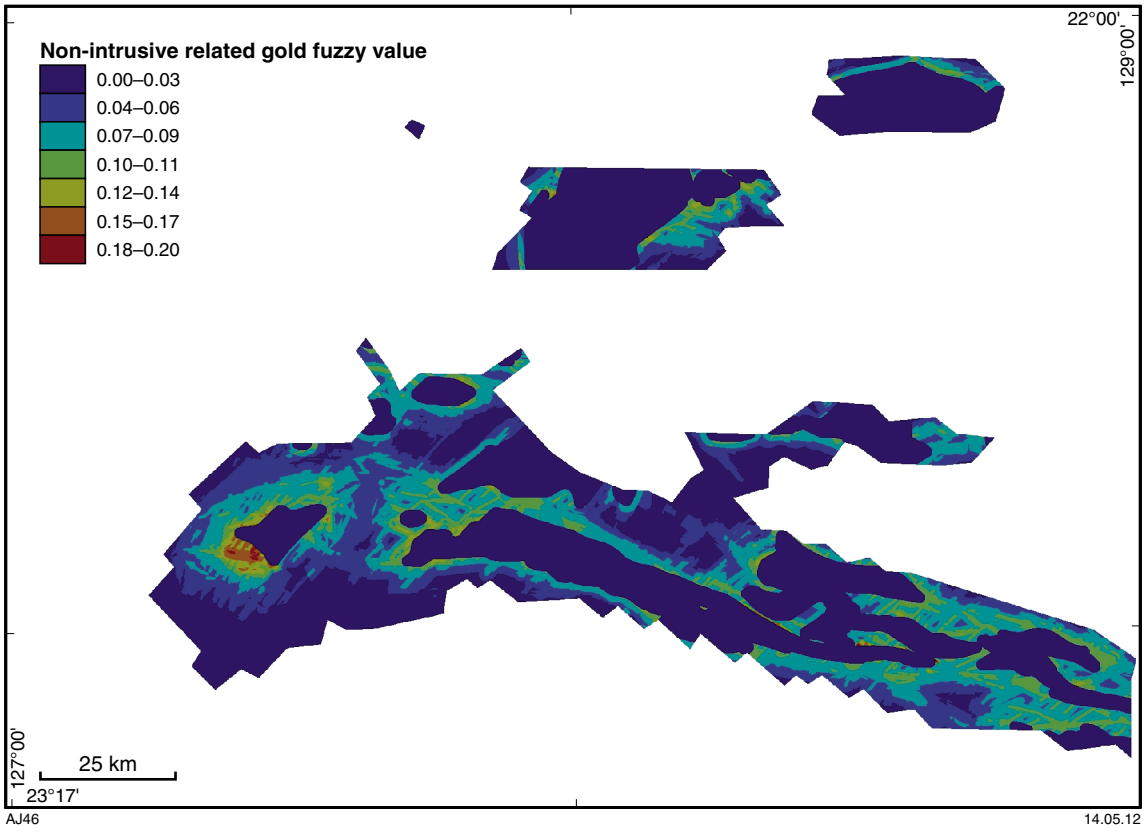

Figure 27. Fuzzy prospectivity model for the intrusive-related gold mineral system

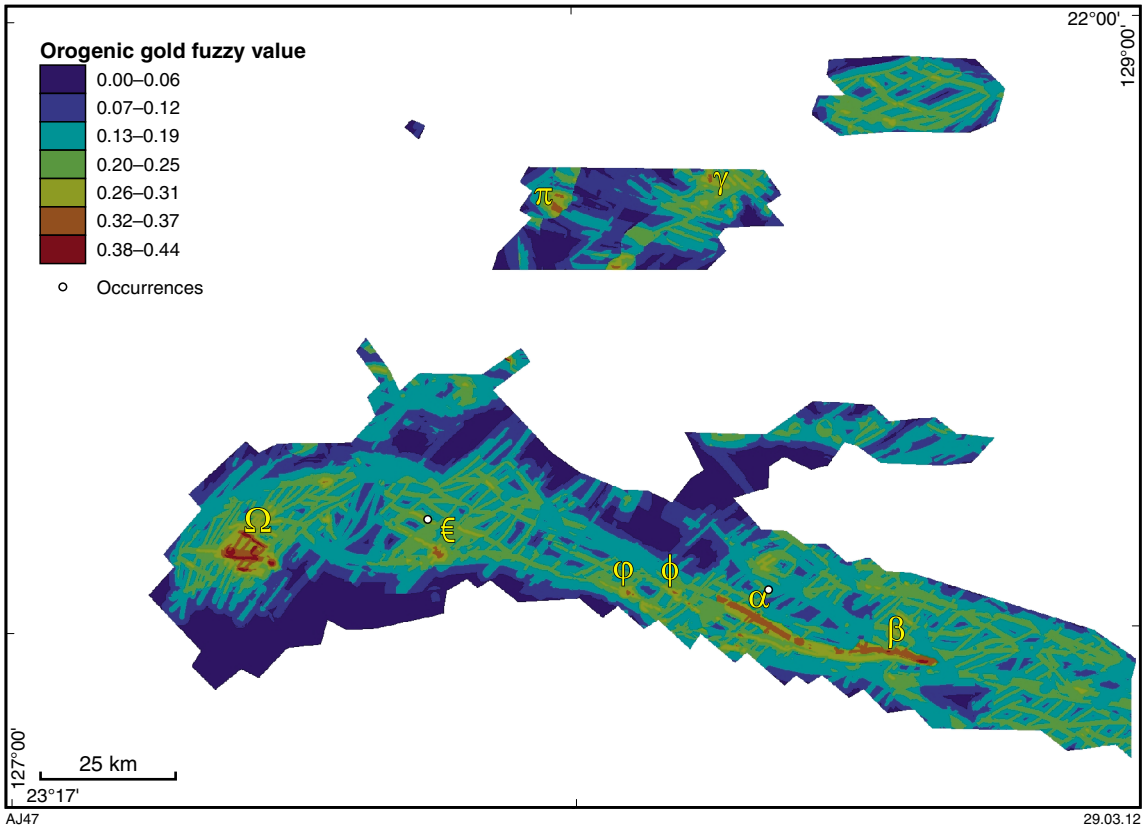

Figure 28. Fuzzy prospectivity model for the orogenic gold mineral system. The granite as a source predictor is disregarded

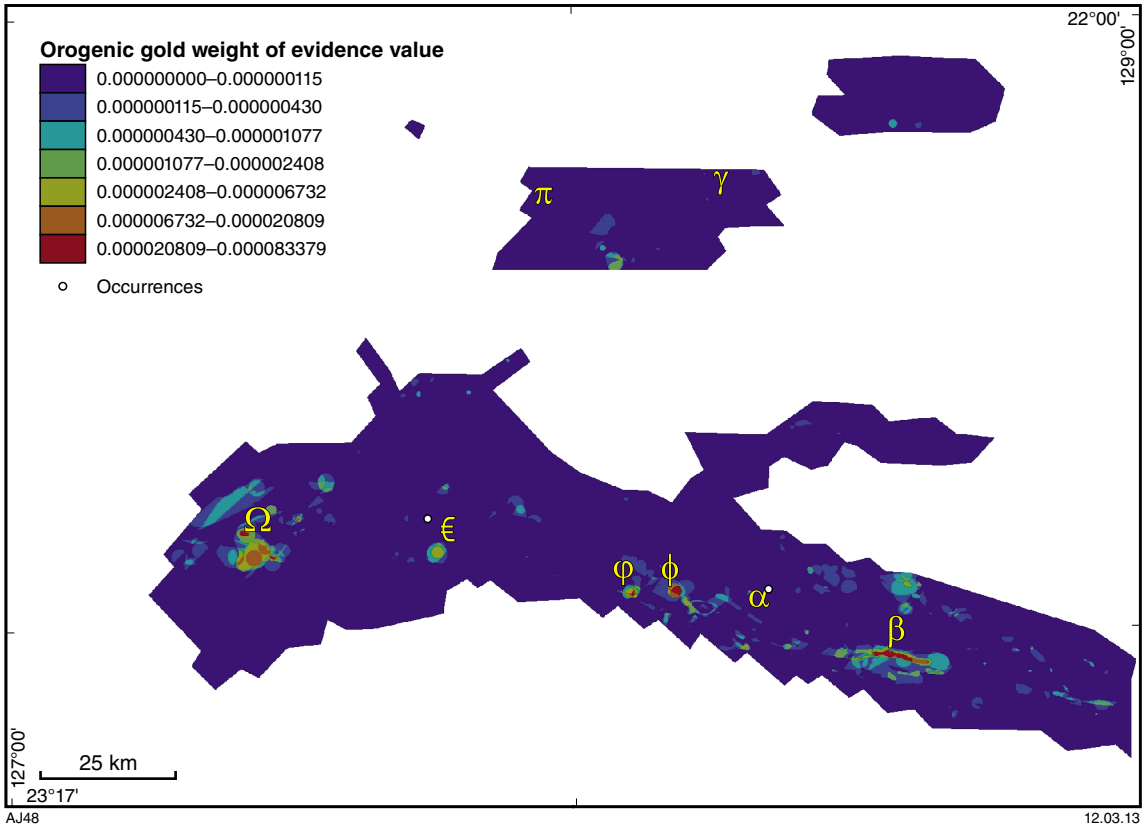

Figure 29. Weights-of-Evidence (WofE) prospectivity model for the orogenic gold mineral system. The granite as a source predictor is disregarded

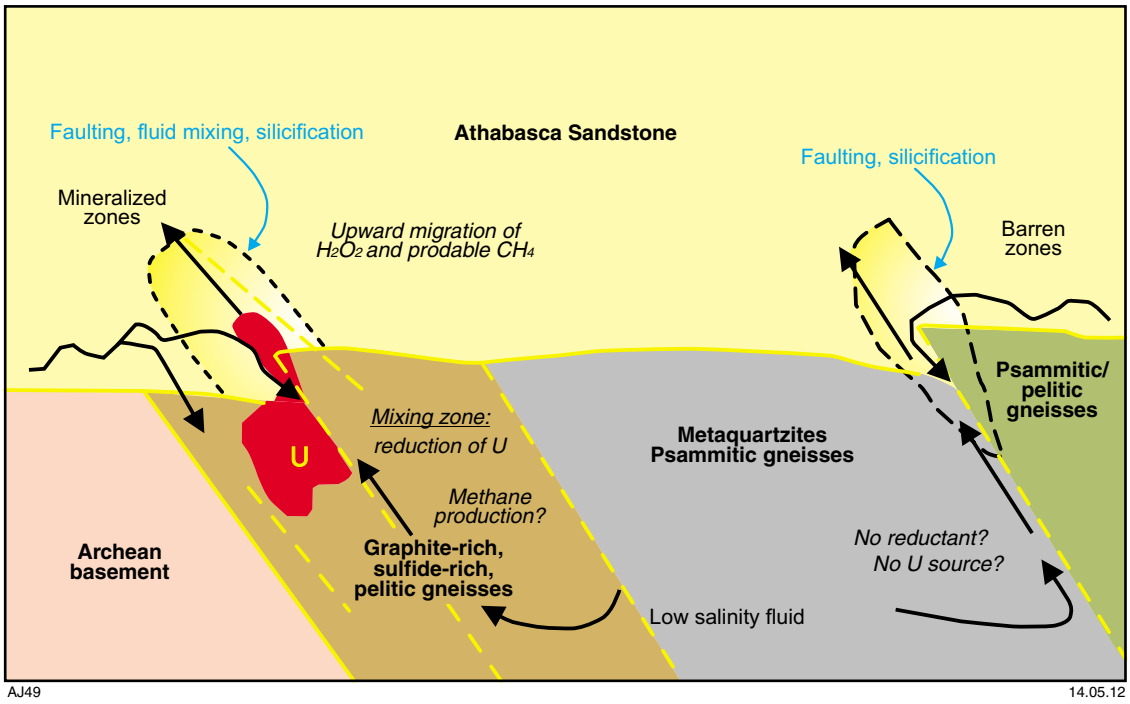

Figure 30. Genesis of unconformity-type uranium deposits (modified after Derome et al., 2003)

required for unconformity-related uranium deposits: 1) uranium-enriched Proterozoic basement rocks (e.g. Lander Rock Formation); 2) c. 1770 and c. 1640 Ma granites, which are presumably enriched in uranium (Figs 3 and 4); 3) a significant Proterozoic unconformity that separates igneous and metamorphic basement rocks from the overlying sedimentary sequences (Fig. 3); 4) deep-penetrating structures that permit fluid migration (Figs 6 and 7); 5) regional compressional structures (i.e. active thrusting and a driving force for fluid migration, Fig. 22); and 6) sites where oxidized basinal brines could interact with reduced strata (e.g. the Bitter Springs Formation). Details of the predictor maps, along with the geological rationale, are given below.

Predictor maps

Using fuzzy GIS analysis, data that do not have a consistent coverage over the entire study area cannot be used. Due to the uneven data coverage (Fig. 9), the unconformity-related uranium prospectivity analysis is undertaken in the same area as the gold analysis. Outcrop is poor, and the area is largely covered by sand-plain (Spaggiari et al., 2008). In this setting, radiometric data, which capture the uranium content of the top few centimetres of the sand, were not used because it was thought that they may not be representative of the bedrock, as the sand may have been transported. Also, the U values do not exceed 4 ppm, and are generally less than 2 ppm.

Predictor maps for source

The key uranium sources in an unconformity-related uranium mineral system (Derome et al., 2003) are: 1) uranium-rich Archean and Paleoproterozoic igneous and metamorphic basement rocks below the unconformity surface; 2) paleoregolith surfaces at the unconformity; and 3) uranium-enriched, Paleoproterozoic intrabasinal clastic sediments above the unconformity surface.

Overlying basin-fill clastic sediments act as a reservoir of oxidised brines that leach uranium from source rocks (McKay and Miezitis, 2001). However, it is difficult to find a proxy for this process in the available datasets. Based on the spatial proxies, three predictor maps for source were derived.

A map showing 'distance to c. 1770 Ma Carrington Suite granites and c. 1640 Ma Mount Webb Granite' was used as a predictor map for uranium sources (Appendix, Map 1). A map showing the distance to the Lander Rock Formation, the locations of which were extracted from the interpreted bedrock geological map (GSWA, 2009), was also used as a source predictor map (Appendix, Map 25). This unit occurs in the hanging wall north of the CAS and is a predominantly siliciclastic package that locally contains some iron-formation, and possibly minor igneous rocks. However, in the associated geochemical dataset, the uranium response is mostly below detection.

The bedrock locations for both the Bitter Springs Formation and Heavitree Quartzite were extracted from the interpreted bedrock geological map (GSWA, 2009b), and a map showing distances to these units was generated (Appendix, Map 26). These units include undeformed Meso- to Neoproterozoic sandstones, which are of favourable age and unconformably overlie the Paleoproterozoic basement rocks (Fig. 22).

Predictor maps for pathways

Key to the transportation of uranium during the mineralizing process is the redox state of the local fluids. Uranium is soluble in its oxidised state and insoluble in its reduced form (Dahlkamp, 1978; Mashkovtsev et al., 1995). The uranium-rich oxidised basinal fluids are directed along the unconformity surface and deep-penetrating faults (plumbing systems for the fluids) into the reduced environments at, or close to, the unconformity. Deposits are often associated with changes in trend of basement faults or their intersection with crosscutting faults. The circulation of oxidised, uranium-enriched, basinal brines could commence along the pre-unconformity surfaces and fault structures, even before the deposition of the overlying clastic sediments, and continue after their deposition (Derome et al., 2003). Predictor maps were created by mapping distances (up to 5 km either side) to the surface traces of the faults and unconformity surfaces in the study area:

1. distance to main D_1 and D_2 structures (Appendix, Maps 4 and 5)

2. distance to unconformities (and intrusive contacts, Appendix, Map 27). Intrusive contacts between the basement and the granites, unconformities between the granites and the overlying sedimentary rocks (Bitter Springs Formation and Heavitree Quartzite), and potential unconformities between the Murraba Basin rocks and the Heavitree Quartzite (Fig. 3; Zhao et al., 1992; Maidment et al., 2007), were extracted from the interpreted bedrock geological map (GSWA, 2009b), and used for the unconformity predictor map (Appendix, Map 28).

Predictor maps for physical traps

Dilatational sites can be created by fault–fault intersections or unconformity–fault intersections. The reactivation of long-lived, deep-penetrating faults can also induce dilational sites. The following predictor maps for physical traps were derived from the available spatial proxies.

The intersections of D_1 and D_2 faults could provide the permeable channels for focused fluid in-flow. Therefore a predictor map that plots the distance to intersections of D_1 faults with D_2 faults (Appendix, Map 15) was generated.

The fault intersection density map (Appendix, Map 16) indicates structural complexity that may contribute to increased space for focusing uranium-bearing fluids. The map was derived by estimating and mapping the density of all types of faults per square kilometre.

The predictor maps 'distance to D_1 fault–unconformity intersection' and 'distance to D_2 fault-unconformity

Table 5. Weights-of-evidence (WofE) table for gold prospectivity analysis

No.	*Predictor map*	*Pre-processing*	*Id*	*Class*	*Area (sq km)*	*No of training points*	*W^+*	*S_W^+*	*W^-*	*S_W^-*	*Contrast*	*Std. Contrast*
(A) PATHWAY												
1	Structure D_1	This continuous-scale distance map was converted into a binary predictor map by using 1.75 km as the threshold buffer distance within which the spatial association between D_1 faults and known gold deposits is maximized.	0	>1.75 km from D_1 fault	2811.98	4	-0.6733	0.5004	0.296	0.2587	-0.9693	0.5633
			1	<1.75 km from D_1 fault	4009.62	15	0.296	0.2587	-0.6733	0.5004	0.9693	0.5633
2	Structure D_2	This continuous-scale distance map was converted into a binary predictor map by using 1.5 km as the threshold buffer distance within which the spatial association between D_2 faults and known gold deposits is maximized.	0	>1.5 km from D_2 fault	1996.84	2	-1.0246	0.7075	0.2358	0.243	-1.2604	0.748
			1	<1.5 km from D_2 fault	4824.76	17	0.2358	0.243	-1.0246	0.7075	1.2604	0.748
3	Main structure D_1	This continuous-scale distance map was converted into a binary predictor map by using 2.5 km as the threshold buffer distance within which the spatial association between D_1 faults and known gold deposits is maximized.	0	>2.5 km from Main D_1 fault	3510.38	6	-0.4894	0.4086	0.3444	0.2779	-0.8338	0.4941
			1	<2.5 km from main D_1 fault	3311.22	13	0.3444	0.2779	-0.4894	0.4086	0.8338	0.4941
4	Main structure D_2	This continuous-scale distance map was converted into a binary predictor map by using 1 km as the threshold buffer distance within which the spatial association between D_2 faults and known gold deposits is maximized.	0	>1 km from main D_2 fault	5862.15	14	-0.1542	0.2676	0.6289	0.4484	-0.7831	0.5222
			1	<1 km from D_2 fault	959.45	5	0.6289	0.4484	-0.1542	0.2676	0.7831	0.5222
5	High gold anomalies over D_1 faults	Each D_1 structure was assigned the highest gold value anywhere along the structure. A threshold Au Z score of 1.0 was used to reclassify the D_1 main faults into high Au anomaly and low Au anomaly faults. Subsequently, a map showing distances to the high Au anomaly D_1 faults was prepared. This continuous-scale distance map was converted into a binary predictor map by using 5 km as the threshold buffer distance within which the spatial association between the high gold anomaly D_1 faults and known gold anomalies is maximized.	0	>5 km from D_1 fault with high gold anomaly	4218.23	5	-0.8559	0.4475	0.6605	0.268	-1.5164	0.5216

Table 5. continued

No.	*Predictor map*	*Pre-processing*	*Id*	*Class*	*Area (sq km)*	*No of training points*	*W^+*	*S_W^+*	*W^-*	*S_W^-*	*Contrast*	*Std. Contrast*
			1	<5 km from D_1 fault with high gold anomaly	2603.37	14	0.6605	0.268	-0.8559	0.4475	1.5164	0.5216
6	High gold anomalies over D_2 faults	See above. In this case, a threshold distance of 4 km was used for preparing the binary map.	0	>4 km from D_1 fault with high gold anomaly	6590.04	17	-0.0769	0.2428	1.1376	0.7102	-1.2145	0.7506
			1	<4 km from D_2 fault with high gold anomaly	231.56	2	1.1376	0.7102	-0.0769	0.2428	1.2145	0.7506
(B) PHYSICAL TRAP												
7	Fault density	Contrast values were determined at cumulatively decreasing fault density values. Optimal spatial association was obtained at a density of 0.71 km per square km. This value was used to reclassify the continuous-scale density map into a binary map.	0	Fault density <0.70 km/sq km	5744.4	13	-0.2081	0.2777	0.6958	0.4094	-0.904	0.4947
			1	Fault density >0.70 km/sq km	1077.2	6	0.6958	0.4094	-0.2081	0.2777	0.904	0.4947
8	Geological contact density	The map was reclassified into 2 classes using a threshold contact density of 1.16 km/sq km. The threshold values were estimated using the method described above.	0	Geological contact density <1.16 km/ sq km								
			1	Geological contact density >1.16 km/ sq km								
9	Geological contact density weighted by competency contrast	The map was reclassified into 2 classes using a comptency contrast-weighted contact density of 1.80 km/ sq km. The threshold values were estimated using the method described above.	0	Comptency contrast-weighted geological contact density <1.80 km/ sq km	6715.24	17	-0.0975	0.2428	2.0436	0.7147	-2.1411	0.7548
			1	Comptency contrast-weighted geological contact density >1.80	94.61	2	2.0436	0.7147	-0.0975	0.2428	2.1411	0.7548

Table 5. continued

No.	*Predictor map*	*Pre-processing*	*Id*	*Class*	*Area (sq km)*	*No of training points*	*W^+*	*S_W^+*	*W^-*	*S_W^-*	*Contrast*	*Std. Contrast*
10	Proximity to fault intersection	The continuous-scale distance map was converted into a binary predictor map by using 1.5 km as the threshold buffer distance within which the spatial association between the intersections and known gold deposits is maximized.	0	>1.5 km from intersections	6269.92	15	-0.1525	0.2585	0.9612	0.5018	-1.1137	0.5645
			1	<1.5 km from intersections	551.68	4	0.9612	0.5018	-0.1525	0.2585	1.1137	0.5645
(C) CHEMICAL TRAP												
11	Fe content — proxy for chemical reactivity	Contrast values were determined at cumulatively decreasing Fe Z score values. Optimal spatial association was obtained at Z score value of 1.09. This value was used to reclassify the continuous-scale density map into a binary map.	0	Fe Z score <1.09	6666	16	-0.1491	0.2503	1.9481	0.5830	-2.0972	-3.3056
			1	Fe Z score >1.10	156	3	1.9481	0.5830	-0.1491	0.2503	2.0972	3.3056
12	Chemical reactivity contrast density	The map was reclassified into 2 classes using a reactivity contrast-weighted contact density of 1.55 km/ sq km. See above (Sr No.7) for the method used in estimating the threshold value.	0	Reactivity contrast-weighted geological contact density <1.55km/ sq km	6690.47	17	-0.0938	0.2428	1.8066	0.7131	-1.9004	0.7533
			1	Reactivity contrast-weighted geological contact density >1.55km/ sq km	119.38	2	1.8066	0.7131	-0.0938	0.2428	1.9004	0.7533
13	As anomaly	As Z score value of 0.56 was used to reclassify the continuous-scale density map into a binary map.	0	As Z score < 0.56	6528.78	16	-0.13	0.2503	1.3496	0.5805	-1.4797	0.6321
			1	As Z score >0.56	281.07	3	1.3496	0.5805	-0.13	0.2503	1.4797	0.6321
14	Sb anomaly	Sb Z score value of 1.33 was used to reclassify the continuous-scale density map into a binary map.	0	Sb Z score <1.33	6714.11	17	-0.0956	0.2428	1.9152	0.7138	-2.0107	0.754
			1	Sb Z score >1.33	107.49	2	1.9152	0.7138	-0.0956	0.2428	2.0107	0.754

intersection' comprises distances to the intersection points of the D_1 and D_2 faults with the unconformities (Appendix, Maps 28 and 29).

The D_1 and D_2 fault–unconformity intersection density maps were derived by estimating and mapping the density of all intersections between D_1 faults and D_2 faults and unconformities per square kilometre (Appendix, Maps 30 and 31).

The 'distance to unconformities' map (Appendix, Map 27) was also used a predictor map for physical traps.

Predictor maps for chemical traps

Fluid mixing — that is, the mixing of oxidized uranium-bearing basinal brines and reduced basement-derived fluids — is widely considered to be a key chemical process for precipitation of uranium in unconformity-related systems. Another important chemical process for uranium precipitation in unconformity-related systems is the reaction between oxidized uranium-bearing brines and reduced wall-rocks along fault planes or unconformity surfaces. The presence of organic matter, sulphides (e.g. pyrite), or reduced iron species (e.g. magnetite) in basal formations of the overlying basin-fill sediments, or in the underlying basement, are good indicators of a reducing environment, and therefore constitute useful spatial proxies for chemical traps in unconformity-related uranium systems (McKay and Miezitis, 2001; Derome et al., 2003).

Uranium content is a direct indicator of uranium precipitation and concentration. The predictor map of uranium content (Appendix, Map 32) was derived by interpolation of uranium values extracted from the geochemical datasets (GSWA, 2009a).

The basal sequences of the Bitter Springs Formation contain organic material. The interpreted bedrock geological map (GSWA, 2009b) was queried to extract the locations of the Bitter Springs Formation and to generate the predictor map 'distance to Bitter Springs Formation' (Appendix, Map 33).

BIFs were interpreted from the aeromagnetic data (Figs 17 and 20), and their density per square kilometre was estimated and mapped to derive the predictor map showing BIF density. As magnetite may indicate reducing conditions, the Fe-rich rock (BIF) map could be a useful predictor map (Appendix, Map 17).

Fuzzy model

Assigning map weights, class weights, and confidence factors

The map weights, class weights, confidence factors, and the fuzzy membership values for each of the 16 predictor maps used in this study, and the rationale for assigning these values, are given in Table 6. The fuzzy membership values were mapped to create fuzzy predictor maps.

Combining fuzzy membership values

Map combination is an intuitive method where different primary and derived predictor maps are combined by a set of rules. A detailed inference diagram (Fig. 31) shows how the different layers are combined and finally integrated using fuzzy operators.

In the first stage of the unconformity-related uranium prospectivity analysis, the fuzzy predictor maps for source, pathway, chemical trap, and physical trap were combined using the *fuzzy OR* operator to create a single fuzzy predictor map for each critical component of the unconformity-related uranium mineral systems.

In the second stage, the fuzzy predictor maps for physical trap and chemical trap were combined using the *fuzzy AND* operator to derive a single predictor map for traps. The *fuzzy AND* operator was selected because both the physical trap sites and the conducive geochemical environment are necessary for precipitation of uranium from mineralizing fluids.

Finally, the three fuzzy predictor maps for source, pathway, and trap, that are essential to form a deposit, were combined using the *fuzzy PRODUCT* operator to create the output fuzzy prospectivity map (Fig. 32). The *fuzzy PRODUCT* was used here instead of AND operator because it returns the minimum value of the sets of cell location. In other words, the *fuzzy PRODUCT* selects locations that have at least a 0.5 or greater possibility of being suitable for all the criteria. The values are relative values.

Prospective areas, with *fuzzy PRODUCT* values between 0.116 and 0.172, (Fig. 32) are highlighted as potential targets for detailed exploration denoted π, €, β, Ω, α, and γ. These targets are mainly located at, or near, the contact between sandstone and underlying metamorphic rocks. The prospective targets are all associated with faulted basement rocks.

The most prospective areas are where the unconformity between the Bitter Springs Formation and the Aileron Province basement occur close to major D_1 structures (e.g. € and α in Fig. 32). Also prospective are the areas at the northern margin of the Murraba Basin where the uranium-rich Carrington Suite granites intrude the basement (e.g. γ, π, Ω). These targets are associated with the locations of the main D_1 structures (Ω), or the main D_2 structures (γ), or both (π). All prospective areas have a close relationship with the main faults and unconformities.

Surficial uranium mineral systems

Surficial uranium deposits (Fig. 33) are classified as uranium concentrations in unconsolidated, near-surface sediments or soils with secondary cementing minerals (e.g. calcite, dolomite). Surficial uranium deposits have formed from the Tertiary to the present-day, by evaporation processes in fluviatile to playa systems in arid to semi-arid climatic conditions (e.g. Langer Heinrich in Namibia, Yeelirrie in Western Australia). Surficial ores are formed

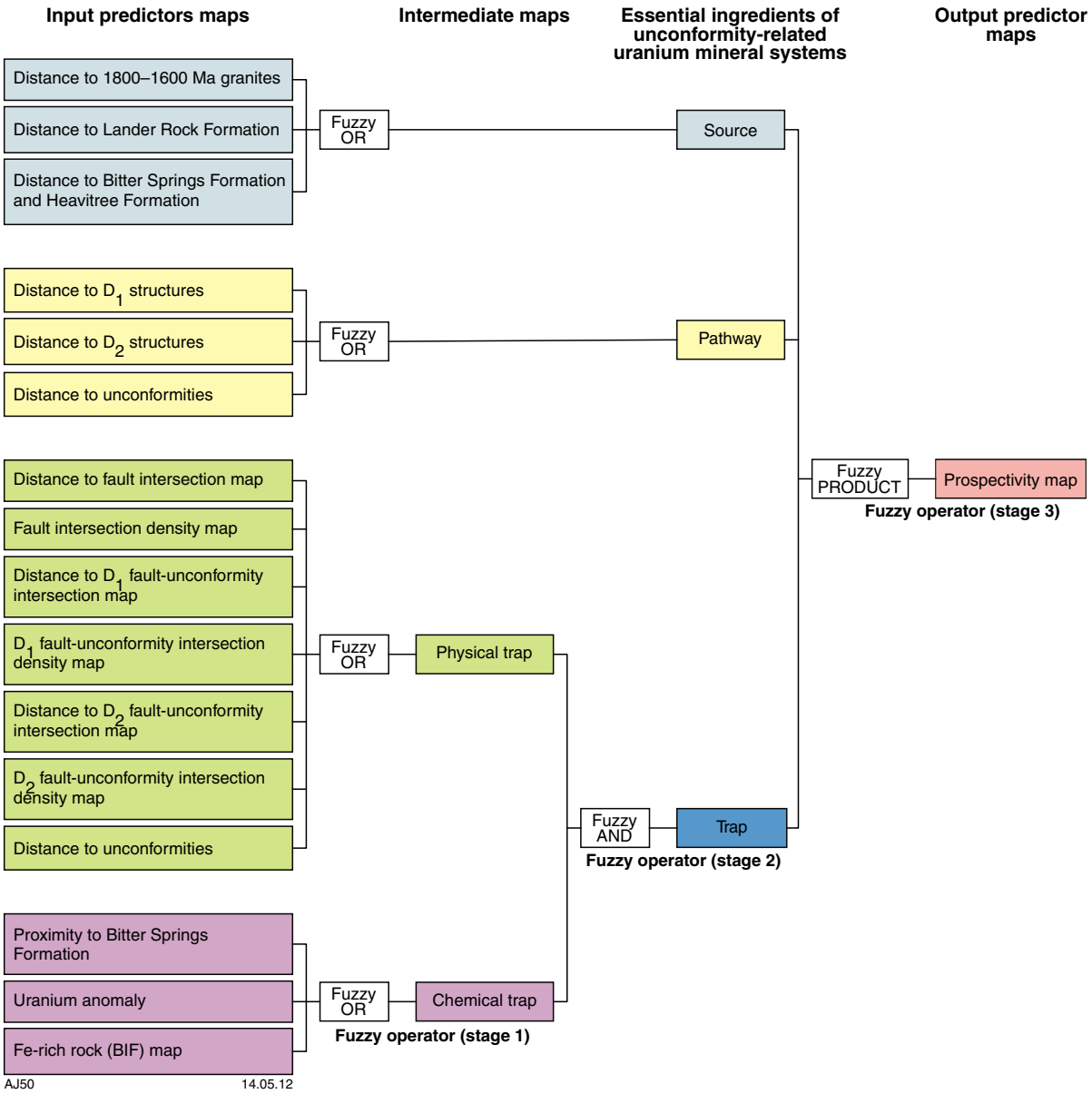

Figure 31. Multi-stage fuzzy inference network used for combining fuzzy unconformity-related uranium predictor maps

from accumulations of carnotite ($K_2(UO_2)_2(V_2O_8{\cdot}3H_2O)$), within calcretized fluvial drainage channels (Fig. 33; Carlisle, 1983). Uranium and potassium are derived by surficial or subsurface weathering, leaching, and transport of uranium and potassium from uranium-rich granitic rocks by both surficial and underground water. The vanadium is derived from mafic–ultramafic rocks in the trap regions (Fig. 33).

The west Arunta Orogen contains all the ingredients required to form surficial uranium deposits, including the presence of extensive (Cenozoic) paleodrainage, calcrete accumulations, playa sediments within and adjacent to drainage lines, appropriate sources of uranium (presence of uranium-enriched granite) and of vanadium (presence of mafic intrusions), as well as arid climatic conditions.

The details of the predictor maps, along with the geological rationale are given in the following paragraphs. The study was conducted over the entire west Arunta Orogen.

Predictor maps

Predictor maps for source

Uranium-rich granitic rocks of any age can be a uranium source. Because of this, occurrences of all granitic rocks, buffered to 25 km, were used to generate a predictor map (Appendix, Map 34).

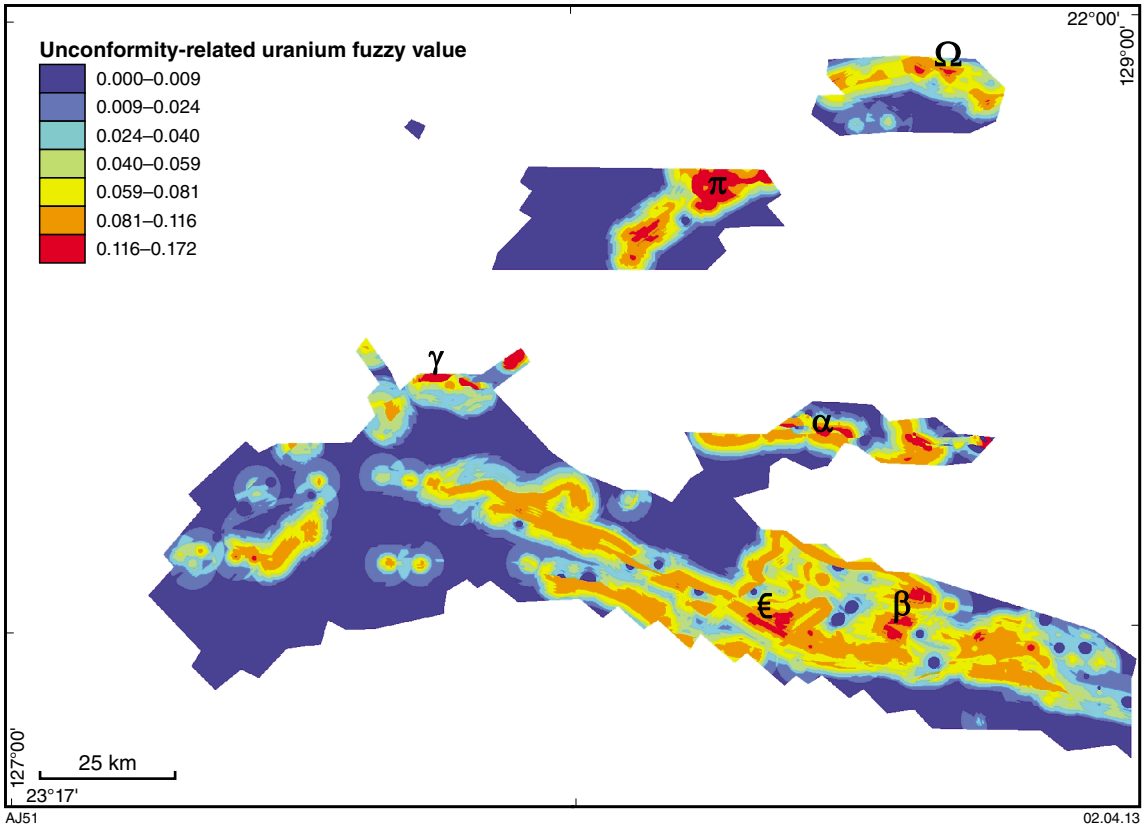

Figure 32. Fuzzy prospectivity model for the unconformity-related uranium mineral system

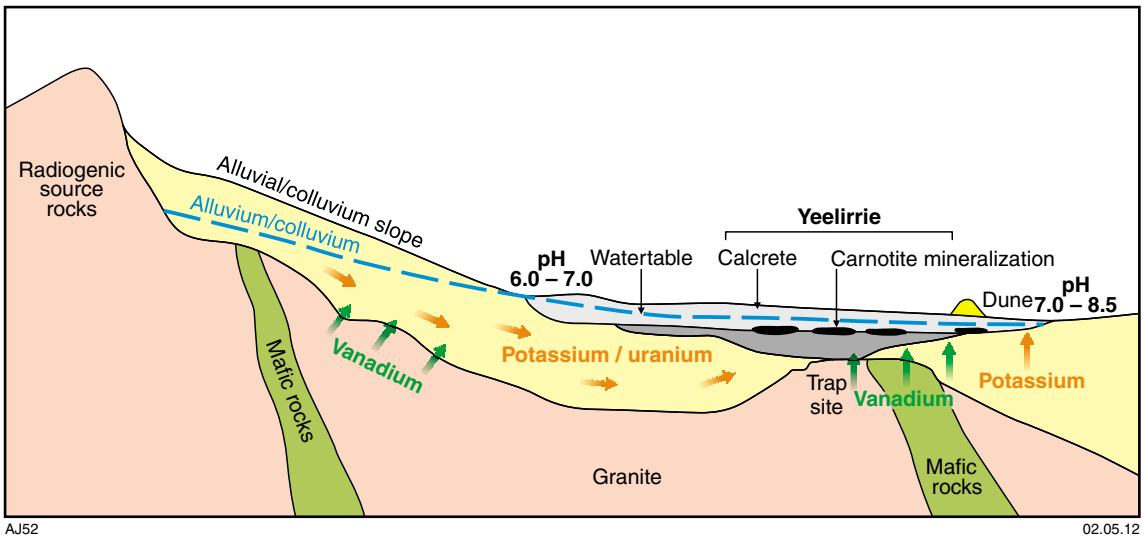

Figure 33. Model depicting the setting and processes involved in the formation of carnotite deposits in calcretized channels (after Carlisle, 1983)

Table 6. Fuzzy table for unconformity-related uranium prospectivity analysis

Critical processes	*Input predictors map*	*Appendix map number*	*Fuzzy membership value map weight*	*Confidence factor*	*Rationale for expert knowledge based weight (fuzzy membership values)*	*Rationale for confidence factor*
Predictor map for source						
	Distance to c. 1770 Ma and c. 1640 Ma granites	1	7	7	Granites typically form good source rocks; however, the uranium content of these granites as shown by GSWA geochem data is quite low. Metamorphosed basement with graphitic rocks absent.	Very few exposures, mainly interpreted
	Distance to Lander Rock Formation	25	6.5	7	Forms basement to the north of Central Australian Suture, predominantly siliciclatic package; contains iron formation and igneous rocks. However, not much uranium in the package.	Very few exposures, mainly interpreted
	Distance to Bitter Springs Formation and Heavitree Formation	26	6	7	Basin fill package; contains undeformed sandstones of Meso- to Neoproterozoic age; uranium enrichment doubtful as per the geochem data. The packages are of right age and unconformably overlie the Paleoproterozoic basement rocks.	Very few exposures, mainly interpreted
Predictor maps for active pathways						
	Distance to main D_1 faults	4	8	7.5	Deep structures penetrate the basement rocks	Interpreted from geophysics with relatively high level of confidence
	Distance to main D_2 faults	5	7	7.5	Age, depth persistence, and relationship with potential uranium mineralization uncertain	Interpreted from geophysics with relatively high level of confidence
	Distance to unconformities	27	7.5	7	Unconformities are possible fluid pathways	
Predictor maps for physical traps						
	Distance to fault intersections	15	6.5	7.5	The relation of D_2 fault with uranium mineralization conceptually uncertain, hence low map weight	Interpreted from geophysics with relatively high level of confidence
	Fault intersection density	16	6.5	7.5	The relation of D_2 fault with uranium mineralization conceptually uncertain, hence low map weight	Interpreted from geophysics with relatively high level of confidence
	Distance to D_1 fault–unconformity intersections	28	8	7	Conceptually good locales for uranium mineralization	Interpreted from geophysics with relatively high level of confidence
	D_1 fault–unconformity intersection density	30	8	7	Conceptually good locales for uranium mineralization	Interpreted from geophysics with relatively high level of confidence
	Distance to D_2 fault–unconformity intersections	29	7	7	Conceptually good locales for uranium mineralization	Interpreted from geophysics with relatively high level of confidence
	D_2 fault–unconformity intersection density	31	7	7	Conceptually good locales for uranium mineralization	Interpreted from geophysics with relatively high level of confidence
	Distance to unconformities	27	9	7	Conceptually the most critical factor for unconformity-related uranium	Interpreted based on literature and 2D geophysical modelling

Table 6. continued

Critical processes	*Input predictors map*	*Appendix map number*	*Fuzzy membership value map weight*	*Confidence factor*	*Rationale for expert knowledge based weight (fuzzy membership values)*	*Rationale for confidence factor*
Predictor maps for chemical traps						
	Uranium anomaly	32	8	7.5	High uranium anomaly is indicative of uranium mineralization	Interpolated from closely spaced geochemical samples, fairly high confidence
	Distance to Bitter Springs Formation	33	7	5	Contains organic material in the basal sequences (possibility of reduced interlayered unit)	Presence of reducing environment inferred from literature
	Fe-rich rocks (banded iron-formation)	17	8	7.5	Magnetite may indicate reducing conditions	Interpolated from closely spaced geochemical samples, fairly high confidence

Predictor maps for pathways

Uranium- and potassium-enriched, oxidised groundwater is the main means of uranium transportation. This enriched groundwater is brought up to the surface by evaporation processes in fluviatile (channel valleys) to playa systems, in arid to semi-arid climatic conditions. In situations where the ground water is close to the surface, evaporation might cause the water to move upwards due to capillary action. A predictor map for paleochannels was produced because they provide pathways for such fluid flow.

The distance to third or higher order present-day drainage systems derived from Shuttle Radar Topography Mission (SRTM) data were used as proxy for paleochannels (Appendix, Map 35). This predictor map was created by mapping these to distances 5 km on each side.

Predictor maps for physical traps

These deposits correspond to epigenetic, near-surface uranium concentrations. Valley calcrete and playa sediments provide a favourable environment for carnotite deposition.

The predictor map of valley calcrete (Appendix, Map 36) was derived from the regolith map and regolith data in GSWA (2009b), surface geological data for 'calcrete' provided by GSWA, and remote sensing data (LANDSAT Thematic Mapper (TM) data). Calcrete outcrops were mapped by querying the regolith datasets and by interpreting LANDSAT TM images. On the LANDSAT TM images, calcrete bodies were easily identified by their characteristic high reflectance on various false-colour composite images. The maps of calcrete were rasterized using a 1 km^2 grid cell size to create input predictor maps showing calcrete occurrence.

The playa sediment map (Appendix, Map 37) was derived from remote sensing data and the regolith map (GSWA, 2009), with a 100 m buffer. Playa sediment occurrences were mapped by querying the regolith dataset in GSWA (2009b), and the surface geological data for 'playa sediment'. This was rasterized using a 1 km^2 grid cell size to create input predictor maps showing playa sediment occurrences.

Predictor maps for chemical traps

Redox processes control uranium precipitation and fixation by vanadium. Only four samples analysed in the regolith geochemical dataset show sufficient vanadium content to be a viable source for contributing to accumulations of carnotite. This limited number of samples does not allow a robust interpolation for generating a reliable predictor map; therefore, no vanadium source map was made.

However, vanadium can be sourced from mafic rocks. Distance to the Bitter Springs Formation (Appendix, Map 33) and to dolerite dykes (Appendix, Map 39) were used as chemical scrubber predictor maps.

The uranium channel in the radiometric data is the best available predictor for surficial uranium content. This

was used to make the uranium content map for surface alluvium and sand cover (Appendix, Map 38).

Fuzzy model

Assigning map weights, class weights, and confidence factors

The predictor maps were assigned fuzzy membership values (based on class weights, map weights, and confidence factors, as described above). The fuzzy membership values for a predictor map indicate the possibility of the occurrence of the specific targeting criterion defined by that predictor map. The map weights, class weights, confidence factors, and the fuzzy membership values for each of the five predictor maps used in this study, including the rationale for assigning these values, are shown in Table 7. The fuzzy membership values were mapped to create fuzzy predictor maps.

Combining fuzzy membership values

A two-stage inference network was designed to combine the fuzzy predictor maps (Fig. 34). In the first stage, the valley calcrete and playa sediment input predictor maps were combined to prepare an integrated map of the physical trap. Since there is only one predictor map for source — namely, distance to granites — this map was used as the predictor map for source. Likewise, the only predictor maps for pathways and chemical traps are the paleochannels and uranium anomalies input predictor maps, respectively. Finally, in the second stage, the three fuzzy predictor maps for source, pathway, and trap were combined using the *fuzzy GAMMA* operator to derive the output fuzzy prospectivity map (Fig. 35). The *fuzzy GAMMA* was used here instead of the *PRODUCT* and *AND* operators because it moderates the tendency of the algebraic sum operator to increase and the tendency of the algebraic product operator to decrease. In other words, it allows enhancement of subtler differences between prospectivity of different unit areas.

The area is characterized by extensive, eolian sand dune cover, so the results derived from the uranium channel of the radiometric data should be treated with caution. Nevertheless, prospective areas are highlighted as potential targets for detailed exploration. The most prospective targets are located at the proximity of paleochannels and sediment playas: areas π, €, β, and γ (Fig. 35). Their *fuzzy GAMMA* values vary between 0.603 and 0.645.

An interesting target is the one running along the northern edge of Lake Mackay (γ), which corresponds to the northern edge of the playa sediment area and paleochannels. These paleochannels are delimited by the northernmost playa sediment surface.

The southern extremity of Lake Mackay (end of π content) has previously been recognized as a prospective area (Toro Energy Ltd, 2009). There is an extensive, high-amplitude uranium channel radiometric anomaly located over the southern part of Lake Mackay (Fig. 35). The radiometric 'plume' is likely to be due to radionucleiide daughters that have been discharged into the lake via modern groundwater flow. The ultimate source of the radionucleiides is speculated to be a concealed uranium mineral system to the south of the lake (Toro Energy Ltd, 2009).

Sediment exhalative mineral systems

Sedimentary Exhalative (SedEx) deposits are sulphide-dominated, Pb–Zn–Ag ore bodies, with sphalerite and galena as the principal ore minerals (Lydon, 1983; Large, 1986).

These deposits form in sedimentary basins through submarine venting of hydrothermal fluids on the seafloor (i.e. with the discharge of metal-bearing brines into reduced sedimentary basins; Goodfellow et al., 1993; Goodfellow and Lydon, 2007). SedEx-type mineral deposits are synsedimentary and are genetically linked to continental rift-margin faults (Fig. 36; Leach et al., 2005; Huston et al., 2006; Goodfellow and Lydon, 2007). Mafic intrusions linked to this continental rift setting act as source of energy for brine circulation (Fig. 36).

The west Arunta Orogen contains all the ingredients required to form SedEx-type deposits: 1) Paleo- to Mesoproterozoic, synsedimentary host rocks (mainly shales and clastic sedimentary rocks) as a main source; 2) structures that would permit fluid migration; 3) sites where basinal brines could interact with reduced strata (e.g. the Bitter Springs Formation); 4) moderate zinc–lead content that could be indicative of hydrothermal alteration; and 5) the presence of evaporites (a source of ligands).

Due to the uneven data coverage (Fig. 9), the SedEx prospectivity analysis was undertaken in the same areas as the gold analysis. This was necessary because many of the SedEx targeting elements (such as the chemical traps) are best represented by geochemical proxies. Otherwise, the analysis would have been confined to pathways, given that source (clastic) rocks have a wide distribution in the area and therefore, would have little effect on the relative prospectivity.

Predictor maps

Predictor maps for ligands

During diagenesis, the sedimentary pile dehydrates and releases highly saline brines (denoted 'a' in Fig. 36). Evaporites form as a result of evaporation of these saline brines. Acting as a source of ligands, evaporites enhance the salinity of hydrothermal fluids and their metal-leaching capacity. However, many big SedEx systems are hosted by basins with no evaporites (Leach et al., 2005).

Although evaporite bodies are interpreted in the west Arunta Orogen using geophysical data, none of these fall within the analysed area. The analysed area comprises rocks from the Paleoproterozoic basement and from the Neoproterozoic to Mesozoic cover.

Table 7. Fuzzy table for surficial uranium prospectivity analysis

Critical processes	*Input predictors map*	*Appendix map number*	*Fuzzy membership value map weight*	*Confidence factor*	*Rationale for expert knowledge based weight (fuzzy membership values)*	*Rationale for confidence factor*
Predictor map for source						
	Distance to all granites	34	8	8	Granites typically form good source rocks; however, the uranium content of these granites as shown by GSWA geochemichal data is quite low	Very few exposures, mainly interpreted
Predictor maps for active pathways						
	3rd or higher order present-day drainage derived from SRTM used as proxy for paleochannels	35	9	6	Best spatial proxy for surficial uranium pathways	Interpreted from SRTM with relatively low level of confidence
Predictor maps for physical traps						
	Distance to Bitter Springs Formation	33	8	8	Organic material in the basal sequences	Presence of reducing environment inferred from literature
	Dolerite dyke density	39	8	8	Mafic rocks provide vanadium to precipitate carnotite	Interpreted from geology map (1:500 000 scale; GSWA)
	Uranium anomaly in surface alluvium or sand cover. Uranium channel of radiometric data is the best predictor.	38	8	9	High uranium anomaly is indicative of uranium mineralisation	Interpolated from closely spaced geochem samples, fairly high confidence

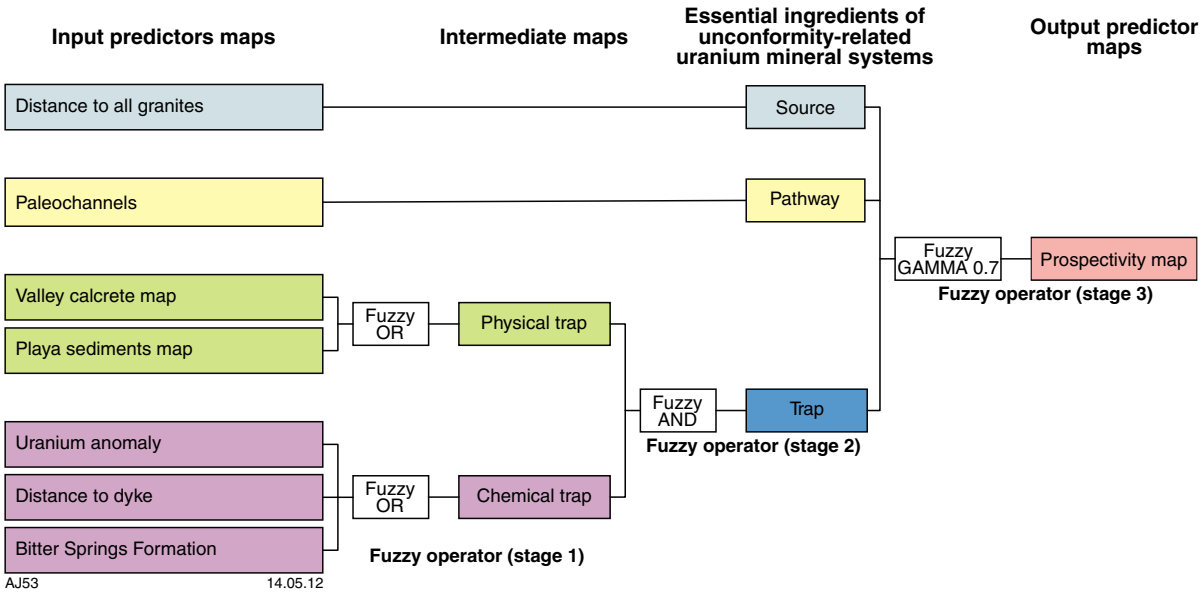

Figure 34. Multi-stage fuzzy inference network used for combining fuzzy surficial uranium predictor maps

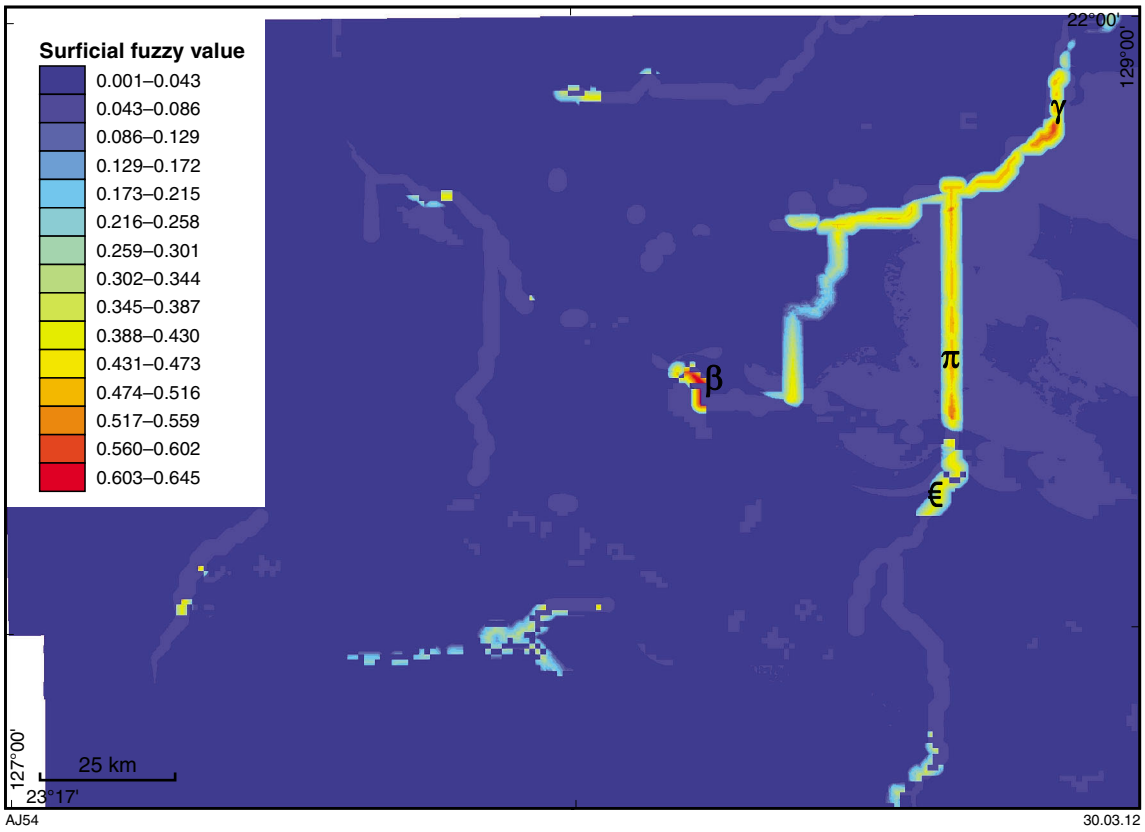

Figure 35. Fuzzy prospectivity model for the surficial uranium mineral system

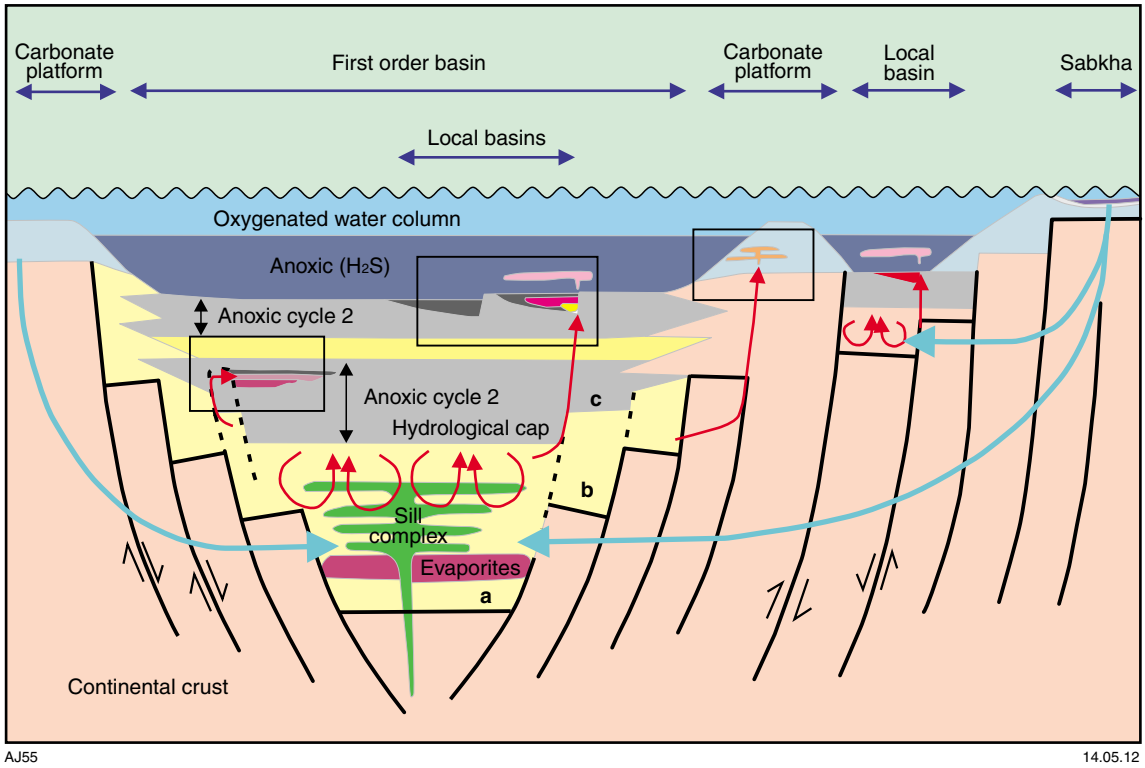

Figure 36. Generalized conceptual model of a typical SedEx minerals system (from Goodfellow and Lydon, 2007). SedEx-type deposits form from oxidised fluids occurring in geopressured, hydrothermal reservoirs (e.g. site a) containing thick successions of syn-rift clastic sediments (e.g. site b), typically with intercalations of evaporites and sealed by impervious, fine-grained marine sediments, such as shales or carbonates (e.g. site c)

Predictor maps for source

The energy for driving brine circulation (Fig. 36) may be induced from high geothermal gradients, possibly related to mantle heat within a rift setting environment, deep brine circulation in geo-pressured basinal sediments, or possible magmatic activity at depth (linked to mafic and felsic magmatic intrusions; Goodfellow et al., 1993).

Dykes and granites are, theoretically, a possible energy source. The mafic dykes interpreted from the aeromagnetic and gravity data either pre-dated sedimentation associated with the Amadeus Basin, or are synchronous with the early phases of its formation (Fig. 20). To help drive a SedEx system, the intrusions must be coeval with the deposition of the sedimentary basin. As the granites clearly pre-date the sedimentation, they have not been taken into account. However, mafic dykes are a possible energy source, and a dyke predictor map was generated by mapping a 5 km wide zone around them (Appendix, Map 39).

Along with sub-seafloor venting of hydrothermal fluids, SedEx metal precipitation requires a supply of reduced sulphur, but hydrothermal fluids are depleted in reduced sulphur. The generally accepted source of required reduced sulphur is bacteriogenic H_2S (Des Marais et al., 1992). H_2S is generated in anoxic water columns and its availability controls metal precipitation.

The Archean is generally regarded as a time of low oxygen and sulfate presence in the ocean. Under these conditions, high concentrations of dissolved iron led to the extensive deposition of banded iron-formations. During the Proterozoic and Phanerozoic, the amount of dissolved iron decreased and a trend towards sulfur-dominated oceans developed (Canfield, 1998; Canfield and Raiswell, 1999; Anbar and Knoll, 2002). This change in ocean chemistry resulted in a build-up of sulfate, a source for bacterial sulfate reduction, producing anoxic (H_2S-rich) water columns that are conducive for precipitation of metals from SedEx-type hydrothermal fluid sources. Consequently, at the continental or basin-wide scale, post-1900 Ma sediment deposition is one criterion indicative of a high potential for SedEx deposits (Goodfellow and Lydon, 2007).

Clastic sedimentary rocks in the west Arunta Orogen, especially shales, were used to make the predictor map for source, based on spatial proxies (Appendix, Map 40, <1900 Ma). Clastic rock units that are younger than 1900 Ma were extracted from the interpreted bedrock geology map (GSWA, 2009b).

Predictor maps for pathways

Key Pb–Zn transport processes in SedEx systems are related to long-lived structures (Goodfellow and Lydon, 2007). Brine transport follows basin-bounding

faults. During fault reactivation, the brines can breach the impervious sediment cap (e.g. shales) over the rift sediments. Brines are then released into the overlying oceanic water. The SedEx deposits are often located in the vicinity of extensional faults (Leach et al., 2005; Huston et al., 2006). It is worth noting that the present-day outcrop pattern in the west Arunta Orogen is due to late Fitzroy Movement stage associated with reactivated faults (see section 'Interpreted linear features').

The key pathways for brine movements are basin-bounding faults and, above all, long-lived structures. Therefore, the predictor maps 'distance to main crustal-scale D_1 faults and D_2 faults' (Appendix, Maps 4 and 5) were created.

Predictor maps for physical traps

It is not possible to generate proxies for physical trap sites for SedEx deposits, (namely, paleoseafloor and topographical depressions on the paleoseafloor) using the available data. For this reason, this predictor could not be used.

Predictor maps for chemical traps

The precipitation of Pb–Zn sulphides occurs when saline brines come into contact with H_2S in the reduced water column at or above the seafloor. H_2S most probably forms from bacteriogenic reduction of seawater sulphates (Des Marais et al., 1992). After sulphide formation, hydrothermal activity continues producing post-ore hydrothermal alteration in the sediments (Goodfellow and Lydon, 2007). Commonly, there are extensive alteration halos of elements such as Fe, Mn, Ba, As, Sb, and P around the deposit (1 to 6 km). These halos provide good targeting criteria on a camp-to-deposit scale.

The basal sequences of the Bitter Springs Formation contain organic material, favourable for creating a reduced environment. This criterion was used to make the predictor map, based on distance to the Bitter Springs Formation (Appendix, Map 33). The information was sourced from the interpreted bedrock geology map (GSWA, 2009).

Pb, Zn, As, Sb, and Fe anomalies make excellent indicators for the presence of SedEx deposits. The predictor maps for the content of these elements (Appendix, Maps 41, 42, 21, 22 and 23, respectively) were derived from the GSWA state geochemistry dataset (GSWA, 2009a), Geoscience Australia's OZCHEM dataset (GA, 2007; GSWA, 2009a), and west Arunta regolith geochemistry (GSWA, 2009b).

Mn, P, and Ba anomalies are good indicators for the presence of a SedEx deposit. The predictor maps for the content of these elements (Appendix, Maps 43, 44, and 45, respectively) were derived from the GSWA state geochemistry dataset (GSWA, 2009a), Geoscience Australia's OZCHEM dataset (GA, 2007; GSWA, 2009a), and west Arunta regolith geochemistry (GSWA, 2009b).

Fuzzy model

Assigning map weights, class weights, and confidence factors

The fuzzy membership values (map weights) and the confidence factors for each of the 13 predictor maps used in this study, including the rationale for assigning these values, are given in Table 8. The predictor maps showing distance to evaporites and distance to magmatism (granite, Table 8) were not used during the SedEx prospectivity analysis (see sections on predictor maps for ligands and source, above).

Combining fuzzy membership values

A two-stage inference network (Fig. 37) is used to combine the predictor maps. In the first stage, the respective predictor maps of the three key components of the SedEx mineral system — namely source, pathways and traps — were combined using the *fuzzy OR* because the presence of any one of the predictor maps is sufficient to infer the presence of the respective component. The outputs of this stage are three fuzzy maps for source, pathways, and traps. In the second stage, these three maps are combined using the *fuzzy PRODUCT* operator to derive the fuzzy prospectivity map for SedEx deposits in the west Arunta Orogen (Fig. 38).

The final GIS model map (Fig. 38) identifies seven clusters (marked α, β, π, €, ζ, θ, and Ω) located within the area of interest. Their *fuzzy PRODUCT* varies from 0.245 – 0.262.

The Paleoproterozoic is generally considered the most prospective period for SedEx deposit formation (Goodfellow and Lydon, 2007). The targets α, β, and € are associated with the Paleoproterozoic basement. Neoproterozoic to Mesozoic rocks in the study area are also taken into account as this period corresponds to a potential episode of SedEx deposition. The target Ω is located within the Amadeus Basin.

Some potential areas for SedEx deposits, such as θ and π, occur along D_1 faults; other targets, such as ζ, are located along D_2 faults. The three most prospective areas α, β, and Ω are situated close to fault intersections between D_1 and D_2 structures and close to dykes. The intersection of these two sets of faults may have produced localized zones of enhanced permeability and allowed highly concentrated SedEx-type fluids to flow.

Evaporites are typically a good proxy to take into account during the prospectivity analysis but in this study they occur outside of the area analysed. In fact, many SedEx deposits are not associated with evaporites in sediment successions (Leach et al., 2005). In others words, evaporites are not always the most prospective stratigraphic layer. In any case, the areas of evaporites interpreted from magnetic data in the west Arunta Orogen could not be included in the prospectivity analysis datasets as there are no geochemical data available for those areas.

Table 8. Fuzzy table for SedEx prospectivity analysis. The predictor maps for dykes and granites (magmatism), as well as distance to evaporite, are disregarded (see text for explanation)

Critical processes	*Input predictors map*	*Appendix map number*	*Fuzzy membership value map weight*	*Confidence factor*	*Rationale for expert knowledge based weight (fuzzy membership values)*	(Interpolation of values; values may be negative or unknown — if so, then not taken into account) *Rationale for confidence factor*
Predictor map for source						
	Distance to dykes	39	8	7.5	Good potential source	Interpreted from magnetic and gravity data
	Presence of clastic package, especially shales	40	9	8	Shales are made of thin grains that can precipitate large amounts of SedEx-type minerals	Interpreted from geology map (1:500 000 scale; GSWA)
Predictor maps for active pathways						
	Distance to main D_1 faults	4	8	9	Deep structures, penetrate the basement rocks, long-lived fault	Interpreted from geophysics with relatively high level of confidence
	Distance to main D_2 faults	5	8	9	Deep structures, penetrate the basement rocks, long-lived fault	Interpreted from geophysics with relatively high level of confidence
Predictor maps for physical traps						
	Proximity to Bitter Springs Formation (possibility of reduced interlayered unit)	33	8	7	Organic material in the basal sequences	Presence of reducing environment inferred from literature
	Lead anomaly	41	9	7.5	Direct indicator of lead	(Interpolation of values; values may be negative or unknown — if so, then not taken into account)
	Zinc anomaly	42	9	7.5	Direct indicator of zinc	(Interpolation of values; values may be negative or unknown — if so, then not taken into account)
	Arsenic anomaly	21	7	7.5	Indicator of SedEx-type mineral	(Interpolation of values; values may be negative or unknown — if so, then not taken into account)
	Antimony anomaly	22	7	7.5	Indicator of SedEx-type mineral	(Interpolation of values; values may be negative or unknown — if so, then not taken into account)
	Iron anomaly	23	7	7.5	Indicator of SedEx-type mineral	(Interpolation of values; values may be negative or unknown — if so, then not taken into account)
	Manganese anomaly	43	7	7.5	Indicator of SedEx-type mineral	(Interpolation of values; values may be negative or unknown — if so, then not taken into account)
	Phosphorus anomaly	44	7	7.5	Indicator of SedEx-type mineral	(Interpolation of values; values may be negative or unknown — if so, then not taken into account)
	Barium anomaly	45	7	75	Indicator of SedEx-type mineral	(Interpolation of values; values may be negative or unknown — if so, then not taken into account)

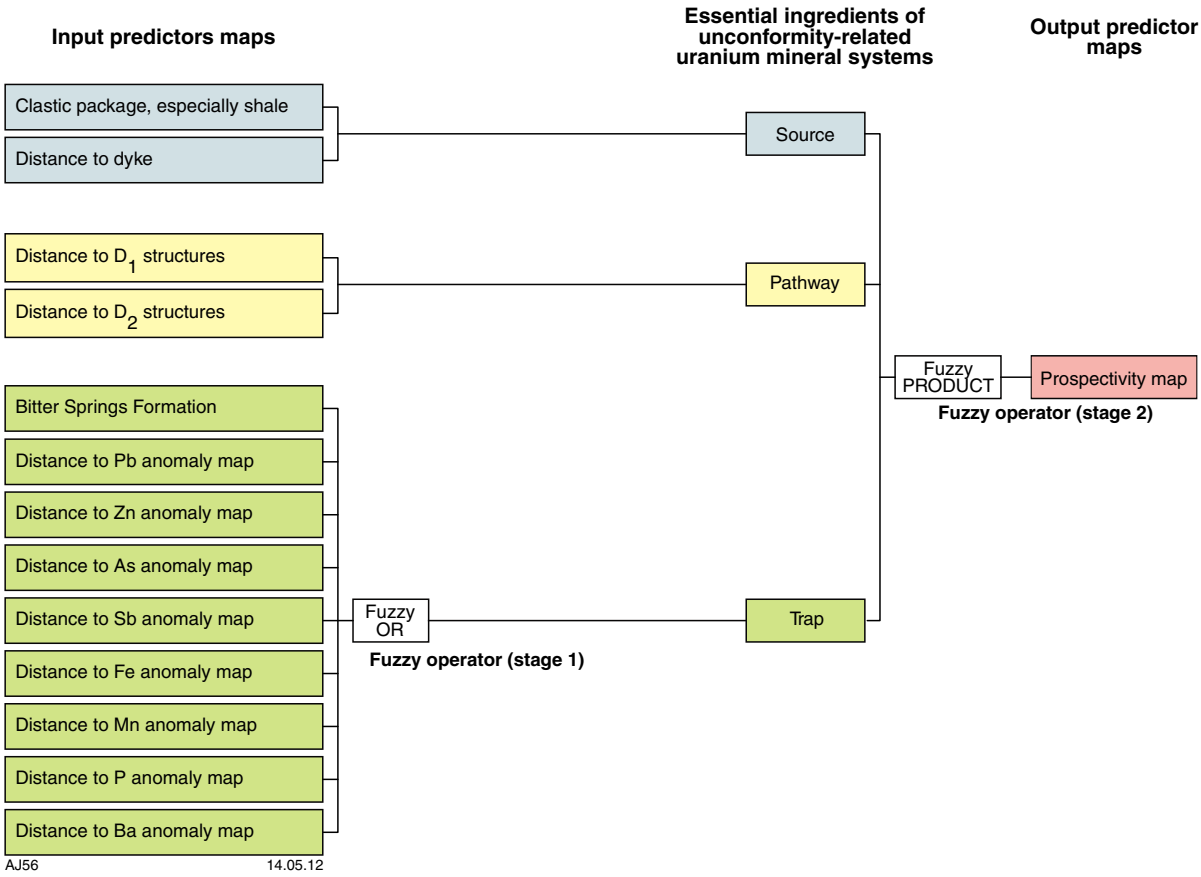

Figure 37. Multi-stage fuzzy inference network used for combining fuzzy SedEx predictor maps

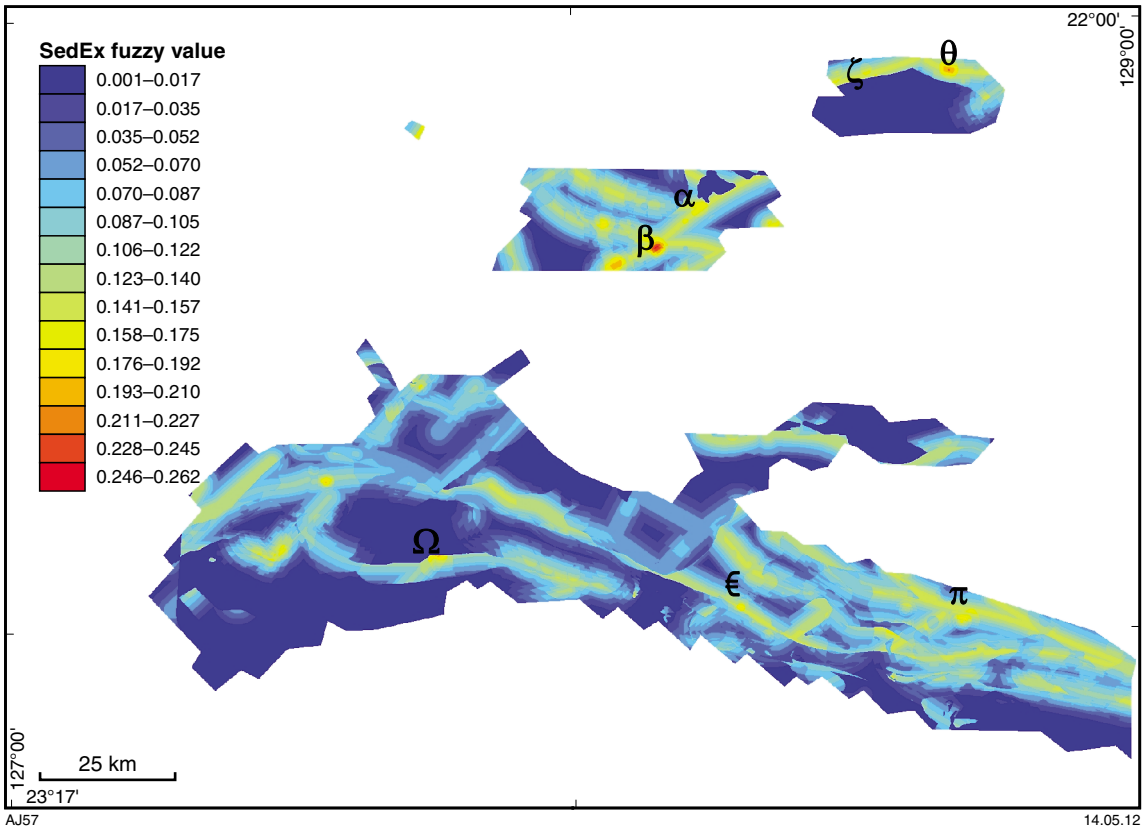

Figure 38. Fuzzy prospectivity model for the SedEx mineral system

Our goal was to explore the west Arunta Orogen for SedEx mineralization potential using our understanding of the mineral system. Despite the presence of good conditions for SedEx-type deposition (favourable age of host sediments and ideal rift-setting environment), the prospectivity analysis does not highlight any outstanding target areas that could be related to Zn–Pb mineralization. This is probably due to low Pb and Zn content value, and the absence of evaporite in the analysed areas.

Discussion and conclusions

The west Arunta Orogen is the western part of a Paleoproterozoic to Paleozoic terrane located in central Australia. Its Paleoproterozoic basement is unconformably overlain by sedimentary units of the Amadeus, Murraba, and Canning basins. Because of its geographical remoteness and poor outcrop, the geology and geological history of the west Arunta Orogen is poorly understood, and its exploration potential is largely undefined.

To assess the prospectivity of the west Arunta Orogen, an integrated interpretation of all available geoscientific data was undertaken, with emphasis placed on interpreting the major structures. The main datasets used were regional gravity and aeromagnetic data, geochemical data, limited geological information from outcrops, limited geochronological data, and the interpreted bedrock geology map (GSWA, 2009b), as well as various sources of information from the Northern Territory Geological Survey (e.g. seismic and MT data). Based on the analysis of these data, the west Arunta Orogen is interpreted as a basement-involved, thick-skinned thrust terrane with fault blocks comprising both west Arunta Orogen basement rocks and sedimentary rocks from the overlying basins. Multiple phases of deformation have taken place and the present-day outcrop pattern is probably controlled to a large extent by 'late stage' tectonic events, such as the Alice Springs Orogeny, recorded in the sedimentary basins.

The west Arunta Orogen is considered to be most prospective for orogenic-gold, unconformity-related and surficial uranium, and SedEx-style lead–zinc mineralization. The GIS-based prospectivity analysis, based on the Mineral Systems Approach (MSA), was undertaken for these styles of deposit. In each case, geological proxies for metal source, metal transport pathways, and metal depositional sites were sought based on the known characteristics of such deposits and their mechanisms of formation, and the interpreted geology of the west Arunta Orogen.

Using this MSA, a series of prospectivity maps were generated using GIS-based prospectivity analysis. These maps show the spatial distribution of prospectivity for cells with an area of 1 km^2. These products are not expected to show locations of the deposits themselves. Rather, they are intended to be tools to assist in exploration strategy development and decision making by illustrating the spatial variation in geological favourability for each type of deposit, within the constraints of the available data, assumptions about the local geology, and the way these deposits form.

Mineral prospectivity of the west Arunta Orogen

Orogenic gold deposits

Orogenic gold deposits are characteristically associated with deformed and metamorphosed mid-crustal blocks, often occurring adjacent to major crustal structures. For the west Arunta Orogen orogenic gold system, the key constituents are: 1) a source in the c. 1770 and c. 1640 Ma granites, which locally show Au enrichment; 2) conducive conditions for the transportation of gold as indicated by the presence of major, deep structures; 3) physical trapping environments indicated by lithological competency contrasts and fault density; 4) chemical trapping environments indicated by iron-rich lithological units and anomalous concentrations of metals associated with the occurrence of gold.

Both *fuzzy* and WofE gold prospectivity analyses (Figs. 28 and 29) indicate that the west Arunta Orogen has potential for the occurrence of orogenic gold systems, particularly in the vicinity of the Mount Webb Granite (especially in areas labelled φ, ϕ, and β). The WofE analysis, based on the spatial distribution of high gold content in geochemical samples (Fig. 24), highlights a west-northwest trend, parallel to D_1 structures and the CAS. This empirical observation suggests that D_1 structures, and particularly the CAS, may control the location of mineralization.

Unconformity-type uranium deposits

Unconformity-type uranium deposits occur in close proximity to major unconformities between quartz-rich sandstones comprising the basal portion of relatively undeformed sedimentary basins, and deformed metamorphic basement rocks. For the unconformity-related uranium system in the west Arunta Orogen, the MSA key constituents consist of: 1) a uranium source in the c.1770 and c. 1640 Ma granites in the basement — in particular, where granite intrudes the Lander Rock Formation; 2) a uranium-enriched source in the intrabasinal clastic sedimentary rocks of the Canning Basin that acts as a reservoir of oxidised brines; 3) unconformities and structures that control the flow of mineralizing fluids, with fault–fault and fault–unconformity intersections likely to focus the flow of fluids; 4) the presence of chemical environments that favour uranium deposition — for example, sediments deposited in reducing conditions, or sediments rich in organic materials. The most prospective ground for unconformity-related uranium is the area around the Carrington Suite in the Aileron Province (Fig. 32).

Surficial-type uranium deposits

Surficial uranium deposits are broadly defined as near-surface uranium concentrations in sediments or soils with secondary cementing minerals (e.g. calcite). All essential elements for the surficial uranium mineral system are present in the west Arunta Orogen: 1) a uranium source

in basement granites; 2) the transport path of uranium-enriched fluids indicated by the presence of paleochannels; 3) a uranium-trapping environment comprising occurrences of valley calcrete and playa sediments (Fig. 35). The most prospective area corresponds with the location of the trapping environment; a consequence of the widespread source areas and mobility of uranium when in solution.

Sedimentary exhalative deposits

Sedimentary exhalative (SedEx) deposits occur in a marine basin environment, related to discharge of metal-bearing brines into the seawater. Key targeting elements for SedEx deposits in the west Arunta Orogen are: 1) a source of clastic sediments; 2) extent of fault systems for the favourable pathways component of the MSA; 3) deposition parameters (reduced or organic environment to trigger Pb–Zn complexation, and mechanical and structural focusing to concentrate SedEx-rich liquid). A few areas are demarcated, although on the whole the area does not appear to have very high prospectivity for SedEx deposits (Fig. 38) because of low lead and zinc content, as well as a paucity of known evaporites in the area analysed.

Limits and advantages of the method

Two basic approaches to prospectivity analysis were utilized. In the GIS-based fuzzy logic analysis, exploration targets were identified using spatial datasets, our understanding of the west Arunta Orogen crustal architecture, and syntheses of the different mineral systems. To improve the accuracy of any fuzzy results, newly acquired data can easily be integrated to any mineral systems analysis. For instance, for the surficial uranium mineral system, thermal remote sensing data would give better quality information about the location of paleochannels.

In the GIS-based WofE analysis the same spatial datasets as the fuzzy logic analysis were used, but the analysis was driven by the empirical spatial distribution of high mineral content (high geochemical values) in the study area. Compared to the fuzzy routine, the data-driven prospectivity method (WofE) is less affected by innate human biases, such as previous exploration experience of the modeller, and can be regarded as relatively objective. However, WofE is not entirely non-discriminatory because the input variables are derived based on the conceptual model of mineralization. However, much of the fuzzy prospectivity analysis is restricted to areas of reasonable data density; therefore, it reveals nothing (or little) about areas where only limited data are available.

In the west Arunta Orogen, the data-driven approach was only used for the gold mineral system. The number of prospects, minor occurrences, and mineral contents for uranium-type and SedEx commodities is too low to carry out a WofE analysis. A systematic geochemistry dataset with homogeneous coverage would be required to do this.

Geology in the third dimension

A major constraint on our geological understanding and prospectivity analysis of the west Arunta Orogen was the difficulty of deriving information about the geology at depth. There are considerable variations in density within both the basement rocks and the overlying sedimentary sequences, which has prevented reliable modelling of the gravity data.

Normally, relatively simple physical property variations exist in sedimentary basin sequences and reasonably consistent physical property contrasts are present between basement and cover. This means, for example, that depth to basement can be estimated from modelling of gravity and magnetic data. However, in the west Arunta Orogen, significant changes in physical properties occur within the basin sequences alone. For instance, the Amadeus Basin contains low density evaporites, and dense volcanic sedimentary rocks and mafic lavas. The lithological variation in the basement rocks is also considerable, and includes the presence of dense and magnetic iron-formation and lower density granitic rocks. This means that in some areas there is no density contrast between the overlying sedimentary rocks and the basement. This combination of circumstances makes modelling of gravity data of little use. However, gravity modelling has demonstrated that the gross structural style inferred for the west Arunta Orogen is consistent with the observed variations in gravity, although no further constraints can be obtained.

Another major limitation on understanding the third dimension and prospectivity mapping is the assumption that the present-day map pattern of the geology is similar to what it was at the time of mineralization. For example, it is clear that major thrust faulting has occurred, which may have juxtaposed different units after mineralization events, destroying primary relationships. It is also difficult to constrain the timing of events, and our understanding of the fourth dimension is minimal. This lack of knowledge makes the mineral systems approach difficult to apply with respect to source. For example, during the prospectivity analysis, various assumptions were made about in situ gold and uranium deposition in contact with wall rocks, when it fact, fluid mixing may have been the main mechanism, possibly with reducing fluid sourced from unknown geological sources at depth.

Acknowledgements

Our work on the west Arunta Orogen has benefited from the open discussions between GSWA and the CET team. We acknowledge all those involved at every level. The positive and insightful comments provided by both reviewers Warren Ormsby and Julie Hollis are gratefully acknowledged.

References

Abeysinghe, PB 2003, Mineral occurrences and exploration activities in the Arunta–Musgrave area: Geological Survey of Western Australia, Record 2002/9, 33p.

Agterberg, FP 1989, Systematic approach to dealing with uncertainty of geoscience information in mineral exploration: Proceedings of the 21st International Symposium on Application of Computers in the Minerals Industry (APCOM) Symposium, v. 18, p. 165–178.

Agterberg, FP and Bonham-Carter, G 1990, Deriving weights of evidence from geoscience contour maps for the prediction of discrete events: Proceedings of the 22nd International Symposium on Application of Computers in the Minerals Industry (APCOM) Symposium, Berlin, Germany, v. 2, p. 381–395.

Ahmad, M, Wygralak, AS and Ferenczi, PA 1999, Gold deposits of the Northern Territory: Northern Territory Geological Survey, Report 11, 95p.

Ahmad M, Wygralak AS and Ferenczi PA 2009, Gold deposits of the Northern Territory (2nd edition): Northern Territory Geological Survey, Report 11 (2nd edition update by AS Wygralak AS and IR Scrimgeour).

Ambrose, G 2006, Northern Territory of Australia, onshore hydrocarbon potential, 2006: Northern Territory Geological Survey, Record 2006-003, 69p.

Anbar, AD and Knoll, AH 2002, Proterozoic ocean chemistry and evolution: A bioinorganic bridge?: Science, v. 297, p. 1137–1142, doi: 10.1126/science.1069651.

Aspinall, PJ and Hill, AR 1983, Clinical inferences and decisions — I. Diagnosis and Bayes' theorem: Ophthalmic and Physiologic Optics, v. 3, p. 295–304.

Bagas, L, Bierlein, FP, English, L, Anderson, J, Maidment, D and Huston, DL 2008, An example of a Paleoproterozoic back-arc basin: petrology and geochemistry of the ca. 1864 Ma Stubbins Formation as an aid towards an improved understanding of the Tanami Orogen, Western Australia: Precambrian Research, v. 166, no. 1–4, p. 168–184.

Bagas, L, Bierlein, FP, Anderson, JAC and Maas, R 2010, Collision-related granitic magmatism in the Granites–Tanami Orogen, Western Australia: Precambrian Research, v. 177, p. 212–226.

Biermeier, C, Stüwe, K, Foster, DA and Finger, F 2003, Thermal evolution of the Redbank Thrust system, central Australia; geochronological and phase-equilibrium constraints: Tectonics, v. 22, no. 1, 23p, doi:10.1029/2001TC901033.

Blake, DH 1977, Webb, Sheet SF 52-10: Bureau of Mineral Resources and Geological Survey of Western Australia, 1:250 000 Geological Series Explanatory Notes, 19p.

Bonham-Carter, G F 1994, Geographic Information Systems for geoscientists: Modelling with GIS: Pergamon Press, Oxford, UK, 398 p.

Bonham-Carter, GF and Agterberg, FP 1990, Application of a microcomputer-based geographic information system to mineral-potential mapping, *in* Microcomputer-based Applications in Geology, II, Petroleum *edited by* JT Hanley and DF Merriam: Pergamon Press, New York, USA, p. 49–74.

Brown, WM, Groves, DI and Gandoll, T 2004, Application of spatial data analysis in a GIS database to Archean orogenic gold deposits, from the Kalgoorlie Terrain, in Proceedings of the Society of Economic Geologists, Predictive Mineral Discovery Under Cover: 74th Annual Meeting of the Society of Economic Geologists Conference and Exhibition, 27 September to 1 October, 2004, Perth, Western Australia.

Buick, IS, Miller, JA, Williams, IS and Cartwright I 2001, Ordovician high-grade metamorphism of a newly recognised late Neoproterozoic terrane in the northern Harts Range, central Australia: Journal of Metamorphic Geology, v. 19, p. 373–394.

Burgess, JM, Johnstone, AL, Schaefer, BF, Brescianini, RF and Tingate, PR 2002, New perspectives of the Amadeus Basin, Northern Territory: Petroleum Exploration Society of Australia Journal, v. 29, p.14–23.

Canfield, DE and Raiswell, R 1999, The evolution of the sulfur cycle: American Journal of Science, v. 299, p. 697–723.

Canfield, DE 1998, A new model for Proterozoic ocean chemistry: Nature, v. 396, p. 450–453, doi:10.1038/24839.

Carlisle, D 1983, Concentration of uranium and vanadium in calcrete and gypcrete, in Residual Deposits edited by RCL Wilson: Geological Society, London, Special Publication No. 11, p. 185–195.

Cawood, PA and Korsch, RJ 2008, Assembling Australia: Proterozoic building of a continent: Precambrian Research, v. 166, p. 1–38.

Cheng, Q 2007, Mapping singularities with stream sediment geochemical data for prediction of undiscovered mineral deposits in Gejiu, Yunnan Province, China: Ore Geology Reviews, v. 32, p. 314–324.

Claoué-Long, JC and Edgoose, C 2008, The age and significance of the Ngadarunga Granite in Proterozoic central Australia: Precambrian Research, v. 166, no. 1–4, p. 219–229, doi:10.1016/j.precamres.2007.06.026

Claoué-Long, JC, Edgoose, C and Worden, K 2008, A correlation of Aileron Provenance stratigraphy in central Australia: Precambrian Research, v. 166, no. 1–4, 230–245, doi:10.1016/j.precamres.2007.06.022.

Claoué-Long, J and Hoatson, D 2005, Proterozoic mafic–ultramafic intrusions in the Arunta Region, central Australia. Part 2: Event chronology and regional correlations: Precambrian Research, v. 142, no. 3-4, p. 134–158, doi:10.1016/j.precamres.2005.08.006.

Close, DF, Scrimgeour, IR, Edgoose, CJ, Cross, A, Claoué-Long, J, Kinny, P and Meixner, A 2003a, Redefining the Warumpi Province, *in* Annual Geoscience Exporation Seminar (AGES) 2003, Record of abstracts *edited by* TW Munson and IR Scrimgeour: Northern Territory Geological Survey, Record 2003-001.

Close, DF, Edgoose, CJ and Scrimgeour, IR 2003b, Hull and Bloods Range: Northern Territory Geological Survey, 1: 100 000 Geological Map Series Explanatory Notes, 46p.

Close, DF, Scrimgeour, IR, Edgoose, CJ and Cross, A 2004, Late Palaeoproterozoic development of the SW margin of the North Australian Craton: Geological Society of Australia Abstracts v. 73, p. 149

Close, DF, Scrimgeour, IR, Edgoose, CJ, Wingate, MTD and Selway, K 2005, Late Paleoproterozoic accretion of a 1690–1660 Ma magmatic arc onto the North Australian Craton: Geological Society of Australia Abstracts, v. 81, p. 36.

Close, DF, Scrimgeour, IR and Edgoose, CJ 2006, Evolution and mineral potential of the Paleoproterozoic Warumpi Province, *in* Evolution and Metallogenesis of the North Australian Craton, Conference Abstracts *edited by* P Lyons and DL Huston: Geoscience Australia, Record 2006/16, p. 9–10.

Close, DF and Scrimgeour, IR 2009, Deep seated structures and mineralisation in the Arunta region: Annual Geoscience Exploration Seminar Abstracts, 23–25 March 2009, Alice Springs Convention Centre, Northern Territory.

Collins, WJ and Shaw, RD 1995, Gechonological constraints on orogenic events in the Arunta Inlier: a review: Precambrian Research, v. 71, p. 315–346.

Cox, SF, Knackstedt, MA and Braun, J 2001, Principles of structural control on permeability and fluid flow in hydrothermal systems: Reviews in Economic Geology, v. 14, 1–24.

Cross, A, Claoué-Long, JC, Scrimgeour, IR, Ahmad, M and Kruse, PD 2005, Summary of results of the joint NTGS–GA geochronology project: Rum Jungle, basement to the southern Georgina Basin and eastern Arunta Region, 2001–2003: Northern Territory Geological Survey, Record 2005–006.

Dahlkamp, FJ 1978, Classification of uranium deposits: Mineralium Deposita, v. 13, p. 83–104.

Dentith, MC and Cowan, DR 2011, Using potential field data for petroleum exploration targeting, Amadeus Basin, Australia: Exploration Geophysics, v. 42, no. 3, p. 190–198.

Department of Mines and Petroleum (DMP) 2012, MINEDEX – Mines and mineral deposits database: Department of Mines and Petroleum, Perth, Western Australia, viewed April 2012, <http:// www.dmp.wa.gov.au/minedex>.

Derome, D, Cuney M, Cathelineau, M, Dubessy, J and Bruneton, P 2003, A detailed fluid inclusion study in silicified breccias from the Kombolgie sandstones (Northern Territory, Australia): Application to the genesis of Middle-Proterozoic unconformity-type uranium deposits: Journal of Geochemical Exploration, v. 80, p. 259–275.

Des Marais, DJ, Strauss, H, Summons, RE and Hayes, JM 1992, Carbon isotope evidence for the stepwise oxidation of the Proterozoic environment: Nature, v. 359, p. 605–609, doi:10.1038/359605a0.

Dunlap, WJ and Tessyier, C 1995, Paleozoic deformation and isotopic disturbance in the southeastern Arunta Block, central Australia: Precambrian Research, v. 71, p. 229–250.

Dyson, IA and Marshall, TR 2007, Neoproterozoic salt nappe complexes and salt-withdrawal mini-basins in the Amadeus Basin, *in* Proceedings of the Central Australian Basins Symposium (CABS) *edited by* TJ Munson and GJ Ambrose: Northern Territory Geological Survey; Central Australian Basins Symposium, Alice Springs, Northern Territory, 16–18 August, 2005, Proceedings; Special Publication, no. 2, p. 108–118 <http://conferences.minerals.nt.gov.au/cabsproceedings/>.

Edgoose, CJ, Close, DF and Scrimgeour, IR 2008, Lake Mackay, Northern Territory, SF 52-11 (2nd edition), 1:250 000 geological map series: Northern Territory Geological Survey, Darwin.

Fitzgerald, LG 1998, H296 Mt Webb project, Western Australia; Annual Technical Exploration Report for Licenses 80/2039 to 80/2042, for the period 23rd October 1996 to 31st December 1997: Geological Survey of Western Australia, Statutory mineral exploration report, A/54975 (unpublished).

Flöttmann, T and Hand, M 1999, Folded basement-cored tectonic wedges along the northern edge of the Amadeus Basin, central Australia: evaluation of orogenic shortening: Journal of Structural Geology, v. 21, p. 399–412.

Flöttmann, T, Hand, M, Close, DF, Edgoose, C and Scrimgeour, IR 2004, Thrust tectonic styles of the intracratonic Alice Springs and Petermann Orogens, Central Australia, *in* Thrust Tectonics and Hydrocarbon Systems *edited by* KR McClay: American Association of Petroleum Geologists. Memoir v. 82, p. 538–557.

Foss, C and Marshall, TR 2005, Beaten with a blunt object, can we get more out of geophysics in the Amadeus Basin?: Symposium Handbook, Central Australian Basins Symposium, Alice Springs, p. 28–29.

Fruzetti, O 1971, The Clarke Copper Mine, Mount Doreen, NT: Northern Territory Geological Survey, Technical Report GS1971-002.

Geological Survey of Western Australia (GSWA) 2009a, GeoChem database: Geological Survey of Western Australia, viewed October 2009, <http://geochem.dmp.wa.gov.au/geochem/>.

Geological Survey of Western Australia (GSWA) 2009b, West Arunta, 2009 update: Geological Survey of Western Australia, Geological Exploration Package.

Geoscience Australia (GA) 2007, OZCHEM National Whole Rock Geochemistry Database: Geoscience Australia, viewed October 2007, <https://www.ga.gov.au/products/servlet/controller?event=FILE_SELECTION&catno=65464>.

Glass, LM and Phillips, D 2006, The Kalkarindji Continental Flood Basalt Province: A new Cambrian Large Igneous Province in Australia with possible links to mass extinction: Geology, v. 34, p. 461–464.

Goleby, BR, Shaw, RD, Wright, C, Kennett, BLN and Lamberk, K 1989, Geophysical evidence for 'thick-skinned' crustal deformation in central Australia: Nature, v. 337, p. 325–330.

Goleby, BR, Wright, C, Collins, CDN and Kennett, BLN 1988, Seismic reflection and refraction profiling across the Arunta Block and Ngalia and Amadeus Basins: Australian Journal of Earth Sciences, v. 35, p. 275–294.

Goleby, BR, Huston, DL, Lyons, P, Vandenberg, L, Bagas, L, Davies, BM, Jones, LEA, Gebre-Mariam, M, Johnson, W, Smith, T and English, L 2009, The Tanami deep seismic reflection experiment: An insight into gold mineralization and Paleoproterozoic collision in the North Australian Craton: Tectonophysics, v. 472, no. 1–4, p. 169–182.

Goodfellow, WD and Lydon, JW 2007, Sedimentary exhalative (SEDEX) deposits, *in* Mineral deposits of Canada: A synthesis of major deposit types, district metallogeny, the evolution of geological provinces, and exploration methods *edited by* WD Goodfellow: Geological Association of Canada, Mineral Deposits Division, Special Publication 5, p. 163–183.

Goodfellow, WD, Lydon, JW and Turner, RJW 1993, Geology and genesis of stratiform sediment-hosted (SEDEX) zinc–lead–silver sulphide deposits: Geological Association of Canada Special Paper 40, p. 201–251.

Groves, DI 1993, The crustal continuum model for late-Archaean lode-gold deposits of the Yilgarn Block, Western Australia: Mineral Deposita, v. 28, p. 357–387.

Groves, DI, Goldfarb, RJ, Gebre-Mariam, M, Hagemann, SG and Robert, F 1998, Orogenic gold deposits: a proposed classification in the context of their crustal distribution and relationship to other gold deposit types: Ore Geology Reviews, v. 13, p. 7–27.

Grey, K 1990, Birrindudu Basin, in Geology and Mineral Resources of Western Australia: Geological Survey of Western Australia, Memoir 3, p. 349–362.

Hagemann, SG and Cassidy, KF 2000, Archaean lode gold deposits, *in* Gold in 2000 *edited by* SG Hagemann and PE Brown: Reviews in Economic Geology, v. 13, p. 9–68.

Hagemann, SG and Cassidy, KF, submitted, Advances in understanding of the Archean orogenic gold system: implications for a genetic model and exploration, Ore Geology Reviews.

Haines, PW, Allen, HJ and Grey, K 2010, The Amadeus Basin in Western Australia: a forgotten corner of the Centralian Superbasin: Geological Survey of Western Australia Annual Review 2008–09, p. 48–57.

Haines, PW, Hand, M and Sandiford, M 2001, Paleozoic syn-orogenic sedimentation in central and northern Australia: a review of distribution and timing with implications for intracontinental orogens: Australian Journal of Earth Sciences, v. 48, 911–928.

Hand, M and Buick, IS 2001, Tectonic history of the Reynolds – Anmatjira Ranges: a case study of reactivation in central Australia, *in* Continental Reactivation and Reworking *edited by* JA Miller, R Holdsworth, IS Buick and M Hand: Geological Society, London, Special Publication 184, p. 237–260.

Hand, M and Sandiford, M 1999, Intraplate deformation in central Australia, the link between subsidence and fault reactivation: Tectonophysics, v. 305, p. 121–140.

Hanley, LM and Wingate, MTD 2000, SHRIMP zircon age for an Early Cambrian dolerite dyke: an intrusive phase of the Antrim Plateau Volcanics of northern Australia: Australian Journal of Earth Sciences, v. 47, p. 1029–1040.

Hart, CJR 2007, Reduced intrusion-related gold systems, in Mineral deposits of Canada: A synthesis of major deposit types, district metallogeny, the evolution of geological provinces, and exploration methods *edited by* WD Goodfellow: Geological Association of Canada, Mineral Deposits Division, Special Publication No. 5, p. 95–112.

Heckerman, DE, Horvitz, EJ and Nathwani, BN 1992, Towards normative expert systems: Part I the Pathfinder project: Methods of Information in Medicine, v. 31, p. 90–105.

Hoatson DM, Sun, S and Claoué-Long, JC 2005, Proterozoic mafic–ultramafic intrusion in the Arunta Region, central Australia, Part 1: Geological setting and mineral potential: Precambrian Research, v. 142, p. 93–133.

Hocking, RM, Playford, PE, Haines, PW and Mory, AJ 2008, Paleozoic geology of the Canning Basin — a field guide: Geological Survey of Western Australia, Record 2008/18, 39p.

Hollis, J, Carson, C and Glass, L 2008, The discovery of an Archean inlier in Arnhem Land: Northern Territory Geological Survey, Record 2008-002, p. 13–14.

Hollis, J, Carson, C and Glass, L 2009, SHRIMP U–Pb zircon geochronological evidence for Neoarchean basement in western Arnhem Land, Northern Australia: Precambrian Research, v. 174, p. 364–380.

Huston, DL, Stevens, B, Southgate, PN, Muhling, P and Wyborn, L 2006, Australian Zn–Pb–Ag ore-forming systems: A review and analysis: Economic Geology, v. 101, p. 1117–1157.

Huston, DL, Whelan, JA, Jaireth, S, Kirkby, A, Gerner, E, Close, D, Blewett, R, Scrimgeour, I and Korsch, RJ 2011, Implications of the Georgina–Arunta seismic survey to energy and mineral systems: Northern Territory Geological Survey, Record 2011-003, p. 86–93.

International Atomic Energy Agency, 2000, Methods of Exploitation of Different Types of Uranium Deposits: International Atomic Energy Agency, Vienna, Austria, IAEA-TECDOC-1174, 75p.

Jackson, MPA, Roberts, DG and Snelson, S 1995, Salt Tectonics: A Global Pespective: American Association of Petroleum Geologists, Memoir 65.

Jefferson, CW, Thomas, DJ, Gandhi, SS, Ramaekers, P, Delaney, G, Brisbin, D, Cutts, C, Portella, P and Olson, RA 2007, Unconformity-associated uranium deposits of the Athabasca Basin, Saskatchewan and Alberta: Geological Survey of Canada, Bulletin, v. 588, p. 23–67.

Joly, A, McCuaig, TC and Bagas, L 2010, The importance of early crustal architecture for subsequent basin-forming, magmatic and fluid flow events: The Granites–Tanami Orogen example: Precambrian Research, v. 182, no. 1–2, p. 15–29.

Joly, A, Porwal, A and Mc Cuaig, TC 2012, Exploration targeting for orogenic gold deposits in the Granites-Tanami Orogen: Mineral system analysis, targeting model and prospectivity analysis: Ore Geology Reviews, v. 48, p. 349–383.

Jones, AG 1999, Imaging the continental upper mantle using electromagnetic methods: Lithos, v. 48, no. 1–4, p. 57–80.

Kemp, LD, Bonham-Carter, GF and Raines, GL 1999, Arc-WofE: ArcView extension for weights of evidence mapping, viewed April 2012, <http://ige.unicamp.br/wofe>.

Kennard, JM, Jackson, MJ, Romine, KK, Shaw, RD and Southgate, PN 1994, Depositional sequences and associated petroleum systems of the Canning Basin, WA, *in* The Sedimentary Basins of Western Australia *edited by* PG Purcell and RR Purcell: Proceedings of the Western Australian Basins Symposium, 1994, p. 657–676.

Kirkland, CL, Wingate, MTD, Spaggiari, CV and Tyler, IM 2009a, 184363: metasandstone, Mount Tietkens; Geochronology Record 821: Geological Survey of Western Australia, 5p.

Kirkland, CL, Wingate, MTD, Tyler, IM and Spaggiari, CV 2009b, 184367: metagranodiorite, Dwarf Well; Geochronology Record 846: Geological Survey of Western Australia, 4p.

Kirkland, CL, Wingate, MTD, Spaggiari, CV and Tyler, IM 2009c, 184341: quartzite, Lake Mackay; Geochronology Record 818: Geological Survey of Western Australia, 5p.

Kirkland, CL, Wingate, MTD, Spaggiari, CV and Tyler, IM 2009d, 184364: metasyenogranite, Buck Hills; Geochronology Record 845: Geological Survey of Western Australia, 4p.

Kirkland, CL, Wingate, MTD, Spaggiari, CV and Tyler, IM 2009e, 184359: metarhyodacite, Dovers Hills; Geochronology Record 815: Geological Survey of Western Australia, 4p.

Kirkland, CL, Wingate, MTD, Spaggiari, CV and Tyler, IM 2009f, 184353: monzogranite, Kiwirrkura; Geochronology Record 820: Geological Survey of Western Australia, 4p.

Kirkland, CL, Wingate, MTD, Spaggiari, CV and Tyler, IM 2009g, 184342: sandstone, Alec Ross Range; Geochronology Record 819: Geological Survey of Western Australia, 5p.

Kirkland, CL, Wingate, MTD, Spaggiari, CV and Tyler, IM 2009h, 184336: sandstone, Pollock Hills; Geochronology Record 816: Geological Survey of Western Australia, 5p.

Kirkland, CL, Wingate, MTD, Spaggiari, CV and Tyler, IM 2009i, 184339: sandstone, Pollock Hills; Geochronology Record 817: Geological Survey of Western Australia, 5p.

Knox-Robinson, CM and Wyborn, LAI 1997, Towards a holistic exploration strategy: using geographic information systems as a tool to enhance exploration: Australian Journal of Earth Sciences, v. 44, p. 453–463.

Korsch, RJ and Kennard, JM 1991, Geological and Geophysical Studies in the Amadeus Basin, Central Australia: Bureau of Mineral Resources, Bulletin 236.

Korsch, RJ and Lindsay, JF 1989, Relationships between deformation and basin evolution in the intracratonic Amadeus Basin, Central Australia, *in* Deformation of Crustal Rocks *edited by* A Ord: Tectonophysics, v. 158, p. 5–22.

Korsch, RJ, Goleby, BR, Leven, JH and Drummond, BJ 1998, Crustal architecture of central Australia based on deep seismic reflection profiling: Tectonophysics, v. 288, no. 1–4, p. 57–69.

Korsch, RJ, Blewett, RS, Close, DF, Scrimgeour, IR, Huston, DL, Kositcin, N, Whelan, JA, Carr, LK and Duan, J 2011, Geological interpretation and geodynamic implications of deep seismic reflection and magnetotelluric line 09GA-GA1: Georgina Basin–Arunta region, Northern Territory, *in* Annual Geoscience Exploration Seminar (AGES) 2011, Record of abstracts, Northern Territory Geological Survey, Record 2011–003.

Kreuzer, OP, Etheridge, MA, Guj, P, Maureen, E, McMahon, ME, Darren, J and Holden, DJ 2008, Linking mineral deposit models to quantitative risk analysis and decision-making in exploration: Economic Geology, v. 103, p. 829–850.

Kreuzer, OP, Markwitz, V, Porwal, AK and McCuaig, TC 2010, A continent-wide study of Australia's uranium potential. Part I: GIS-assisted manual prospectivity analysis: Ore Geology Reviews, v. 38, no. 4, 334–366.

Lambeck, K, Burgess, G and Shaw, RD 1988, Teleseismic travel-time anomalies and deep crustal structure in central Australia: Geophysical Journal International, v. 94, p. 105–124.

Lang, JR and Baker, T 2001, Intrusion-related gold systems: the present level of understanding: Mineralium Deposita, v. 36, p. 477–489.

Large, DE 1986, The paleotectonic setting of Rammelsberg and Meggen, Germany — A basin analysis study, *in* The genesis of stratiform sediment-hosted lead and zinc deposits *edited by* RJW Turner and MT Einaudi: Stanford University Publications, Geological Sciences, Conference proceedings, v. 20, p. 109–112.

Leach, DL, Bradley, DC, Huston, D, Pisarevsky, SA, Taylor, RD and Gardoll, SJ 2010. Sediment-hosted lead–zinc deposits in Earth history: Economic Geology, v. 105, p. 593–625.

Leach, DL, Sangster, DF, Kelley, KD, Large, RR, Garven, G, Allen, CR, Gutzmer, J and Walters, S 2005, Sediment-hosted lead–zinc deposits: A global perspective: Economic Geology, 100th Anniversary Volume, p. 561–608.

Lindsay, JF 1999, Heavitree Quartzite, a Neoproterozoic (ca. 800–760 Ma), high-energy, tidally influenced, ramp association, Amadeus Basin, central Australia: Australian Journal of Earth Sciences, v. 46, p. 127–140.

Lindsay, JF and Korsch, RJ 1991, The evolution of the Amadeus Basin, central Australia, *in* Geological and Geophysical Studies in the Amadeus Basin, Central Australia *edited by* RJ Korsch and B Kennard: Australian Bureau of Mineral Resources, Geology and Geophysics Bulletin, v. 236, p. 7–32.

Lusted, LB 1968, Introduction to Medical Decision Making, Charles Thomas: Springfield, 271p.

Lydon, JW 1983, Chemical parameters controlling the origin and deposition of sediment-hosted stratiform lead–zinc deposits: Mineralogical Association of Canada Short Course Handbook 9, p. 175–250.

Mackie, AM 1984, Geology of the Green Parrot and Reward silver–lead deposits Jervois Range, Northern Territory: Proceedings of the Darwin Conference, Australasian Institute of Mining and Metallurgy Transactions, p. 323–328.

Maidment, DW, Hand, M and Williams, IS 2002, The extent of Cambrian metasediments and the Ordovician Larapinta Event, eastern Arunta Province, central Australia: Geological Society of Australia Abstracts, no. 67, p. 180.

Maidment, DW 2005, Palaeozoic high-grade metamorphism within the Centralian Superbasin, Harts Range region, central Australia: Australian National University, Canberra, Australian Capital Territory, PhD thesis (unpublished).

Maidment, DW, Hand, M and Williams, IS 2005, Tectonic cycles in the Strangways Metamorphic Complex, Arunta Inlier, central Australia: geochronological evidence for exhumation and basin formation between two high grade metamorphic events: Australian Journal of Earth Sciences, v. 52, p. 205–215.

Maidment, DW, Williams, IS and Hand, M 2007, Testing long-term patterns of basin sedimentation by detrital zircon geochronology, Centralian Superbasin, Australia: Basin Research, v. 19, p. 335–360.

Markwitz, V, Porwal, A and Kreuzer, O 2008, Regalpoint collaborative Research project: final technical report, CET, 166 p.

Marshall, TR and Dyson, IA 2007, Halotectonics – a key element of Amadeus Basin development and prospectivity: Proceedings of the Central Australian Basins Symposium, Alice Springs, p. 119–135.

Mashkovtsev, GA, Kislyakov, YM, Miguta, AK, Modnikov, IS and Shchetochkin, VN 1995, Uranium deposits: main types and concepts for detection: Changes and events in uranium deposit development, exploration, resources, production and the world supply–demand relationship: International Atomic Energy Agency and OECD Nuclear Energy Agency, Vienna, Austria, IAEA-TECDOC-961, p. 297–306.

Mawby J, Hand, M and Foden, J 1999, Sm–Nd evidence for high-grade Ordovician metamorphism in the Arunta Block, central Australia: Journal of Metamorphic Geology, v. 17, p. 653–668.

McCuaig, TC, Beresford, S and Hronsky, JMA 2010, Translating the mineral systems approach into an effective exploration targeting system: Ore Geology Reviews, v. 38, no. 3, p.128–138.

McCuaig, TC and Kerrich, R 1998, P–T–t–deformation–fluid characteristics of lode gold deposits: Evidence from alteration systematics: Ore Geology Reviews, v. 12, p. 381–453.

McKay, AD and Miezitis, Y 2001, Australia's Uranium Resources, Geology and Development of Deposits: Australian Geological Survey Organisation – Geoscience Australia Mineral Resource Report 1, 184p.

Meteoric Resources 2009, New gold anomaly at Mt Webb: ASX release, 20 October 2009, <http://www.meteoric.com.au/>.

Mikucki, EJ 1998, Hydrothermal transport and depositional processes in Archean lode-gold systems; a review: Ore Geology Reviews, v. 13, no. 1, p. 307–321.

Mishra, B and Panigrahi, MK 1999, Fluid evolution in the Kolar gold field: Evidence from fluid inclusion studies: Mineralium Deposita, v. 34, p. 173–181.

Myers, JS 1990, Arunta Orogen and Billiluna Complex, in Geology and Mineral Resources of Western Australia: Geological Survey of Western Australia, Memoir 3, p. 286–288.

Myers, JS, Shaw, RD and Tyler, IM 1996, Tectonic evolution of Proterozoic Australia: Tectonics, v. 15, no. 6, p. 1431–1446.

Nakamura, A, Duan, J, Costelloe, RD, Holzschuh, J and Maher, J 2011, 2009 Georgina–Arunta seismic and MT surveys – acquisition and processing, *in* Annual Geoscience Exploration Seminar (AGES) 2011, Record of abstracts: Northern Territory Geological Survey, Record 2011-003.

Norman, AR and Clarke, GL 1990, A barometric response to late compression in the Strangways Metamorphic Complex, Arunta Block, Central Australia: Journal of Structural Geology, v. 12, p. 667–684.

Organisation for Economic Co-operation and Development Nuclear Energy Agency, International Atomic Energy Agency 2005, Uranium 2005: Resourced, Production and Demand ('Red Book'), OECD Publications, Paris, France, 388p.

Page, RW, Hoatson, DM, Sun, S and Foudoulis, C 1995, High-precision geochronology of Palaeoproterozoic layered mafic–ultramafic intrusions in the East Kimberley: Australian Geological Survey Organisation Research Newsletter, v. 22, p. 7–8.

Pan, GC and Harris, DP 2000, Information Synthesis for Mineral Exploration: Oxford University Press, New York, USA, 461 p.

Phillips, GN and Groves, DI 1983, The nature of Archaean gold-bearing fluids as deduced from gold deposits of Western Australia: Journal of the Geological Society of Australia, v. 30, no. 1, 25–39.

Plumb, KA 1979, The tectonic evolution of Australia: Earth Science Reviews, v. 14, p. 205–249.

Plumb, KA, Derrick, GM, Needham, RS and Shaw, RD 1981, The Proterozoic of northern Australia, *in* The Precambrian of the Southern Hemisphere *edited by* DR Hunter: Elsevier, Amsterdam, p. 205–307.

Porwal, A 2006, Mineral potential mapping with mathematical geological models: University of Utrecht, The Netherlands, PhD thesis, ITC (International Institute for Geo-Information Science and Earth Observation) publication no. 130, Enschede, 289p.

Porwal, A, Carranza, EJM and Hale, M 2003, Extended weights-of-evidence modelling for predictive mapping of base-metal deposit potential in Aravalli province, western India: Exploration and Mining Geology, v. 10, no. 4, p. 155–163.

Porwal, AK and Kreuzer, OP 2010, Introduction to the Special Issue: Mineral prospectivity analysis and quantitative resource estimation: Ore Geology Reviews, v. 38, p. 121–127.

Ramaekers, P, Jefferson, CW, Yeo, GM, Collier, B, Long, DGF, Catuneanu, O, Bernier, S, Kupsch, B, Post, R, Drever, G, McHardy, S, Jiricka, D, Cutts, C and Wheatley, K 2007, Revised geological map and stratigraphy of the Athabasca Group, Saskatchewan and Alberta, *in* EXTECH IV: Geology and Uranium EXploration TECHnology of the Proterozoic Athabasca Basin, Saskatchewan and Alberta *edited by* CW Jefferson and G Delaney: Geological Survey of Canada, Bulletin 588 (*also* Geological Association of Canada, Mineral Deposits Division, Special Publication 4; Saskatchewan Geological Society, Special Publication 18), p. 155–192.

Rubatto, D, Williams, IS and Buick, IS 2001, Zircon and monazite response to prograde metamorphism in the Reynolds Range, central Australia: Contributions to Mineralogy and Petrology, v. 140, p. 458–468.

Schroder, RJ and Gorter, JD 1984. A review of the recent exploration and hydrocarbon potential of the Amadeus Basin, Northern Territory: Australian Petroleum Production and Exploration Association Journal, v. 24, no. 1, p. 19–41.

Scrimgeour, IR 2004, A revised province definition and Palaeoproterozoic framework for the Arunta Orogen, central Australia: Geological Society of Australia Abstracts, no. 73, p. 185.

Scrimgeour, IR 2006a, An overview of the North Australian Craton, *in* Evolution and metallogenesis of the North Australian Craton *edited by* P Lyons and DL Huston: Geoscience Australia, Record 2006/16, p. 1–2.

Scrimgeour, IR 2006b, The Arunta Region: Links between tectonics and mineralisation, *in* Annual Geoscience Exploration Seminar (AGES) 2006, Record of abstracts: Northern Territory Geological Survey, Record 2006-002, p. 7–10.

Scrimgeour, IR, Kinny, PD, Close, DF and Edgoose, CJ 2005a, High-T granulites and polymetamorphism in the Southern Arunta Orogen, Central Australia: evidence for a 1.64 Ga accretion event: Precambrian Research, v. 142, p. 1–27.

Scrimgeour, IR, Close, DF and Edgoose, CJ 2005b, Mount Liebig, Northern Territory — 1:250 000 geological map series explanatory notes, SF 52-16: Northern Territory Geological Survey, Darwin.

Scrimgeour, IR and Raith, JG 2001a, High-grade reworking of Proterozoic granulites during Ordovician intraplate tranpression, eastern Arunta Inlier, central Australia, *in* Continental Reactivation and Reworking *edited by* JA Miller, R Holdsworth, IS Buick and M Hand: Geological Society, London, UK, Special Publication 184, p. 261–287.

Scrimgeour, IR and Raith, JG 2001b. Tectonic and thermal events in the northeastern Arunta Province: Northern Territory Geological Survey, Report 12.

Selway, K, Hand, M, Heinson, GS and Payne, JL 2009, Magnetotelluric constraints on subduction polarity: Reversing reconstruction models for Proterozoic Australia: Geology, v. 37, no. 9, p. 799–802.

Shaw, RD and Black, LP 1991, The history and tectonic implications of the Redbank Thrust Zone, central Australia, based on structural, metamorphic and Rb–Sr isotopic evidence: Australian Journal of Earth Sciences, v. 38, p. 307–332.

Shaw, RD, Etheridge, MA and Lambeck, K, 1991, Development of the late Proterozoic to mid-Paleozoic, intracratonic Amadeus Basin in central Australia: a key to understanding tectonic forces in plate interiors: Tectonics, v. 10, no. 4, p. 688–721.

Shaw, RD, Goleby, BR, Korsch, RJ and Wright, C 1992b, Basement and cover thrust tectonics in central Australia based on the Arunta-Amadeus seismic reflection profile, *in* Basement Tectonics 9 *edited by* MJ Rickard, HJ Harrington and PR Williams: Kluwer Academic Publishers, Dordrecht, The Netherlands, p. 55–84.

Shaw, RD, Zeitler, PK, McDougall, I and Tingate PR, 1992a, The Paleozoic history of an unusual intracratonic thrust belt in central Australia based on ^{40}Ar–^{39}Ar, K–Ar and fission track dating: Journal of the Geological Society of London, v. 149, p. 937–954.

Shaw, RD, Stewart, AJ and Black, LP 1984, The Arunta Inlier: a complex ensialic mobile belt in central Australia. Part 2. Tectonic history: Australian Journal of Earth Sciences, v. 31, p. 457–484.

Shaw, RD, Wellman, P, Gunn, P, Whitaker, AJ, Tarlowski, C and Morse, MP 1995, Australian crustal elements map: a geophysical model for the tectonic framework of the continent, Australian Geological Survey Organisation Research Newsletter, v. 23, p. 1–3.

Simpson, F and Bahr, K 2005, Practical magnetotellurics: Cambridge University Press, Cambridge, UK, 254p.

Singer, DA and Kouda, R 1999, A comparison of the weights of evidence method and probabilistic neural networks: Natural Resources Research, v. 8, no. 4, p. 287–298.

Smith, SA, Tingate, PR, Griffiths, CM and Hull, JNF 1999, The structural development and petroleum potential of the Roebuck Basin: The Australian Petroleum Production and Exploration Association Journal, v. 39, no. 1, p. 364–385.

Spaggiari, CV, Morris, PA and Tyler, IM 2008, New exploration datasets for the western Arunta: could this be the next Olympic Dam? Geological Survey of Western Australia, Record 2008/2, p. 15–19.

Teyssier, C, Amri, C and Hobbs, BE 1988, South Arunta Block: the internal zones of a Proterozoic overthrust in central Australia: Precambrian Research, v. 40/41, p. 157–173.

Thompson, JFH, Sillitoe, RH, Baker, T, Lang, JR and Mortensen, JK 1999, Intrusion-related gold deposits associated with tungsten–tin provinces: Mineralium Deposita, v. 34, p. 197–217

Toro Energy Ltd 2009, Uranium mineralisation discovered in greenfields work at Lake Mackay, WA: ASX Release, 28 October 2009, <http://www.toroenergy.com.au>.

Toro Energy Ltd 2010, Uranium exploration summary — WA and NT: ASX Release, 21 December 2010, <http://www.toroenergy.com.au>.

Tyler, IM 2005, Australia — Proterozoic, in Encyclopedia of Geology *edited by* RC Selley, LRM Cocks and IR Plimer: Elsevier, Oxford, United Kingdom, p. 208–211.

Vozoff, K 1986, Magnetotelluric methods: Geophysics Reprint Series, 5: Society of Exploration Geophysicists, Tulsa, OK, USA, 763p.

Vry, JK, Compston, W and Cartwright, I 1996, SHRIMP II dating of zircons and monazites: reassessing the timing of high-grade metamorphism and fluid flow in the Reynolds Range, north Arunta Block, Australia: Journal of Metamorphic Geology, v. 14, p. 335–350.

Walter, MR, Veevers, JJ, Calver, CR and Grey, K 1995, Neoproterozoic stratigraphy of the Centralian Superbasin: Precambrian Research, v. 73, p. 173–195.

Warren, RG and Shaw, RD 1985. Volcanogenic Cu–Pb–Zn bodies in granulites of the central Arunta Block, central Australia: Journal of Metamorphic Geology, v. 3, p. 481–499.

Warren, RG, Stewart, AJ and Shaw, RD 1974, Summary of information on mineral deposits of the Arunta Complex, Alice Springs area, Northern Territory: Bureau of Mineral Resources, Australia, Record 1974/117.

Warren, RG, Stewart, AJ and Shaw, RD 1975, Arunta Block—mineralization, *in* Economic Geology of Australia and Papua New Guinea *edited by* CL Knight: Australasian Institute of Mining and Metallurgy Monograph, v. 5, p. 443–447.

Wells, AT 1968, MacDonald, WA sheet SF/52-14: Geological Survey of Western Australia 1:250 000 Geological Series.

Weste, G 1989, Northern Territory Geological Survey petroleum basin study — Western Amadeus Basin: Government Printer, Northern Territory, Darwin.

Wingate, MTD, Kirkland, CL and Haines, PW, 2012, 143743, dacite, Pollock Hills; Geochronology Record 1047: Geological Survey of Western Australia.

Worden, KE, Carson, CJ, Close, DF, Donnellan, N and Scrimgeour, IR 2008, Summary of results. Joint NTGS–GA geochronology project: Tanami Region, Arunta Region, Pine Creek Orogen and Halls Creek Orogen correlatives, January 2005–March 2007: Northern Territory Geological Survey, Record 2008–003.

Wyborn, LAI, Heinrich, CA and Jaques, AL 1994, Australian Proterozoic mineral systems: essential ingredients and mappable criteria, *in* Australian Mining Looks North – the Challenges and Choices *edited by* PC Hallenstein: Australian Institute of Mining and Metallurgy Publication Series, v. 5, p. 109–115.

Wyborn, LAI , Hazell, M, Page, R, Idnurm, M and Sun, S 1998, A newly discovered major Proterozoic granite-aleration system in the Mount Webb region, central Australia, and implications for Cu–Au mineralisation: Australian Geological Survey Organisation Research, Newsletter, No. 28, p. 1–5.

Wright, C, Goleby, BR, Collins, CDN, Korsch, RJ, Barton, T, Sugiharto, S and Greenhalgh, SA 1990, Deep seismic profiling in central Australia: Tectonophysics, v. 173, p. 247–256.

Zhao, JX and McCulloch, M 1993, Sm–Nd mineral isochron ages of Late Proterozoic dyke swarms in Australia: evidence for two distinctive events of mafic magmatism and crustal extension: Chemical Geology, v. 109, p. 341–354.

Zhao, JX and McCulloch, M 1995, Geochemical and Nd isotopic systematics of granites from the Arunta Inlier, central Australia: implications for Proterozoic crustal evolution: Precambrian Research, v. 71, p. 265–299.

Zhao, JX, McCulloch, MT and Bennett, VC 1992, Sm–Nd and U–Pb zircon isotopic constraints on the provenance of sediments from the Amadeus Basin, central Australia: evidence for REE fractionation: Geochimica et Cosmochimica Acta, v. 56, p. 921–940.

Appendix

Predictor maps

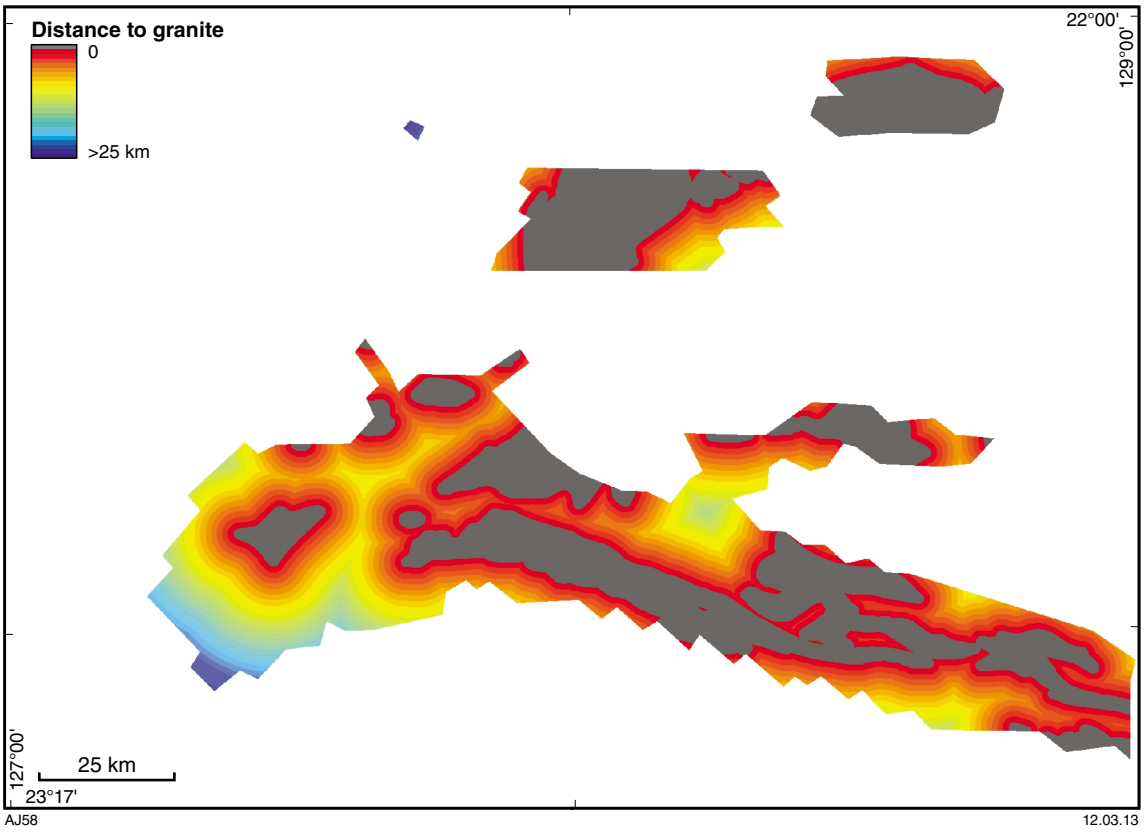

Map 1. **Predictor map for source: proximity to Carrington Suite and Mount Webb granites (up to 25 km)**

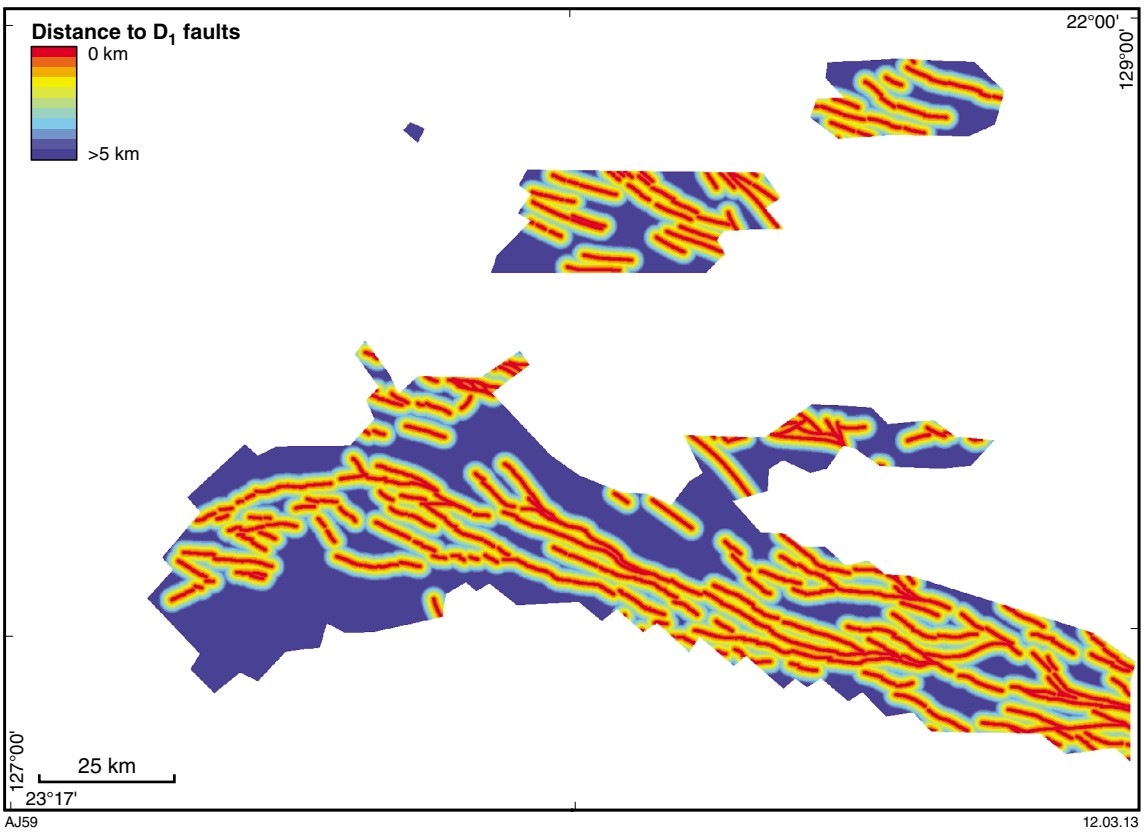

Map 2. **Predictor map for pathway: proximity to all D_1 faults with 5 km buffer zone**

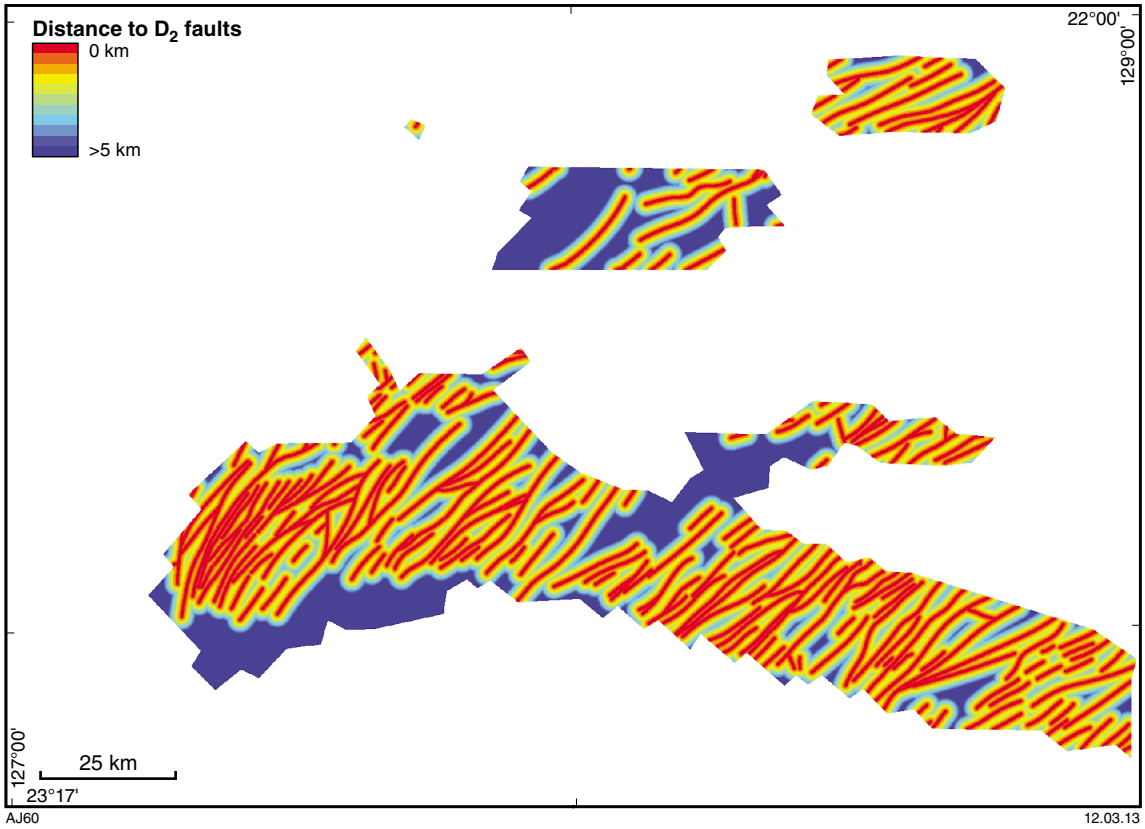

Map 3. **Predictor map for pathway: proximity to all D_2 faults with 5 km buffer zone**

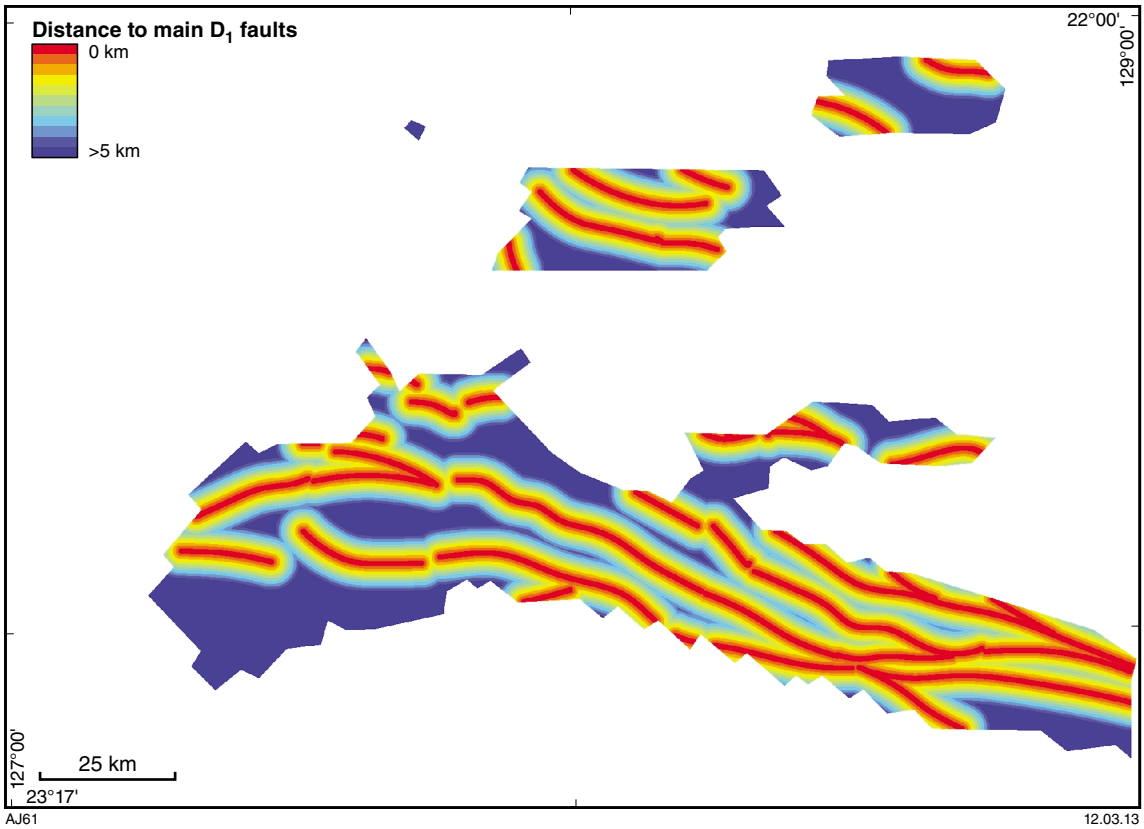

Map 4. **Predictor map for pathway: proximity to main D_1 faults with 5 km buffer zone**

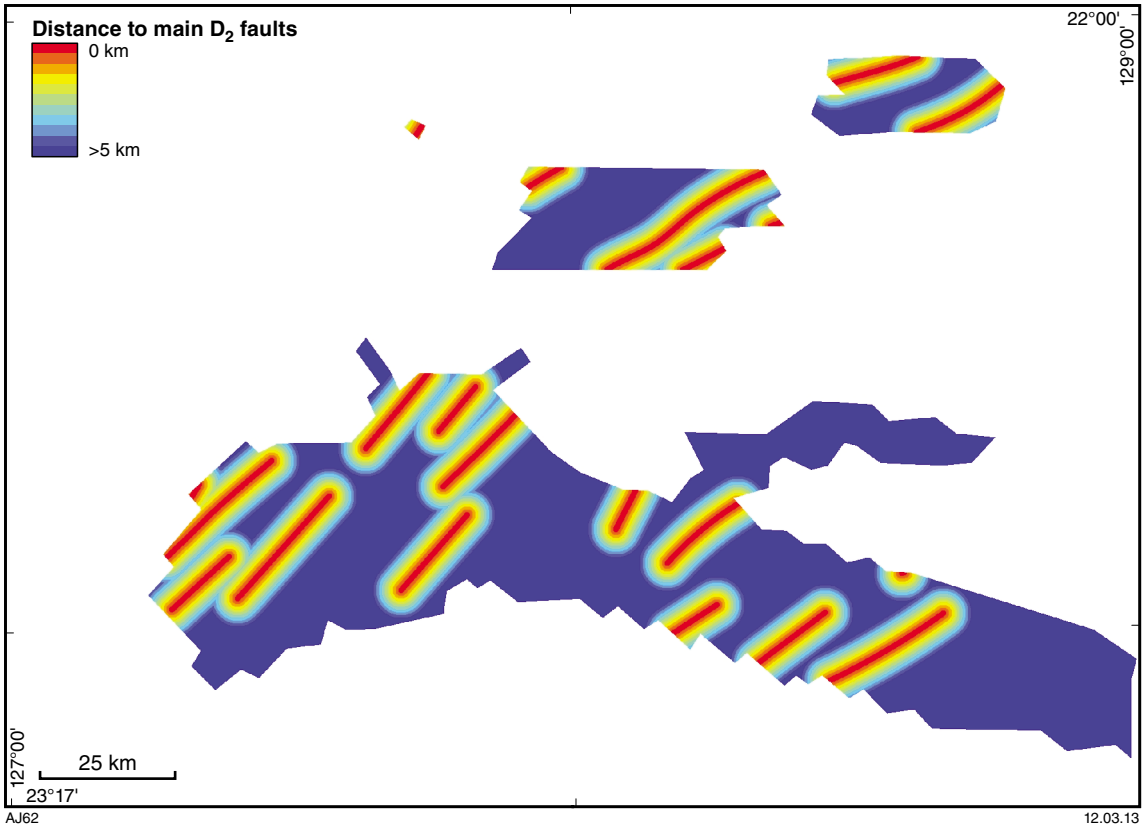

Map 5. **Predictor map for pathway: proximity to main D_2 faults with 5 km buffer zone**

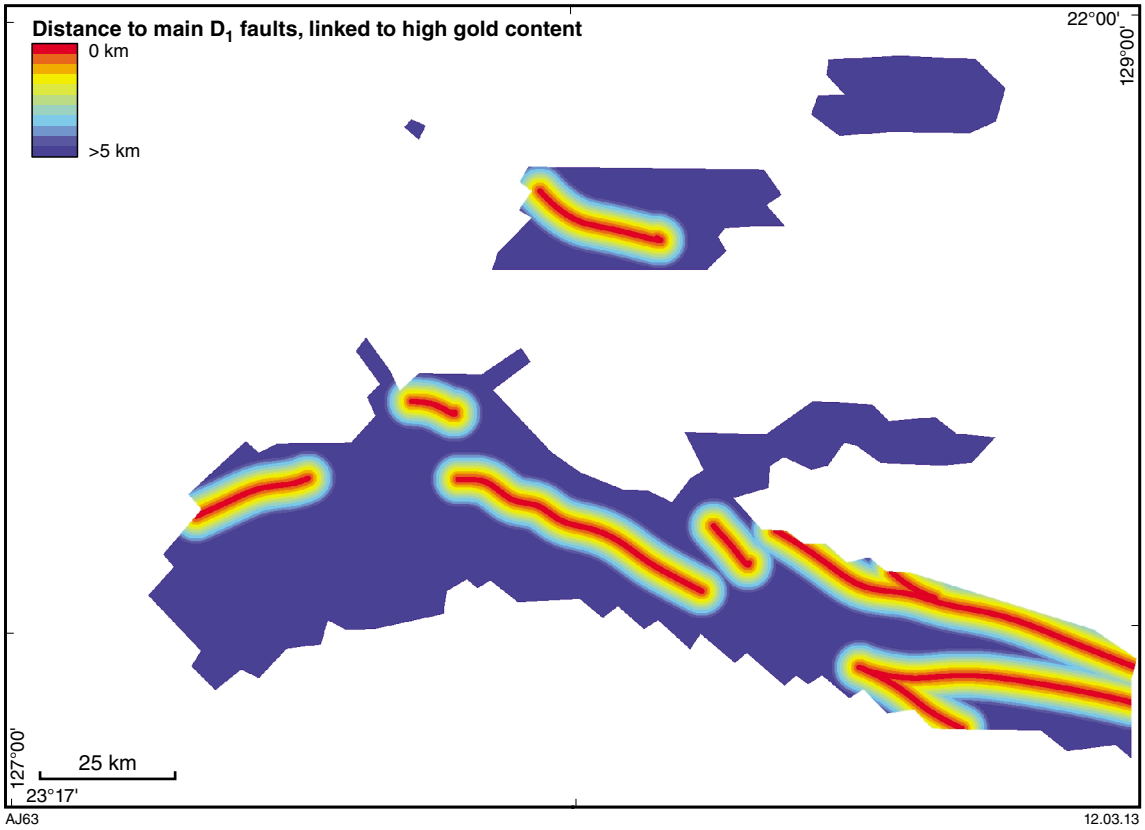

Map 6. **Predictor map for pathway: high (positive) Z log gold contents over main D_1 faults. Zones shown in red indicate areas very close to main D_1 faults that are linked to high gold contents; zones shown in blue correspond to the contrary**

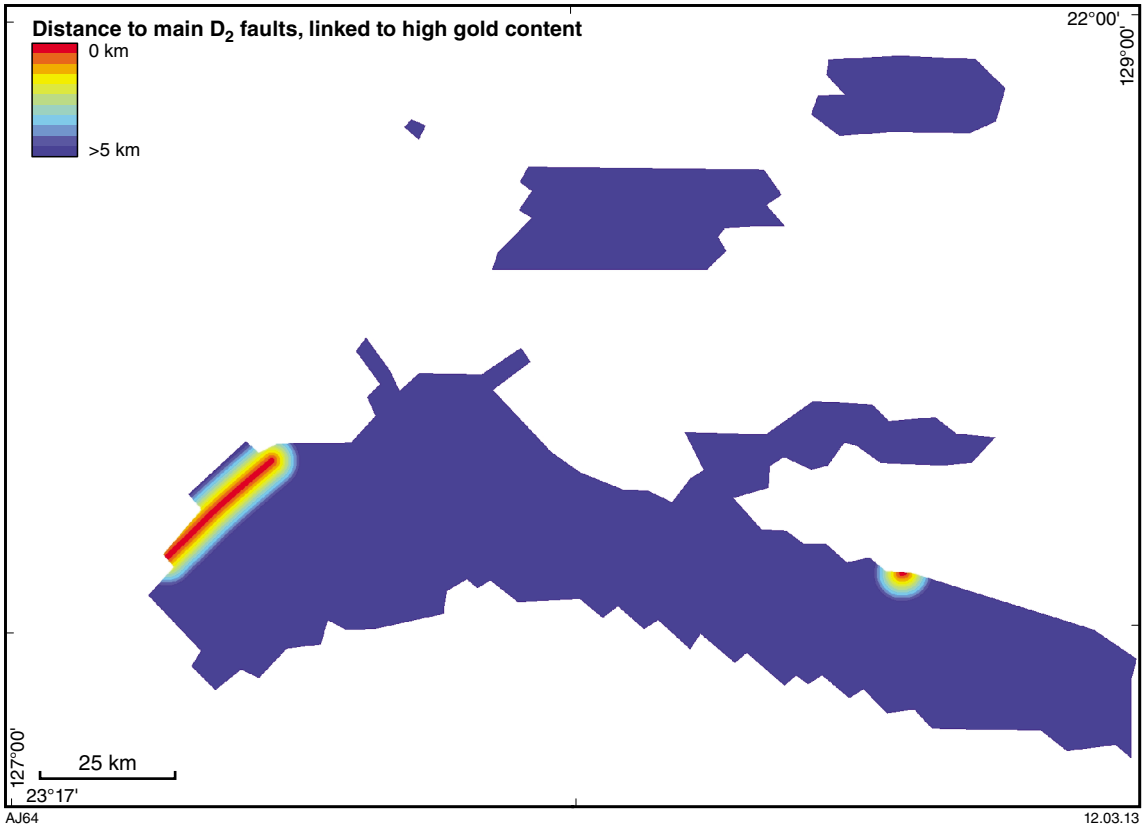

Map 7. **Predictor map for pathway: high (positive) Z Log gold contents over main D_2 faults. Zones shown in red indicate areas very close to main D_2 faults that are linked to high gold contents; zones shown in blue correspond to the contrary**

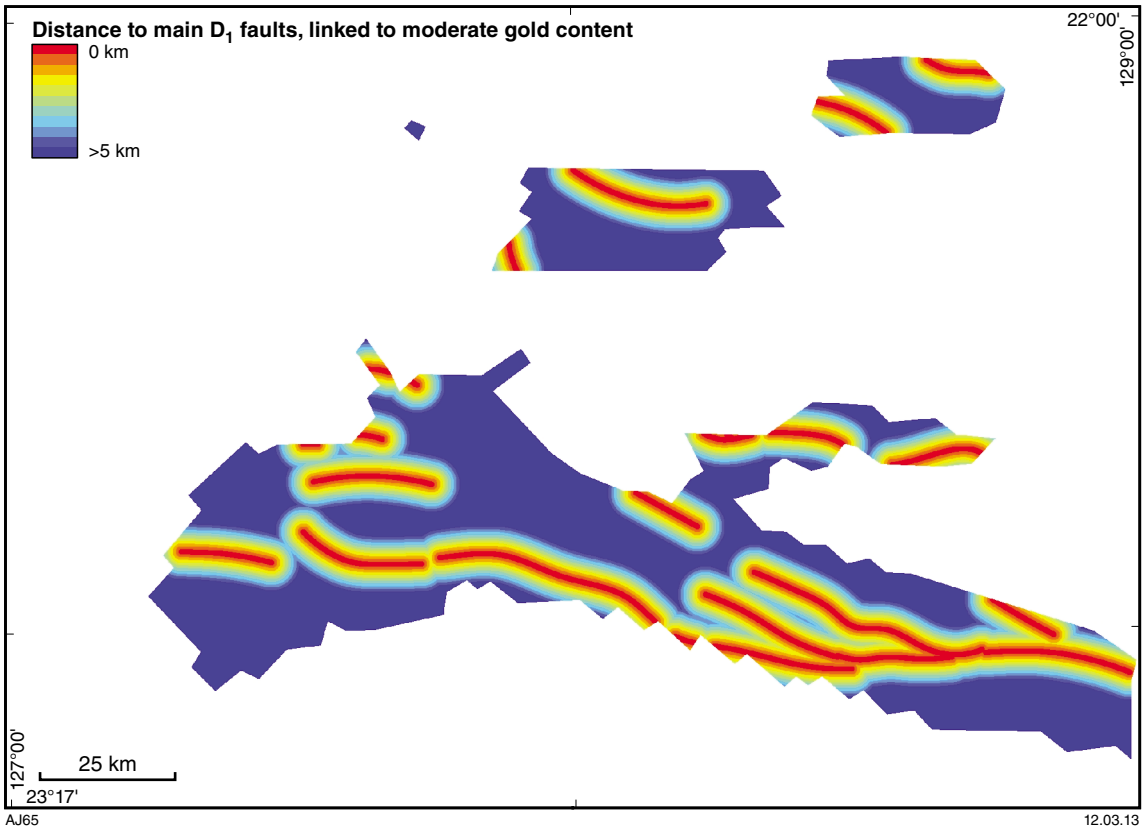

Map 8. **Predictor map for pathway: low to medium (positive) Z Log gold contents over main D_1 faults. Zones shown in red indicate areas very close to main D_1 faults that are linked to high gold contents; zones shown in blue correspond to the contrary**

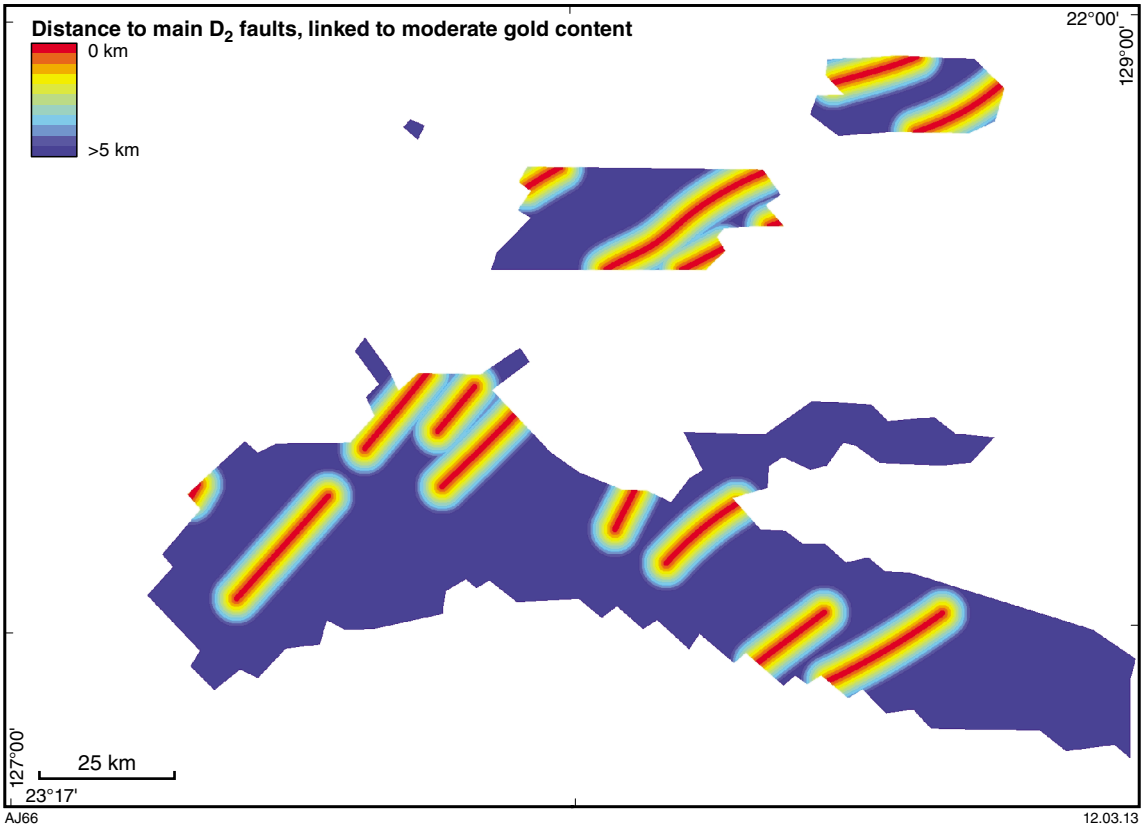

Map 9. **Predictor map for pathway: low to medium (positive) Z Log gold contents over main D_2 faults. Zones shown in red indicate areas very close to main D_2 faults that are linked to high gold contents; zones shown in blue correspond to the contrary**

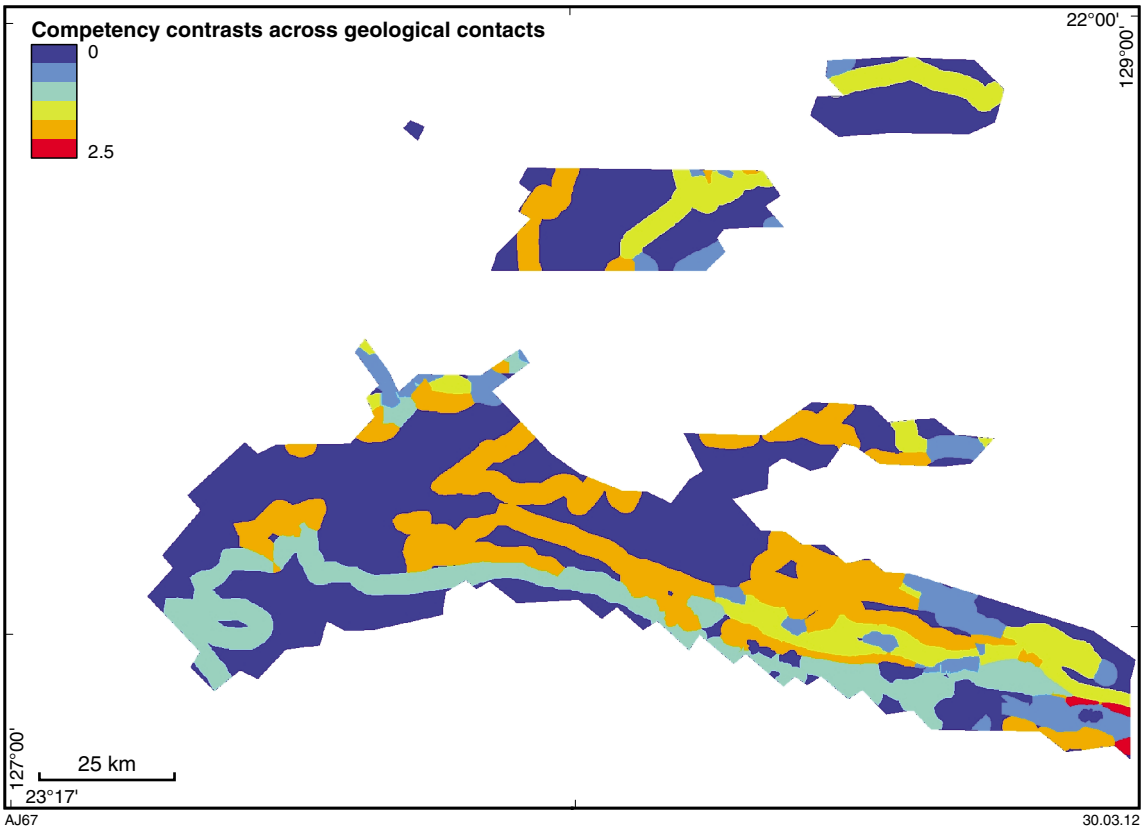

Map 10. **Predictor map for physical trap: competency contrasts across geological contacts**

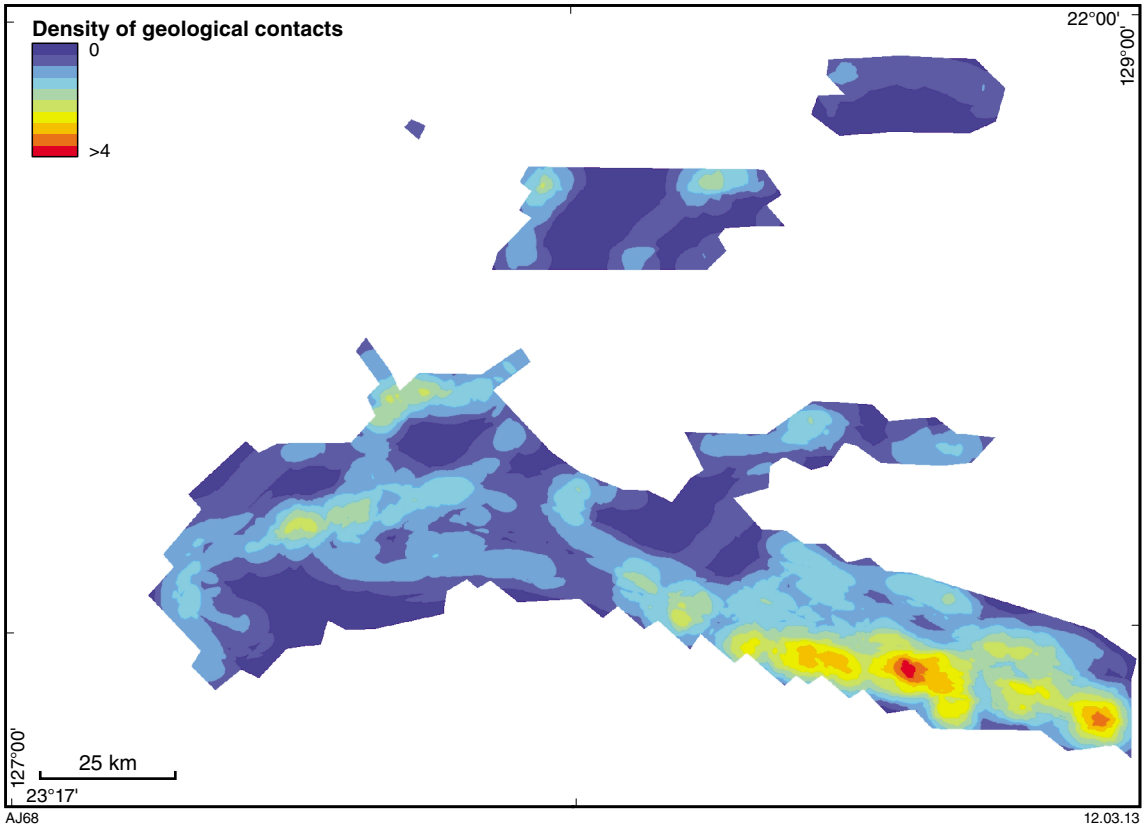

Map 11. **Predictor map for physical trap: density of geological contacts. Red indicates areas of highest intensity of geological contacts; blue corresponds to the contrary**

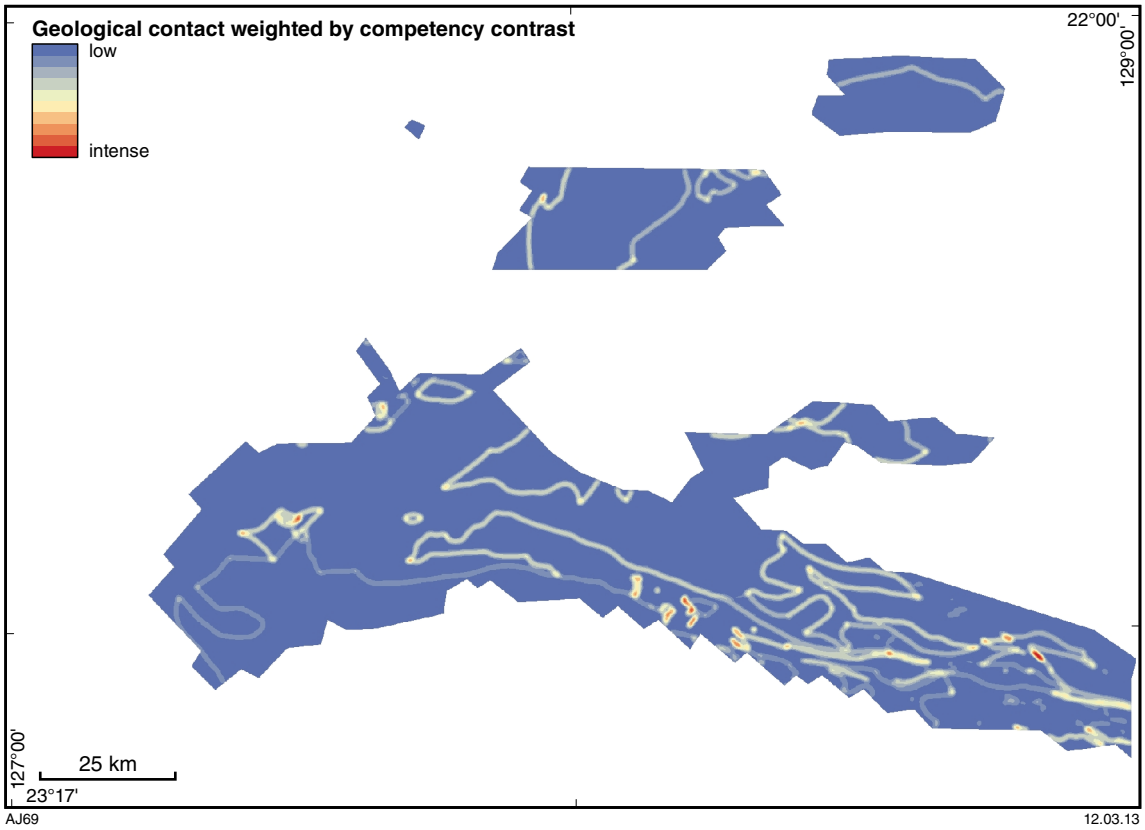

Map 12. **Predictor map for physical trap: competency contrast across geological contacts weighted by competency contrast. Red indicates areas with the most intense competency contrast weighted by geological contact; blue corresponds to the contrary**

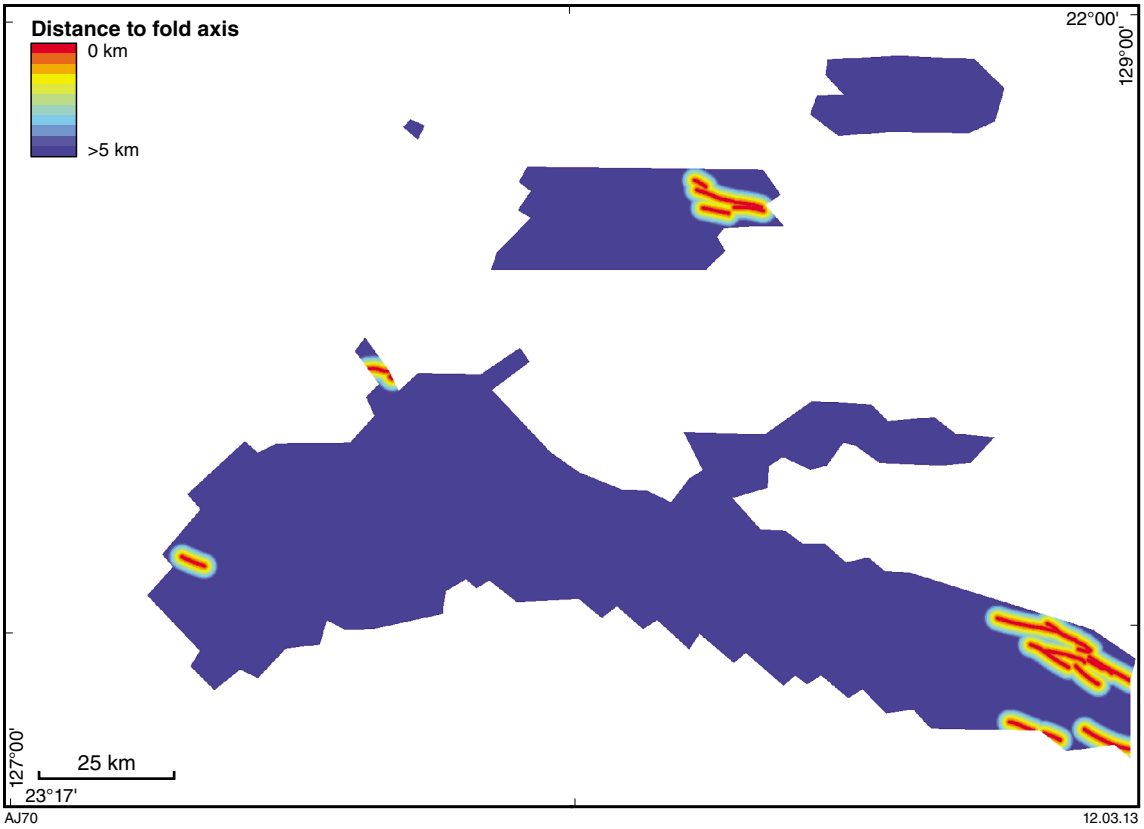

Map 13. **Predictor map for physical trap: proximity to fold axes. Red indicates areas closest to fold axes; blue corresponds to areas farthest from fold axes**

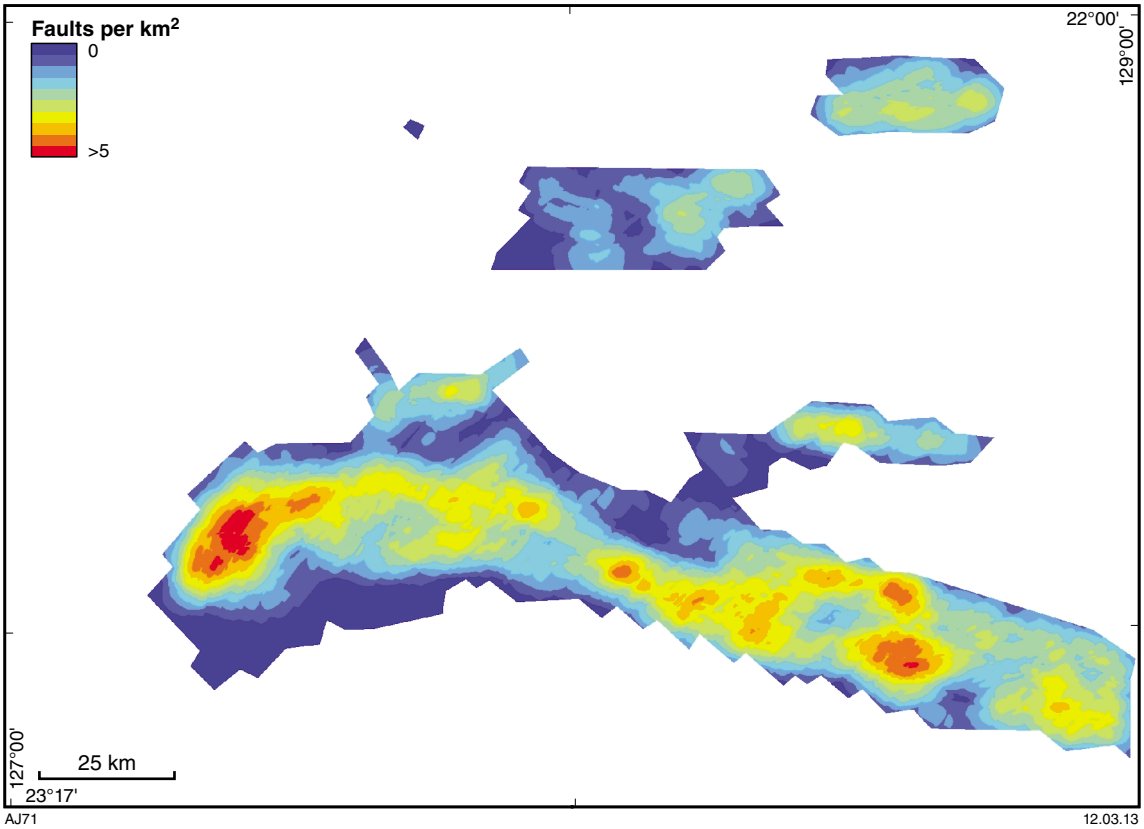

Map 14. **Predictor map for physical trap: fault density. Red indicates areas with the most numerous faults; blue corresponds to the contrary**

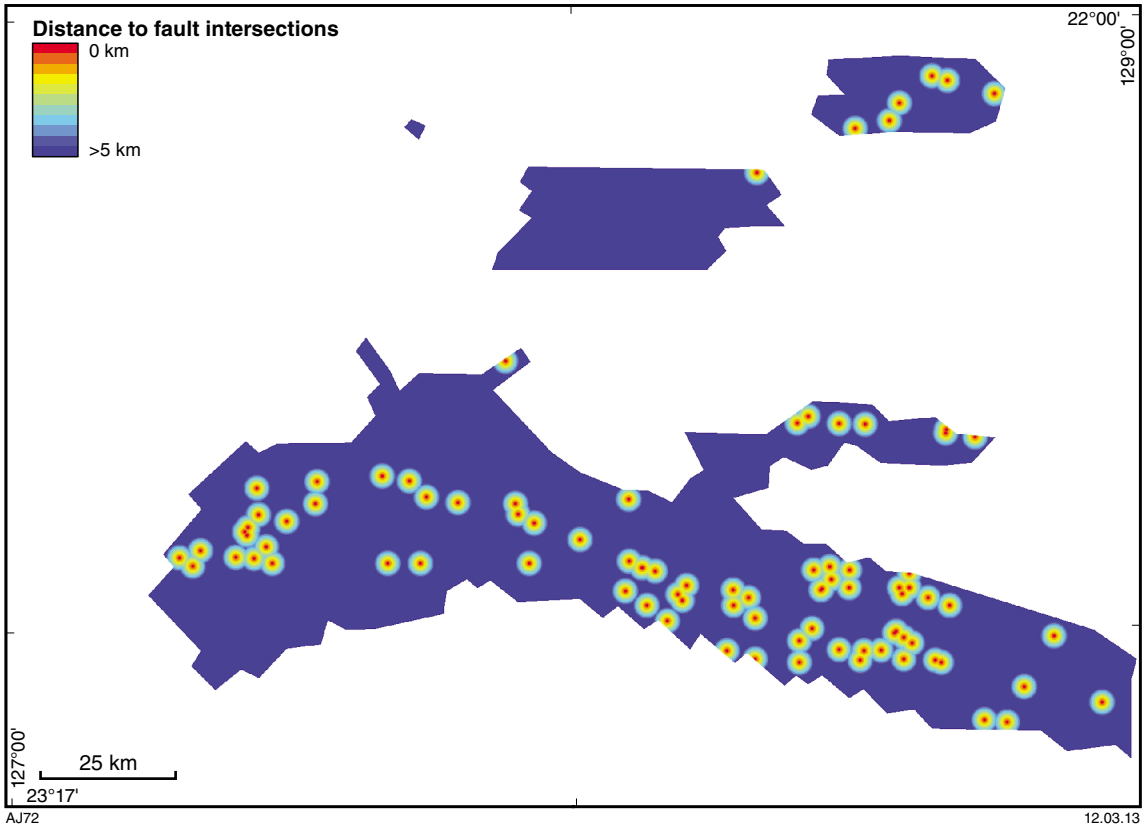

Map 15. **Predictor map for physical trap: proximity to D_1 fault – D_2 fault intersections. Red indicates areas close to fault intersections; blue corresponds to the contrary**

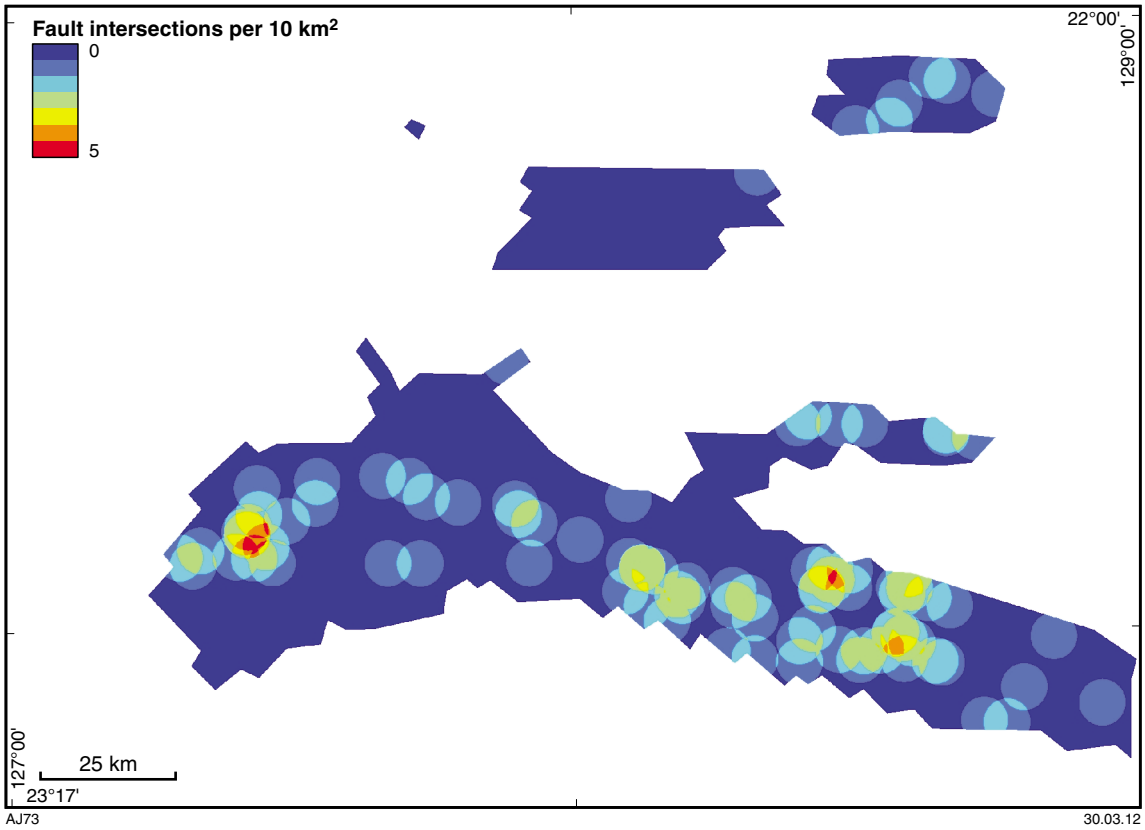

Map 16. **Predictor map for physical trap: proximity to fault intersection density. Red indicates areas with high density per square kilometre of fault intersection; blue corresponds to areas with low density per square kilometre of fault intersection**

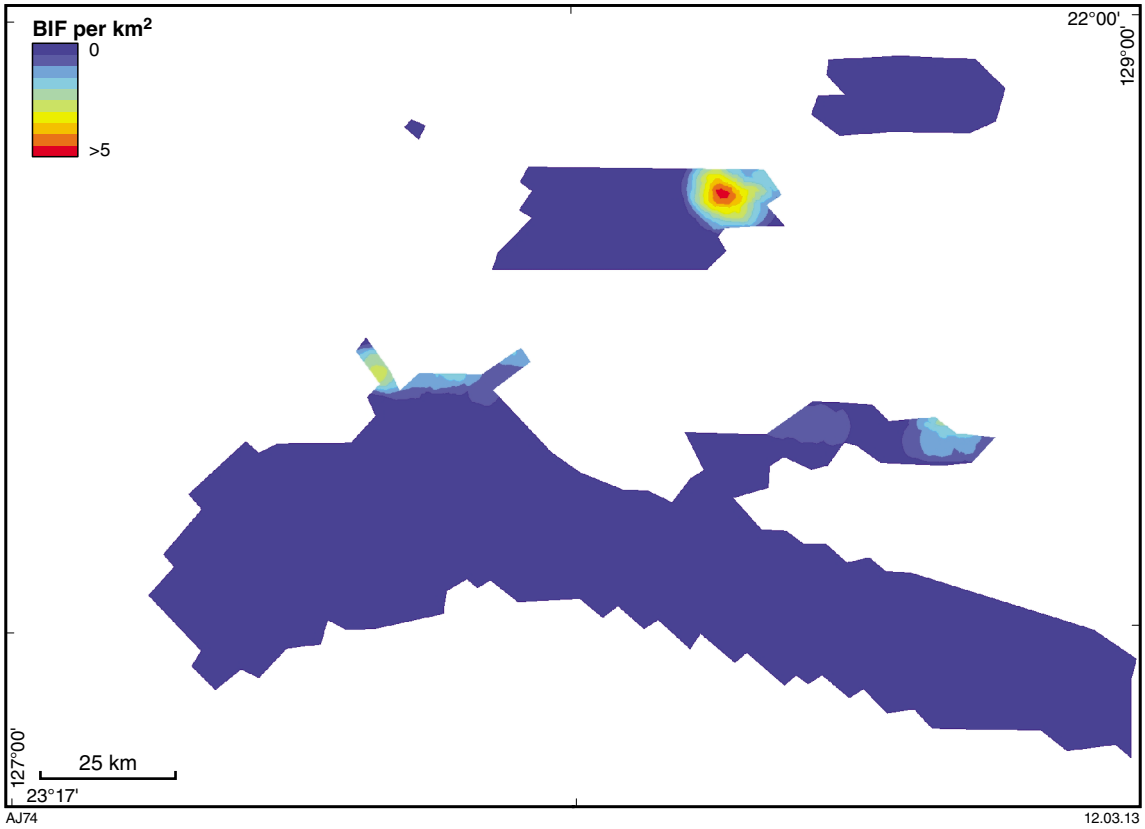

Map 17. **Predictor map for chemical trap: Fe-rich rocks (banded iron-formation, BIF). Red indicates areas with the most numerous occurrences of BIF; blue corresponds to the contrary**

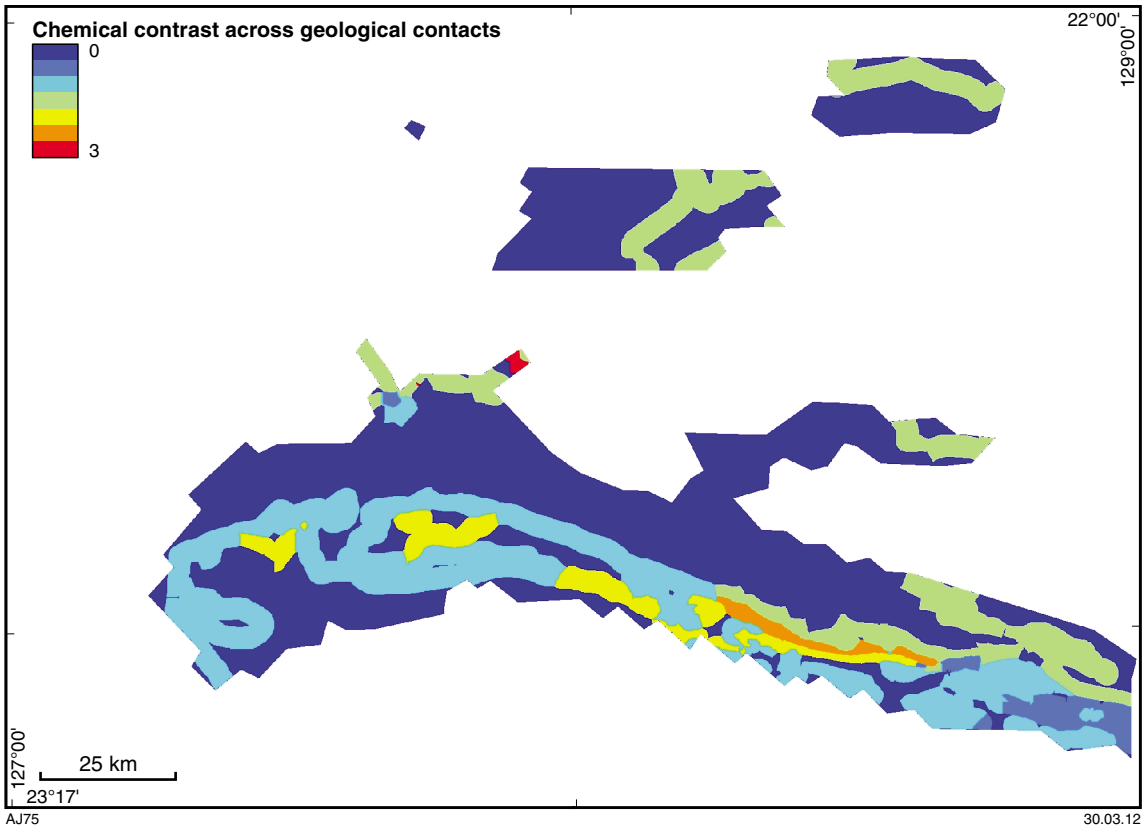

Map 18. Predictor map for chemical trap: chemical contrast across geological contacts

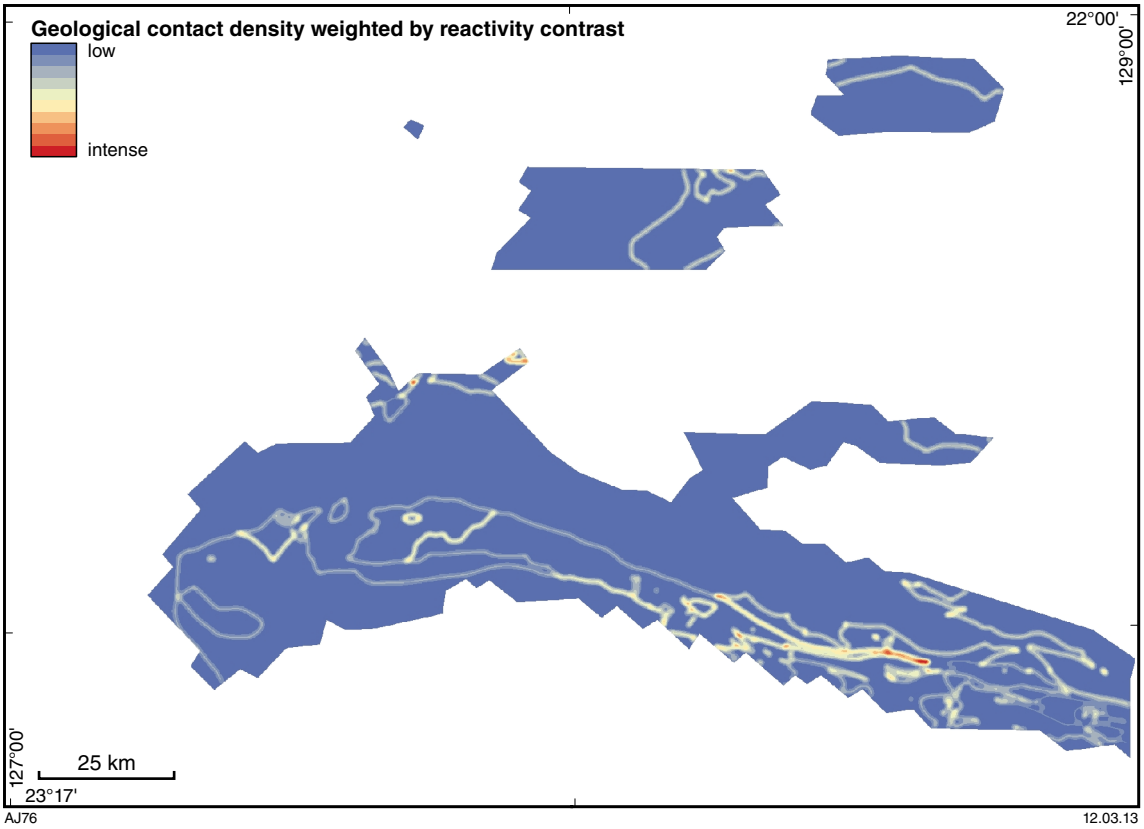

Map 19. **Predictor map for chemical trap: geological contact density weighted by chemical contrast. Red indicates areas with highest density of geological contacts; blue corresponds to the contrary**

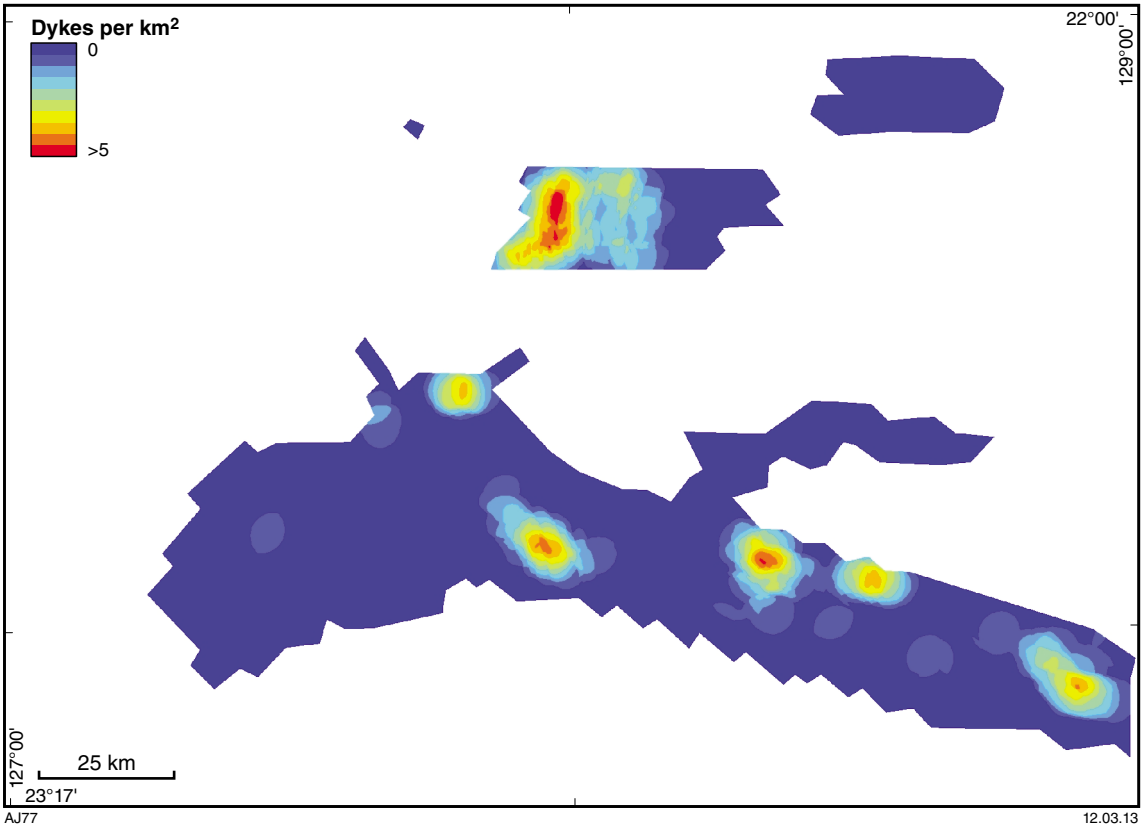

Map 20. **Predictor map for chemical trap: dolerite dyke density. Red indicates areas with the most numerous dykes per square kilometre; blue corresponds to the contrary**

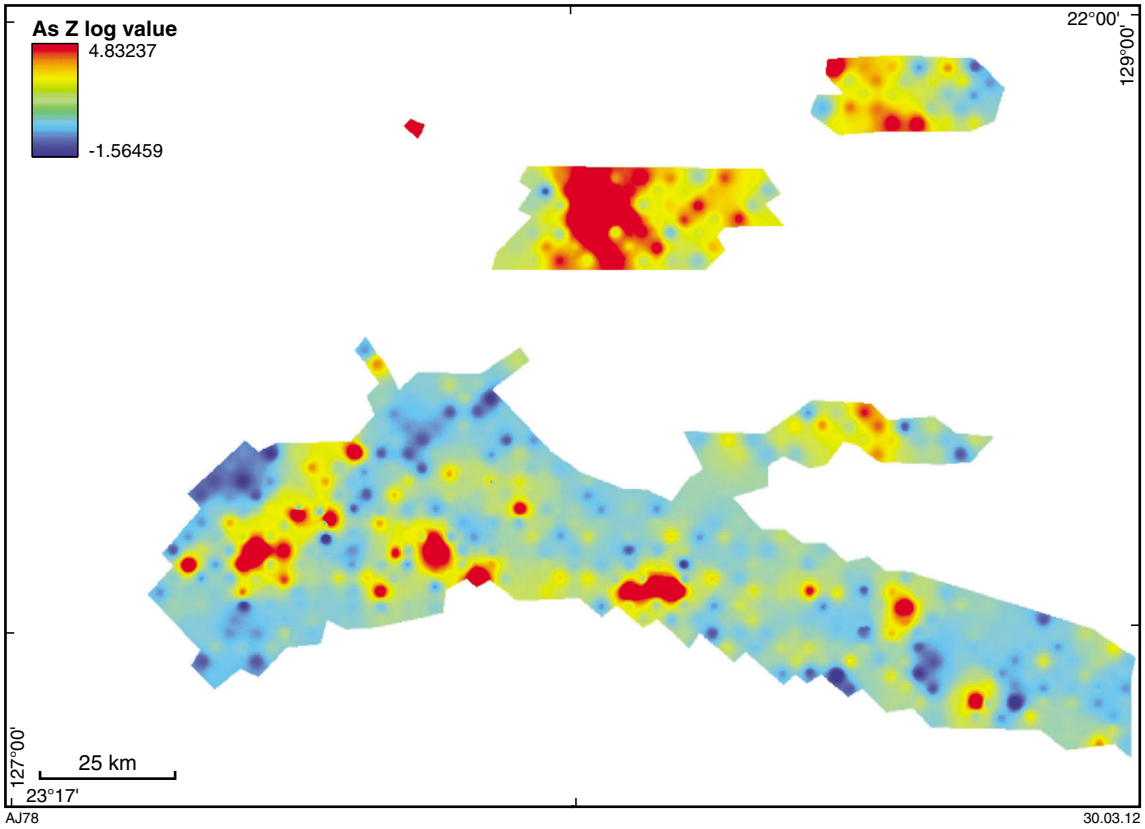

Map 21. **Predictor map for chemical trap: arsenic (As) Z log value. Red indicates areas with the highest arsenic content within the area of interest; blue corresponds to the contrary**

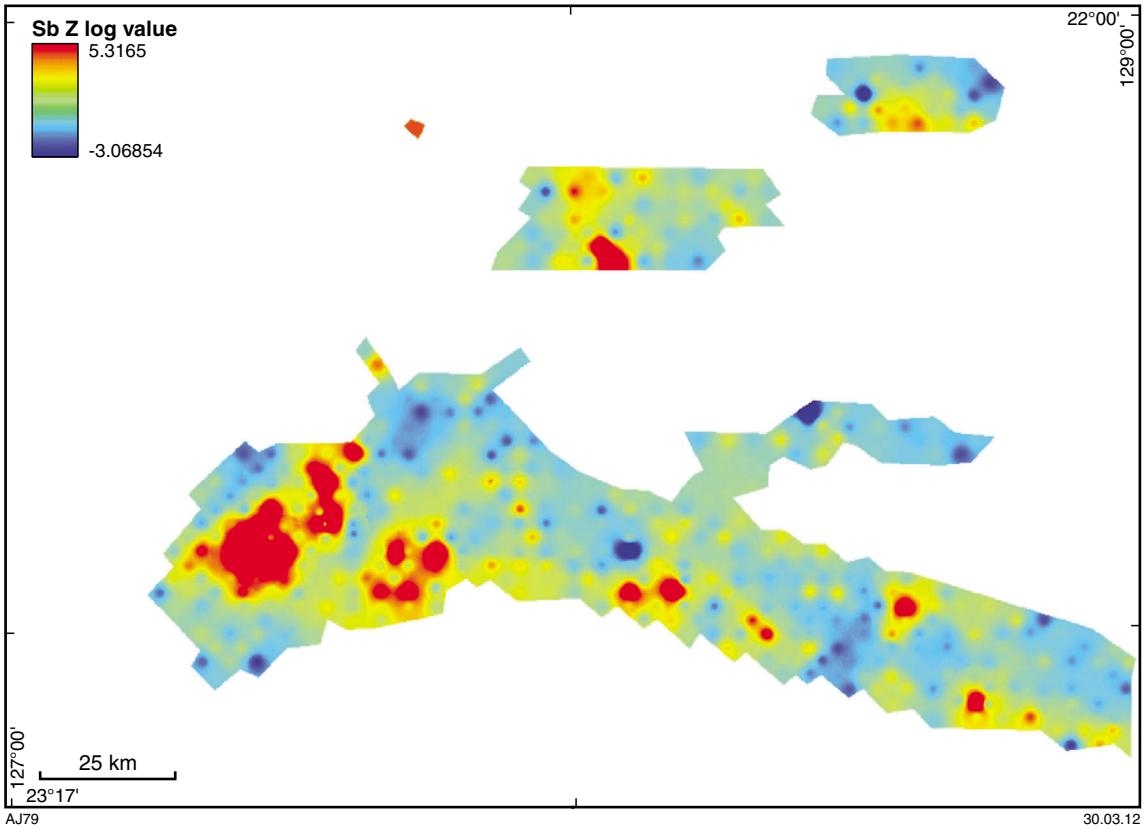

Map 22. **Predictor map for chemical trap: antimony (Sb) Z log value. Red indicates areas with the highest antimony content within the area of interest; blue corresponds to the contrary**

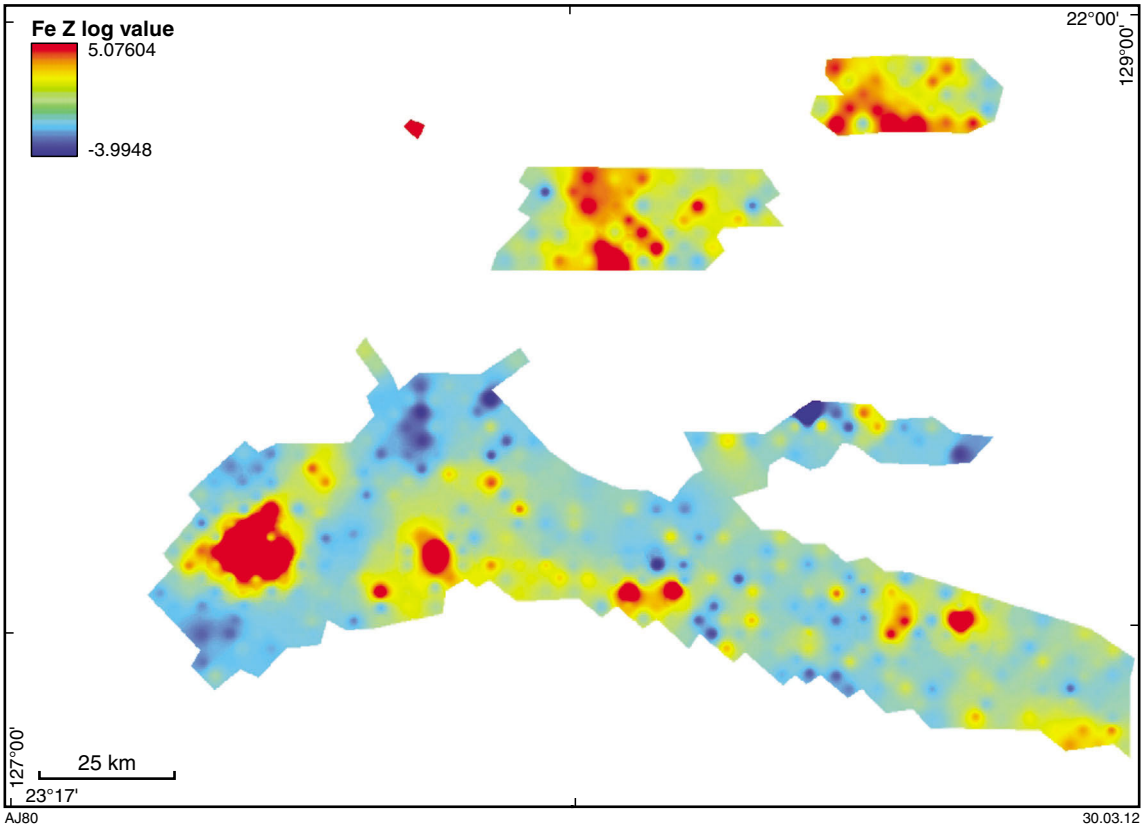

Map 23. **Predictor map for chemical trap: iron (Fe) Z log value. Red indicates areas with the highest iron content; blue corresponds to the contrary**

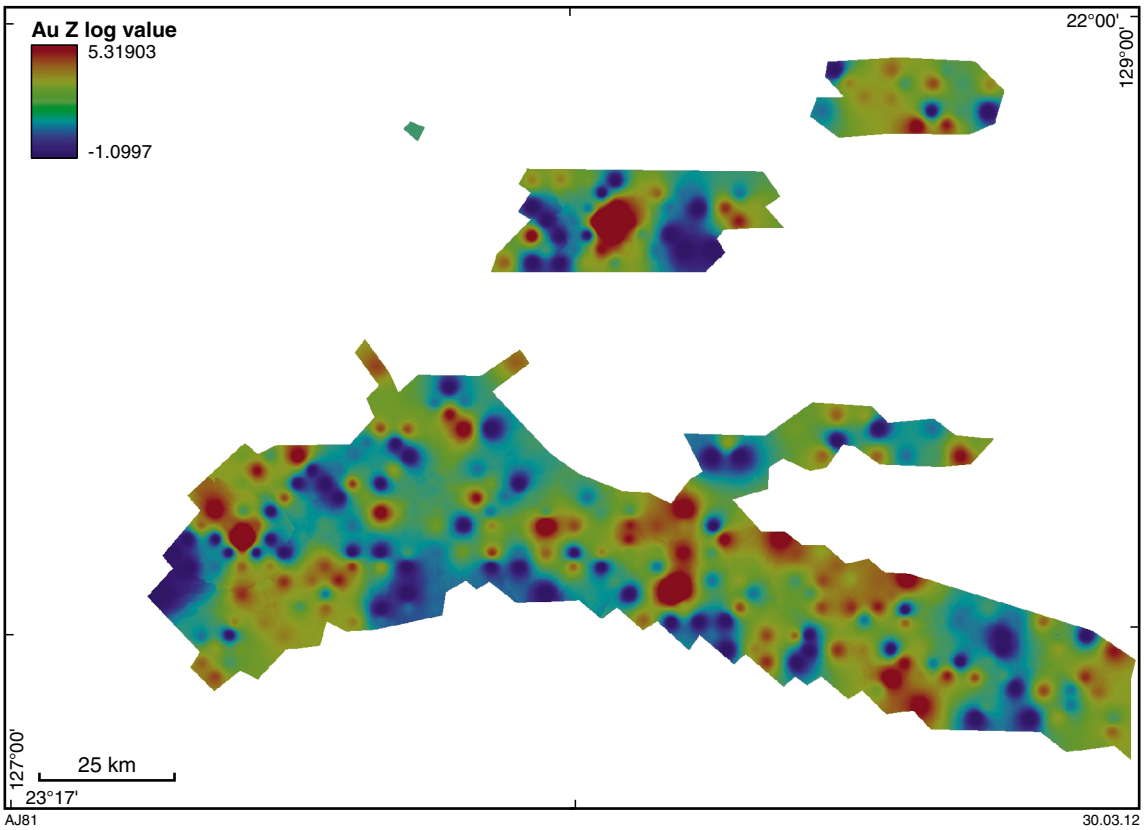

Map 24. **Predictor map for chemical trap: gold (Au) Z log value. Red indicates areas with the highest gold content; blue corresponds to the contrary**

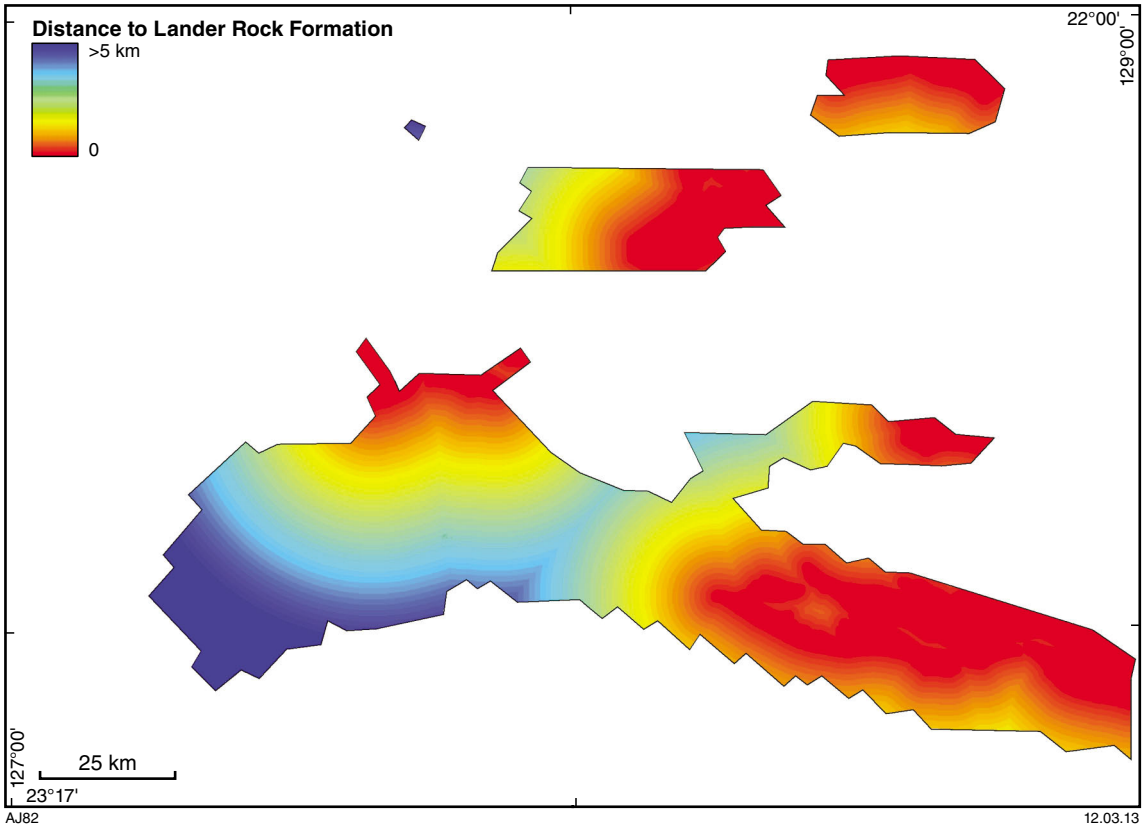

Map 25. **Predictor map for source: proximity to Lander Rock Formation (Aileron Province), up to 5 km distance**

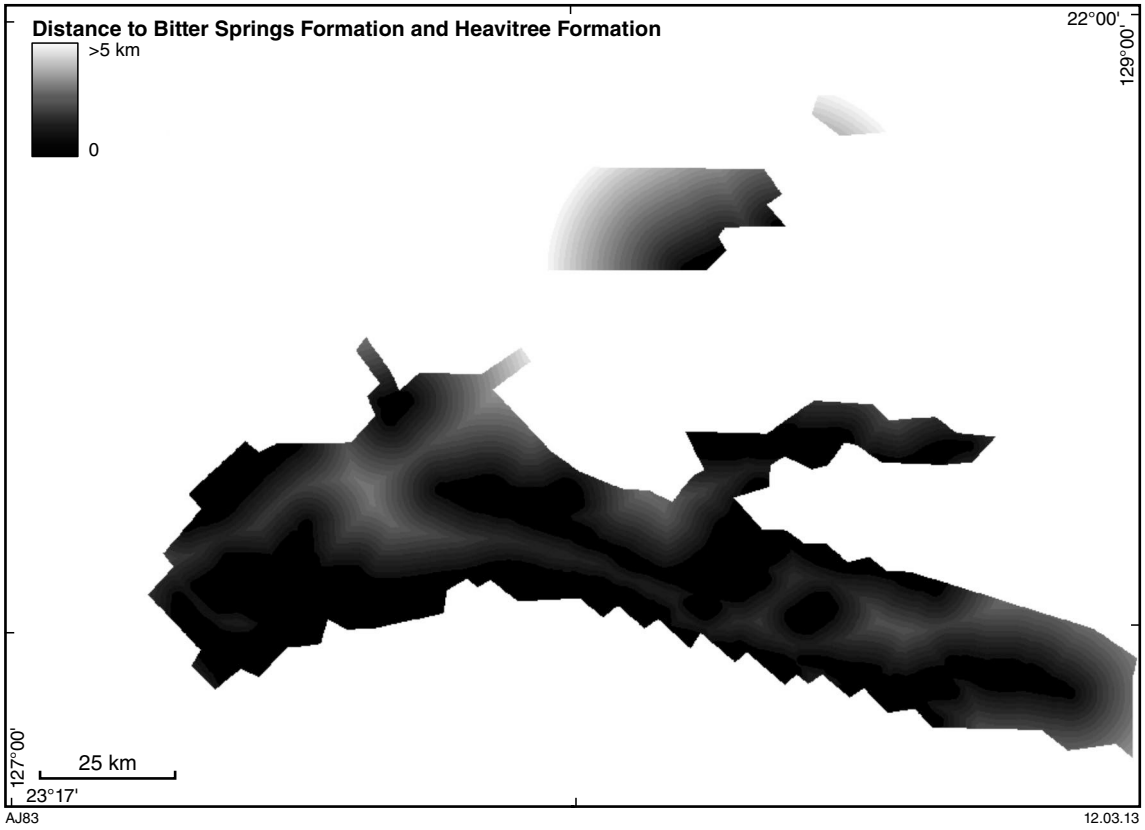

Map 26. **Predictor map for source: proximity to sandstone (Bitter Springs Formation and Heavitree Quartzite), up to 5 km distance**

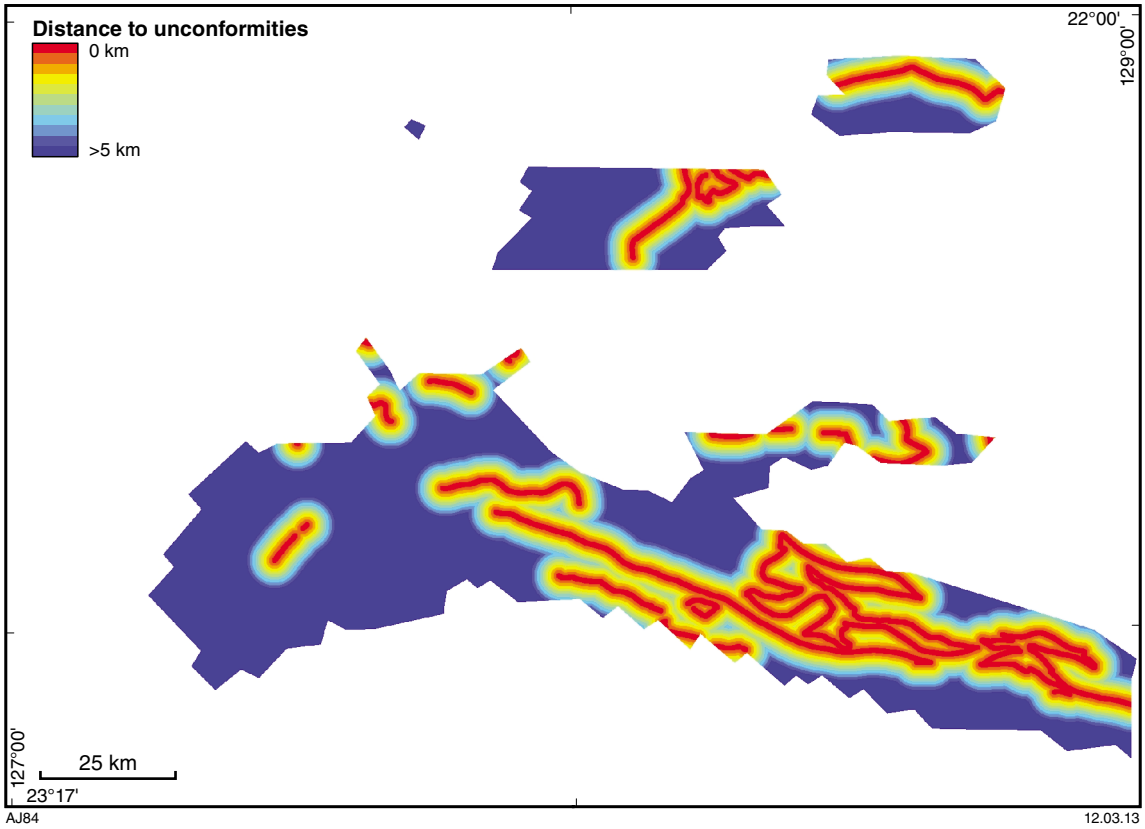

Map 27. **Predictor map for pathway: proximity to unconformities with a 5 km buffer zone**

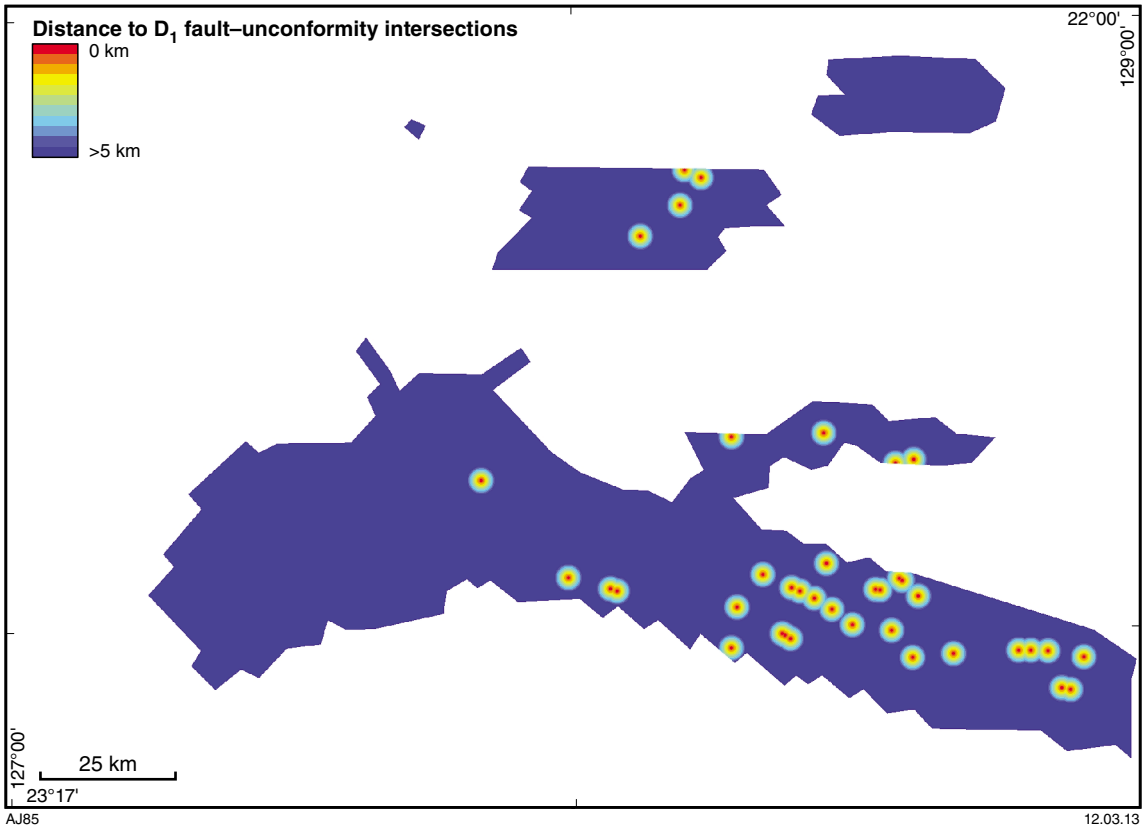

Map 28. **Predictor map for physical trap: proximity to D_1 fault–unconformity intersections. Red indicates areas close to fault intersections; blue corresponds to the contrary**

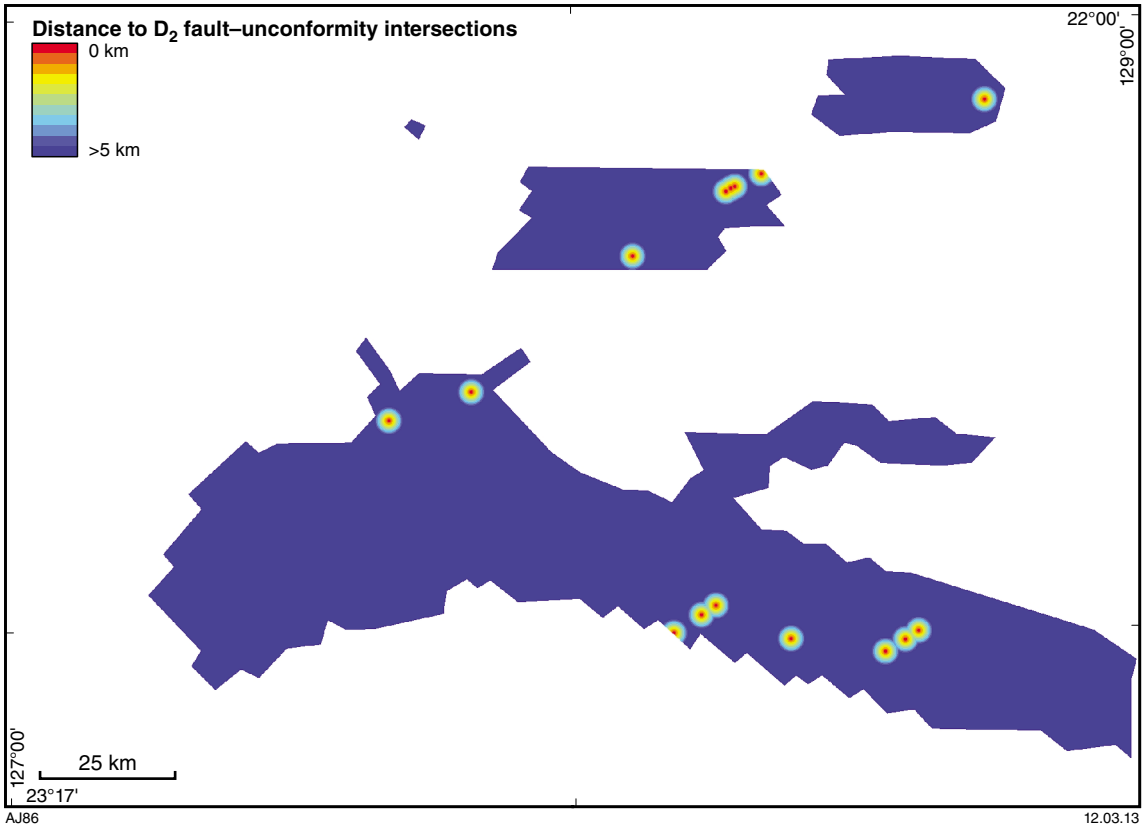

Map 29. **Predictor map for physical trap: proximity to D_2 fault–unconformity intersections. Red indicates areas close to fault intersections; blue corresponds to the contrary**

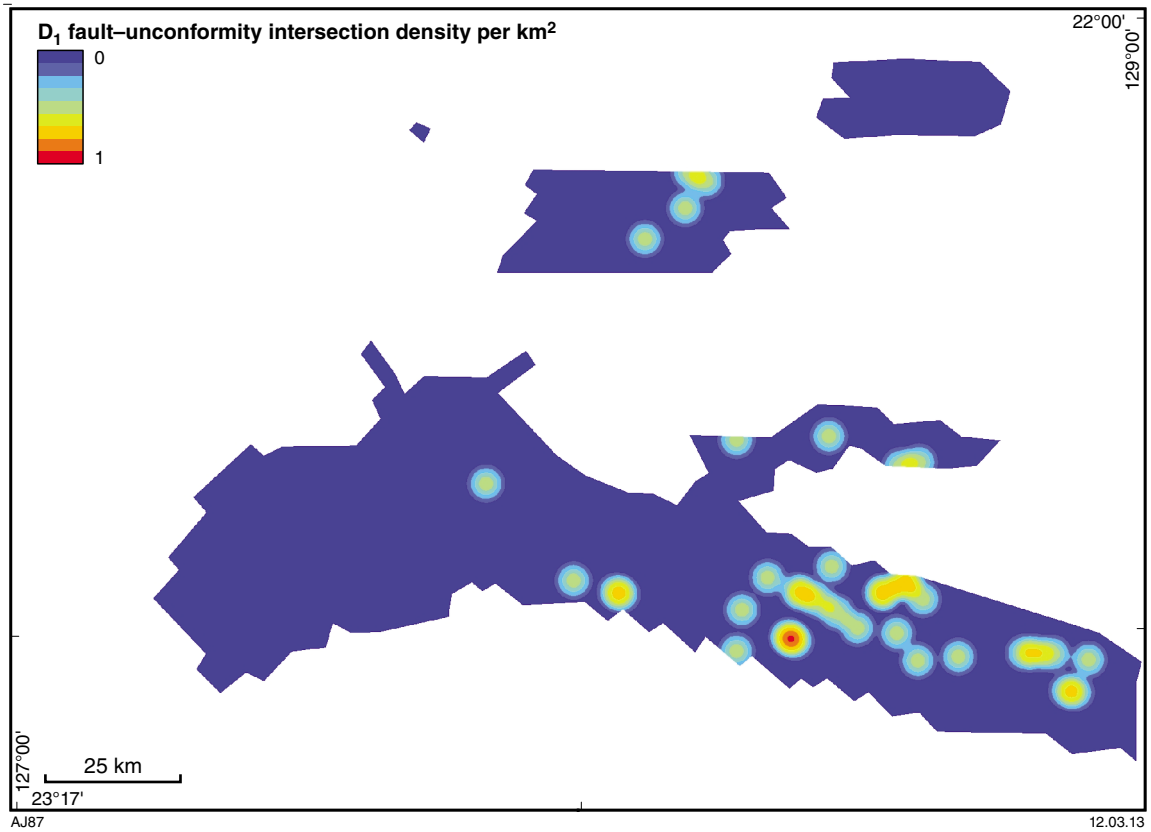

Map 30. **Predictor map for physical trap: proximity to D_1 fault–unconformity intersection density. Red indicates areas with high density per square kilometre of fault–unconformity intersection; blue corresponds to area with low density per square kilometre of fault–unconformity intersection**

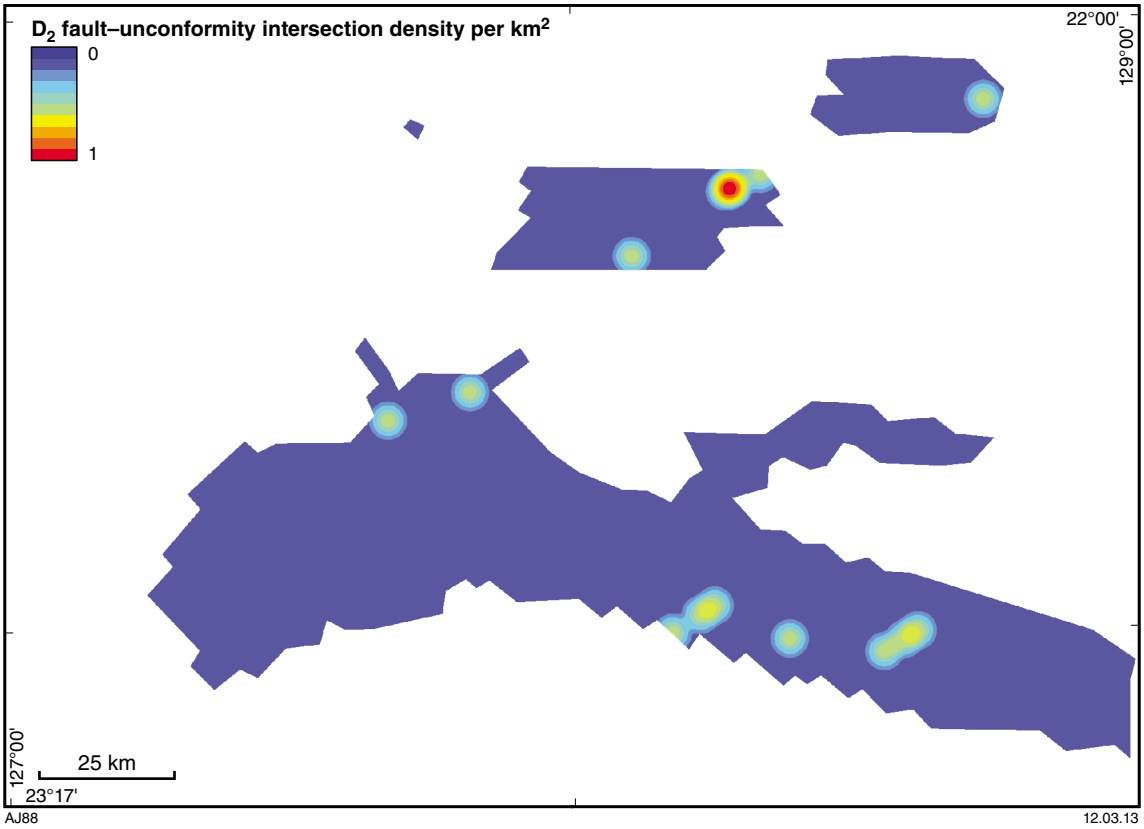

Map 31. **Predictor map for physical trap: proximity to D_2 fault-unconformity intersection density. Red indicates areas with high density per square kilometre of fault–unconformity intersection; blue corresponds to area with low density per square kilometre of fault–unconformity intersection**

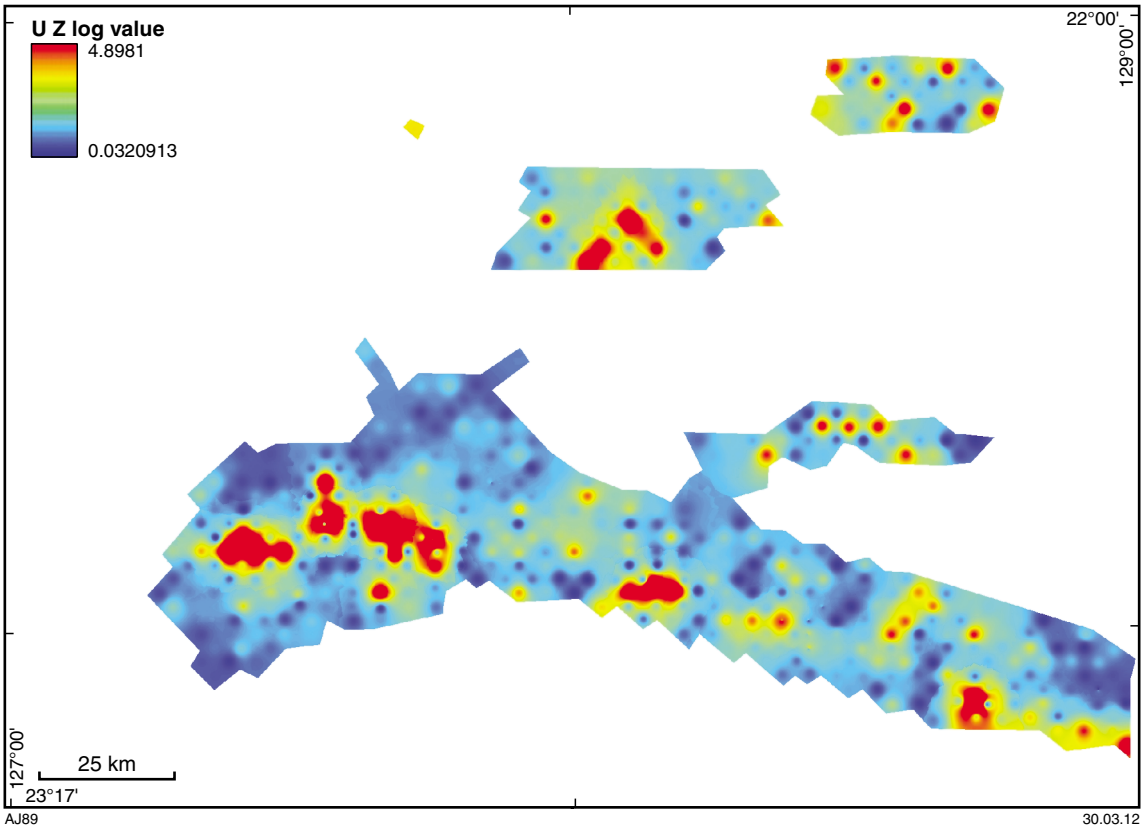

Map 32. **Predictor map for chemical trap: uranium (U) Z log value. Red indicates areas with the highest uranium contents; blue corresponds to the contrary. Data from GSWA geochemical datasets (GSWA, 2009b)**

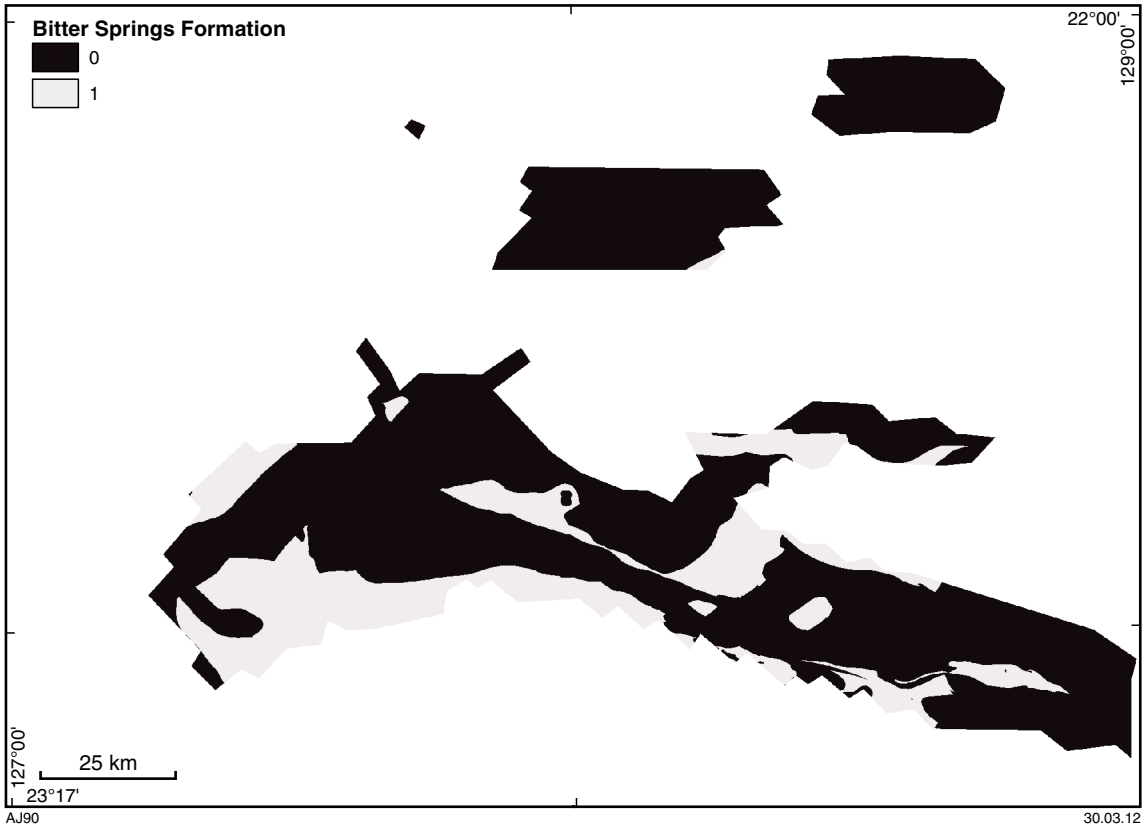

Map 33. **Predictor map for chemical trap: Bitter Springs Formation. Zero corresponds to the absence of the Bitter Springs Formation; 1 corresponds to its presence**

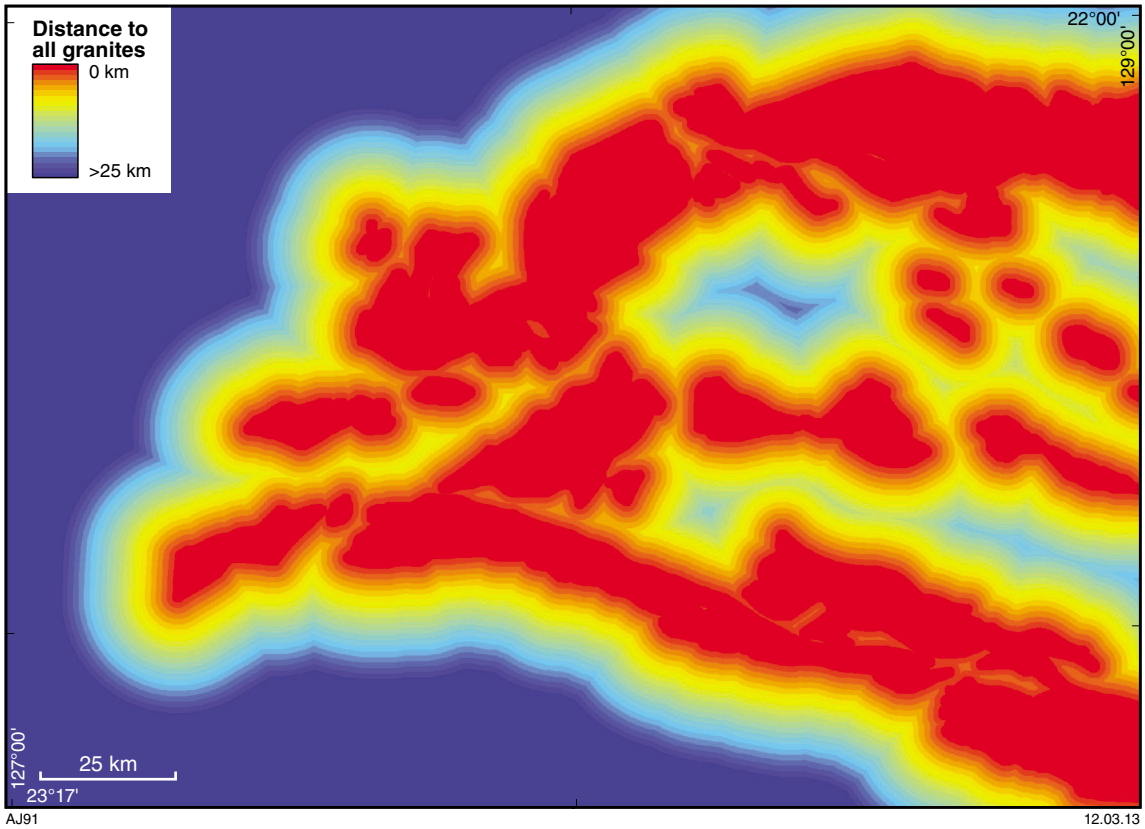

Map 34. Predictor map for source: proximity to all granites (up to 25 km)

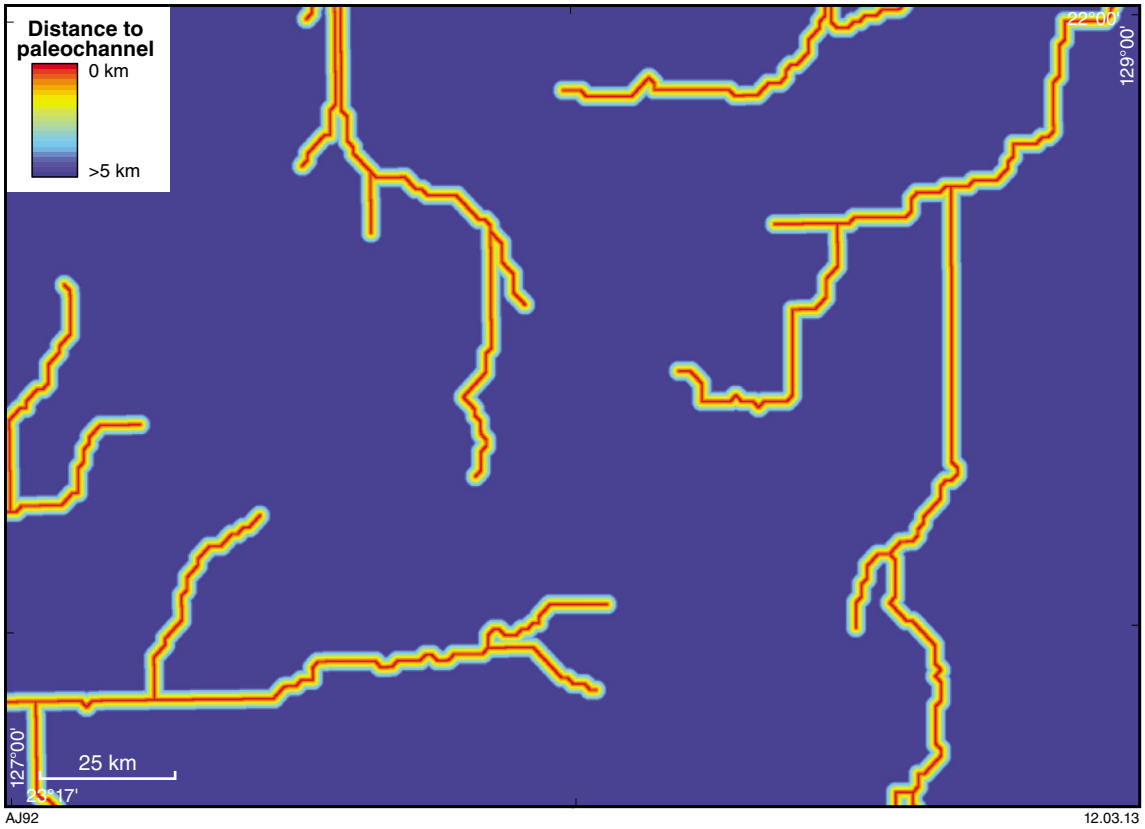

Map 35. Predictor map for pathway: proximity to paleochannels with a 5 km buffer zone

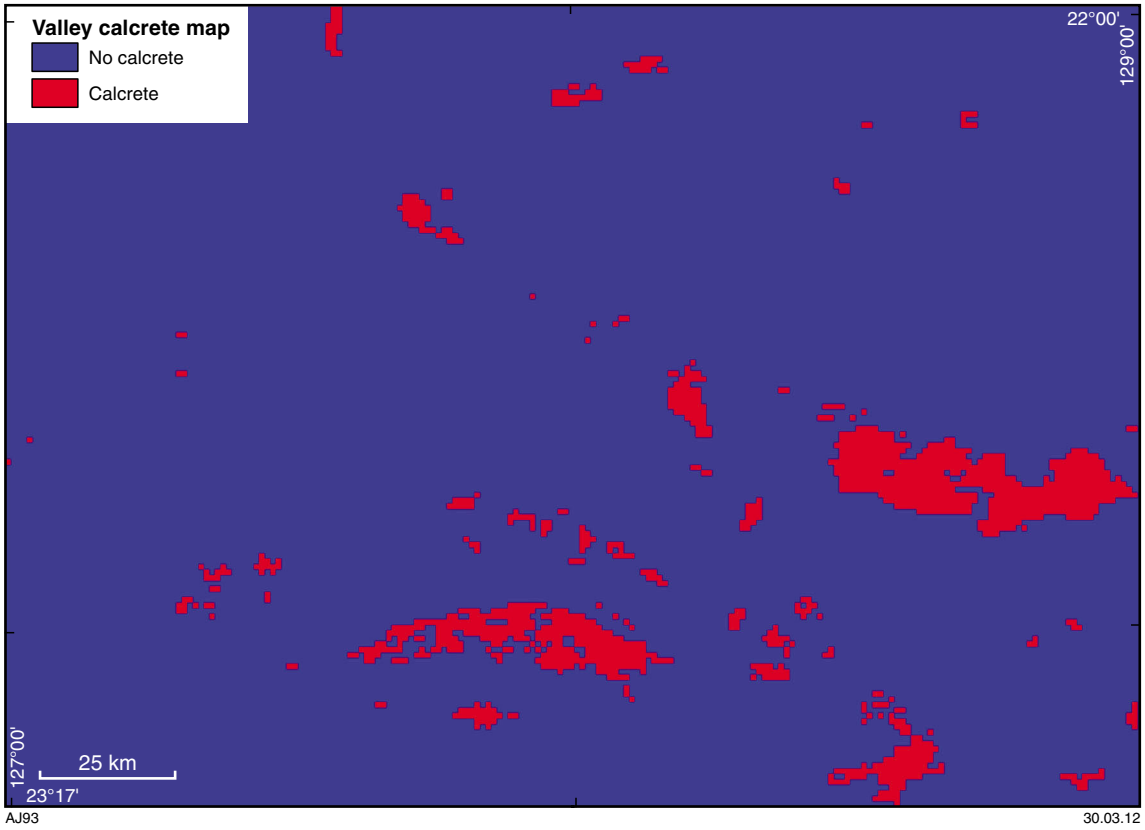

Map 36. Predictor map for physical trap: valley calcrete map. Red indicates the presence of valley calcrete; blue indicates its absence

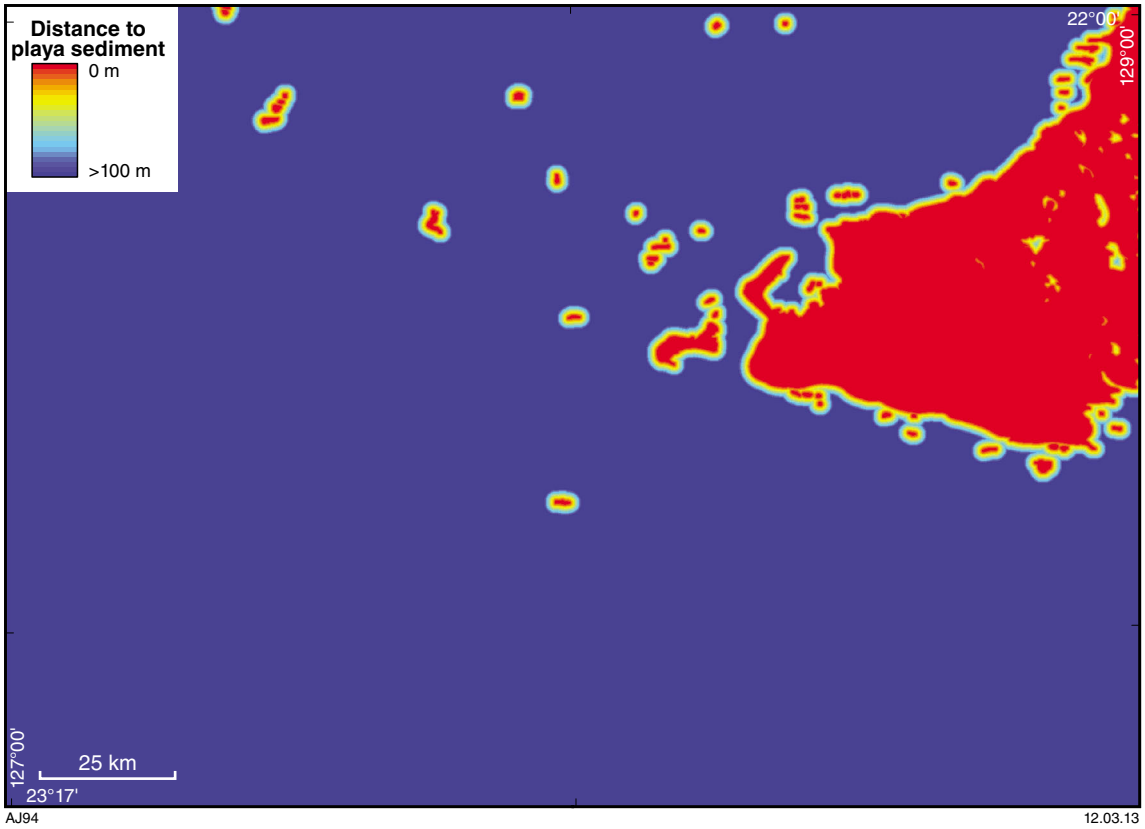

Map 37. **Predictor map for physical trap: proximity to playa sediments map. Red indicates the presence of playa sediments; blue corresponds their absence; other colours make up the 100 m buffer zone**

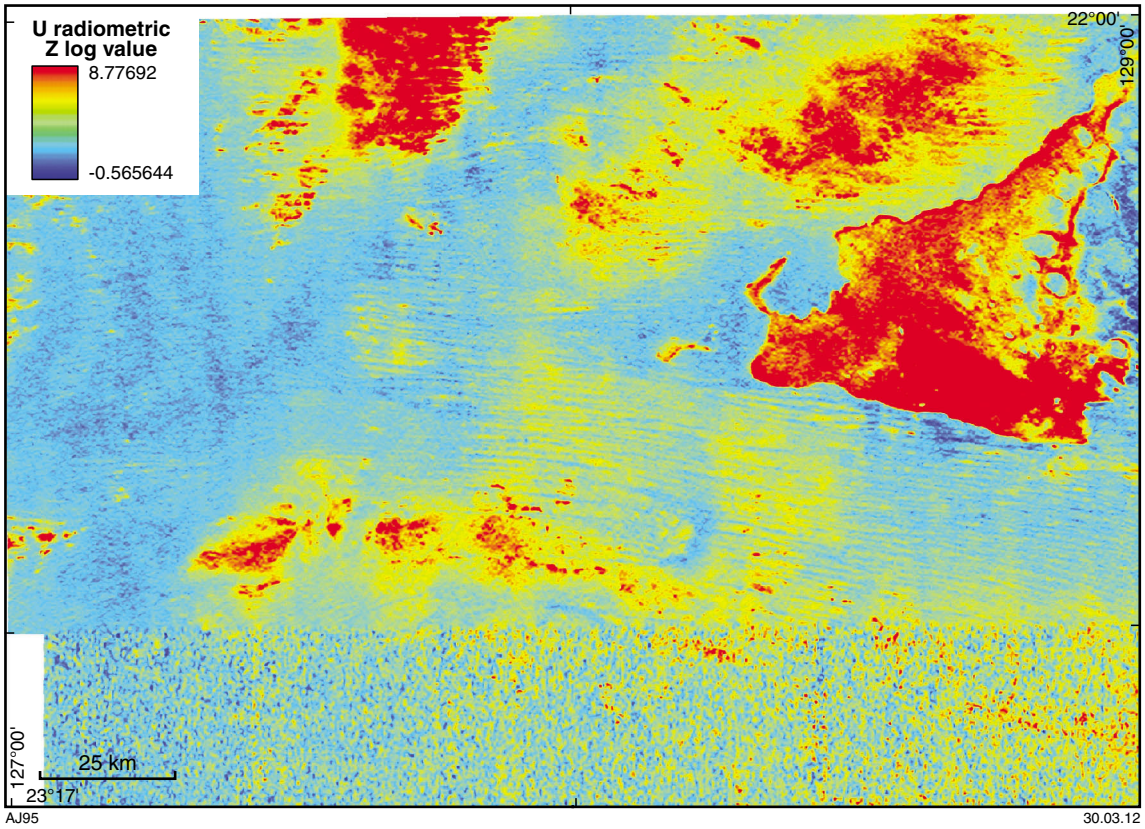

Map 38. **Predictor map for chemical trap: uranium (U) Z log value (radiometrics). Red indicates areas with the highest uranium contents; blue corresponds to the contrary**

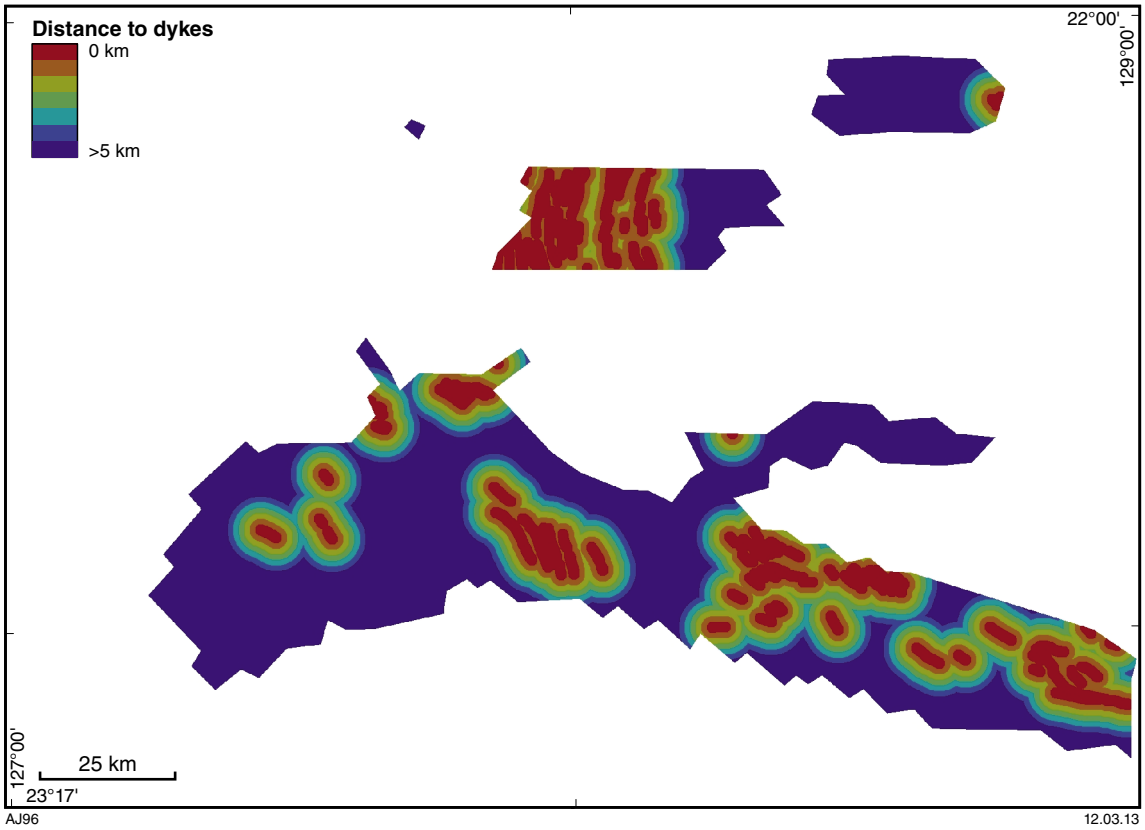

Map 39. Predictor map for source: distance to dykes with a 5 km buffer zone

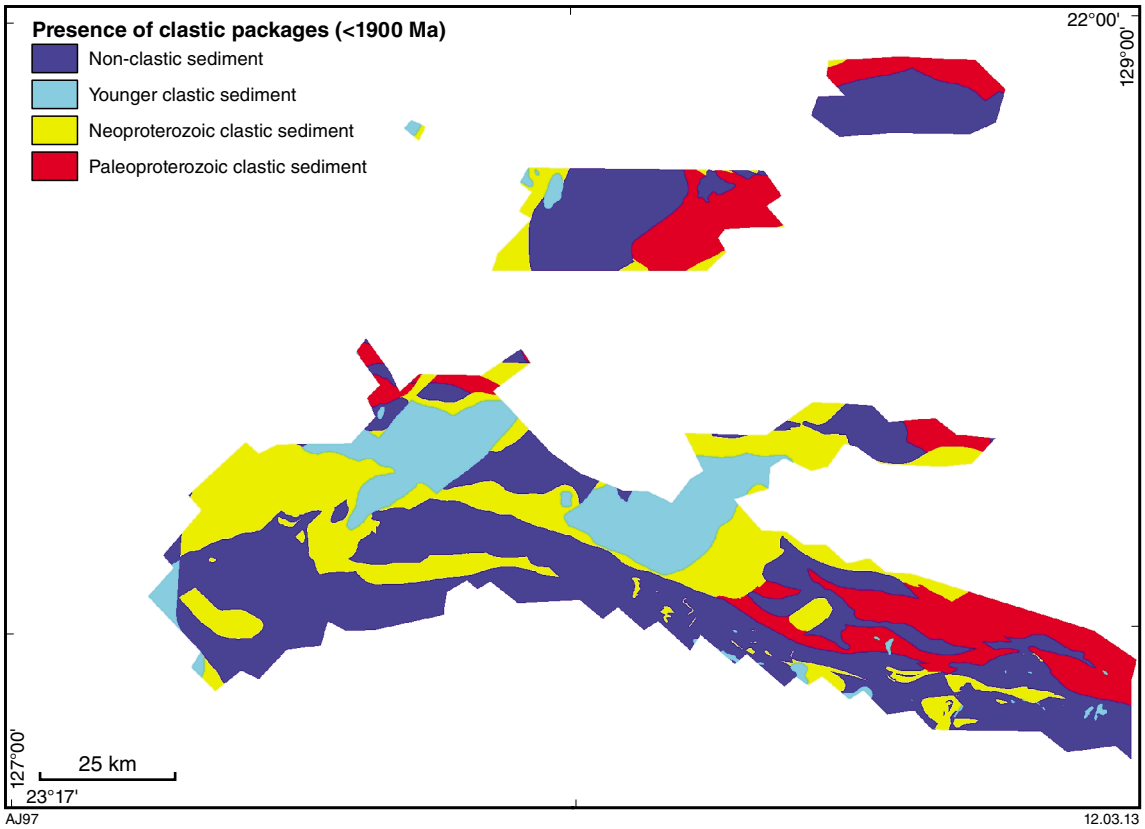

Map 40. Predictor map for source: presence of clastic packages (<1700 Ma)

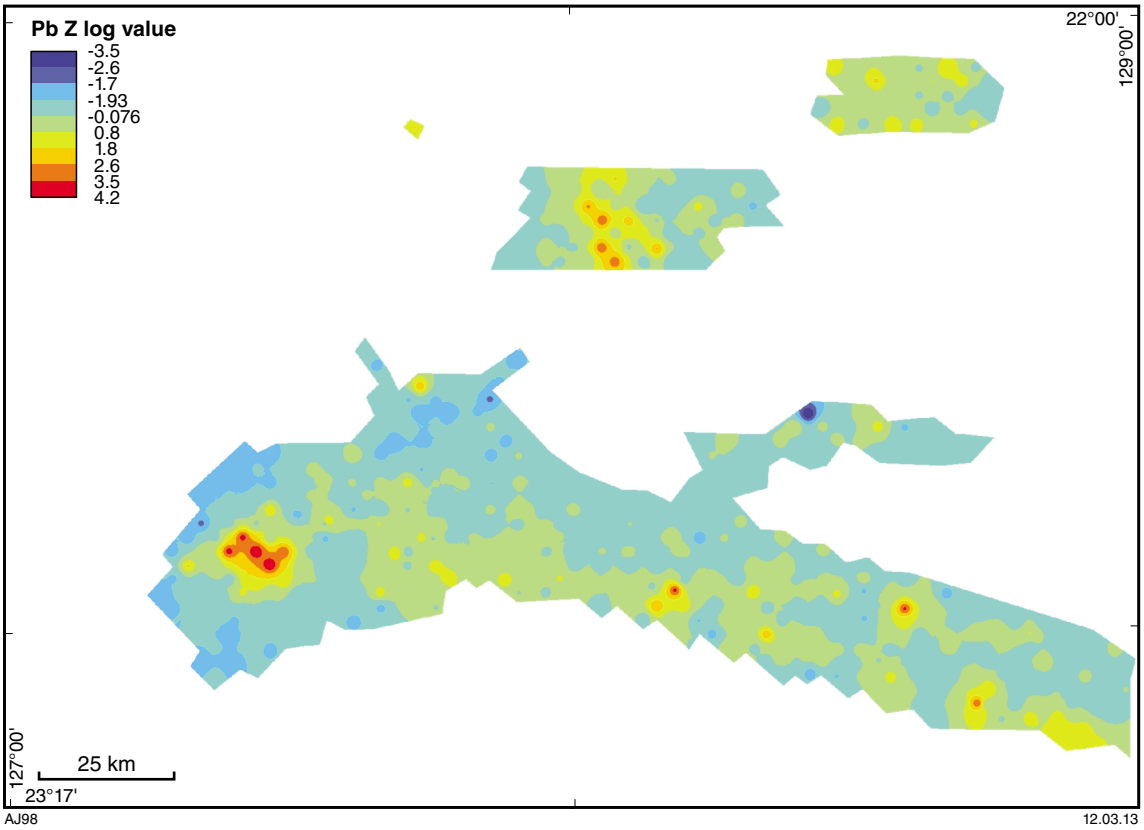

Map 41. **Predictor map for chemical trap: lead (Pb) Z log value. Red indicates zones with the highest lead content, blue corresponds to the contrary**

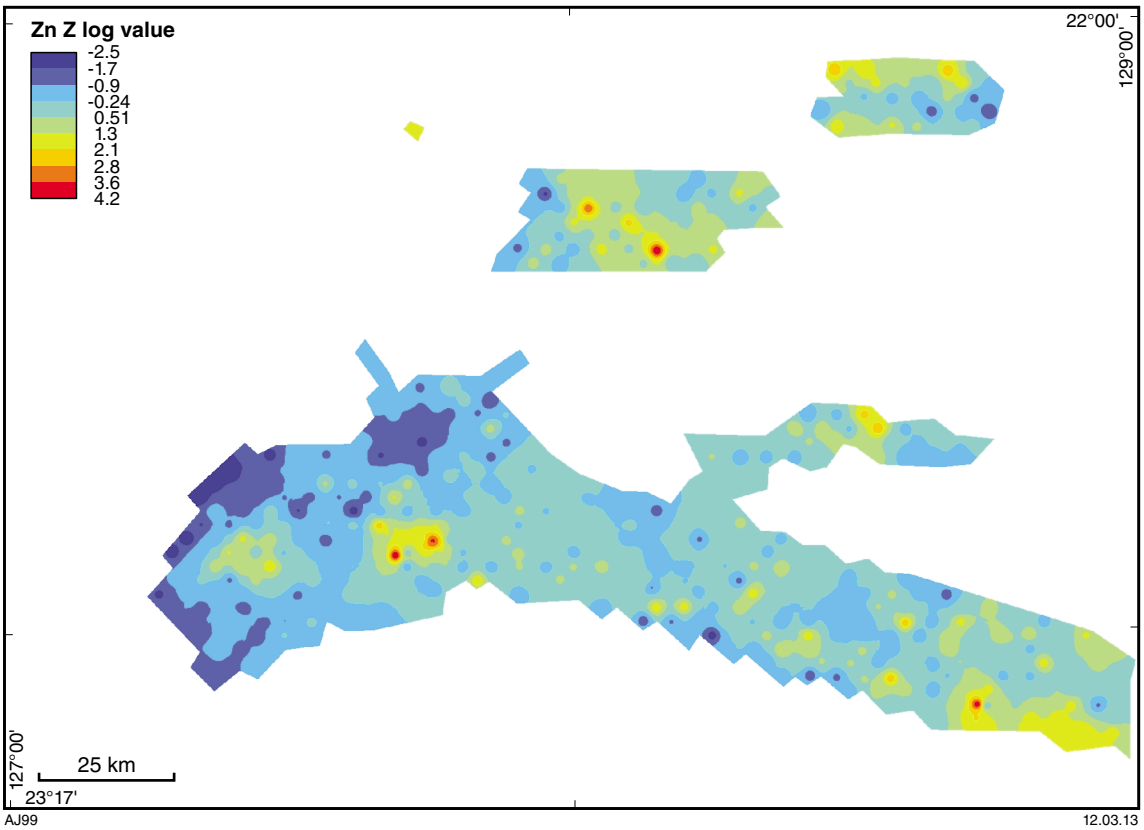

Map 42. **Predictor map for chemical trap: zinc (Zn) Z log value. Red indicates zones with the highest zinc content; blue corresponds to the contrary**

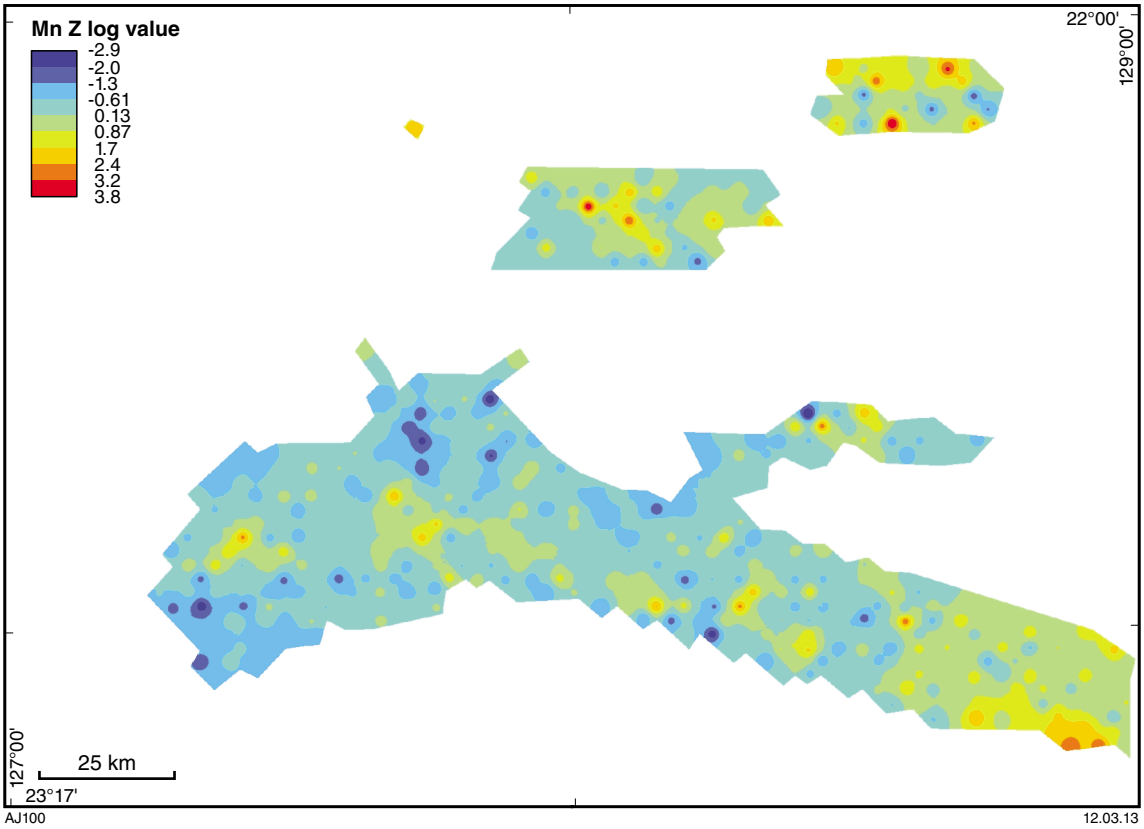

Map 43. **Predictor map for chemical trap: manganese (Mn) Z log value. Red indicates zones with the highest manganese content; blue corresponds to the contrary**

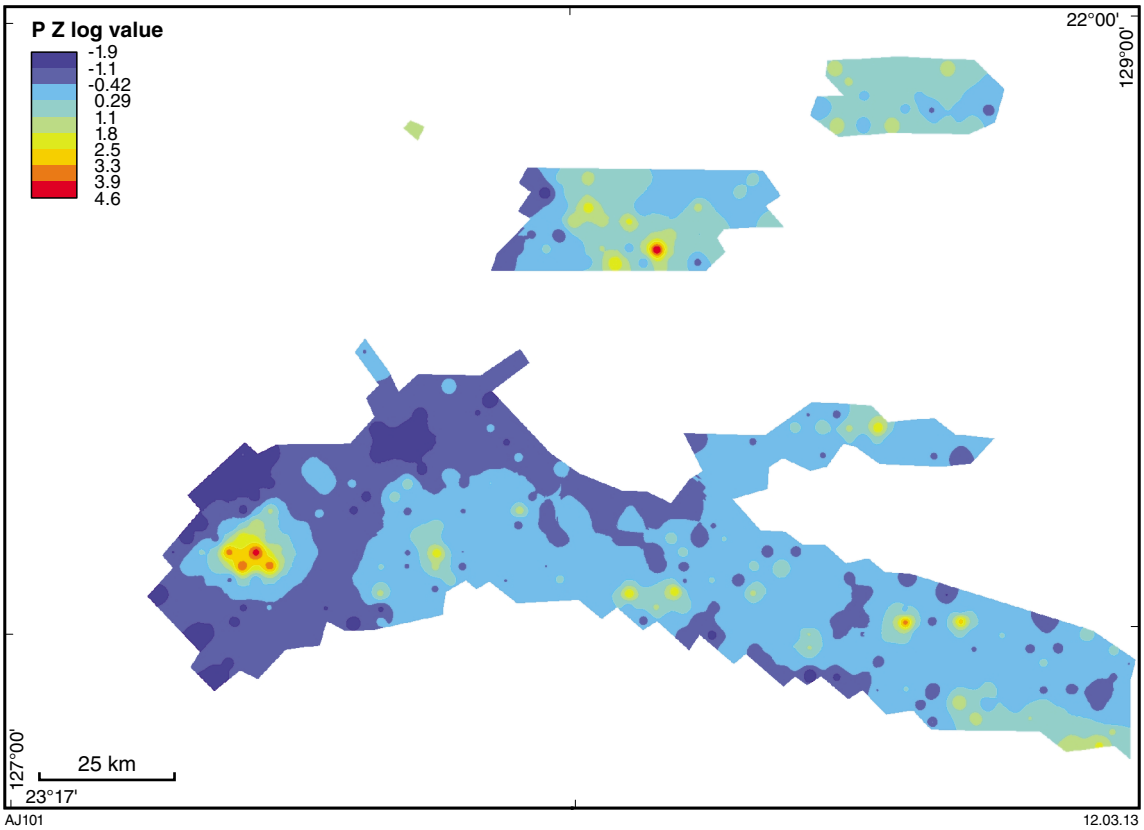

Map 44. **Predictor map for chemical trap: phosphorus (P) Z log value. Red indicates zones with the highest phosphorus content; blue corresponds to the contrary**

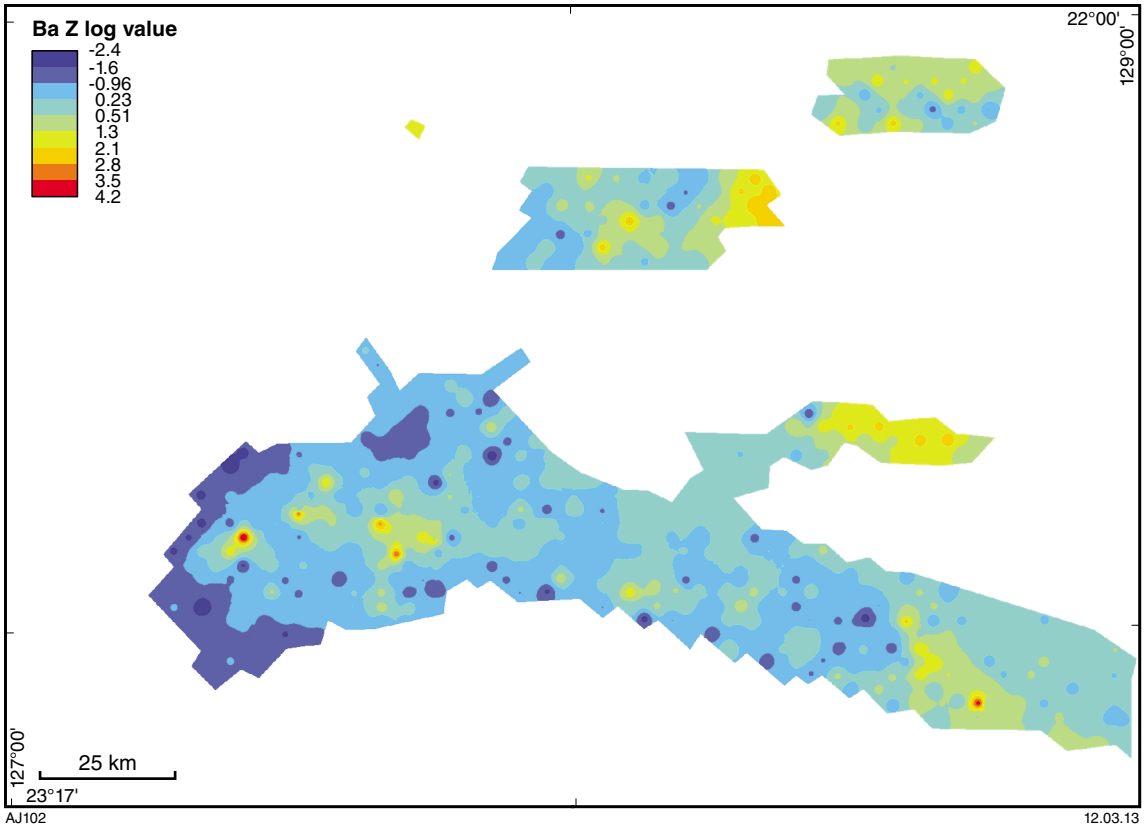

Map 45. **Predictor map for chemical trap: barium (Ba) Z log value. Red indicates zones with the highest barium content; blue corresponds to the contrary**

There has been minimal mineral exploration in the Paleoproterozoic West Arunta Orogen and in its cover rocks, located in remote east-central Western Australia. In this study, an integrated geological–geophysical approach, incorporating all available geoscientific data, was used to interpret the gross structure and deformation history of the region. The resulting geological and geophysical maps were then used for a GIS-based prospectivity analysis based on the mineral systems approach.

Reconnaissance-scale mineral prospectivity mapping for gold, uranium, and sediment-exhalative (SedEx) style base-metal mineralization incorporates spatial analysis techniques for data integration and analysis. The targeting criteria selected were based on a mineral systems model for deposit formation and the approach used involves production of a series of predictor maps based on the occurrence of geological features associated with the relevant model. Each predictor map was then related to metal source, fluid pathways, and chemical and physical trap zones.

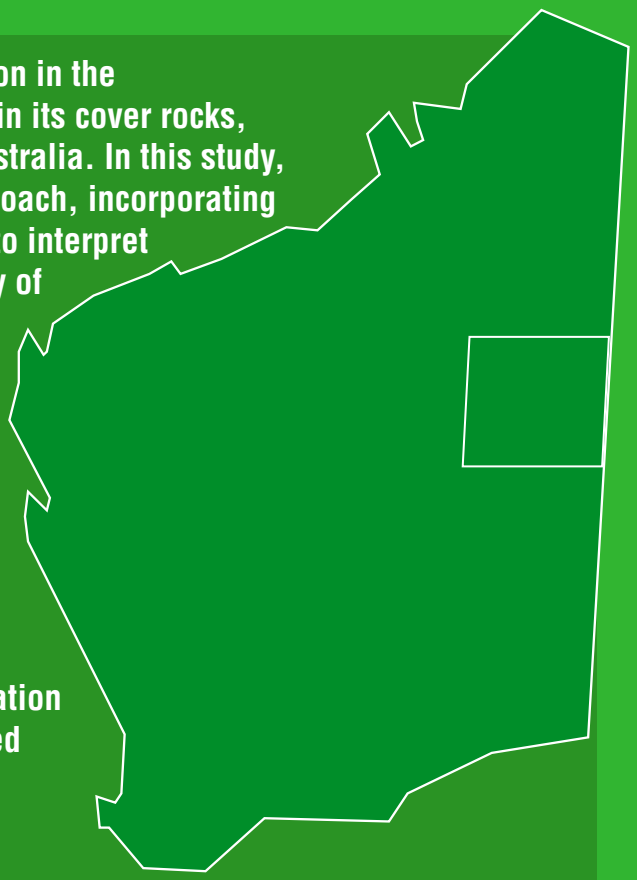

Further details of geological products and maps produced by the Geological Survey of Western Australia are available from:

Information Centre
Department of Mines and Petroleum
100 Plain Street
EAST PERTH WA 6004
Phone: (08) 9222 3459 Fax: (08) 9222 3444

http://www.dmp.wa.gov.au/GSWApublications

Joly et al.

AN INTEGRATED GEOLOGICAL AND GEOPHYSICAL STUDY OF THE WEST ARUNTA OROGEN AND ITS MINERAL PROSPECTIVITY

REPORT 113